Forschungszentrum Karlsruhe
Technik und Umwelt

Wissenschaftliche Berichte
FZKA 5868

Neutronics of the High Flux Test Region of the International Fusion Materials Irradiation Facility (IFMIF)

E. Daum, U. Fischer, A. Yu. Konobeyev[1], Yu. A. Korovin[1], V.P. Lunev[2],
U. von Möllendorff, P.E. Pereslavtsev[1], M. Sokcic-Kostic, A. Yu. Stankovsky[1],
P.P.H. Wilson, D. Woll

Institut für Materialforschung

Institut für Neutronenphysik und Reaktortechnik

Institut für Reaktorsicherheit

Projekt Kernfusion

[1] Institute of Nuclear Power Engineering,
249020 Obninsk, Kaluga region, Russian Federation

[2] Institute of Physics and Power Engineering,
249020 Obninsk, Kaluga region, Russian Federation

Forschungszentrum Karlsruhe GmbH, Karlsruhe
1997

Abstract

The report describes the work performed by Forschungszentrum Karlsruhe, in collaboration with INPE Obninsk, on the neutronics of the projected International Fusion Materials Irradiation Facility (IFMIF) during the IFMIF Conceptual Design Activity (September 1994 to December 1996). The work encompassed the generation and processing of evaluated nuclear data sets for neutron energies up to 50 MeV, the generation of a Monte Carlo routine describing neutron production in the deuteron-lithium source, and the calculation of three-dimensional distributions of the spectral neutron flux density and the rates of displacement damage, gas production and nuclear heating, as well as their gradients, in the high flux region of the test cell. For these distributions, results from 'uncollided' calculations by two different codes, INS and MCNP, and results from transport calculations by MCNP, in each case for two different deuteron beam profiles, are presented and compared. Results are also presented to a helium cooled and a NaK cooled test module, and the comparison with fusion reactor conditions is made.

Neutronik der Hochfluß-Testregion der International Fusion Materials Irradiation Facility (IFMIF)

Zusammenfassung

Der Bericht beschreibt die Arbeiten zur Neutronik der projektierten International Fusion Materials Irradiation Facility (IFMIF), die während der IFMIF Conceptual Design Activity (September 1994 bis Dezember 1996) vom Forschungszentrum Karlsruhe in Zusammenarbeit mit INPE Obninsk durchgeführt wurden. Die Arbeiten umfaßten die Erstellung und Aufbereitung ausgewerteter Kerndatensätze für Neutronenenergien bis 50 MeV, die Erstellung einer Monte Carlo-Routine zur Beschreibung der Neutronenerzeugung der Deuteron-Lithium-Quelle und die Berechnung von dreidimensionalen Verteilungen spektraler Neutronenflußdichten, Verlagerungsschädigungsraten, Gaserzeugungsraten und nuklearer Aufheizraten sowie den Gradienten dieser Größen in der Hochflußregion der Testzelle. Für diese Verteilungen werden Ergebnisse aus 'uncollided' Berechnungen mit zwei verschiedenen Rechenprogrammen, INS und MCNP, und Ergebnisse aus Transport-rechnungen mit MCNP, und zwar jeweils für zwei verschiedene Deuteronenstrahlprofile, vorgelegt und verglichen. Es werden Ergebnisse für einen heliumgekühlten und einen NaK-gekühlten Testmodul vorgestellt, und der Vergleich mit Fusionsreaktorbedingungen wird vorgenommen.

Contents

1. Introduction

The International Fusion Materials Irradiation Facility (IFMIF) is a projected high intensity neutron source for materials testing. It will operate in parallel with the test reactor facility ITER to support the development of materials, e.g., low activation structural materials, to be used in DEMO and/or other fusion power reactors. IFMIF is being designed under co-ordination of the International Energy Agency (IEA) by an international team which consists of members from the European Union, Japan and the USA.

The geometry of the chosen neutron source, the samples and the test equipment necessitates detailed three-dimensional neutron and photon transport calculations for designing the test cell and setting up test programs.

The 2-year Conceptual Design Activity (CDA) phase of IFMIF ended on December 31, 1996. Its results are documented in a comprehensive report [Mar96] which, however, does not provide the space to describe the neutronics work in detail. CDA neutronics work* was contributed by Argonne National Laboratory (USA), Japan Atomic Energy Research Institute and Forschungszentrum Karlsruhe. The present report documents the neutronics work performed by Forschungszentrum Karlsruhe together with its contractual collaborator Institute of Nuclear Power Engineering (INPE), Obninsk, Russia. It constitutes, in this sense, an addendum to [Mar96].

The concept of IFMIF is shown in fig. 1-1. Two linear accelerators provide continuous-wave deuteron beams of 35 to 40 MeV, 125 mA each. These beams impinge, at ±10° inclination from the normal, on a flat liquid lithium jet, where they illuminate a common spot, or 'beam footprint', of 5 cm vertically × 20 cm horizontally. The lithium jet thickness is 26 mm, about 6 mm more than the deuteron range at 40 MeV. The lithium has a free surface toward the beams but is supported on its rear side by a 1.6 mm thick steel backplate. The test cell is the volume behind the backplate. It is subdivided into high, medium, low and very low flux regions. The neutronics of the 0.5 litre high flux region is the subject of this report.

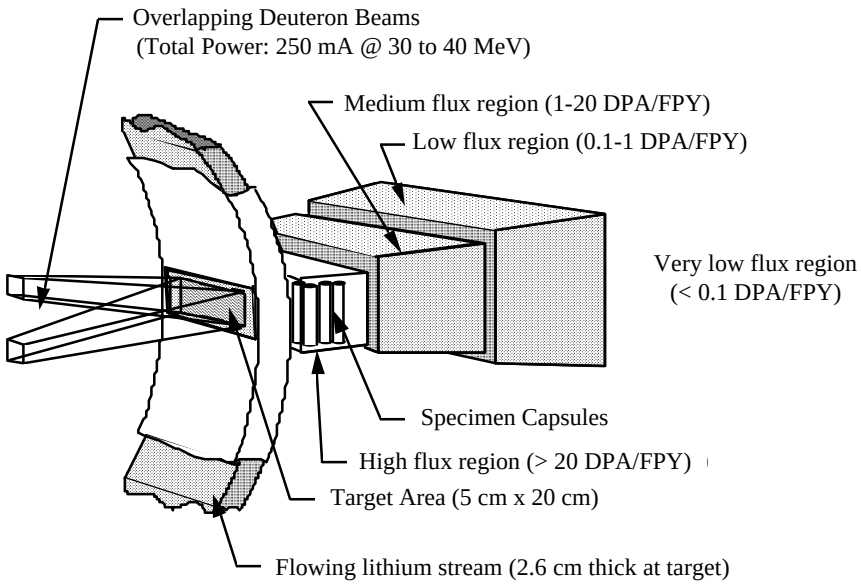

Figure 1-1 Components of IFMIF: deuteron beams, lithium target and test cell [Mar96].

* The term 'neutronics work' is restricted here in that it excludes the neutron and gamma ray shielding of the facility, which is the subject of work at ENEA, Bologna, Italy.

The deuteron-lithium neutron source concept was selected at the IEA-Workshop in Karlsruhe in 1992 [Ehr94] where the results of the IEA-Neutron Source Working Group [Dor90, Dor94] were discussed. Under the assumption that such a neutron source should be available not much later than the year 2000, it was concluded finally that a d-Li stripping source is the best choice due to its high source intensity and suitable shape of its neutron spectrum, although different from the spectrum of a deuterium-tritium fusion reactor. At meetings in 1993 and 1994, the IEA Fusion Power Co-ordinating Committee accepted the technical conclusions of the 1992 Karlsruhe Workshop and the proposal of the IEA Executive Committee to start a Concept Design Activity (CDA) on IFMIF.

The fusion reactor spectrum, produced by the d+t compound nucleus reaction at very low incident kinetic energy, consists of a peak at 14 MeV and (due to neutron interactions) a continuum down to thermal energy. In contrast, the nuclear interaction of multi-MeV deuterons with the two isotopes of natural lithium, Li-6 and Li-7, comprises a number of different neutron emitting reactions. The maximum possible energy gain in these (occurring in the ^{7}Li(d,n)2α reaction) is 15.1 MeV. With some simplification, this means that a neutron emitted in the forward direction may have an energy up to the energy of the incident deuteron plus 15 MeV.

The most important nuclear reaction mechanism for multi-MeV deuterons is deuteron stripping. The bulk of the neutrons from this process have energies around 50% of the deuteron energy. Furthermore, only a fraction of the deuterons will react at or near their full incidence energy, while most of them are slowed down by atomic collisions to lower energies before they undergo a nuclear reaction. The high energy tail in the neutron spectrum is, therefore, only a small fraction of the total flux. Nevertheless, its importance must not be underestimated, because many additional threshold reaction channels become available with increasing energy.

Due to the differences between d+t and d+Li neutron sources, there were two important prerequisites to the detailed IFMIF neutronics calculations:

- A program of nuclear data evaluation covering incident neutron energies up to 50 MeV had to be started. Up-to-date files of such evaluated data did not exist previously, because deuterium-tritium fusion does not give neutrons beyond about 14 MeV and, therefore, the nuclear data files prepared for fusion work usually end at 20 MeV. The evaluation work is described in chapter 2. The processing of the new files of evaluated data into working libraries for a transport code also required some development work, which is described in chapter 3.
- A computer model to describe the d+Li neutron production in sufficient detail, flexible with respect to deuteron energy, beam-target geometry etc., had to be developed and implemented. This is described in chapter 4.

A correct description of the irradiation effects in the test cell requires neutron transport calculations, that take into account the modifications of the spectral neutron flux density by neutron-nucleus collisions. However, valuable approximate information can be gained, with much less calculational effort, by uncollided calculations. In these, the neutron transport, i.e. the influence of the test cell matter on the neutron field is neglected, and the neutron field as it would be supplied by the source into a void is considered. This approximation is reasonable because fast neutrons are a very penetrating radiation. The mean free path of, e.g., a 14 MeV neutron in most metals is about 5 cm, comparable with the dimensions of the high-flux test region. Uncollided calculations have been instrumental especially at the beginning of the IFMIF study, before the evaluated nuclear data for neutron transport were available.

In the first parts of chapter 5, both uncollided and collided calculations of the neutron field and the engineering responses, i.e., displacement damage, gas production in materials and nuclear heating, as well as their gradients, are presented. For the uncollided case, results from two different codes, INS (analytical) and MCNP (Monte Carlo transport), are compared. All these calculations have been made for two different deuteron beam profiles, a flat (uniform) and a more realistic (non-uniform) one. Since the high flux test region in these calculations is homogeneous, smooth spatial distributions are obtained that can be visualised in contour plots. In section 5.7, MCNP calculations in the realistic , heterogeneous geometries of a helium gas cooled and a NaK (sodium-potassium) liquid metal cooled high flux test module, as designed within the CDA, are reported. Their results are given numerically, and they are compared with the results for the ITER and DEMO fusion reactor designs.

In chapter 6 the results and conclusions are summarised and recommendations are given.

2. Nuclear Data Evaluation

2.1 General remarks

The first step towards the IFMIF neutron transport calculations has been, as pointed out above, to provide files of evaluated nuclear data extending to 50 MeV neutron energy. Therefore, a comprehensive nuclear data evaluation programme was started in collaboration between Forschungszentrum Karlsruhe and INPE Obninsk. The produced files include integral, single-differential and double-differential cross-sections. The files are formatted according to the ENDF-6 rules so that they may be processed with existing codes (e.g. NJOY system) into working libraries for different transport codes, e.g. of the continuous-energy Monte Carlo or the multi-group discrete-ordinates type.

The part of the IFMIF test cell covered in this report is the high flux region, a volume of about 500 cm^3 close to the target. It consists, from the neutronics point of view, of a steel structure filled with test samples that are separated by spaces containing a coolant. The coolant may be either helium gas, which has negligible neutron interactions, or NaK eutectic liquid metal. ^{56}Fe data are used for transport calculations of a test cell loaded with steel samples. For neutron transport applications this is a good approximation since this nuclide constitutes about 80% of modern fusion relevant steels. The remaining nuclides do not strongly alter the neutron transport. Therefore, evaluated data for ^{56}Fe suffice for calculations of the helium cooled case, and with addition of data for ^{23}Na and ^{39}K the NaK cooled case can be covered.

Therefore, the first files were generated for ^{56}Fe, ^{23}Na and ^{39}K. The evaluation work yielding these three files is described in sections 2.2 to 2.4. The ^{56}Fe file includes cross-sections not only for describing neutron transport but also for calculating the engineering responses, i.e., the rates of displacement damage, hydrogen and helium production, and nuclear heating caused by both neutron and gamma interactions. For ^{23}Na and ^{39}K, such additional data will be incorporated in the future. 'Complete' files similar to the ^{56}Fe file have been produced meanwhile also for ^{52}Cr and ^{51}V, and 'neutron transport' files also for ^{28}Si and ^{12}C. In the future, all the files will be extended into 'complete' ones, and further files will be produced for other relevant nuclides.

2.2 Data evaluation methodology

The coupled-channels optical model realised in the ECIS code [Ray88] has been used to provide total cross-sections, elastic cross-sections and the direct contribution to discrete inelastic scattering cross-sections.

Neutron induced threshold reaction cross-sections and double differential cross-sections for non-elastic reactions were obtained using the geometry dependent hybrid exciton and evaporation models. The numerical calculations were performed by a modified ALICE code [Bla88]. The principal changes in the code concern incorporation of algorithms for describing pre-equilibrium cluster emission (d,t,^{3}He,α) [Kon94a, Kon96], pre-compound γ-ray emission [Obl88, Kon97], and calculation of the nuclear level density according to the generalised superfluid model [Ign79].

The calculations of pre-equilibrium nucleon spectra were performed on the basis of the GDH model taking into account multiple nucleon emission using the approach of [Bla83]. The exciton state density was calculated according to the Ericson-Strutinsky formula, taking into account the Pauli principle and pairing of nuclear levels. To define the intranuclear transition rate, λ_+ , nucleon-nucleon interaction cross-sections corrected for the Pauli principle were

used. The normalisation factor for calculating λ_+ was taken as unity. Inverse reaction cross-sections were calculated through the optical model. The angular distributions of the emitted neutrons were obtained using the Kalbach parametrisation [Kal88].

The non-equilibrium complex particle emission spectra were calculated in the framework of the coalescence pick-up model [Iwa82, Sat82] combined with the hybrid exciton model as shown in [Kon94a]. The contribution of direct processes to deuteron emission spectra was obtained by a phenomenological model [Kon96].

Non-equilibrium γ-ray spectra have been calculated according to Oblozinsky's model [Obl88]. The possible contribution of the „quasi-deuteron“ mechanism for γ-emission has been evaluated on the basis of an newly elaborated approach [Kon97].

The equilibrium particle emission spectra were calculated using the Weisskopf evaporation model. The generalised superfluid nuclear model [Ign79] has been applied to describe the level density.

The method for threshold reaction cross-section calculations was tested using experimental data for neutron induced reactions contained in EXFOR and measured cross-sections for proton induced reactions (p, xn yp zα) on ^{56}Fe and neighbouring target nuclei.

For some reaction channels the cross-section evaluation was based on the empirical [Yao92a, Yao92b] and the semi-empirical systematics [Kon94b, Dit96] at energies around 14.5 MeV. Additional corrections were applied to fit the newly evaluated data to the data from well established libraries at low energies. The data are given in the ENDF-6 format. In the 'complete' files, MF=1, 2, 3, 4, 6, 12, 14 and 15 are used.

2.3 Data evaluation for ^{56}Fe

2.3.1 Total and scattering cross-sections

The total cross-section and the differential cross-sections for elastic and discrete inelastic scattering were calculated on the basis of the coupled-channels model. The optical model parameters were taken from [Art80] and slightly corrected for discrete levels included in the calculations and for achieving agreement with available neutron data at energies above 20 MeV. The parameters of the potential are

$V = 49.747 - 0.4295E_n - 0.0003E_n^2$	r_v=1.287	a_v = 0.56
$W_v = 0.201E_n - 0.165$	r_{wv}=1.345	a_{wv}=0.47
$W_s = 2.563 - 0.128\ (E_n-6)$	r_{ws}=1.3448	a_{ws}=0.47
V_{so} = 6.2	r_{so}=1.12	a_{so}=0.47

where E_n is the primary neutron energy, V, W_v, W_s and V_{so} are respectively the real, imaginary volume, imaginary surface and spin-orbit parts of the potential in MeV, and r_i and a_i are respectively the corresponding radii and diffusenesses in fm.

The calculated total (σ_{tot}) and non-elastic (σ_{non}) cross-sections are shown in fig. 2-1. For comparison, the results of calculations using other potentials [Ber81, Bec69, Wil64], available experimental data and data from the ENDF/B-VI, JENDL-3, and BROND-2 libraries are also presented. The data show that the above potential yields the most realistic evaluation of σ_{tot}. At energies below 20 MeV the calculated σ_{tot} and σ_{non} are close to the JENDL-3 data.

The calculated angular distributions for the elastic and inelastic scattering for the five lowest levels at 20 MeV incident neutron energy are close to the JENDL-3 evaluation. Similar

agreement with JENDL-3 was found for the calculated neutron threshold cross-sections. On this basis it was decided to use many data from that library to create a full data file for the entire neutron energy range 0 - 50 MeV.

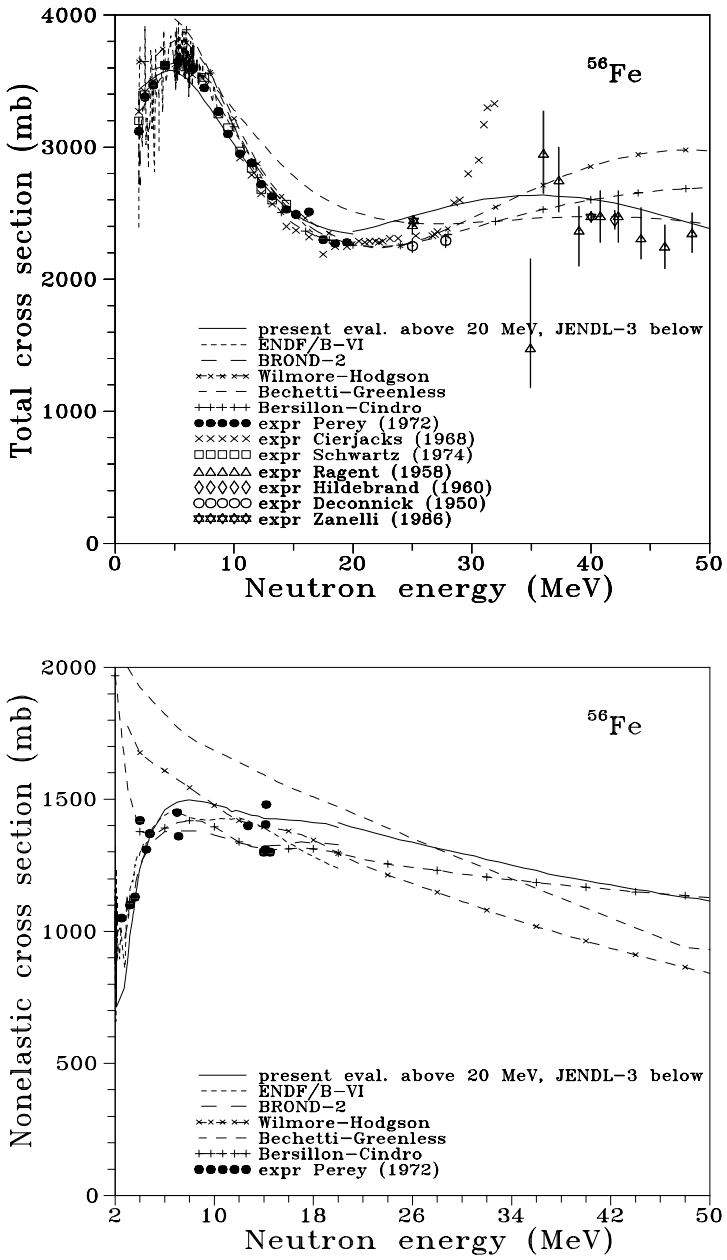

Figure 2-1 Comparison of the total and non-elastic cross-sections for ^{56}Fe calculated with different potentials in the present work with cross-sections taken from the ENDF/B-VI, JENDL-3 and BROND-2 libraries and experimental data.

2.3.2 Threshold reaction cross-sections and particle emission spectra

The threshold reaction cross-sections were calculated using different theoretical approaches. Experimental data and predictions from systematics have been used for the data evaluation.

At energies below 20 MeV the cross-section values obtained have been adjusted to JENDL-3 or ENDF/B-VI data.

Fig. 2-2 shows the cross-sections obtained for the (n,2n), (n,p), (n,np), (n,α), (n,t) and (n,^{3}He) reactions, together with data from the ENDF/B-VI, JENDL-3, BROND-2 libraries, cross-sections calculated using the systematics [Yao92a, Yao92b, Kon94b, Dit96] and EXFOR data.

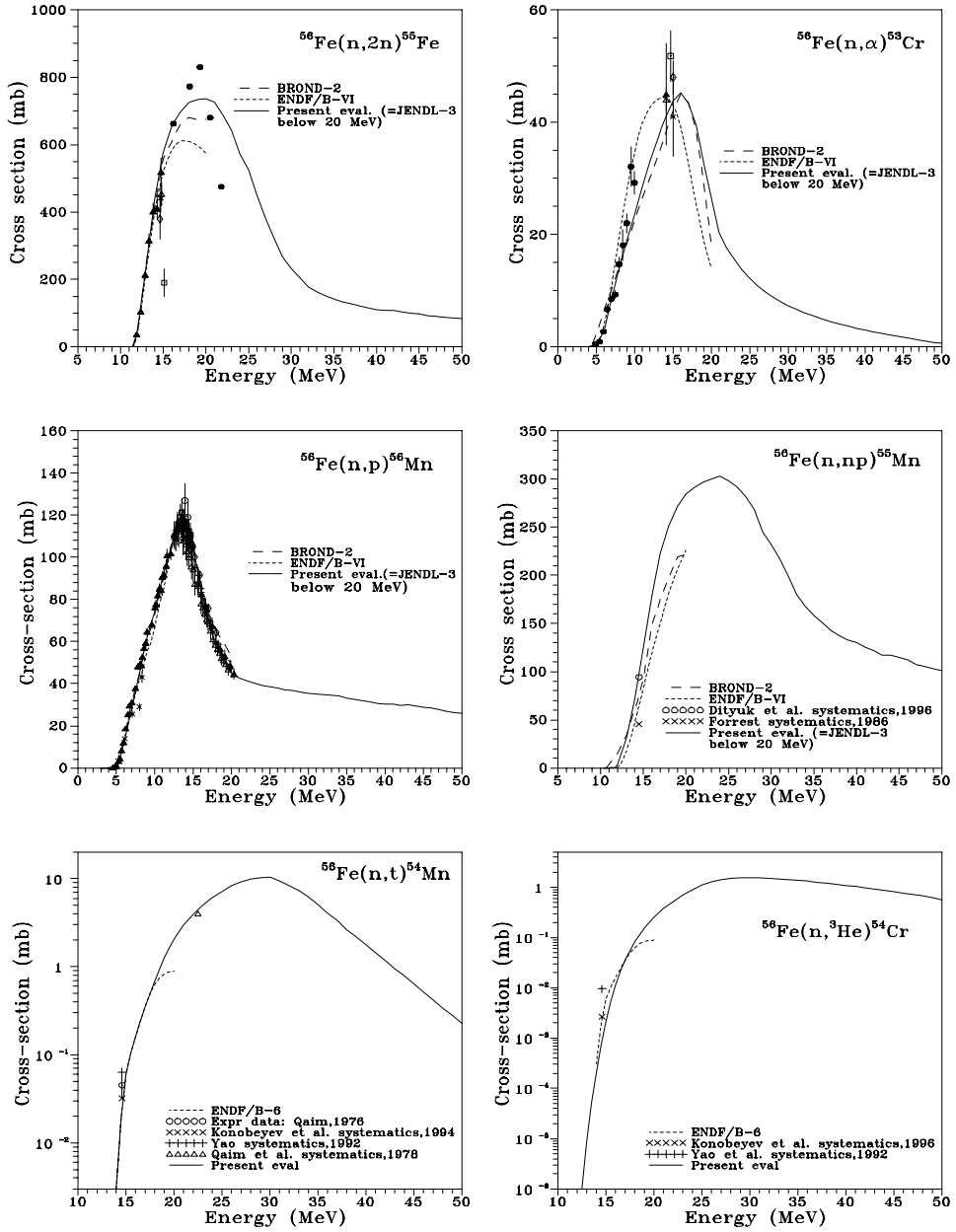

Figure 2-2 Comparison of the (n,2n), (n,p), (n,np), (n,α), (n,t) and (n,^{3}He) reaction cross-sections for ^{56}Fe evaluated in the present work with cross-sections taken from the ENDF/B-VI, JENDL-3 and BROND-2 libraries, predicted by systematics, and experimental data.

Comparison of the data in fig. 2-2 shows that the (n,2n) data included in the resulting file reproduce the measured cross-section in the best way. For (n,np) the data obtained are close to new semi-empirical systematics [Dit96] predictions. For (n,t) the obtained cross-sections

are in better agreement with experimental data [Qai78] than the cross-sections from ENDF/B-VI.

Figs. 2-3 to 2-5 show examples of the calculated neutron, proton and α-particle spectra for incident neutron energies of 14 and 50 MeV. The obtained neutron, proton and α-particle production cross-sections are shown in Fig. 2-6. The evaluated cross-sections for the neutron producing reactions are presented in Fig. 2-8.

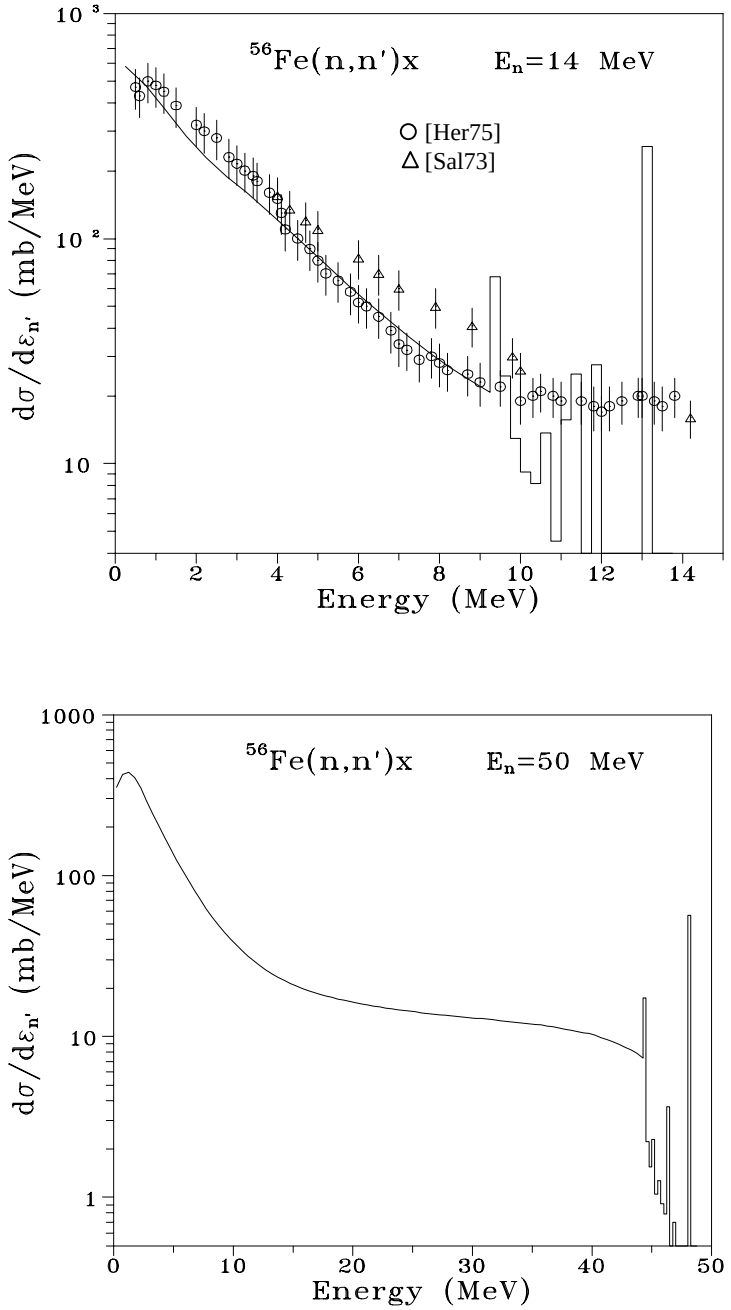

Figure 2-3 Neutron spectra emitted from ^{56}Fe at incident neutron energies 14 and 50 MeV contained in the data file and available experimental data.

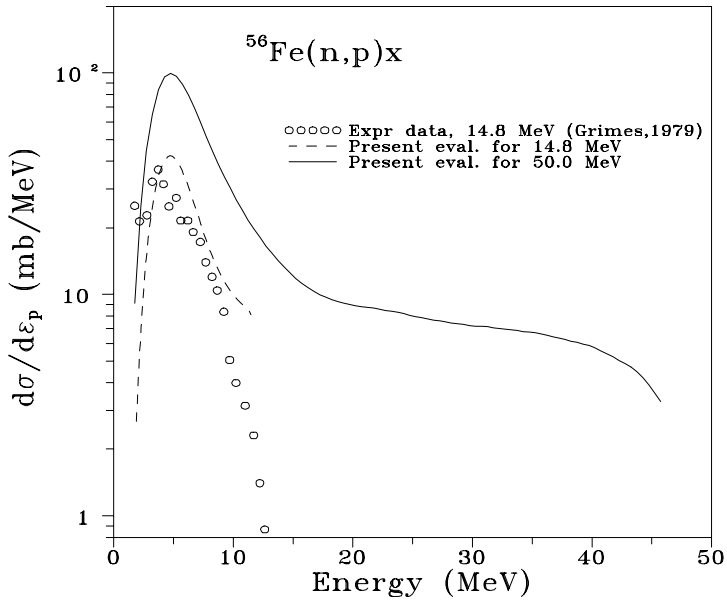

Figure 2-4 Proton spectra from ^{56}Fe at incident neutron energies 14.8 and 50 MeV contained in the data file and available experimental data.

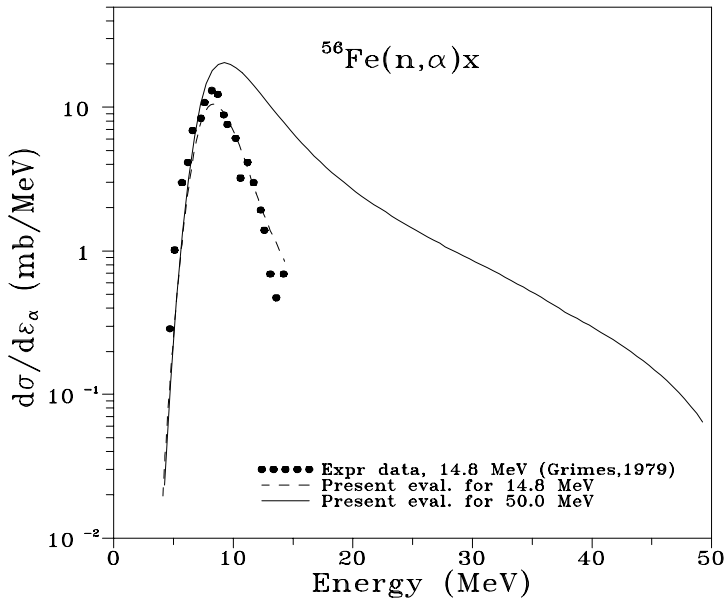

Figure 2-5 α-particle spectra from ^{56}Fe at incident neutron energies 14.8 and 50 MeV contained in the data file and available experimental data.

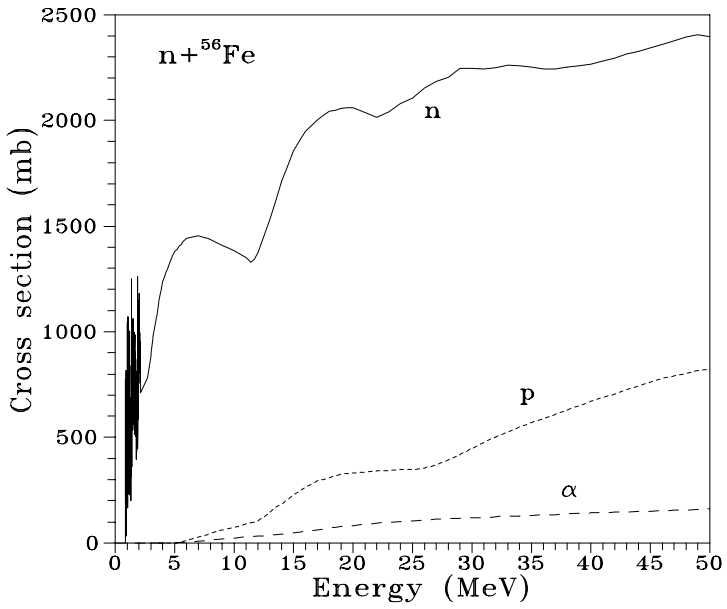

Figure 2-6 Neutron, proton and α-particle production cross-sections for ^{56}Fe irradiated by neutrons of up to 50 MeV.

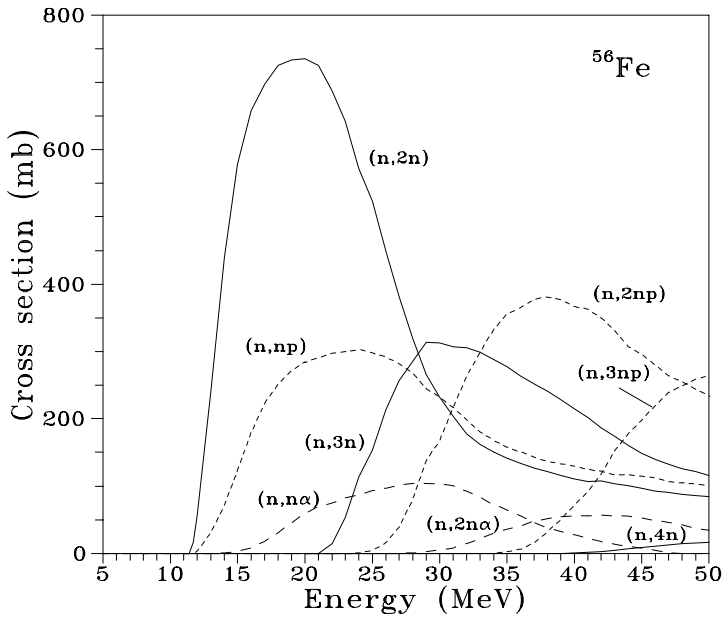

Figure 2-7 Neutron producing reactions on ^{56}Fe at incident neutron energies up to 50 MeV.

2.3.3 γ-ray emission spectra

Single radiative transitions [Obl88] were assumed to be the main origin of non-equilibrium γ-rays. To obtain the possible contribution of the „quasi-deuteron“ mechanism to γ-emission, the energy distributions $d\sigma^{qd}/d\varepsilon_\gamma$ for photons emitted in the elementary n+p→d+γ interactions of the primary particle with the nucleons of the nucleus were calculated. The corresponding emission rate and γ-spectra were then obtained using the formalism of the hybrid exciton model. In the calculation of $d\sigma^{qd}/d\varepsilon_\gamma$ the Pauli exclusion principle and other effects connected with the influence of nuclear matter on the n+p interactions were taken into account. A detailed description of the approach is given in [Kon97].

The γ emission spectra were calculated in the neutron energy range 20 - 50 MeV. For lower energies the data included in the final file were taken from ENDF/B-VI ((n,γ) reaction) and from JENDL-3 (other γ-producing reactions).

Figs. 2-8 and 2-9 show the γ-emission spectra contained in the file for incident neutron energies 14 and 50 MeV respectively.

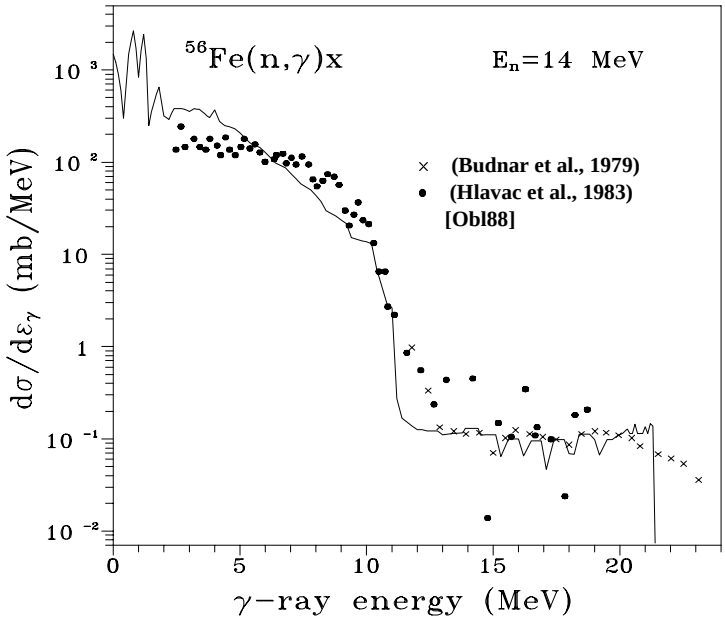

Figure 2-8 γ-ray spectra from ^{56}Fe at 14 MeV incident neutron energy contained in the data file.

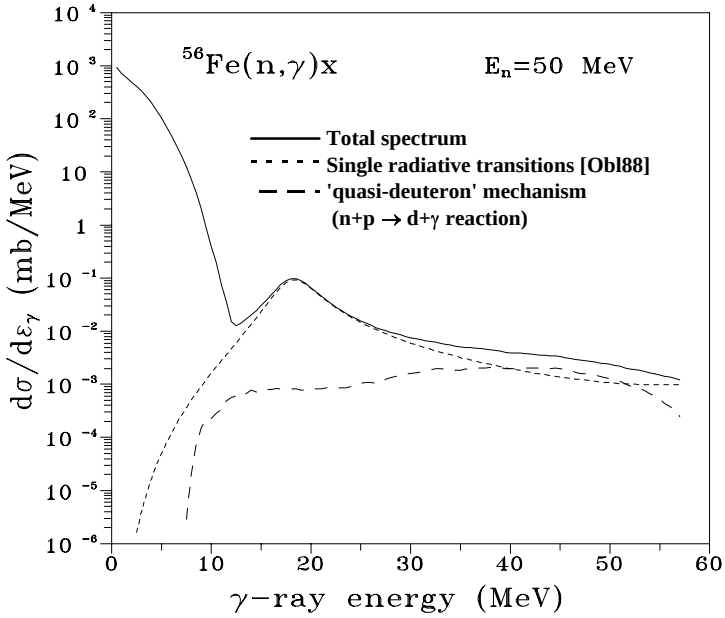

Figure 2-9 γ-ray spectra from ^{56}Fe at 50 MeV incident neutron energy contained in the data file.

2.3.4 Recoil spectra

For the single reactions (n,n'), (n,p), (n,α) at energies up to the (n,2n) reaction threshold the ALICE code has been used to obtain recoil spectra $d\sigma/d\varepsilon_R$ for residual nuclei. At energies above 11 MeV the DISCA code [Kon92a, Kon92b, Kon93] based on the modified intranuclear cascade evaporation model has been applied to calculate $d\sigma/d\varepsilon_R$.

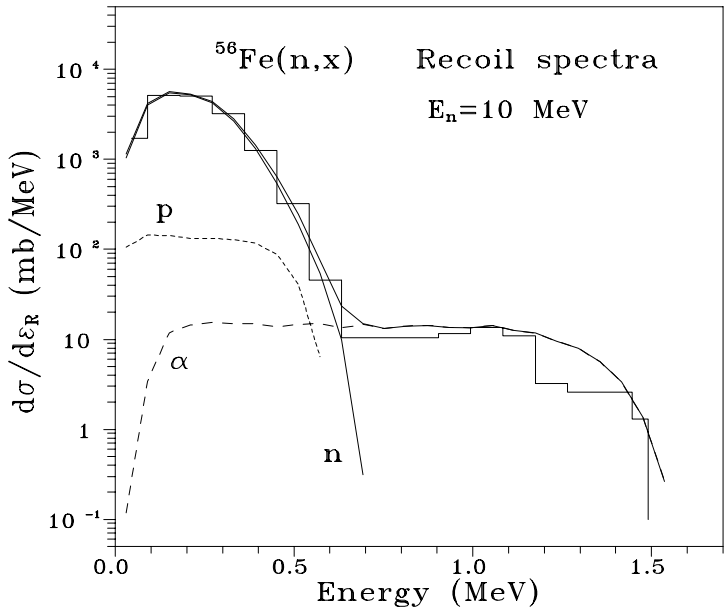

Figure 2-10 Recoil spectra for non-elastic neutron interactions with ^{56}Fe at E_n = 10 MeV calculated by ALICE (smooth curve) and DISCA (histogram). Contributions of neutron, proton and α particle emitting reactions calculated by ALICE are also shown separately.

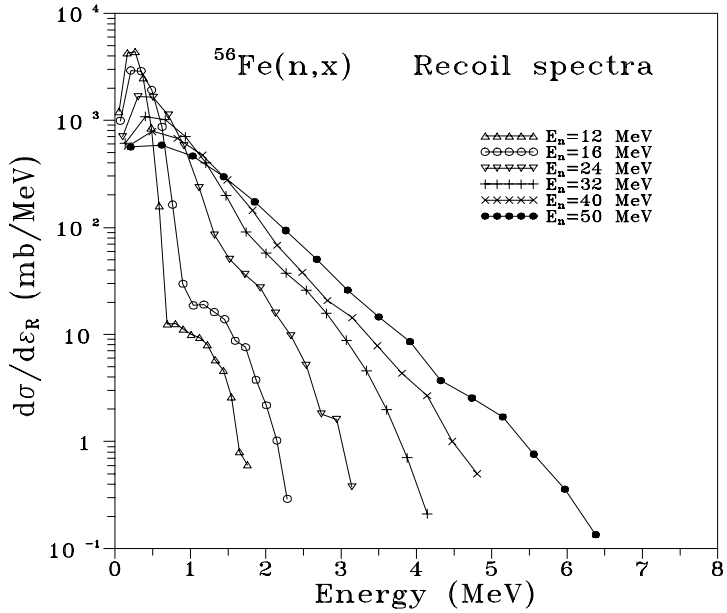

Figure 2-11 Recoil spectra for non-elastic neutron interactions with ^{56}Fe at different incident neutron energies calculated by DISCA

The recoil spectra at E_n=10 MeV primary neutron energy calculated by the codes ALICE and DISCA are compared in fig. 2-10. The contributions of neutron, proton and α-particle emission to the recoil spectra are also shown. The spectra calculated using the two different approaches can be seen to be in good agreement. Examples of the recoil spectra calculated using the DISCA code at different primary neutron energies are shown in fig. 2-11.

2.4 Data evaluation for ^{23}Na and ^{39}K

For ^{23}Na and ^{39}K, the calculations of the total non-elastic cross-section, differential elastic and inelastic discrete scattering cross-sections have been performed with the C.C. potential from [Kik94]. Comparison of the cross-sections calculated for ^{23}Na with different potentials shows that the data obtained using that potential are in relatively best agreement with the results of a cross-section evaluation [Bar89] based on experimental data.

Fig. 2-12 shows the evaluated cross-sections for the (n,2n), (n,α), (n,p), (n,nα), (n,t) and (n,^{3}He) reactions on ^{23}Na. Along with the cross-sections obtained the figure presents the data from the ENDF/B-VI, JENDL-3, BROND-2 and ADL-3 [Gru93] libraries, the cross-sections predicted by systematics [Yao92a], and experimental data.

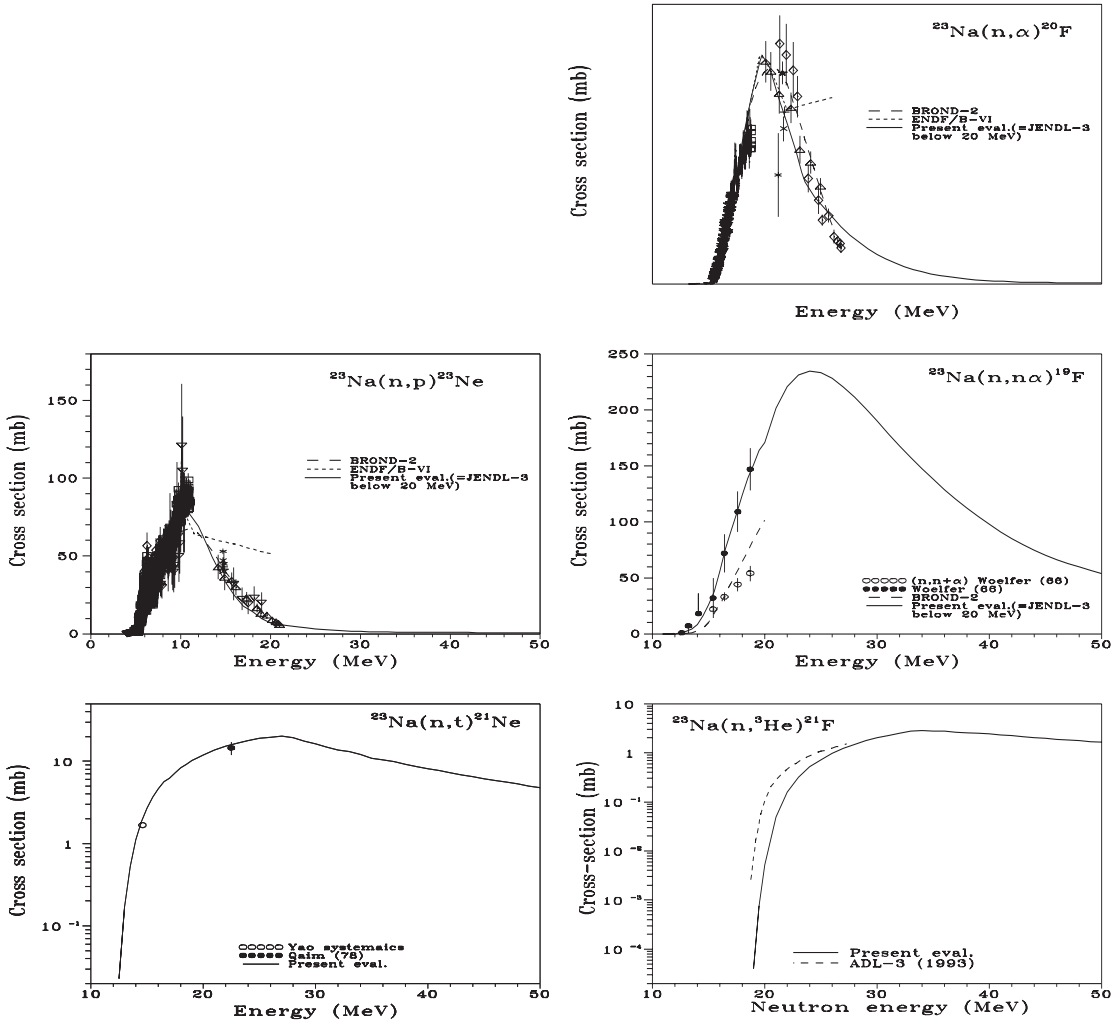

Figure 2-12 Comparison of the (n,2n), (n,α), (n,p), (n,nα), (n,t) and (n,^{3}He) reaction cross-sections for ^{23}Na evaluated in the present work with those from the ENDF/B-VI, JENDL-3, BROND-2 and ADL-3 libraries, predictions by systematics, and experimental data.

The comparison shows that the cross-sections for the (n,2n) reaction obtained in the present work (and the data from JENDL-3 below 20 MeV) agree best with the results of the latest measurements. The evaluated excitation functions for the (n,p) and (n,α) reactions have no unphysical "breaks" compared to ENDF/B-VI and, for the (n,nα) reaction, reproduce the experimental energy dependence of the cross-sections in the best way.

For ^{23}Na(n,t) the cross-sections evaluated in the present work are in agreement with the systematics [Yao92a] prediction at 14.6 MeV and experimental data [Qai78] at 22.5 MeV. For the (n,^{3}He) reaction the data obtained are compatible with an evaluation by other authors [Gru93].

Fig. 2-13 illustrates the cross-sections for n+^{39}K reactions: (n,2n), (n,α),(n,p), (n,np), (n,t), (n,^{3}He) obtained in the present work, taken from JENDL-3, the systematics predictions [Yao92a, Yao92b, Kon94b] and experimental data. The figure shows that the JENDL-3 data agree neither with experimental data for the (n,α) reaction nor with the latest measurements of the (n,np) reaction and have an unphysical energy dependence for the (n,p) reaction. The results of the present evaluation are in agreement with the experimental data and systematics predictions. To obtain a full data set for 0 - 50 MeV the resonance parameters and some other data at energies below 20 MeV for ^{23}Na and ^{39}K were taken from JENDL-3.

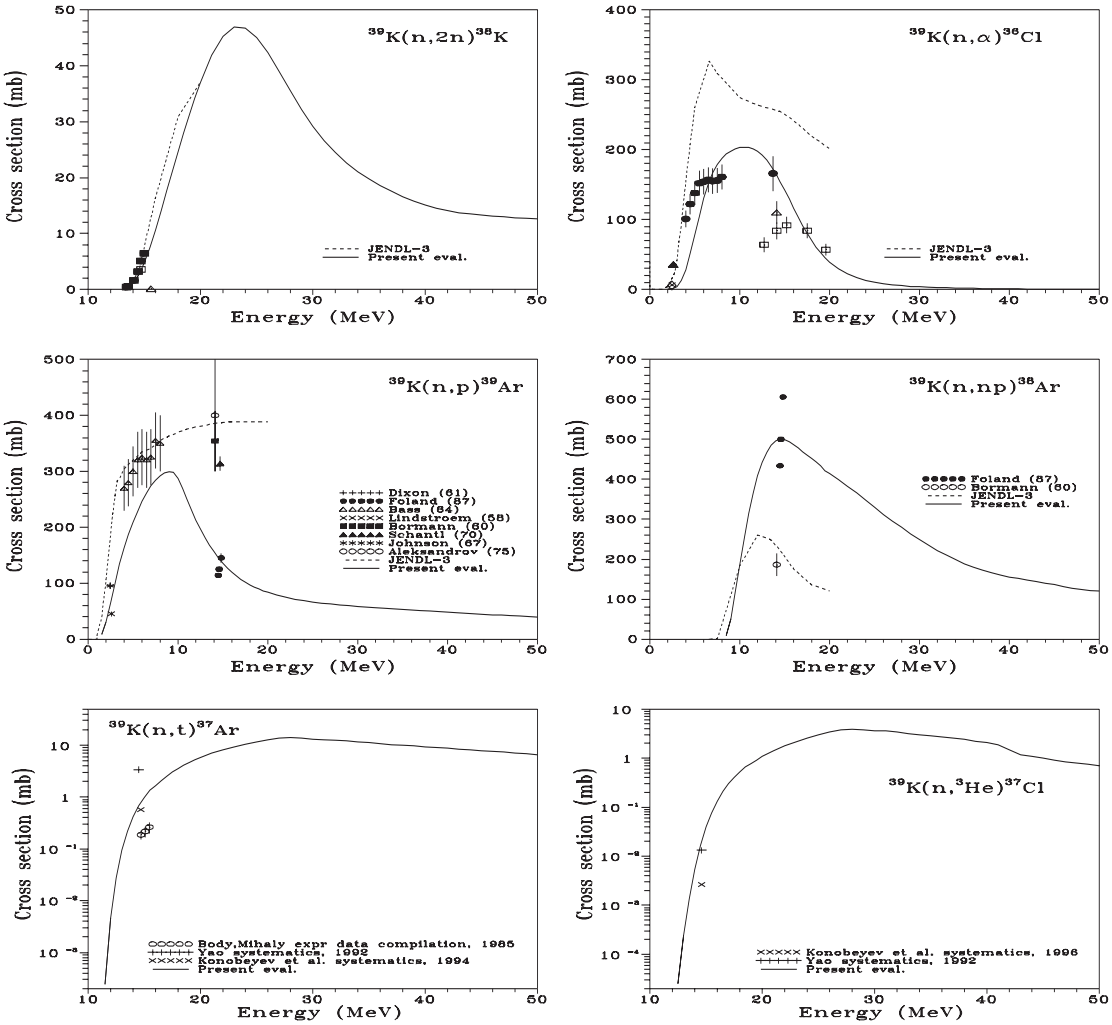

Figure 2-13 Comparison of the (n,2n), (n,α), (n,p), (n,np), (n,t) and (n,^{3}He) reaction cross-sections for ^{39}K evaluated in the present work with cross-sections from JENDL-3, predictions by systematics, and experimental data.

3. Nuclear Data and Their Processing for Use with MCNP

3.1 Cross-section data types and formats

The evaluated high energy cross-section data have been prepared in the ENDF-6 data format [Ros90] to allow the processing with the NJOY-code [Mac94]. Special care was taken to find, in the given frame of the ENDF-format, an appropriate data representation for the variety of kinematically allowed reaction channels with subsequent emission of particles (n, p, t, ^{3}He, α, ..).

The goal in establishing a high energy nuclear data file for subsequent applications in neutronics calculations is to provide first the data needed for neutron and photon transport calculations, and second, the data needed for calculating the required nuclear ('engineering') responses, e. g. specific reaction rates, nuclear heating, gas production and radiation damage rates.

The objective of using the processed high energy cross-section data in Monte Carlo continuous energy calculations with the MCNP-code [Bri93] results in additional constraints for the data representation. In particular, MCNP makes explicit use of the neutron yields (the number of secondary neutrons per incident neutron at each incident energy), i.e. it cannot handle non-normalised energy-angle distributions implicitly containing energy-dependent neutron yields. For that reason, the ACER module of NJOY, which is being used for processing the ENDF-6 formatted cross-section data into an ACE library for the MCNP Monte Carlo codes, is not capable of dealing with some of the ENDF-6 format options that on the other hand would be appropriate to represent multiple particle emission cross-section data.

The following cross-section data types have to be provided for allowing neutron-photon transport calculations and obtaining the relevant nuclear responses:

- Neutron reaction cross-sections („excitation functions") dependent on the neutron incidence energy (stored on file MF=3 in the ENDF-6 format).
- Angular distributions for elastically and inelastically scattered neutrons leaving the residual nucleus in discrete excitation states (MF=4 data).
- Energy-angle distributions for inelastically scattered neutrons with continuum excitation of the residual nucleus and for secondary particles (n, p, α, ..) emitted in many particle reactions (MF=6 data) .

3.1.1 Reaction cross-sections (MF=3 data)

MF=3 reaction cross-section data should be, in principle, provided on the ENDF data file for all of the kinematically allowed reaction types to enable the calculation of the corresponding reaction rates. However, this is unfeasible in the given ENDF format in view of the variety of open reaction channels above 20 MeV neutron incidence energy. To cope with that, ENDF format rules include the option to use lumped cross-sections for specific reaction types, e.g. MT=5, defined as reaction with a neutron in the entrance channel and any particle in the exit channel (n, anything). For the high energy range cross-section data, it is most appropriate to include all of the multiple particle emission cross-sections in MT=5. However, reaction types contained in MT=5 must not be present additionally on the file as separate reactions to avoid double counting in the processing procedure. For use with calculations of specific nuclear responses, the data are to be stored on a separate data file (e.g. a response data file

comprising all of the possible reaction cross-sections and other responses). Table 3-1 gives a summary of the MF=3 reaction cross-section data provided for ^{56}Fe + n.

In addition to the standard reaction types, e.g. (n, γ), (n,p), (n, α), (MT=102, ...) being not part of the lumped cross-section data types, specific redundant cross-sections may be stored on the file, e.g. neutron, proton and α- production.

3.1.2 Energy-angle distributions (MF=6 data)

Energy-angle distributions are needed for following the particle transport through phase-space. While it is sufficient for elastic scattering and discrete inelastic scattering to have the angular distributions (because there is a unique energy-angle correlation for two-particle reactions), full energy-angle distributions are required for all many particle reaction types producing secondary particles that have to be transported (e.g. neutrons, photons). In addition, energy-angle distributions are required for reactions producing charged particles if radiation damage and nuclear heating has to be calculated.

According to the ENDF-6 format rules energy-angle distributions can be stored on file MF=6. There are various options to represent the data on the file, dependent on the reaction type, the underlying nuclear physics and the usefulness of a representation (for instance Legendre polynomial coefficients, tabulated distributions, Kalbach-Mann systematics, laboratory or centre-of-mass representation, cf. e.g. [Ros90]).

Table 3-1 Reaction cross-section data of ^{56}Fe + n stored on ENDF file MF=3

ENDF MT-type	Cross-section type	Definition	Comment
MT=1	Total cross-section		required
MT=2	Elastic scattering		required
MT=3	Non-elastic	Sum of MT=4,5,102-108, 111, 112	redundant
MT=4	Total inelastic cross-section	Sum of MT=51-77, 91 (continuum inelastic scattering)	redundant
MT=5	(n, anything) - reaction	Sum of all reaction cross sections not given explicitly, e.g. (n,p), (n, α), (n,2n), .., (n,5n), (n,2n2p), in particular many particle reaction types	required for processing with energy-angle (MF=6) distribution data of secondary particles; reactions included in MT=5 must not be stored additionally on the file (e.g. no separate MT=103 (n,p) data allowed as already contained in MT=5)
MT=51-77	Discrete inelastic scattering	Inelastic neutron scattering with discrete excitation of the residual nucleus	required for processing with angular distribution data (MF=4) and photon production data
MT=102	(n, γ)	radiative neutron capture	required for photon production
MT=104	(n,d)	deuteron production	required for responses only
MT=105	(n,t)	triton production	required for responses only
MT=106	(n, He-3)	He-3 production	required for responses only
MT=203	(n, xp)	total proton production	required for responses only
MT=207	(n,xα)	total α production	required for responses only

Reaction type MT=5 (neutron in, anything out) has been proven to be the most suitable data type for storing multiple particle emission reaction cross-section data with their energy-angle distributions and energy-dependent particle yields on file MF=6. According to the ENDF-6 format rules, MT=5, MF=6 may contain sub-sections for each specified secondary particle type with the corresponding particle yields and the associated normalised energy-angle distribution at each given neutron incidence energy point. This representation is accepted by NJOY/ACER and is appropriate for use with MCNP requiring energy dependent particle yields.

For ^{56}Fe + n, MT=5 subsections are included for n, p, α, γ, and the recoil nucleus. The sub-sections for secondary charged particle, photons and recoil nuclei are needed to allow calculating radiation damage cross-sections and kerma factors with MT=5 data. The energy-angle distribution is stored as tabulated data in the laboratory system on the file MF=6 (i.e. ENDF-6 option LAW=7 [Ros90]). This representation is most appropriate with regard to the involved nuclear reaction physics. In particular, it does not rely on nuclear physics approximations (e.g. Kalbach-Mann) that apply only for a specific mass or energy range. The quality of the LAW=7 data is only governed by the underlying nuclear physics models used to produce them.

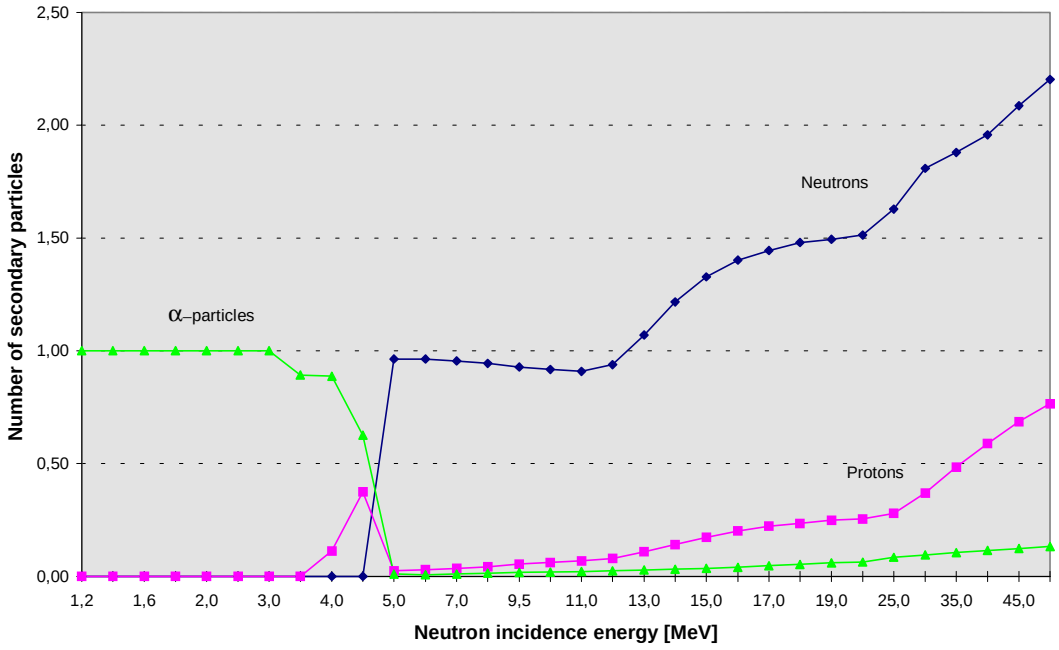

Figure 3-1 Particle yields for n, p, and α-emission of non-elastic ^{56}Fe + n reactions included in reaction type MT=5.

3.1.3 Angular distributions (MF=4 data)

Angular distributions are given for elastic and discrete inelastic scattering (levels 51 - 77 for ^{56}Fe + n) on file MF=4. These data are represented in terms of Legendre polynomials (up to 20 moments) in the centre-of-mass system as prescribed by the ENDF format rules for such reactions. Based on two-body kinematics, the resulting energy-angle distributions are generated by NJOY as part of the data processing. The ENDF-6 restriction to 20 Legendre polynomials at maximum may create a problem for neutron incidence energies higher than 50 MeV. For that case, an alternative solution would be to store angular distributions for elastic

and level-inelastic scattering on file MF=6, then making use of the LAW=2 (two-body scattering) and LANG=12 (tabulated angular distribution) option.

3.1.4 Photon production cross-sections (MF=6 data)

Photon production data are required for enabling transport calculations for photons generated through neutron induced nuclear reactions. In addition, photon production data are required for calculating responses like the nuclear heating. Also, well qualified photon production data are needed to properly obtain the recoil and damage energy for the MT=5 reaction, i.e. all nuclear reactions except MT=2, 51-90 (i.e. elastic and level inelastic scattering). No photon interaction data have to be provided, as these are included in the MCPLIB photon data library up to 100 MeV photon energy available with the MCNP code.

Depending on the reaction type, photon production data may be provided on the data file in different ways. The following choice has been made for the ^{56}Fe+n high energy cross-section data file:

- For reaction type MT=5, energy-angle distribution data are included as sub-section in MF=6 (see above).
- For discrete inelastic scattering (MT=51-77) and radiative neutron capture (MT=102) reactions, a file MF=12 is added including the photon multiplicities for emission of discrete photons.
- For radiative neutron capture (MT=102), additionally photon angular (file MF=14) and energy spectra (file MF=15) data are provided to represent the continuous photon energy spectra. Isotropic emission of photons in the centre-of-mass system is assumed, however, in the current high energy cross-section data files.

3.2 Data processing with NJOY/ACER and NJOY/HEATR

Once the high energy cross-section data are provided in an ENDF-6 format as described in section 3.1, processing of the data file is straightforward with NJOY/ACER. As a result, an ACE (a compact ENDF format) data file is provided that can be used with MCNP for coupled neutron-photon transport calculations.

The following steps are required to get a full ACE-file starting from the basic ENDF-6 formatted ASCII file:

1) Creation of a pointwise (PENDF) data file using NJOY module RECONR (for reconstruction of the pointwise cross-sections from resonance parameter data).

2) Doppler broadening of the data for the specified temperature (300 K) using NJOY module BROADR.

3) Generation of pointwise heat production (kerma factors) and radiation damage energy cross-sections that are added to the PENDF file using NJOY module HEATR

4) Processing of the PENDF data into the ACE format for MCNP.

All of these steps may be performed in a single NJOY run. Table 3-2 shows a sample input file used for the generation of the ^{56}Fe ACE file. Note that the content of the resulting ACE cross-section data file cannot be controlled via the ACER input file. It is only governed by the presence of the data on the input PENDF file. Therefore, reaction types for use in subsequent

MCNP-calculations either have to be stored on the basic ENDF-6 formatted file (e.g. MT=203, 207) or to be provided in an intermediate NJOY processing step (e.g. kerma factors, radiation damage cross-sections). In addition, other reaction data can be made available through a separate response data file that can be used along with MCNP calculated spectra for obtaining the required responses.

Table 3-2 NJOY input file for generating ^{56}Fe ACE data file.

```
*tape20 is the basic PENDF fe56 ASCII data file in ENDF-6 format */
0
6
*moder*
20 -21
*reconr*
-21 -22
*pendf tape for fe56 INPE evaluation 96*/
2656 2 0
.005 0 6 /
*26-fe-56 INPE evaluation 96*/
*processed by the njoy nuclear data processing system*/
0/
*broadr*
-22 -23
2656 1 0 0  0.
.002 1.e+6 /
300.
0/
*heatr*
20 -23 -24 25
2656 8 0 0 0 1
302 304 305 443 444 445 446 447
*acer*
-21 -24 0 26 27
1 1 1 .95 /
*26-fe-56 INPE evaluation 96 */
2656 300.
0.002 1
/
*stop*
```

Radiation damage energy cross-sections and heat production cross-sections are generated by the NJOY module HEATR (step 3 above). Heat production data are described on the basis of the kerma (Kinetic Energy Release in Materials) factor concept [Abd75] both for neutrons and photons.

The kerma factor $k_{ij}(E)$ for material *i* and reaction *j* and neutron energy E (given in units of eV·barn) is defined according to

$$k_{ij}(E) = \sum_{l} \overline{E_{ijl}}(E) \cdot \sigma_{ij}(E)$$

where $E_{ijl}(E)$ is the total kinetic energy of all secondary charged particles (the recoil nucleus itself, p, d, t, α, ..) produced by the reaction and $\sigma_{ij}(E)$ is the associated nuclear cross-section. Thus the kerma factor involves that part of the released reaction energy that is deposited locally and finally results in the nuclear heating. The kerma factor is defined separately for neutron and photon interactions, as photons do not react locally (at the site of their birth in a nuclear reaction) but are transported through the material. Therefore, the energy carried away by photons must not be included when calculating the neutron kerma factors. Frequently, this causes problems when proper photon production data are missing on the data file. With the MT=5, MF=6 data concept, however, the kinetic energy of the secondary charged particles (including the recoil nucleus) is directly obtained by integrating the energy-angle distributions stored in the corresponding subsections on the file. For elastic and discrete inelastic scattering, on the other hand, no photon production data are needed to calculate the neutron kerma factor.

The calculation of the damage energy production follows a similar path. The damage energy is defined as that part of the released reaction energy that may result in atomic displacements. Therefore, it depends on the recoil spectra and the partition of the recoil energy between electronic excitation and atomic motion. The recoil spectra for MT=5 are again obtained by integration (over angle) of the MF=6 data for the recoil nucleus, while for elastic and discrete inelastic scattering they are obtained on the basis of the two-body kinematics. The partition function used by NJOY/HEATR for calculating the damage energy was derived by Robinson [Rob71] on the basis of the Lindhard slowing down model [Lin63]. The damage energy cross-section is provided in terms of eV·barn by NJOY/ACER. For converting to the DPA (displacements per atom) cross-section (in barn) according to the NRT- displacement damage model [Nor75], a factor $0.8/2E_d$ has to be applied to the damage cross-section. Here, E_d is the displacement energy, i.e. the energy required for displacing an atom from its lattice site. For Fe, E_d = 40 eV is a recommended value [Gre81].

Processed ^{56}Fe + n cross-section data are displayed in figs. 3-2 through 3-8 and compared to data of other sources where available.

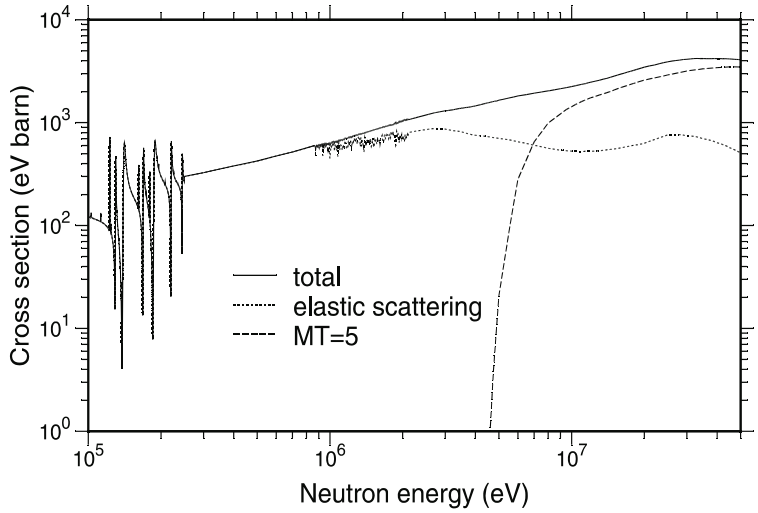

Figure 3-2 Partial and total displacement damage energy cross-sections for ^{56}Fe.

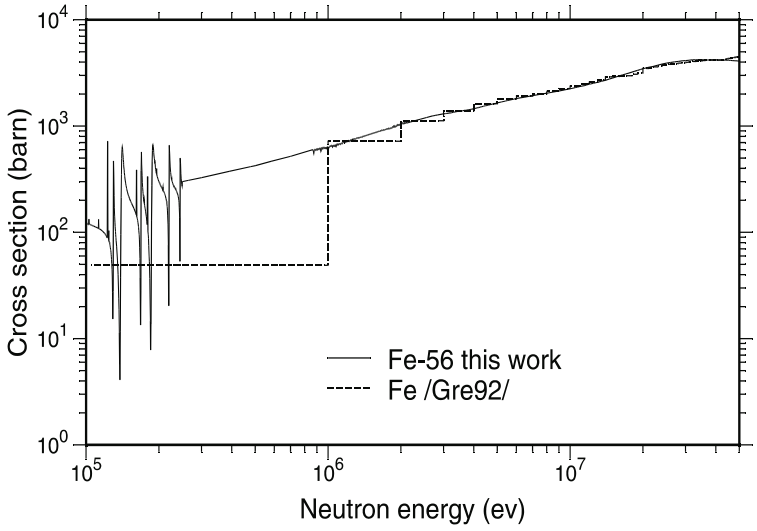

Figure 3-3 Comparison of displacement damage cross-sections for iron.

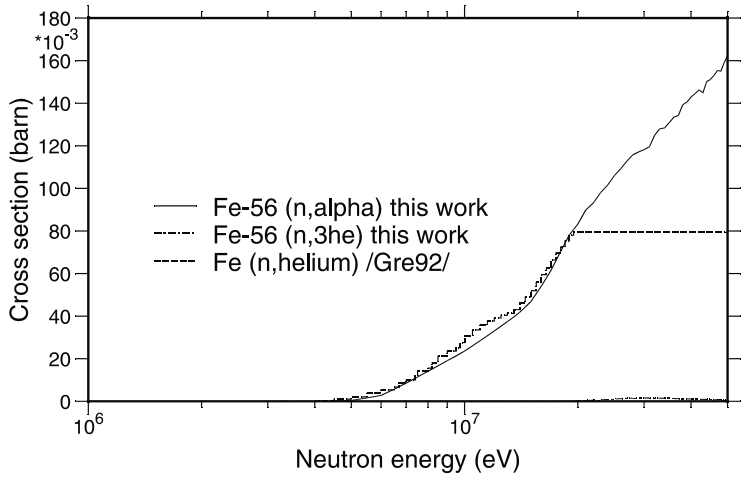

Figure 3-4 Comparison of helium production cross-sections for iron.

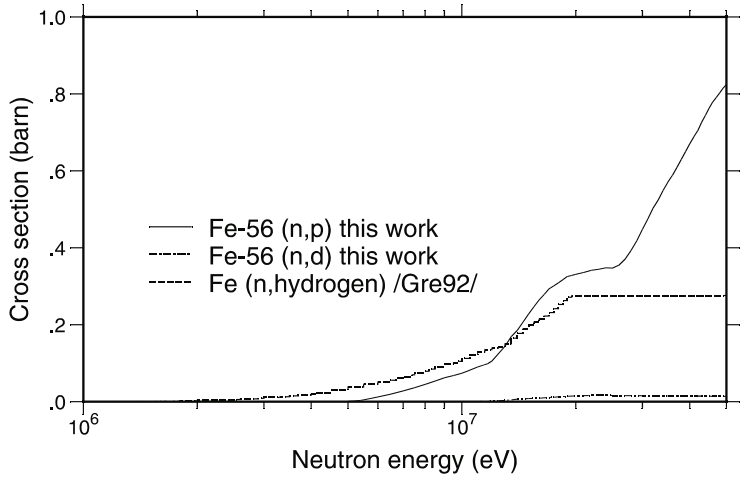

Figure 3-5 Comparison of hydrogen production cross-sections for iron.

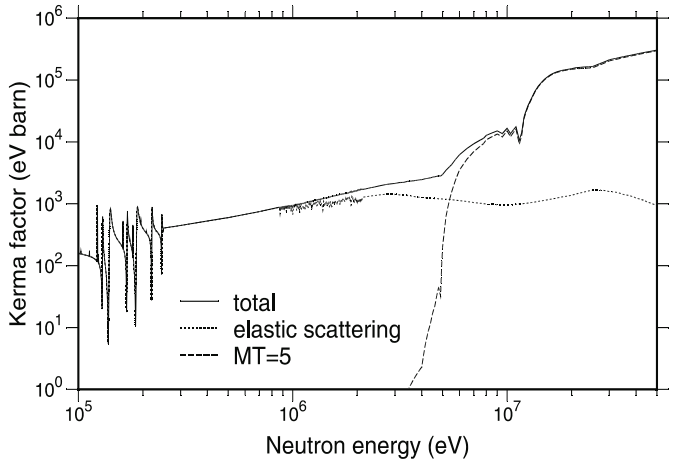

Figure 3-6 Partial and total neutron kerma factors for ^{56}Fe.

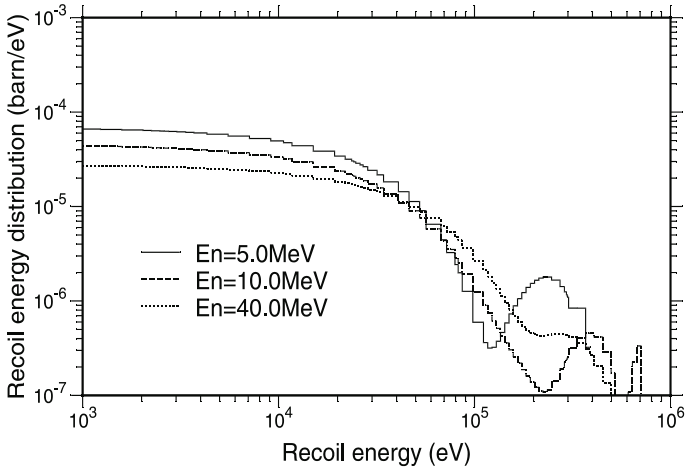

Figure 3-7 Recoil energy spectra of ^{56}Fe due to elastic neutron-nucleus interactions at different neutron incidence energies.

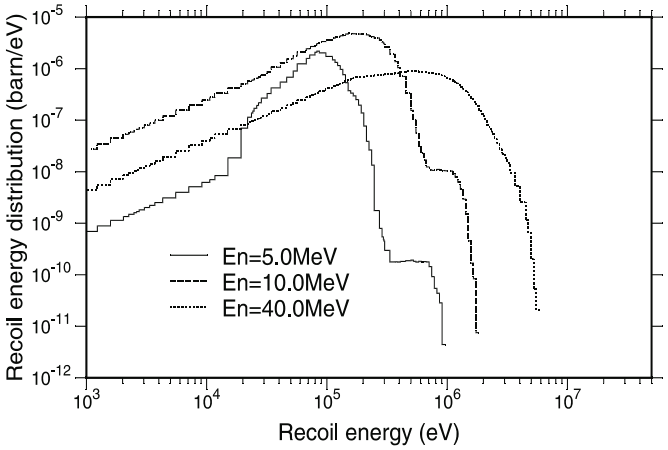

Figure 3-8 Recoil energy spectra of residual nucleus * due to non-elastic (MT=5) neutron interactions with ^{56}Fe at different neutron incidence energies.

* The recoil spectra of the „residual nucleus“ are obtained by a weighted average over all reactions included in MT=5.

4. Neutron Source Model Development

4.1 General Remarks

Neutron transport calculations for the IFMIF project [Mar96] will be important for a variety of reasons. Most important in the early stages is the necessity to accurately determine the neutron flux distribution throughout the test cell to aid in the design process. A true assessment of the technical and economic feasibility of the project is only possible by the accurate calculation of the neutron fluxes and resulting engineering responses throughout the test assemblies. Such calculations can be used to determine the available test volume for certain damage rates and the expected flux spectra at particular design locations. Perhaps most important is the ability to compare the flux spectra and engineering responses of IFMIF to the characteristic flux spectra and engineering responses expected in a fusion reactor, and therefore determine the suitability of IFMIF as a fusion irradiation simulation environment.

During the operating of IFMIF, similar detailed neutron transport calculations will be required. The users will need predictions of the neutron fluxes and engineering responses in different test cell locations to determine which location best suits their sample and interests. These predictions will also be useful to determine any special handling requirements of the samples due to induced radioactivity when they leave the test cell.

Due to the complex, three-dimensional geometry of the facility, a Monte Carlo calculation is required to perform an accurate analysis of the neutron spectra and responses throughout the test facility. To fully implement the neutron transport calculation as a Monte Carlo calculation requires a source model which can produce a randomly sampled source neutron from the deuterium-lithium reaction.

This chapter includes a full description of the model used to represent the physical system and reaction mechanisms and its implementation as an MCNP [Bri93] source routine. In addition to describing the development of a theoretically based reaction model, suitable for random sampling and fitted to experimental data, there is some discussion of the development of a model to represent the deuteron beam distribution.

4.2 Physical Model

There are three main components to the physical model of a deuteron-lithium neutron source system: deuteron slowing down in lithium, Li(d,n) reaction mechanics, and beam energy density distribution. Of these, the reaction mechanics is the most complicated and historically has been modelled by the two independent theories of stripping and compound reactions [Man81,Oya95]. These two theories must be combined to provide a reasonable approximation to current experimental data. In this case, we are very grateful for the experimental double differential neutron yield data of Sugimoto (JAERI) [Sug95] as shown in Figure 4-1.

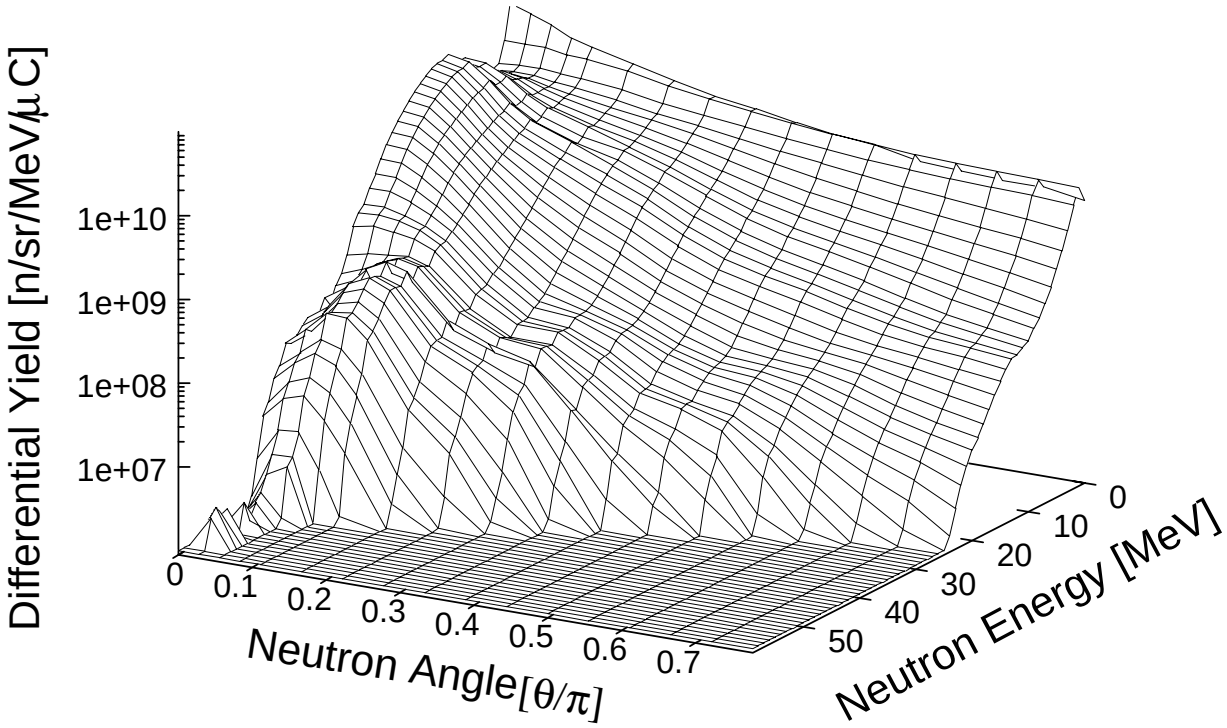

Figure 4-1 Angle and Energy dependent neutron yield from 35 MeV deuterons incident on a lithium target (JAERI).

4.2.1 Serber Stripping

Basic theory

The basic semi-classical theory for stripping reactions was first developed by Serber in 1947 [Ser47]. This theory simply considers the deuteron nucleus as a two particle system and models the stripping reaction as one particle hit the target nucleus while the other continues in the original direction. While it is equally likely that the neutron may be trapped by the target nucleus, the case of interest here is when the proton strikes the target nucleus and the neutron continues freely. The binding energy of the deuteron is taken into account by assuming some internal rotation of the two particles and thus, a distribution of directions peaked heavily in the forward direction results. The distribution as defined by Serber is:

$$\frac{\partial^2 \sigma_s}{\partial \mathrm{E}_n \partial \Omega_n} = \frac{1}{2} \frac{E_d \varepsilon_b}{\left[\left(E_n - \frac{E_d}{2}\right)^2 + E_d \varepsilon_b\right]^{3/2}} \frac{\theta_o}{\left(\theta_o^2 + \theta_n^2\right)^{3/2}}$$

where:

E_d = deuteron energy [MeV]

e_b = deuteron binding energy = 2.18 MeV

E_n = neutron energy [MeV]

θ_o = Serber angle = $\sqrt{\frac{\varepsilon_b}{E_d}}$

θ_n = neutron angle

and is shown in figures 4-2 and 4-3. The most important features of these distributions are the sharp peaks at E_d/2 in the energy domain and in the forward direction in the angular domain.

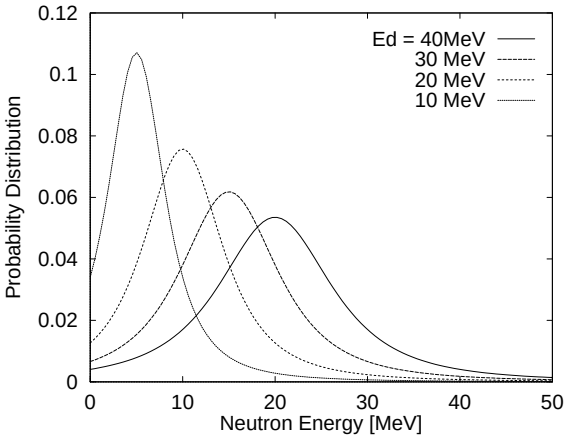

Figure 4-2 Energy distribution of Serber stripping cross-section for various initial deuteron energies.

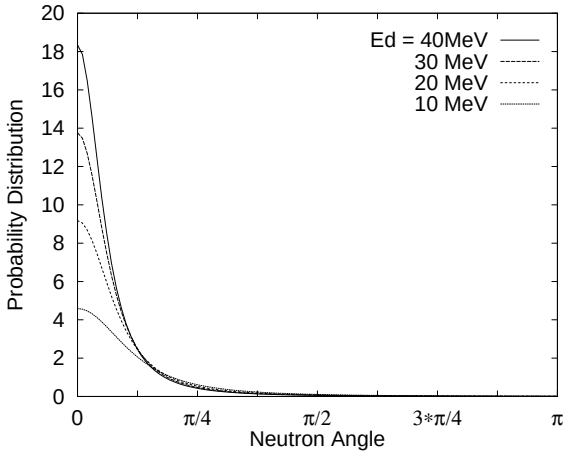

Figure 4-3 Angular distribution of Serber stripping cross-section for various initial deuteron energies.

Serber's analysis also found that the cross-section for this type of reaction above some threshold should be independent of the initial deuteron energy and have a value of:

$$\sigma = \frac{\pi}{2} R R_d$$

where:

R = target nucleus radius [cm]

R_d = deuteron radius [cm].

This threshold is derived from the assumption that the perpendicular displacement of the neutron during the impact is small compared to the deuteron radius. If not, the neutron would likely impact the target nucleus after the proton and the stripping theory would not apply. Since the reaction lifetime is a function of the deuteron energy and target nucleus radius, and the perpendicular displacement is a function of the binding energy of the deuteron, this assumption results in an energy threshold:

$$E_d > 2(R / R_d)\varepsilon_d .$$

This results in an exact threshold of 6 MeV for stripping on Li, but the theory does not fully apply until the energy is somewhat greater than this, say 10 MeV.

While Serber's theory made no assumptions as to the thickness of the target or mass of the constituent nuclei, the distributions defined above have been confirmed for thick light targets (such as for a lithium neutron source) [Aug76]. In particular, it was also found that the total cross-section as defined by Serber did not apply in their case, although no explanation was given.

The Serber stripping theory does have some limitations. Most important are the non-zero tails of the Serber distribution in the energy domain. This results in non-zero probability of the generation of both

negative energy neutrons and neutrons with energies much greater than the incoming deuteron energy. Neither of these domains are physically possible within the assumptions of Serber's stripping theory, and thus the distribution must be limited to the domain [0,E_d].

It is also important to mention that the Serber theory is developed for two opposite extreme cases: opaque nuclei and transparent nuclei. Since the difference in the angular distribution between the two cases is small, the more simple angular distribution for transparent nuclei was used. The distribution for neutron energy for the opaque case was used, as it is more realistic.

Shaping Function

Some shaping function must be used to define how this distribution should be weighted when combining it with the compound reaction model defined below. This shaping function should be dependent, in principle, on the deuteron energy, although we have already described that the Serber stripping theory is independent of deuteron energy above the exact threshold, $E_d > 2(R / R_d)\varepsilon_d$ = 6 MeV, or the functional threshold, E_d = 10 MeV. Using this information, during earlier work on the IFMIF project, Oyama [Oya95] suggested a reasonable shaping function of:

$$A_s = \begin{cases} 0 & E_d < 6 \\ 0.005E_d + 0.01 & E_d \in [6,10] \\ 0.06 & E_d > 10 \end{cases}$$

as shown in figure 4-4.

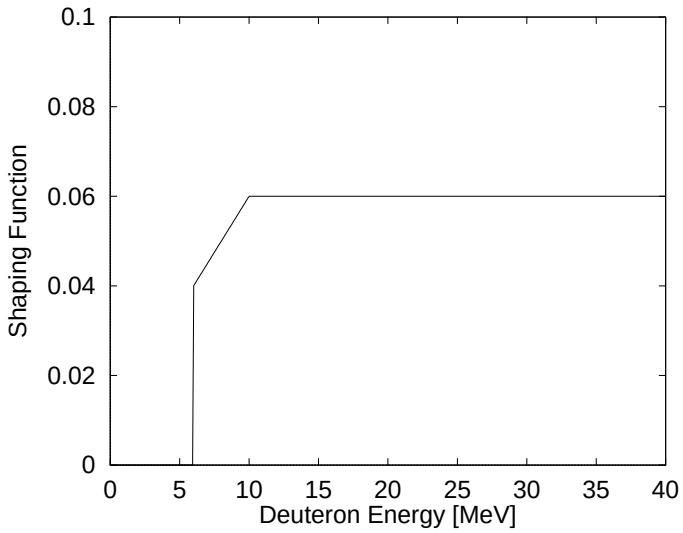

Figure 4-4 Shaping function suggested by Oyama for stripping component.

Beginning with this shaping function, a comparison to the Sugimoto data was performed. In particular, since the stripping component dominates strongly over the compound reaction component in the forward direction, the differential yield at 0 degrees was used to compare to the stripping model and scale the Oyama shaping function. Using this method, as shown in figure 4-5, the shaping function was scaled by a factor of 1.3.

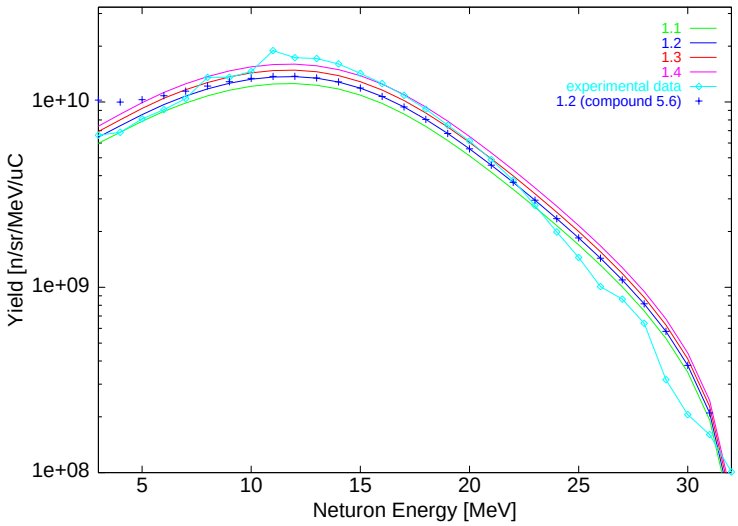

Figure 4-5 Comparison between data and model in forward direction to determine magnitude of stripping component.

4.2.2 Compound Reaction component

Basic Theory

The stripping component, normalised in this way, under-calculates the yield at directions away from forward, and hence, grossly under-calculates the total yield. The solution of this problem is to introduce an isotropic reaction path such as that of the compound reaction mechanism. In this case, an evaporation model will be used to represent the statistical behaviour of compound reactions which result in a continuum of states in the final nucleus. While the angular distribution is, as mentioned above, isotropic, the energy distribution used in this case is:

$$\frac{\partial^2 \sigma_c}{\partial E_n \partial \theta_n} = E_n e^{-E_n/T}$$

where:

T = statistical temperature = $\sqrt{\frac{10E_d}{A}}$,

as shown in figure 4-6.

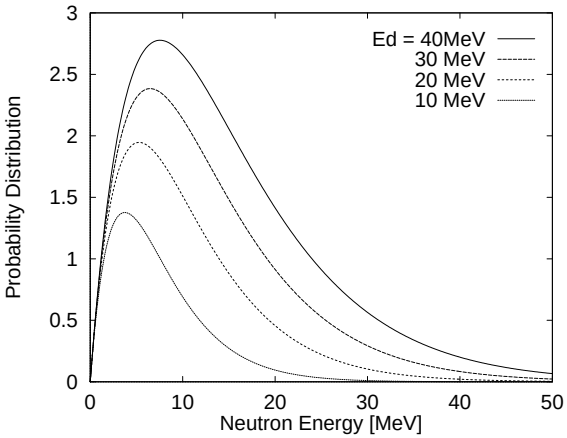

Figure 4-6 Energy distribution of compound reaction cross-section for a variety of deuteron energies.

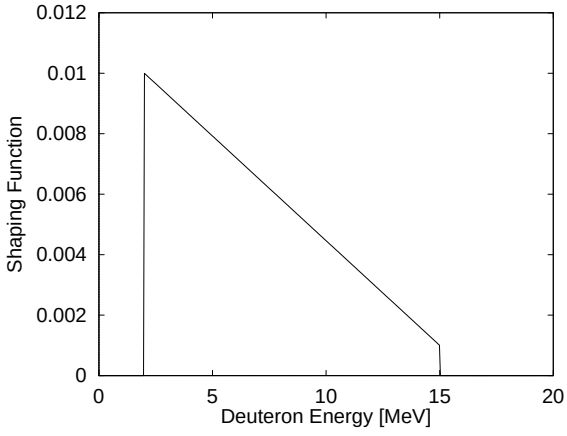

Figure 4-7 Shaping function suggested by Oyama for compound reaction component.

Shaping function

Since compound reactions require that the deuteron penetrates to the nucleus of the lithium, there is a finite threshold at about 2 MeV, the coulomb barrier for lithium. Furthermore, the total cross-section can be expected to drop dramatically for higher energies. Thus, the shaping function proposed by Oyama [Oya95] for this component has a maximum of 0.01 b at 2 MeV and drops by 1 order of magnitude to 15 MeV:

$$A_c = \begin{cases} \dfrac{-0.009E_d + 0.148}{13} & E_d \in [2,15] \\ 0 & o.w. \end{cases}$$

as shown in figure 4-7.

In order to fit this component to the Sugimoto data, a numerical integration of the yield data over the entire phase space was performed to determine the total yield. This was compared to the calculated total yield, and the shaping function scaled accordingly. It was found that for the total yield of 6.16% (0.0616 neutrons per incident deuteron) for the Sugimoto data, the compound reaction shaping function would have to be scaled by a factor of 5.77 (see Figure 4-8).

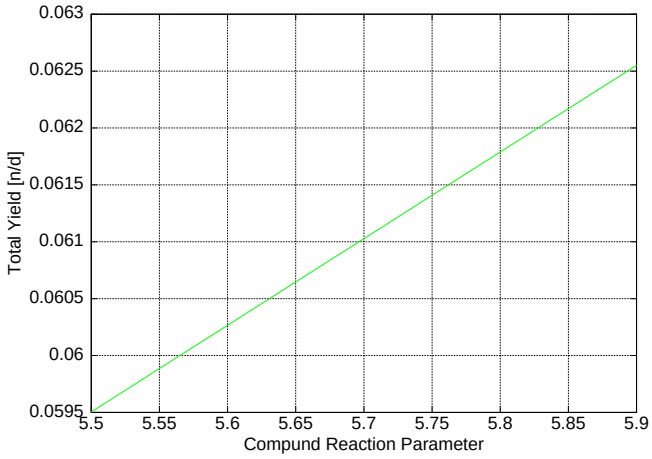

Figure 4-8 Total yield as a function of the compound yield parameter.

4.2.3 Full Phase Space Comparison

A final test of the above methodology can be done by comparing the differential yield of the model to the data in the full phase space. This can be seen in figure 4-9. In this figure, a 3-dimensional wire mesh plot has been created to show, at each point, the higher of the model or the data. Since a comparison of 3-dimensional data is otherwise difficult, this method draws particular attention to those places where the model and data are equal (where the model and data cross), allows for comparison at the edges (at θ/π=0.8), and shows when there is general agreement (frequent proximal crossings). One failing of this method of comparison is that the magnitude of the discrepancy is not clear.

Successes

In general, this model displays good agreement with the Sugimoto data. As required by the fit for the stripping component, the forward direction matches well, particularly in the [0,$E_{d,max}$] domain. Throughout the other directions, there is also a reasonable agreement with the model following the same general shape at the data.

Concerns

There are two regions in particular which deserve further mention. First is the low energy (< 3 MeV), low angle region which shows a great discrepancy. In an analysis of d-Be reactions[Bre89], this peak was found to represent the decay of excited (2.54 MeV) ^{9}Be to the ground state of ^{8}Be producing 0.7 MeV neutrons. In this case, the ^{9}Be could be produced by the absorption of a deuteron into a ^{7}Li nucleus. This effect is not included in any of the current model components and, due to its magnitude, would have a serious impact on the fitting parameter for the compound reactions.

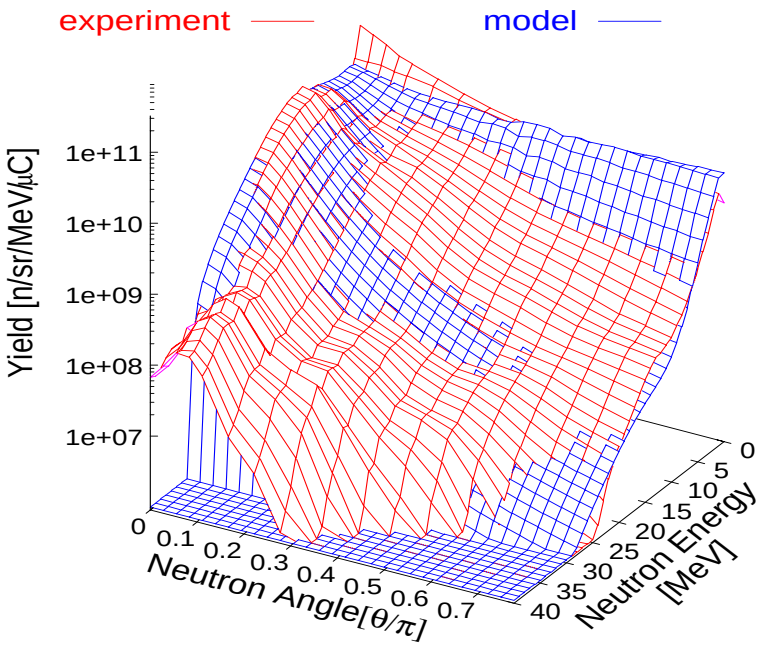

Figure 4-9 Full phase space comparison of neutron source model and experimental data at 35 MeV.

The other region is the high energy region above the initial deuteron energy. The experimental detection of neutrons in this domain suggests a reaction mechanism which is completely missing from the model. There are a number of possibilities for this reaction path, but it is most probably some variation on the stripping reaction mechanism to an isolated final state which cannot be considered statistically as is done in the above models [Man81]. Although the difference between the model and the data can most easily be seen in the high energy domain, it may also represent some of the minor differences throughout the phase space.

While the current model is sufficient for further engineering analyses as it is simultaneously improved, the results of Chapter 5 highlight the need to have a better understanding of the exact total neutron yield from the d-Li reaction. A better study of the nuclear physics behind the reaction mechanisms may shed more light on the particulars of the cross-section model, but it is always most important that the model be validated with experimental data, as is the case here.

4.2.4 Stopping Power model

The model for the stopping power of deuterons in lithium is the standard model for E_d > 1 MeV taken from Anderson and Ziegler [And77]:

$$\frac{dE_d}{dx} = \frac{A_6}{\beta^2}\left[\ln\left(\frac{A_7\beta^2}{1-\beta^2}\right) - \beta^2 - \sum_{i=0}^{4} A_{i+8}\left(\ln E\right)^i\right]$$

where:

A_i = Stopping power fitting coefficients E = deuteron energy [keV/amu]

β = velocity normalised to speed of light

and the stopping power is expressed in units of [eV/(10^{15} atoms/cm^2)].

While this same reference gives models for the deuterons with lower energies (at the end of the path), the shaping functions for the two reaction mechanisms both have zero weight at energies less than 2 MeV, so this is not important. Furthermore, even additional reaction models which may be included in the future would have low yields at such low deuteron energies.

4.2.5 Beam Profile modelling

Original analysis suggested that the deuteron beam could be generally a flat beam with tight gaussian edges in one direction and edge peaks of less than 5% in the other direction, and thus could be modelled as purely rectangular and flat. However, more recent analysis (see fig. 5-2) [Mar96] of beam transport technology suggests that the beam may be more spread out, being roughly flat with wide gaussian edges in one direction with the other direction having large edge peaks (on the order of 25% nominal) and a broadly peaked central region with tight gaussian edges. Because of this change, a new method of modelling the beam profile has been implemented. The beam profile may have an important impact on the flux distribution throughout the test section because of reduced neutron source density caused by a reduced average beam current density.

Basis for Gaussian combination

The beam profile is now modelled by a sum of 3 functions in each direction based on gaussian distributions,

$$G\left(x, x_o, \sigma\right) = \frac{1}{\sqrt{2\pi\sigma}} e^{-\left(x-x_o\right)^2 / 2\sigma}.$$

The basic shape of each direction is defined by

$$I_{x,base}\left(x, x_o, \sigma_o, m_o\right) = \begin{array}{r} m_o \cdot \left[G\left(x, -x_o, \sigma_o\right)\cdot\left(1 - H\left(x + x_o\right)\right) + G\left(x, x_o, \sigma_o\right)\cdot H\left(x - x_o\right)\right] \\ + G\left(0,0,\sigma_o\right)\cdot\left[H\left(x + x_o\right) - H\left(x - x_o\right)\right], \end{array}$$

as shown in figure 4-10. The magnitude of the gaussian "wings", m_o, will normally only have values of 0 or 1, depending on whether sharp or gaussian edges are desired. This basic shape is then modified by two corrections, each of which has the form:

$$I_{x,corr}\left(x, x_c, \sigma_c, m_c\right) = m_c \cdot \left[G(x, -x_c, \sigma_c) + G(x, x_c, \sigma_c)\right]$$

as shown in figure 4-10. The three parameters (centres, standard deviation and magnitude) of both of these corrections are adjusted to fit the data.

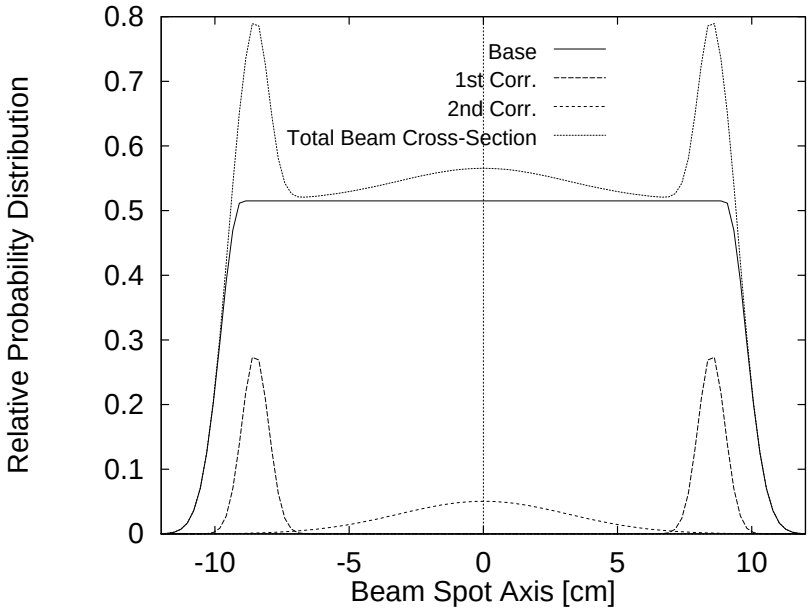

Figure 4-10 Gaussian beam profile model components.

There are two important features of this model. First, the beam must be symmetrical, a reasonable assumption in most cases. Second, if a single central gaussian correction is required, the centre parameter of one of the corrections can simply be set to 0.

The two primary reasons for choosing this model were the fact that the physical beam distributions are based on gaussians and the desire to retain the analytic nature of the model. Since the beams really do exhibit roughly gaussian behaviour, this model can provide the correct edge effects and general shapes throughout. The gaussian fits were chosen because they are easy to randomly sample. While a polynomial fit may be able to give similar agreement to the physical beam profile and also preserve the analytic nature of the model, polynomials of arbitrary degrees are hard to invert for random sampling.

Comparison with beam profiles

A full 3 dimensional representation of the beam model profile is given in figure 4-11. Comparisons with a 3-dimensional quadrant and some cross-sections of the currently expected beam profile are shown in figures 4-12 through 4-14. For this comparison, one quadrant of the given beam profile data was assumed to represent the shape of a symmetrical beam. To better refine the beam model parameters for a particular physical beam, a more refined mesh should be used for the beam analysis.

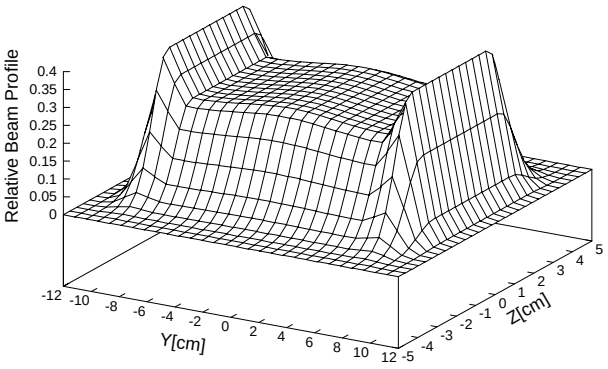

Figure 4-11 Three dimensional representation of beam profile model

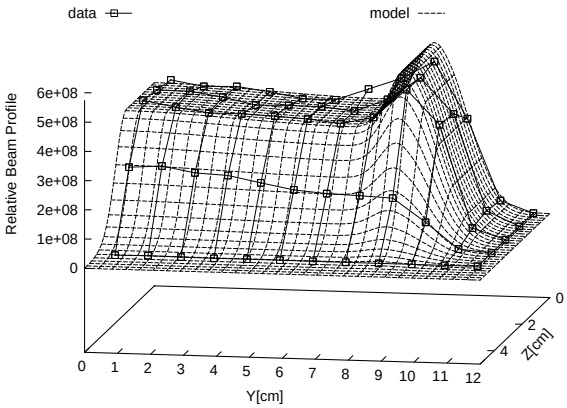

Figure 4-12 Single quadrant comparison of beam model to beam profile data

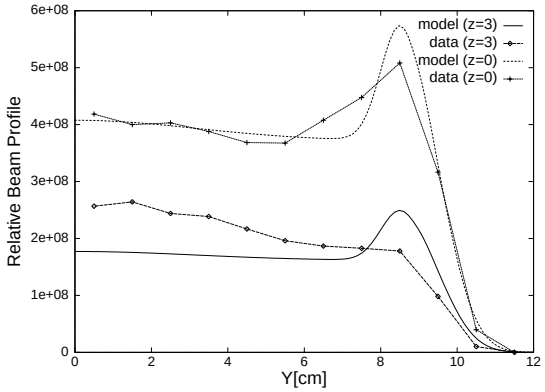

Figure 4-13 Comparison of selected cross-sections in the y-direction of the beam profile model and data

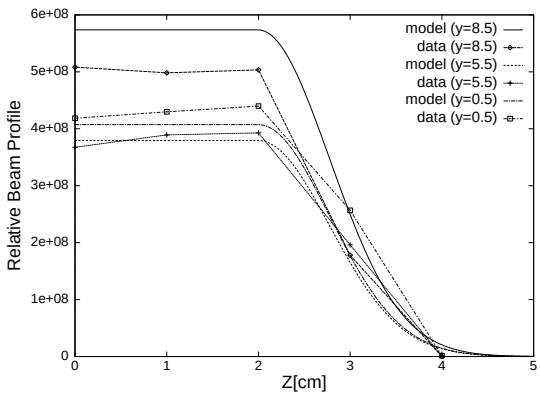

Figure 4-14 Comparison of selected cross-sections in the z-direction of the beam profile model and data

Possible other distributions

The flexibility of this beam model is made apparent with a few examples of other beam profiles. In particular, this method could be used to model beams which are assumed to exhibit previous IFMIF beam specifications (figure 4-15) [Mae96], pure central gaussian behaviour (figure 4-16), pure sharp- or gaussian-edged rectangular behaviour (figures 4-17 and 4-18), or a variety of other possibilities.

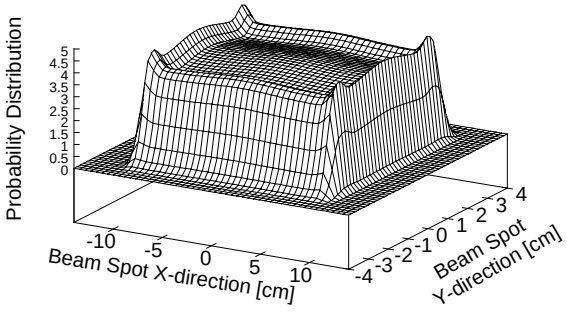

Figure 4-15 Previous IFMIF sample beam distribution

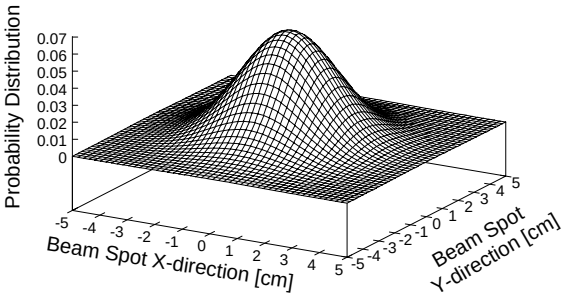

Figure 4-16 Central symmetric gaussian sample beam distribution

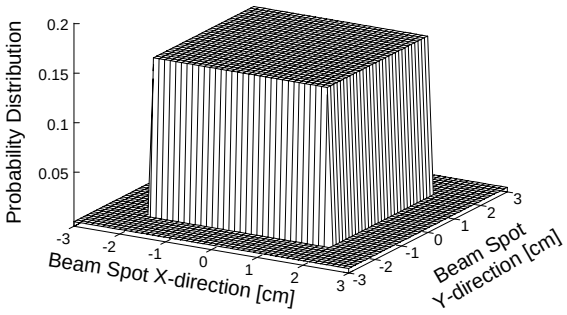

Figure 4-17 "Sharp" (perfect) rectangular sample beam distribution

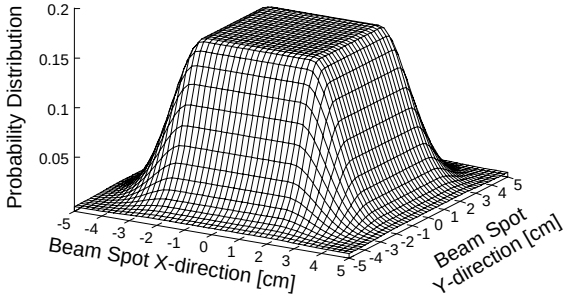

Figure 4-18 Gaussian edged rectangular sample beam distribution

4.3 Source Routine

The Monte Carlo deuteron-light nuclei (McDeLi) source module has been written as a FORTRAN 77 code library with a variety of functions and subroutines. The main interface routines in this module are invoked by a special source routine written with the standard interface as defined by the MCNP4A manual [Bri93].

4.3.1 Input and Usage

Input parameters

The input parameters for the source routine are provided with the standard source definition (MCNP 'SI' input cards) distribution commands. There are 15 distributions which are used to define all the parameters of the beam and target system. In general, the parameters are described by figure 4-19. The source module allows for an arbitrary number of beams which are incident on an arbitrary number of targets. The targets must each be defined in the geometry specifications of the MCNP input file and that assigned cell number noted for use in the parameters below.

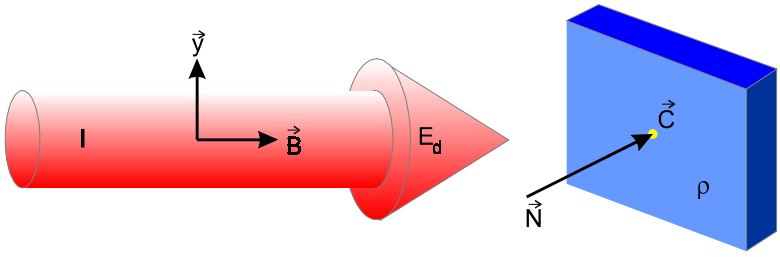

Figure 4-19 Graphical representation of beam and target input parameters

BEAM PARAMETERS	TARGET PARAMETERS
$\vec{B}$ = Beam Direction Vector	
$\vec{y}$ = Beam Orientation Vector	
$\vec{C}$ = Beam Spot Centre	$\vec{N}$ = Target Surface Normal Vector
I = Beam Current [mA]	ρ = Target density [g/cm^3]
E_d = Deuteron Energy [MeV]	

Beam Parameters

The first 12 distribution cards are used to specify all the beam parameters, including the beam profile. The actual distribution numbers are not important, but the order is. Each distribution is either a scalar or vector distribution, with the order of the data in each corresponding to the order of the data in the others. True vector distributions need not be normalised.

i) Target number

The target data which will be provided in the last 3 source distribution cards will be entered in a specific order. This card indicates, for each beam, which target the beam strikes by indicating the number in this order. Note that this is most likely different from the cell number assigned to this target in the MCNP geometry specification.

ii) Beam current [mA]

iii) Beam Energy [MeV]

iv) Beam Direction vector

v) Beam Orientation vector

This vector is perpendicular to the beam direction vector (iv) and defines the first direction of the beam profile. This will become clearer below, but if the beam profile is mapped on a Cartesian plane normal to the beam direction vector, this is one of the two directions of the Cartesian system which are used to define the beam profile as outlined above. The other Cartesian direction will be found by simply taking the cross-product of the beam direction vector and this vector.

vi) Basic beam profile parameters in 1^{st} direction

Following the model described above, this distributions gives three parameters for each beam which define the basic shape of the profile in the direction of the beam orientation vector (v). In this and the following beam profile parameter distributions, the order of the parameters is (centre, standard deviation, magnitude) or, for example, (x_o, σ_o, m_o) for the basic shape parameters.

vii) Basic beam profile parameters in 2^{nd} direction

As (vi) but in the direction which is calculated by crossing the beam orientation and direction vectors.

viii) and (ix): First beam profile correction parameters in 1^{st} (2^{nd}) direction [2 cards]

These parameters are given in the order as defined in (vi) for each beam and follow the model outlined above.

x) and (xi): Second beam profile correction parameters in 1^{st} (2^{nd}) direction [2 cards]

These parameters are given in the order as defined in (vi) for each beam and follow the model outlined above.

xii) Beam spot centre vector

This vector defines the centre position of the symmetric beam spot on the target.

Target parameters

Three cards are used to define the target. As described more below, the targets size is defined only in the MCNP geometry specification, and not in the source definition.

xiii) MCNP Cell number

This card lists the MCNP geometry cell numbers for the targets listed as described for card (i). If there are ≥2 targets, then the MCNP cell numbers for these two targets are ordered to be consistent with card (i).

xiv) Target normal vector

This vector indicates a normal to the surface of the target. The primary importance of this is to convert the beam energy density distribution from the Cartesian system described above (normal to the beam direction vector) to a Cartesian system which is parallel to the target surface.

xv) Target density [g/cm^3]

This density is only used to determine the track length of penetration of the deuteron, and is important for determining the birthplace of the neutron.

Input assumptions

There are a number of assumptions implied by this model and/or set of input parameters.

Target size

For the purpose of sampling for the birthplace of the neutron, the target is assumed to be semi-infinite, occupying the half-space delimited by the plane defined by the target normal and passing through the beam spot centre. When all the birth conditions have been established for the neutron, it is tested to ensure that it is in the MCNP geometry cell specified in card (xiii). If not, the neutrons birth parameters are resampled. This is important because the gaussian definition of the beam profile means that the beam spot is mathematically infinite in its coverage of the target. For this reason, care should be taken to ensure that the target defined in the geometry specification is large enough that most of the randomly sampled locations in the beam spot are not rejected. This condition is satisfied if the physical beam is modelled well and the physical beam spot is smaller than the physical target. If this is not the case, the routine will still function properly, but will be inefficient.

Beam spot assumptions

The beam spot is assumed to by symmetric in both directions, and therefore have a well defined centre. It is also important that the beam not be parallel to the surface of the target, a reasonable assumption since if this was the case, no deuterons would impact the target.

4.3.2 Method

Pre-processing

The parameters for each beam are pre-processed the first time that the source routine is called so that each subsequent call is accelerated. The first task is to numerically integrate the yield as a function of the deuteron energy so that the total yield for that beam can be calculated. This is necessary to generate the normalised relative probability of neutron production from each beam. Next, the beam direction and orientation vectors are normalised and crossed to calculate the other beam

orientation vector. The target normal vector is then normalised in preparation for rotating the beam spot onto the target surface plane.

As already mentioned, the two orientation vectors which define the plane of the beam spot as defined by the beam profile parameters in the input file are normal to the beam direction vector, but will not be in the plane of the target surface if the beam is not normally incident on the target. Therefore, the beam orientation vectors need to be rotated and scaled to a Cartesian system which is parallel to the target surface using the following vector mathematics:

$$\vec{Y} = \hat{y} + m_y \hat{B}$$

$$m_y = -\frac{\hat{y} \cdot \hat{N}}{\hat{B} \cdot \hat{N}}$$

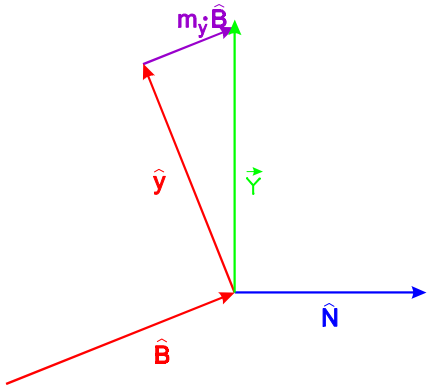

Figure 4-20 Vector diagram to describe beam orientation pre-processing

where the vectors are defined as in figure 4-20, and similarly for the second beam orientation vector. Finally, the normalised relative probabilities of neutron production in each of the four components of the beam profile in each direction are calculated as:

$$p_o = m_o$$
$$p_1 = 2x_o G(x_o, x_o, \sigma_o)$$
$$p_2 = 2m_1$$
$$p_3 = 2m_2$$

$$p_{tot} = \sum_{i=0}^{3} p_i$$

$$\hat{p}_i = \frac{p_i}{p_{tot}}$$

Normal Flow of Operation

Once this pre-processing is complete, the normal operation of the source routine can proceed. The beam of origin is sampled using the normalised relative probability of each beam and the MCNP utility subroutine `SMPSRC`. From this, all the beam specific parameters are manually extracted from the MCNP source information arrays. Given the other beam information, the subroutines of the McDeLi module are invoked through the interface function `dnSmp()` which returns the deuteron energy, neutron energy and angle in the lab frame of reference, target mass and reaction mode (the latter two are primarily for debugging purposes). Given the beam profile parameters, the offset from the centre of the beam spot in the plane normal to the beam direction vector is sampled and this position mapped to the surface of the target to determine the entry position of the deuteron. Finally, the initial and reaction energy of the deuteron and the target density are used to determine the track length of deuteron penetration which is applied along the beam vector from the deuteron entry point to determine the birth place of the neutron. If this birth place is outside the MCNP geometry specification for the target, the beam profile is resampled, keeping the reaction energies and angles, since they are independent of the deuteron entry position.

5. Neutron flux and nuclear response calculations

The main purpose of the IFMIF facility is to produce a neutron environment similar to a future fusion device in order to provide reasonable material irradiation conditions. Since IFMIF is a accelerator based system, the properties of the neutron field depend mainly on the location in the test cell. Therefore, the test cell region is divided into four main parts as sketched in fig. 5-1. The four parts are named high flux, medium flux, low flux and very low flux region. The most important part in the test cell is the high flux region, where the requirements are 0.5 litre volume with a displacement damage rate higher than 20 DPA/FPY (FPY = Full Power Year) for candidate materials. In addition, the neutron flux gradient should be less than or equal to 10 %/cm [Mar 96].

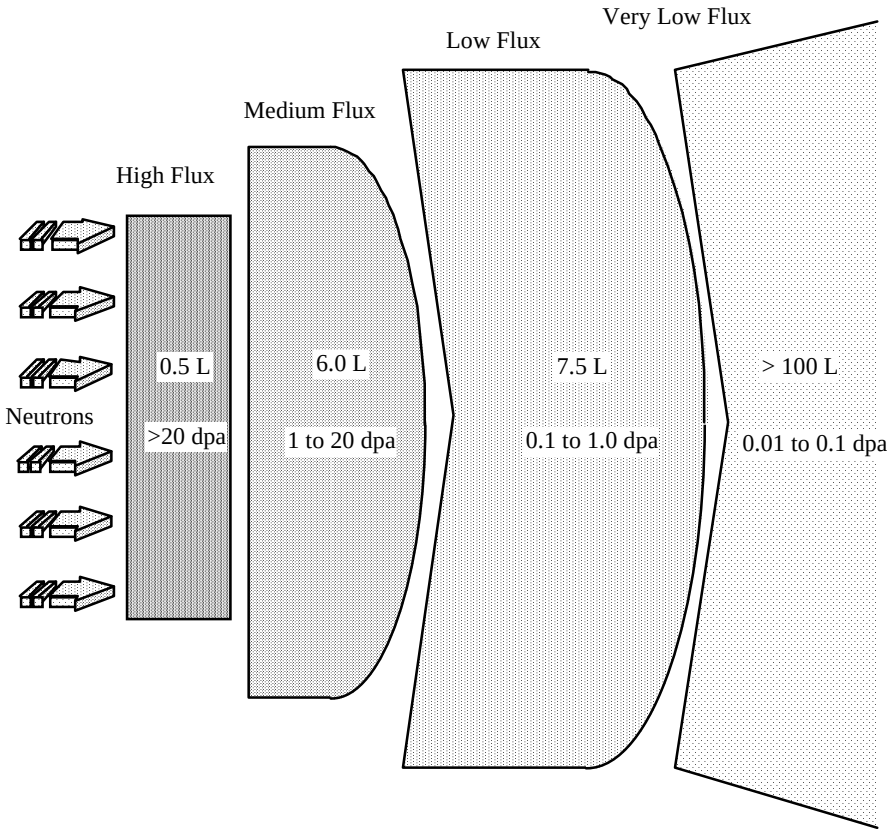

Figure 5-1 Overview on the definition of the volumes of the different flux regions in the IFMIF Test Cell in function of DPA/FPY.

The following discussion concentrates on this most important high flux region. The complexity of the comparison and the difficulties in evaluating accurate results are due to different nuclear data sets, different neutron source models, different calculation parameters and different computer codes. All these parameters, which can affect the calculation results, need to be discussed.

One important result is whether these high flux region requirements can be met, and with what uncertainties.

5.1 Specification of calculation parameters

In order to allow a comprehensive discussion of the various nuclear responses, especially a detailed comparison of the results of the different calculation models, all parameters which can affect the results need to be indicated.

5.1.1 List of calculation parameters

A detailed overview of the calculation parameters is given in table 5-1. The parameters describe the performance of the IFMIF neutron source and are discussed in three different parts, namely accelerator, target and test cell. The accelerator part describes the properties of the deuteron beam, the target part describes the Li-jet and backwall properties and the test cell part describes the properties of the material loading.

Table 5-1 List of all relevant calculation parameters.

Part	Parameter	Explanation
Accelerator	E_d	Primary deuteron energy (30, 35, 40 MeV)
	ΔE_d	Straggling of primary deuteron energy
	I	Electrical beam current in milliamps (mA)
	Angle	Geometrical angle between the beam lines (20°)
	Beam profile	Uniform or non-uniform beam density distribution
	Beam footprint	Size of beam footprint
Target	d_{Li}	Thickness of the lithium jet at the beam footprint area (2.6 cm)
	T_{Li}	Lithium jet temperature. This value affects the lithium density (300 °C, ρ_{Li} = 0.512 g/cm^3)
	D_{Range}	Range model for calculating the deuteron range in Li
	ΔD_{Range}	Longitudinal and transversal range straggling
	d_B	Thickness of the backwall at the beam footprint area (1.6 mm)
	r_B	Backwall curvature
	n-source model	Type of neutron source function model or source function data
Test cell	Calculation code	INS or MCNP calculations
	Sort of calculation	Uncollided (empty test cell or void) or collided (loaded test cell) calculations
	Loading parameters	Loaded material (void, coolant, specimen packages), loading positions, material density, reflecting walls
	Nuclear response	SPECTER [Gre92] or data of this report (chapters 2 and 3)
	Transport data	Data of this report (chapters 2 and 3)
	Kind of results	Point values or averaged values (cell size)

Most of the parameters in the list can be characterised as design dependent. These parameters are necessary to be noted and to be introduced into the computer codes but they are uncritical concerning the neutronics calculation results, because they are well defined. On the other hand, the really sensitive parameters are the neutron source model (and the experimental data on which it is based), the beam profile and footprint. Furthermore, the results are sensitive to the differences between the calculation procedures of the computer codes.

The non-uniform beam profile data used in this calculations are from [Bru96]. A three-dimensional plot of this data is given in figure 5-2. This profile was generated by Monte Carlo simulations of the IFMIF High Energy Beam Transport (HEBT). It shows a beam footprint of about 7 cm x 22 cm and has peaked edges.

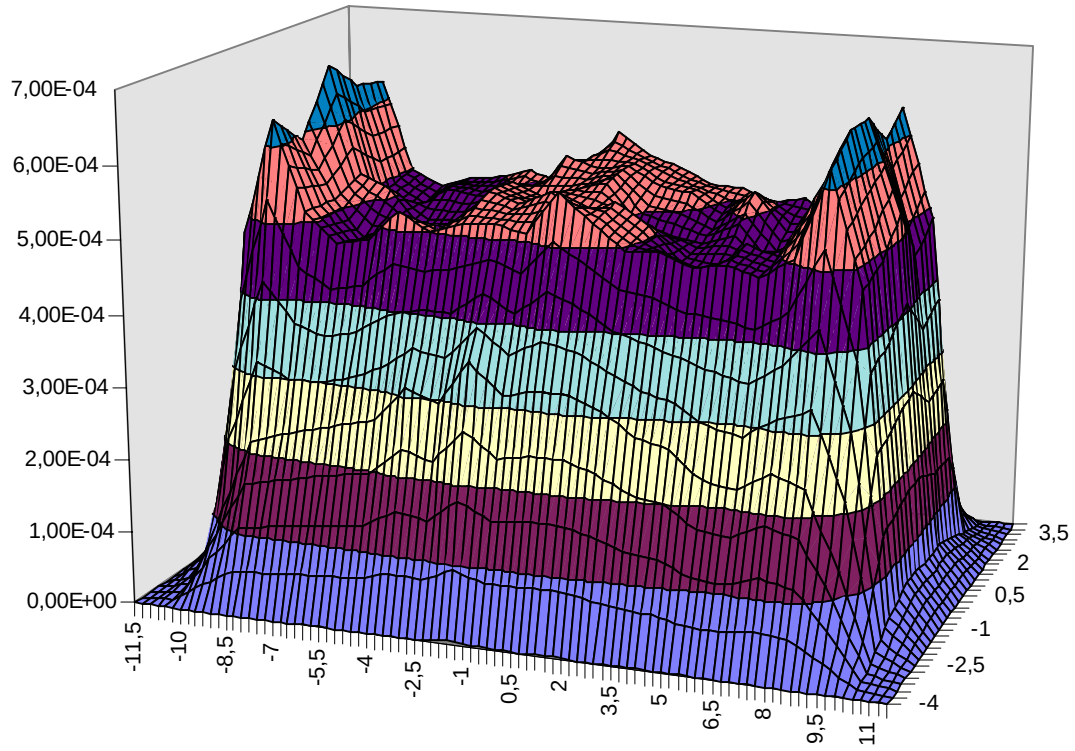

Figure 5-2Three-dimensional view of the non-uniform deuteron beam density distribution [Bru96]. In difference to the uniform beam profile this profile has an enhanced beam footprint and peaked edges.

The properties of the neutron source model developed at FZK, are already discussed in chapter 4. The computer codes differ in their nature: the INS code is an analytical code while the MCNP code is a Monte Carlo Transport Code. With the INS code only uncollided calculations are possible while with the MCNP code uncollided and collided calculations can be performed.

5.1.2 Parameter set for INS calculations

Table 5-2 shows the parameters used in the INS calculations. The source cross-section data for the Li(d,xn) neutron production reactions were provided by F.M. Mann [Man91]. The total neutron yield of these data at 40 MeV deuteron energy is 6.7%. Comparing the angular yield dependence of these data with the experimental results of thick target neutron yield measurements from Johnson et al [Joh80], shows somewhat higher yields for larger angles for the [Man 91] data (see figure 5-3). For this reason a second neutron yield data set with a slightly modified neutron yields[*] [Dau93] at higher emission angles has been produced from the original Mann data. The angular dependent scaling factors have been ascertained from [Joh 80]. This „experimental“ thick target neutron yield data gives a total yield of 5.6 % at 40 MeV.

[*] This data set is referred in the text as ‘experimental data’.

Table 5-2 List of the calculation parameters used with INS calculations

Part	Parameter	Value
Accelerator	E_d	40 MeV
	ΔE_d	not considered
	I	250 mA
	Angle	0°
	Beam profile	Uniform, non-uniform
	Beam footprint	5 x 20 cm^2 (uniform), 7 x 22 cm^2 (non-uniform)
Target	d_{Li}	2.6 cm
	T_{Li}	300 °C, ρ_{Li} = 0.512 g/cm^3
	D_{Range}	ZBL-Theory [Zie 85]
	ΔD_{Range}	not considered
	d_B	1.6 mm
	r_B	none
	n-source model	BNL data [Man 91]
Test cell	Calculation code	INS
	Sort of calculation	Uncollided calculations
	Loading parameters	none
	Nuclear response	[Gre 92]
	Transport data	none
	Kind of results	Point values

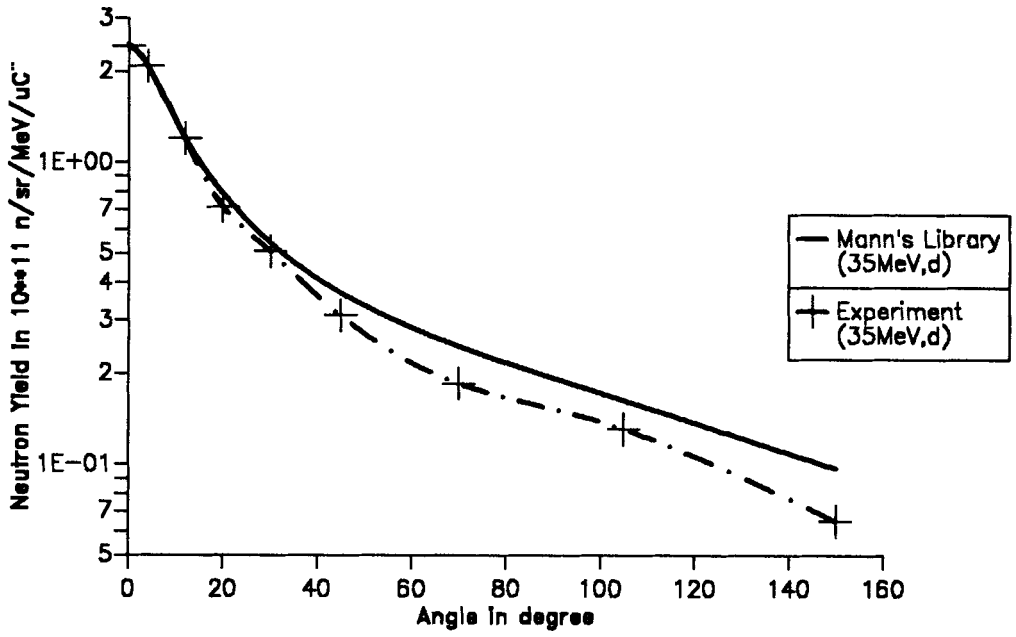

Figure 5-3 Comparison of the angular dependence of the neutron Li(d,xn) neutron yield at 35 MeV for Mann's data [Man 91] and the thick target experiment [Joh 80].

5.1.3 Parameter set for MCNP calculations

Table 5-3 List of the calculation parameters used with MCNP calculations

Part	Parameter	Value
Accelerator	E_d	40 MeV
	ΔE_d	not considered
	I	250 mA
	Angle	20°
	Beam profile	Uniform, non-uniform
	Beam footprint	5 x 20 cm^2 (uniform), 7 x 22 cm^2 (non-uniform)
Target	d_{Li}	2.6 cm
	T_{Li}	300 °C, ρ_{Li} = 0.512 g/cm^3
	D_{Range}	ZBL-Theory [Zie 85]
	ΔD_{Range}	not considered
	d_B	1.6 mm
	r_B	none
	n-source model	Model description [see sec. 4]
Test cell	Calculation code	MCNP calculations
	Sort of calculation	Uncollided and collided calculations
	Loading parameters	various [see individual results in sec. 5.4]
	Nuclear response	data of this report
	Transport data	data of this report
	Kind of results	Averaged values over segmented cells

5.2 Explanation of graphic representations

For a better understanding the data would be visualised as three dimensional plots. To include, however, maximum information in the plots it was decided to show a plane plot to characterise the behaviour of the three dimensional test cell. This representation is explained in fig. 5-4 and shows on the left a three dimensional view of one octant of the space which is equal to one quarter of the high flux test cell. The downstream direction is along the *x*-axis. The major information about the investigated parameters can be obtained by looking at the surfaces A, B and C which are the *x*-*z*-plane, the *y*-*z*-plane and the *x*-*y*-plane The backplate of the neutron production target is located behind plane B in upstream direction. The planes A and C are symmetry planes. The plots used in the discussion are shown in the sketch on the right in fig 5-4.

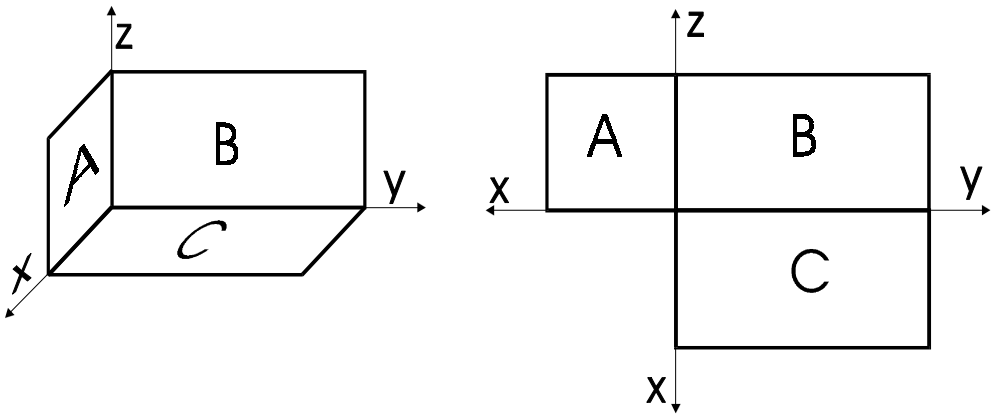

Figure 5-4 Explanation of the plots used in the discussion.

The software used to visualise the data is AVS [AVS92]. The AVS graphical system is a very powerful tool. The AVS module library was extended by some special modules for calculating the volume below an isosurface and for creating Post Script outputs of the images [Wil97].

5.3 Calculations with the INS Code

The INS code (Intense Neutron Source) was developed to calculate uncollided spatially dependent neutron flux spectra in the test cell of an intense neutron source [Dau93]. The programme version used here deals with the d-Li concept. With this neutron flux spectra information, the neutron displacement damage per atom (DPA) and the H- and He- production rates can quickly be calculated for any target element at any position in the test cell. In the case discussed here only nuclear responses of ^{nat}Fe has been used. The basic data flow in the INS code is sketched in fig. 5-5. The INS code consists of the 4 code modules CONVERT, CONTOUR, SPECTRA and DAMAGE.

In the module CONVERT, the double differential nuclear cross-sections for the Li(d,xn) reaction are converted into the FZK internal data format.

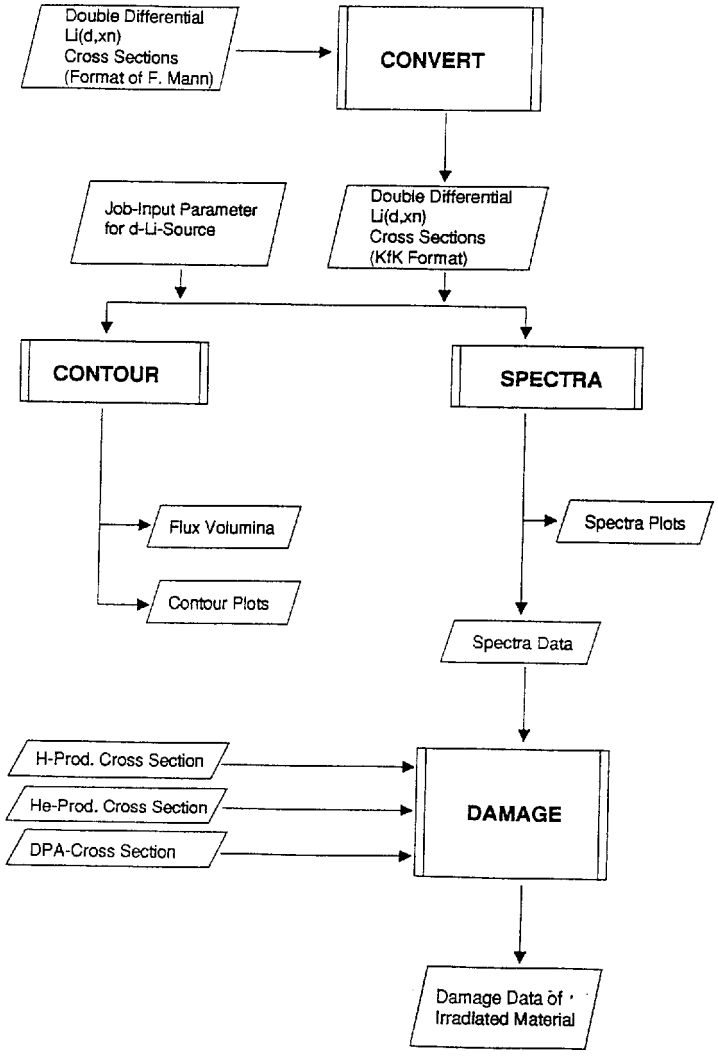

Figure 5-5 Data flow chart of the INS code for the d-Li source

In the module SPECTRA, the neutron flux spectra are calculated. With the algorithm used in this module, it is possible to calculate a neutron flux spectrum at any spatial point in the test cell for a rectangular target. The important parameters are sketched in fig. 5-6. The arrow shows the incoming deuterons. The Li target dimensions are Ta_z and Ta_y. The penetration depth of the deuterons in the Li target is dx and the overall target thickness is d. Since the deuteron energy is decreasing with growing dx, the target is divided into slices. For every slice the differential neutron yield can be calculated. In order to consider the width of the target, every slice is subdivided into small square pieces and the neutron production is normalised to such a small target element. For a given space point, the neutron flux from the distributed target is then calculated by integrating over the whole target. For the non-uniform beam profile case a normalised beam profile function is folded in to weight every target element.

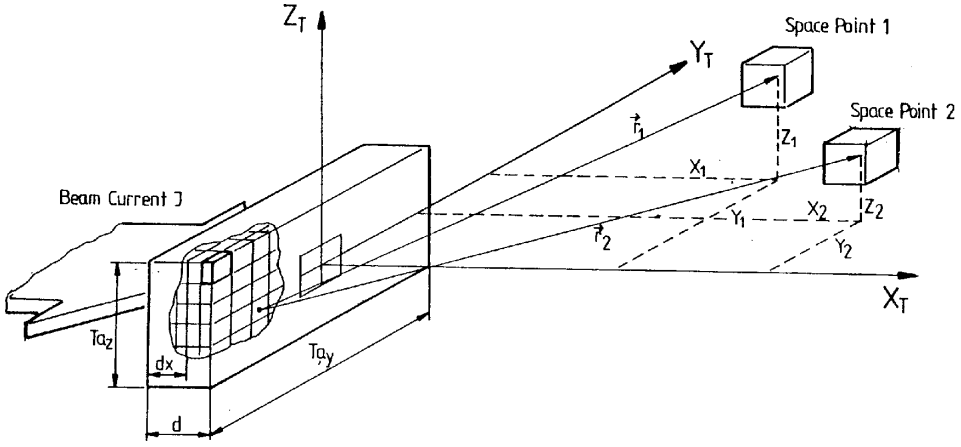

Figure 5-6 Target model as used in the INS code. The spatial points in the test cell and their co-ordinates are symbolised.

In the module CONTOURS, the available volume for an integral neutron flux higher than a given limit is calculated. For the results with the INS code discussed in this report this module was extended. Now it is possible to calculate the available volume as a function of DPA-rate, higher than a given limit. This requires, however, the results of the module DAMAGE.

In the module DAMAGE the irradiation damage parameters like H-, He- and DPA-rate for ^{nat}Fe is calculated. This can be done with the INS code only for an empty test cell (uncollided calculations). This means, the neutron flux spectrum calculated at a given spatial point in the test cell is used to estimate the damage parameters at this point, as if there would be a differential small volume element of the material of interest. Thus this is only an approximation to the real case where the test cell is loaded with material.

A further extension to the INS code is the handling of a non-uniform beam profile. In the former INS version only a uniform beam profile (5 cm x 20 cm) could be considered. The non-uniform beam profile is used because it represents a more realistic description of the deuteron beam. A three dimensional plot of this non-uniform beam profile is given in fig. 5-2.

5.3.1 Uncollided calculations with uniform beam profile

The first step in the discussion of the results is the presentation of the most simple case. These are calculations with a uniform beam profile and an empty high flux test cell. The beam footprint of the uniform beam profile is 5 cm x 20 cm.

Neutron flux

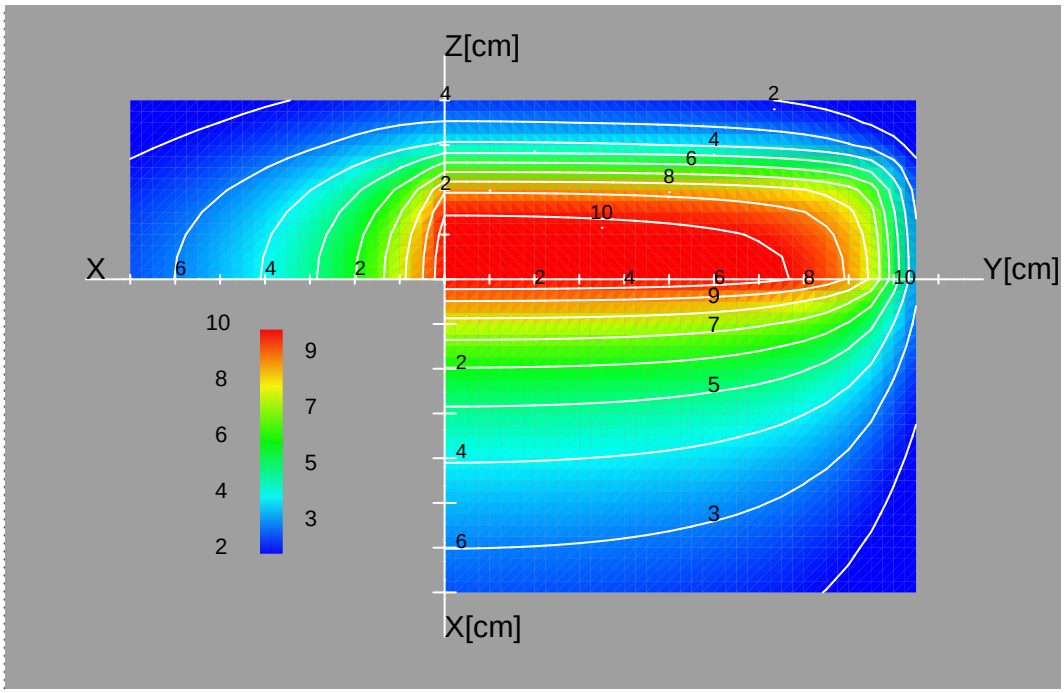

Figure 5-7 Total neutron flux contours. The unit is 10^{14} n/s/cm^2. The plot shows a relatively homogeneous distribution on the backplate surface. (INS, [Man 91] data, uniform beam profile.)

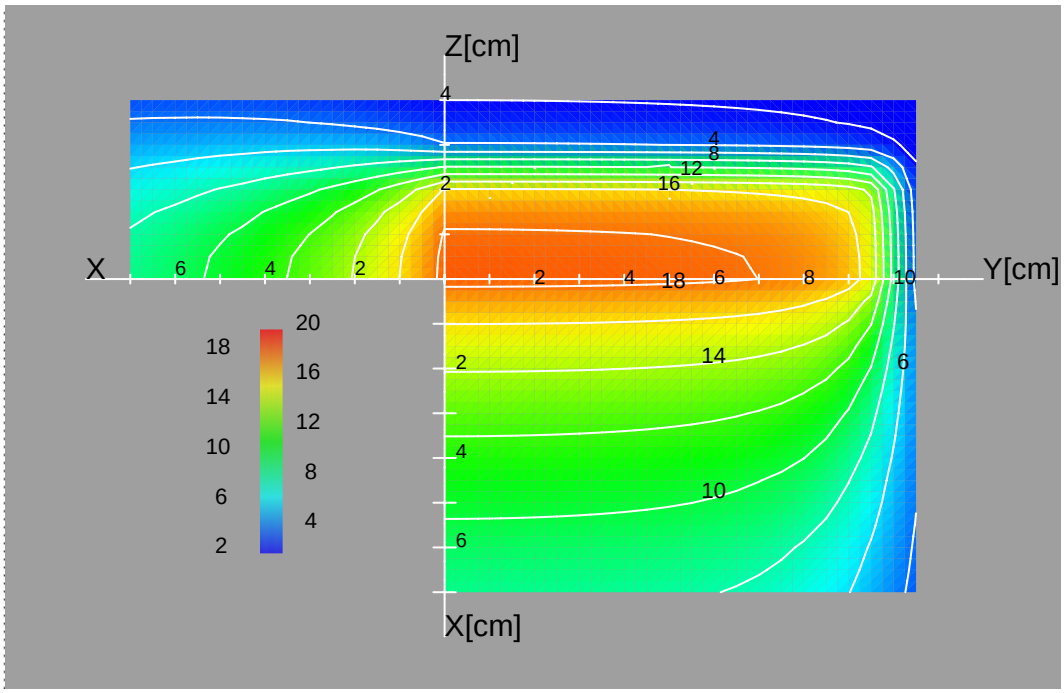

Figure 5-8 Neutron flux contours for neutrons with energies higher than 14 MeV. The unit is 10^{13} n/s/cm^2. The plot shows a relatively homogeneous distribution on the backplate surface. The largest high energy flux appears close to the backplate. (INS, [Man 91] data, uniform beam profile.)

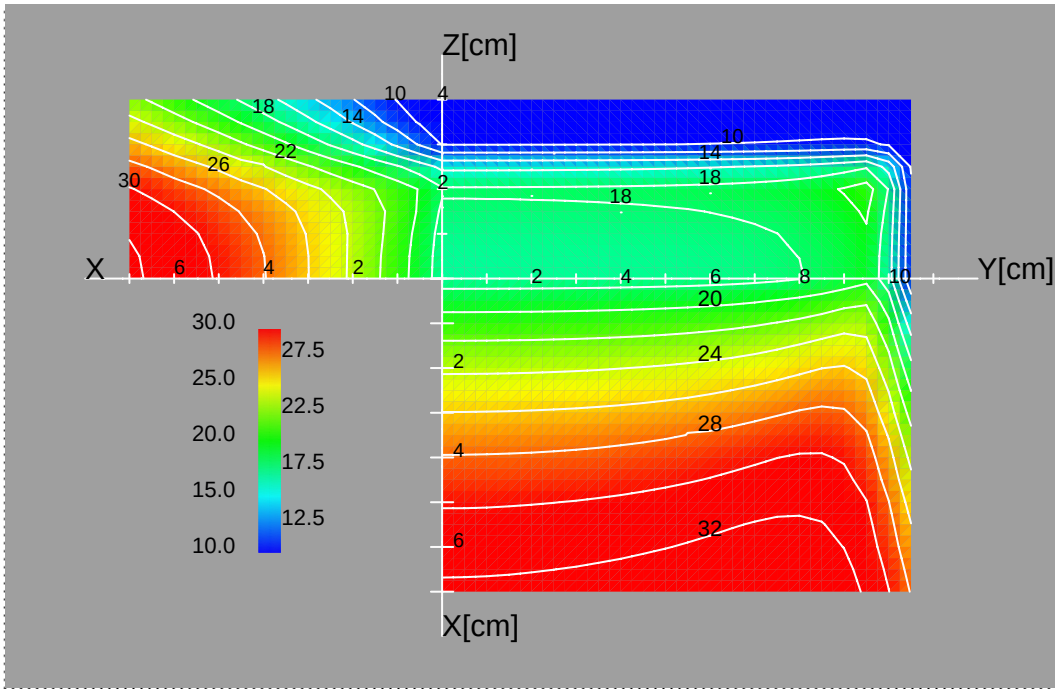

Figure 5-9 Fraction in % of the neutron flux with neutron energies higher than 14 MeV. The fraction increases for downstream locations. (INS, [Man 91] data, uniform beam profile.)

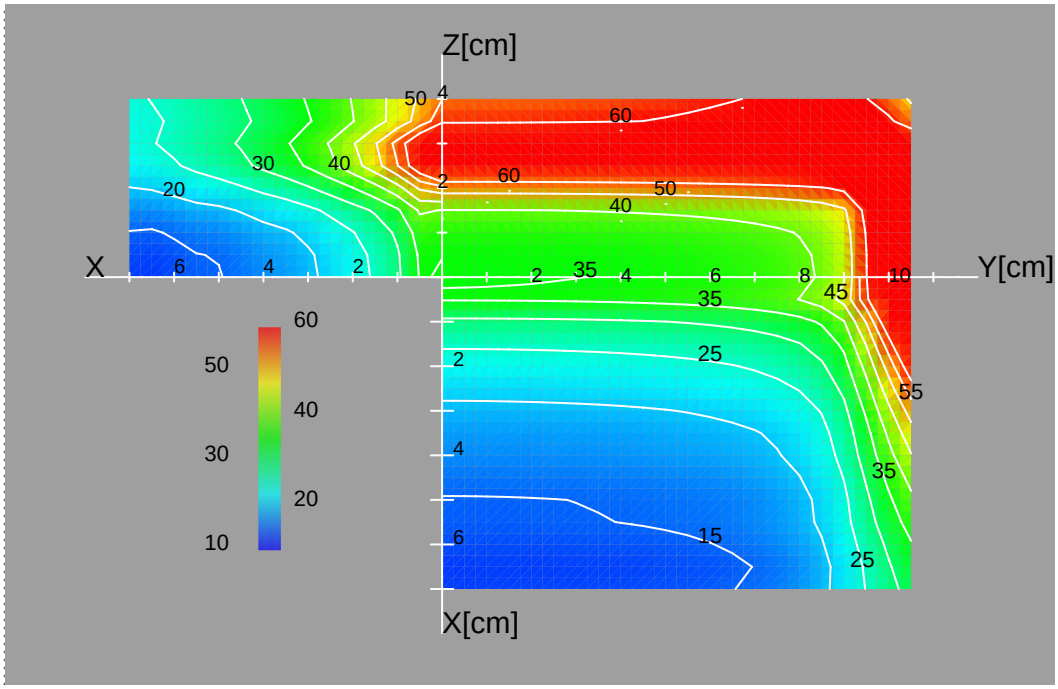

Figure 5-10 Neutron flux gradient contours. The unit is %/cm. (INS, [Man 91] data, uniform beam profile.)

Nuclear responses in Fe

Hydrogen production in Fe

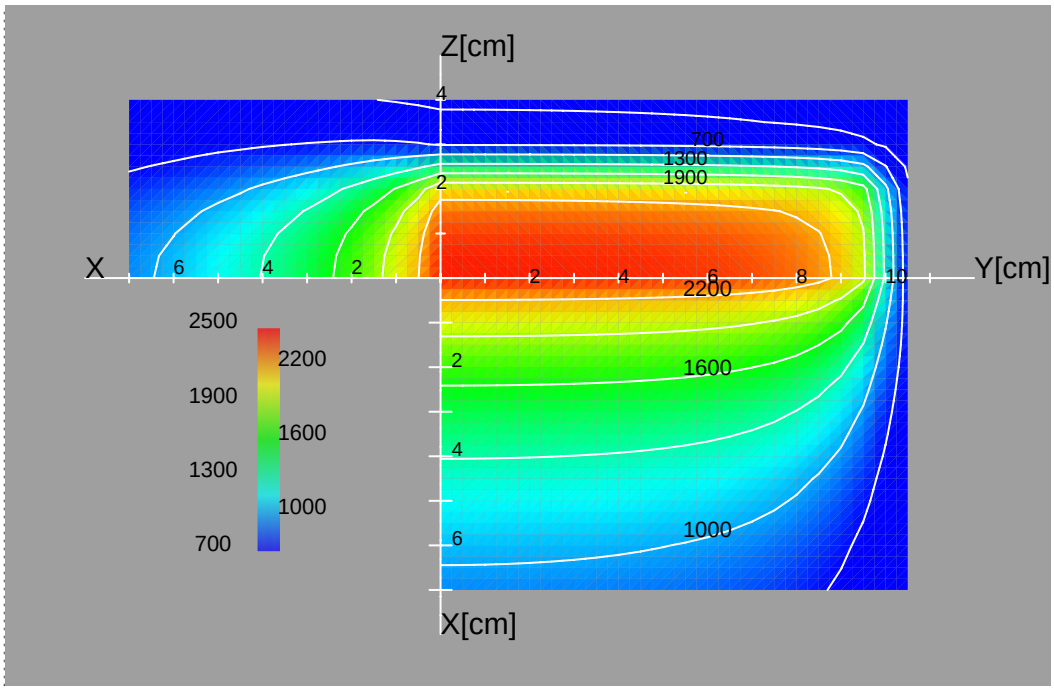

Figure 5-11 Hydrogen production contours in units of atomic parts per million (appm) per full power year (FPY). At the backplate the maximum of > 2200 appm H/FPY appears. (INS, [Man 91] data, uniform beam profile.)

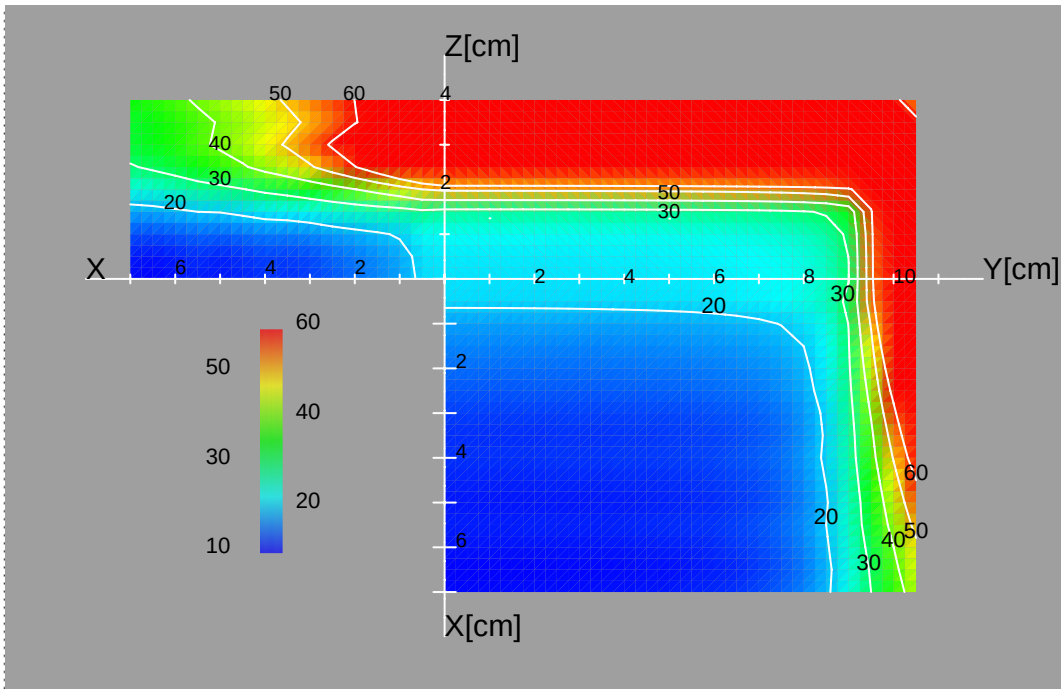

Figure 5-12 Hydrogen production gradients. The unit is %/cm. (INS, [Man 91] data, uniform beam profile.)

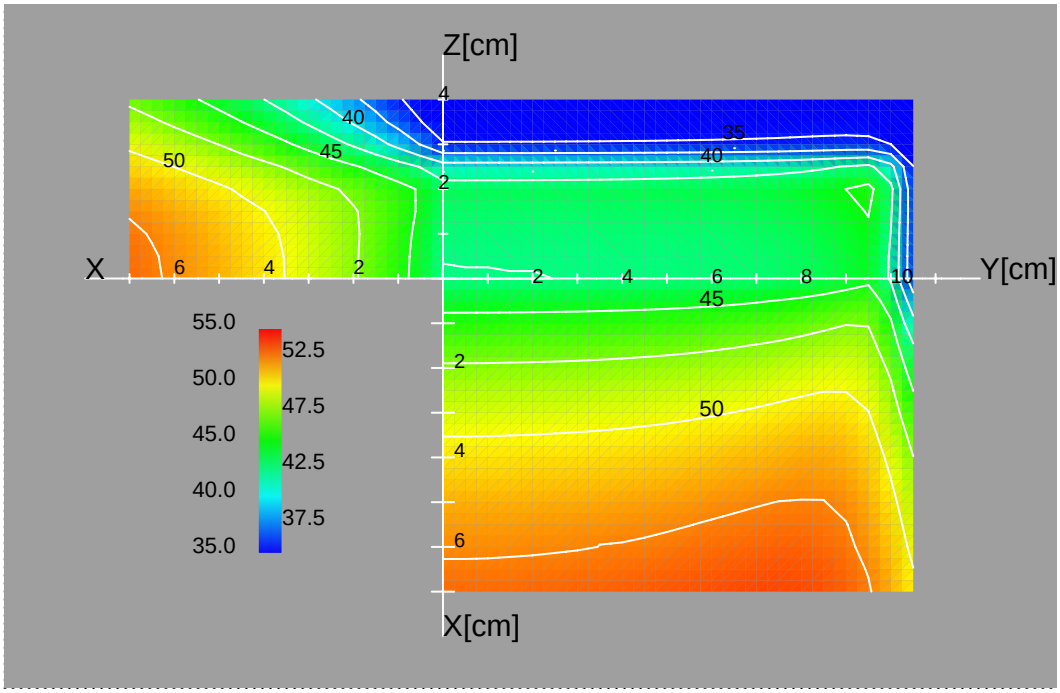

Figure 5-13 Hydrogen to DPA ratios in units of appm/DPA. (INS, [Man 91] data, uniform beam profile.)

Helium Production in Fe

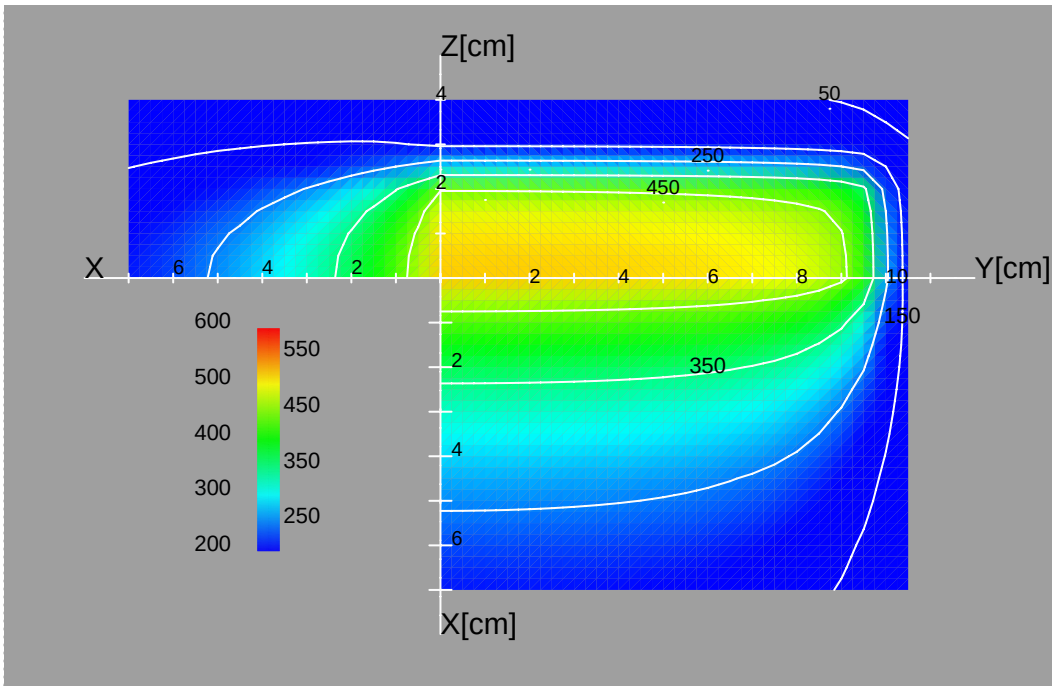

Figure 5-14 Helium production contours in units of atomic parts per million (appm) per full power year (FPY). At the backplate the maximum of > 450 appm He/FPY appears. (INS, [Man 91] data, uniform beam profile.)

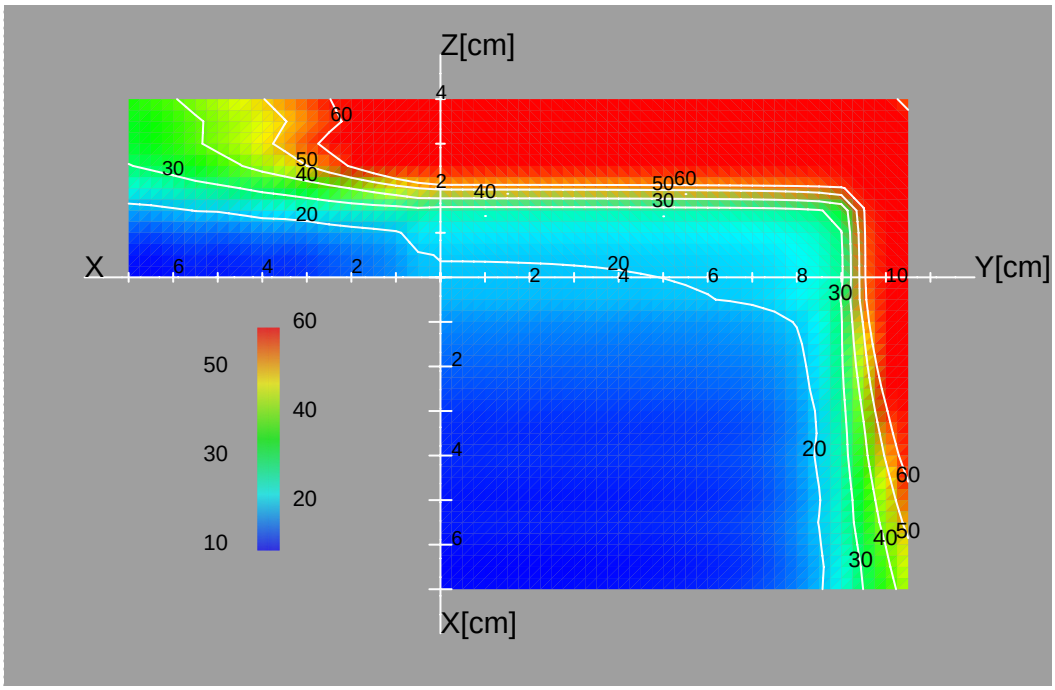

Figure 5-15 Helium production gradients. The unit is %/cm. (INS, [Man 91] data, uniform beam profile.)

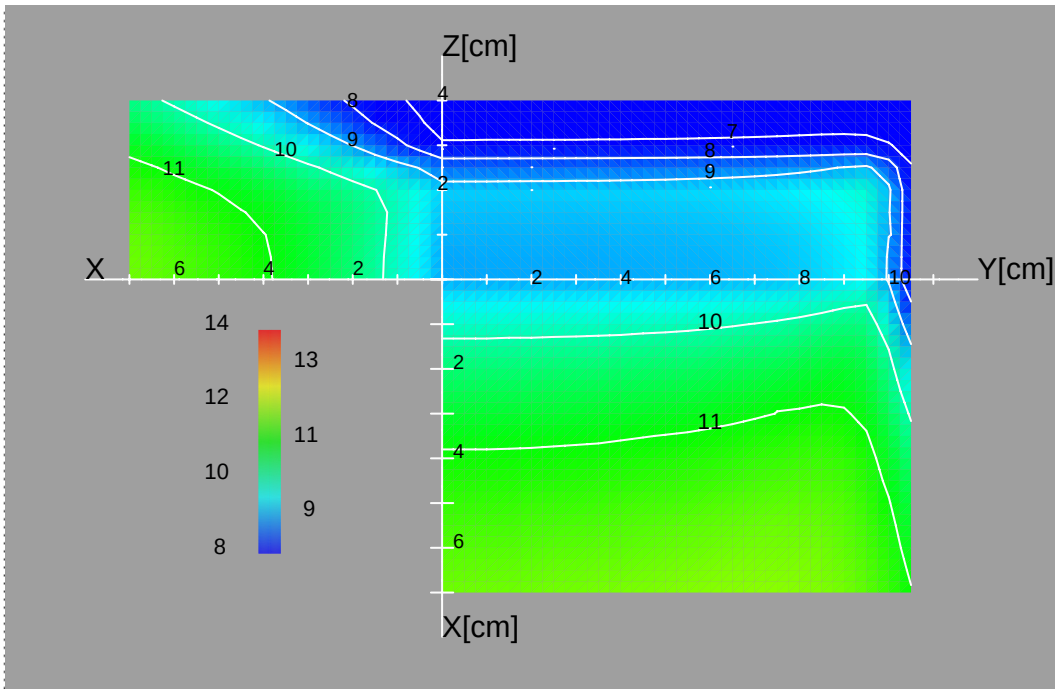

Figure 5-16 Helium to DPA ratio in units of appm/DPA. The He/DPA ratio increases for farther downstream locations. (INS, [Man 91] data, uniform beam profile.)

Displacement damage production in Fe

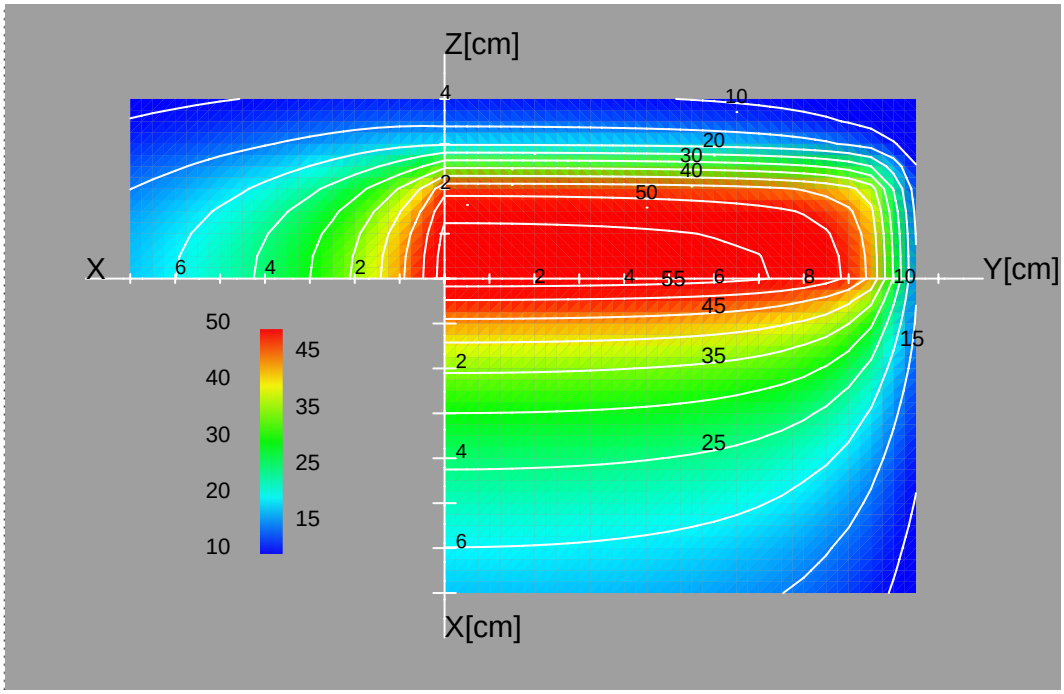

Figure 5-17 Displacement damage contours in units of DPA/FPY. (INS, [Man 91] data, uniform beam profile.)

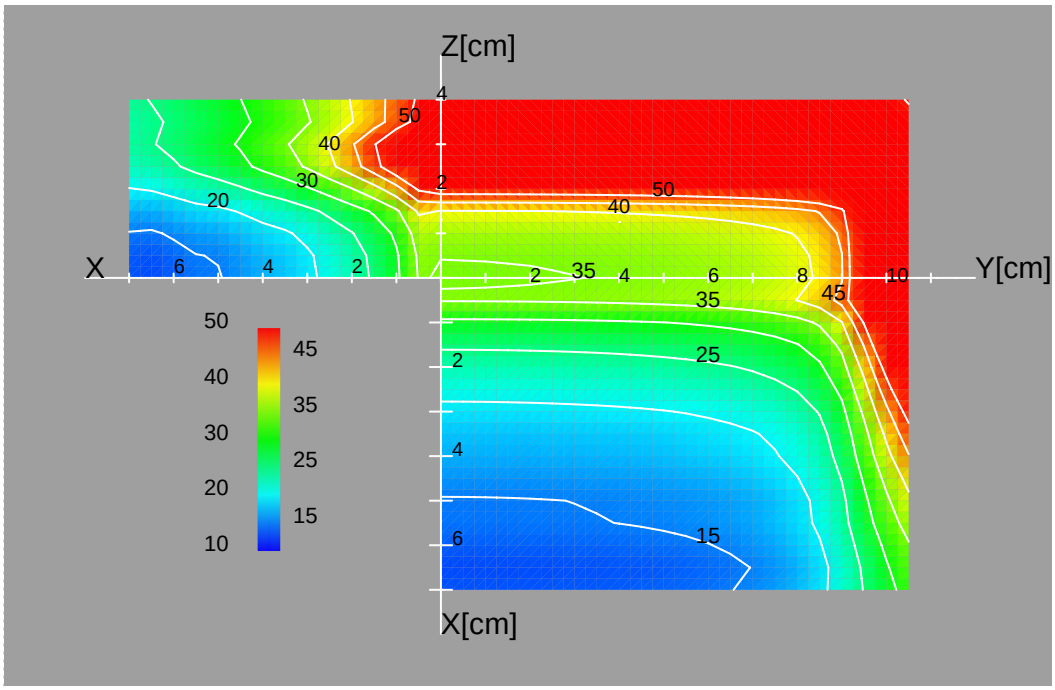

Figure 5-18 Displacement damage gradient contours. The unit is %/cm. (INS, [Man 91] data, uniform beam profile.)

Irradiation volumes

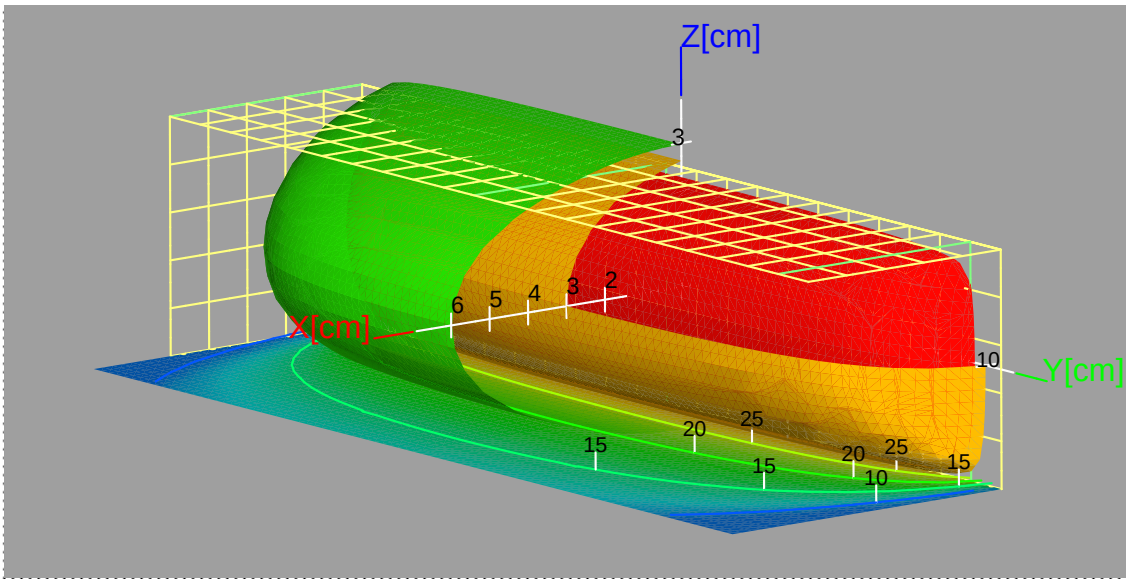

Figure 5-19 Displacement damage cut-out isosurfaces. Each isosurface characterises the available volume for a DPA/FPY limit. Green = 20 DPA/FPY, yellow = 30 DPA/FPY and red = 40 DPA/FPY. The grid structure shows the physical boundary of the helium cooled high flux test module. (INS, [Man 91] data, uniform beam profile.)

The following table shows the irradiation volumes which can achieved with the uniform beam profile and the [Man91] data.

Table 5-4 Irradiation volumes as a function of the minimum displacement damage. The third column shows the available volume inside the present design of the High Flux Test Module (HFTM).

Displacement Damage [DPA/FPY]	Total volume [cm^3]	Volume inside HFTM [cm^3]
20	466	419
30	193	192
40	75	75
50	17	17

Wall Load

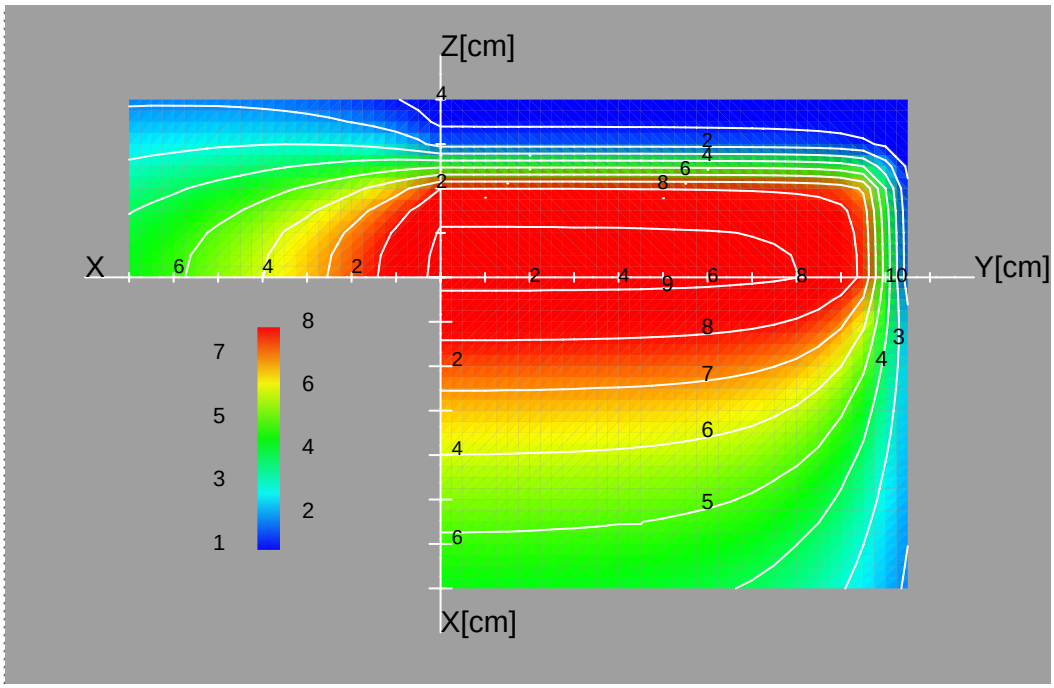

Figure 5-20 Wall load contours in units of MW/m^2. The plot shows a relatively homogeneous distribution on the backplate surface. (INS, [Man 91] data, uniform beam profile.)

5.3.2 Uncollided calculations with non-uniform beam profile

Neutron flux

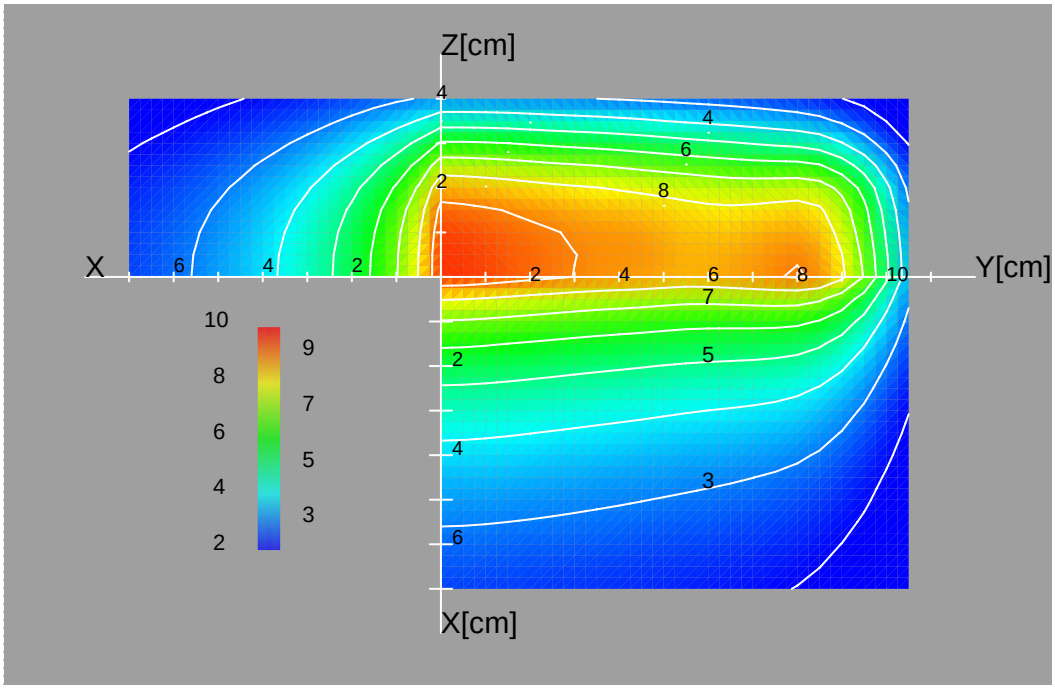

Figure 5-21 Total neutron flux contours. The unit is 10^{14} n/s/cm^2. The plot shows a peaked flux distribution on the backplate surface and also in the x-y-plane the peaked edges of the non-uniform beam profile can be recognised. (INS, [Man 91] data, non-uniform beam profile.)

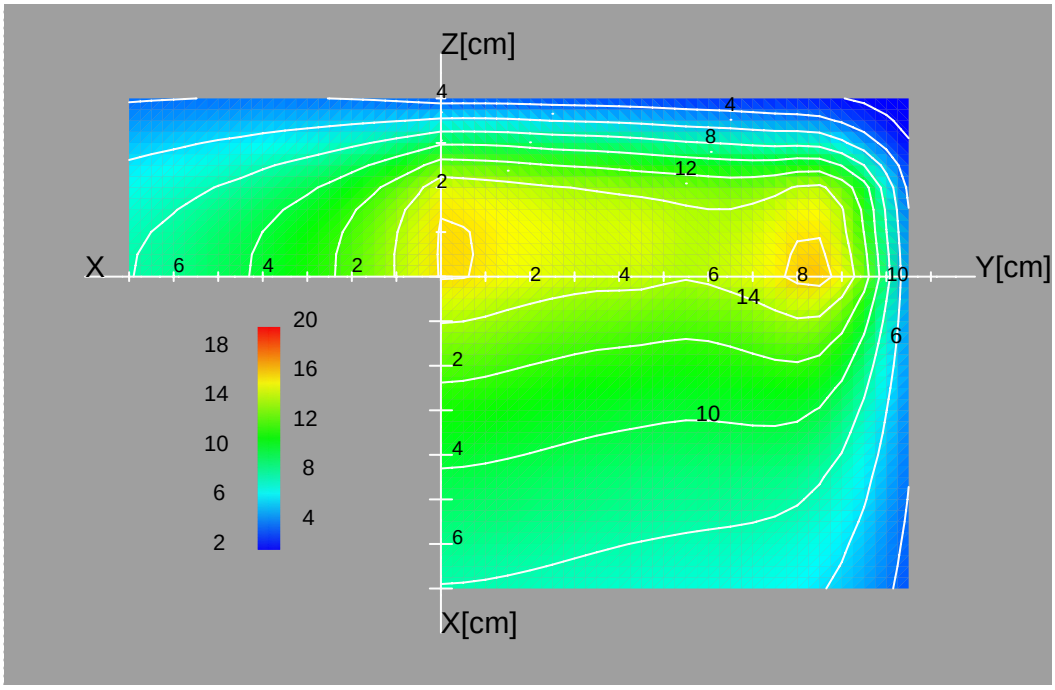

Figure 5-22 Neutron flux contours for neutrons with energies higher than 14 MeV. The unit is 10^{13} n/s/cm^2. (INS, [Man 91] data, non-uniform beam profile.)

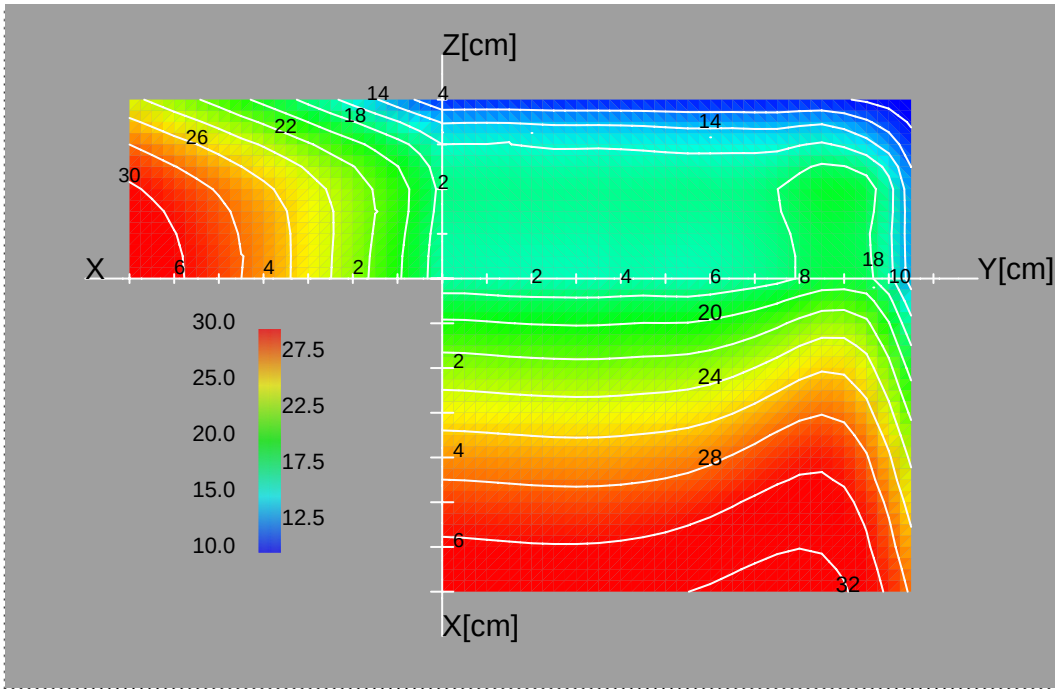

Figure 5-23 Fraction in % of the neutron flux with neutron energies higher than 14 MeV. The fraction increases for downstream locations. (INS, [Man 91] data, non-uniform beam profile.)

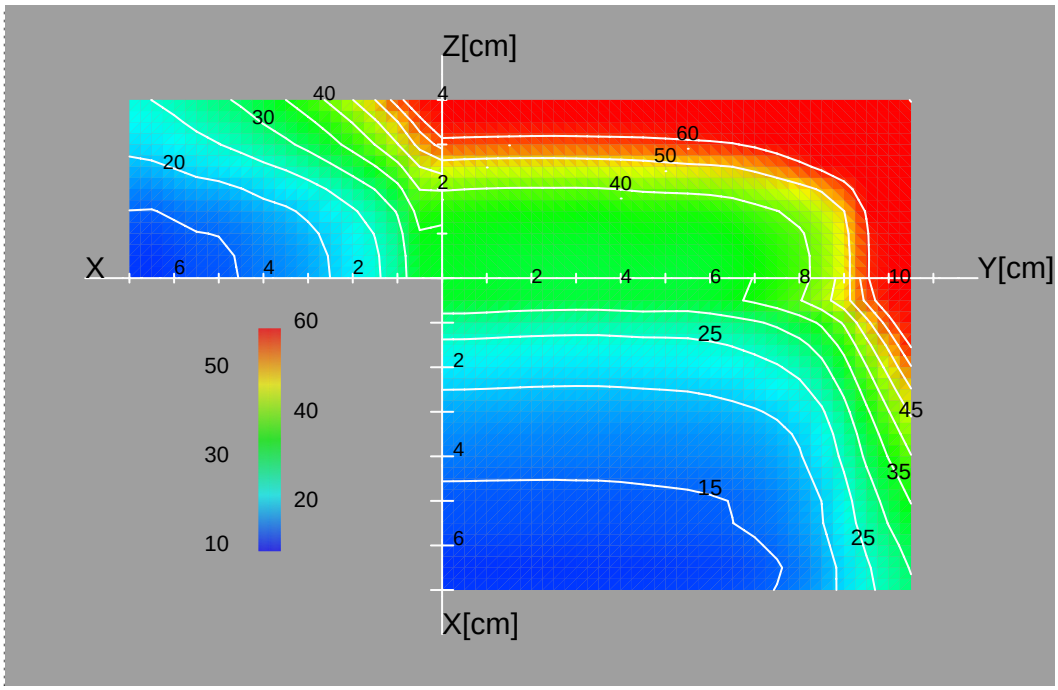

Figure 5-24 Neutron flux gradient contours. The unit is %/cm.(INS, [Man 91] data, non-uniform beam profile.)

Nuclear responses in Fe

Hydrogen production in Fe

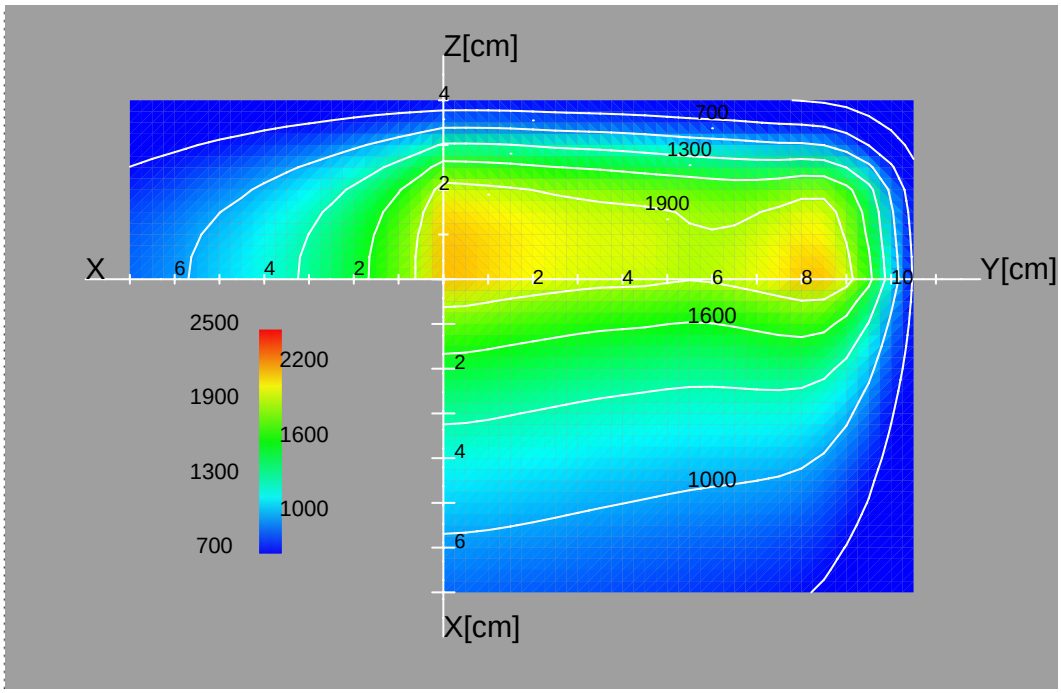

Figure 5-25 Hydrogen production contours in units of atomic parts per million (appm) per full power year (FPY). (INS, [Man 91] data, non-uniform beam profile.)

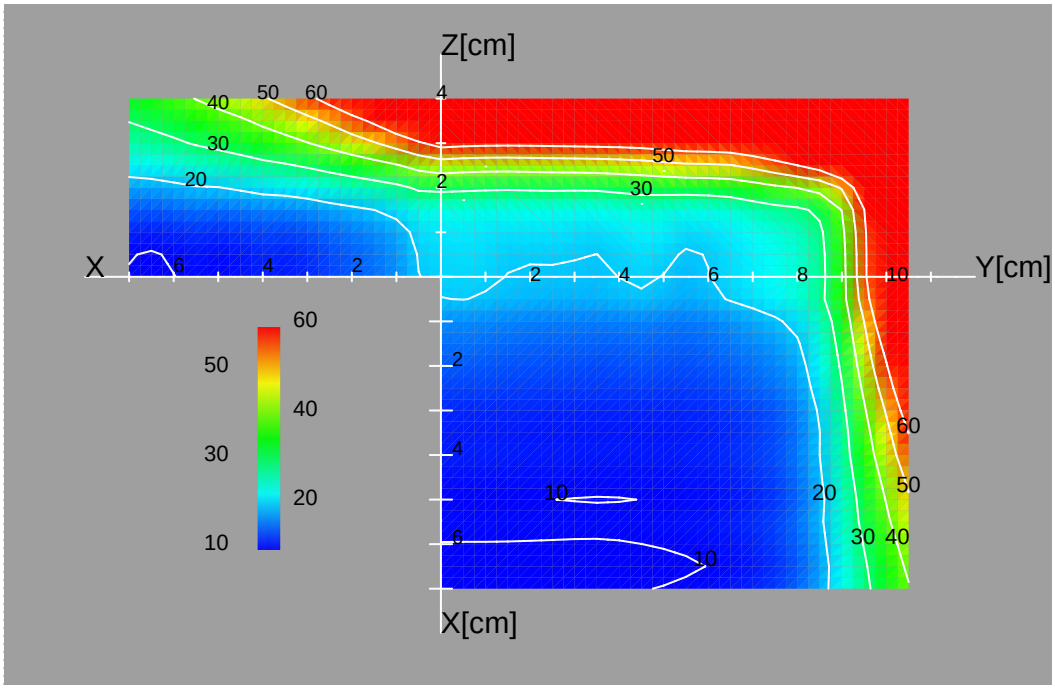

Figure 5-26 Hydrogen production gradients. The unit is %/cm. (INS, [Man 91] data, non-uniform beam profile.)

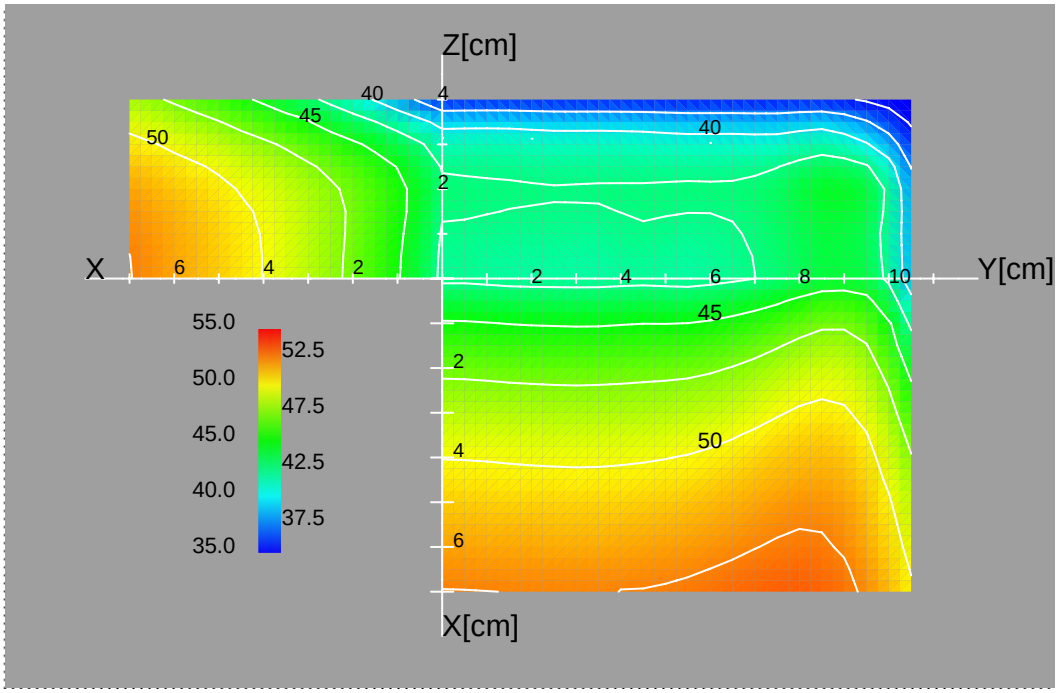

Figure 5-27 Hydrogen to DPA ratios in units of appm/DPA. (INS, [Man 91] data, non-uniform beam profile.)

Helium Production in Fe

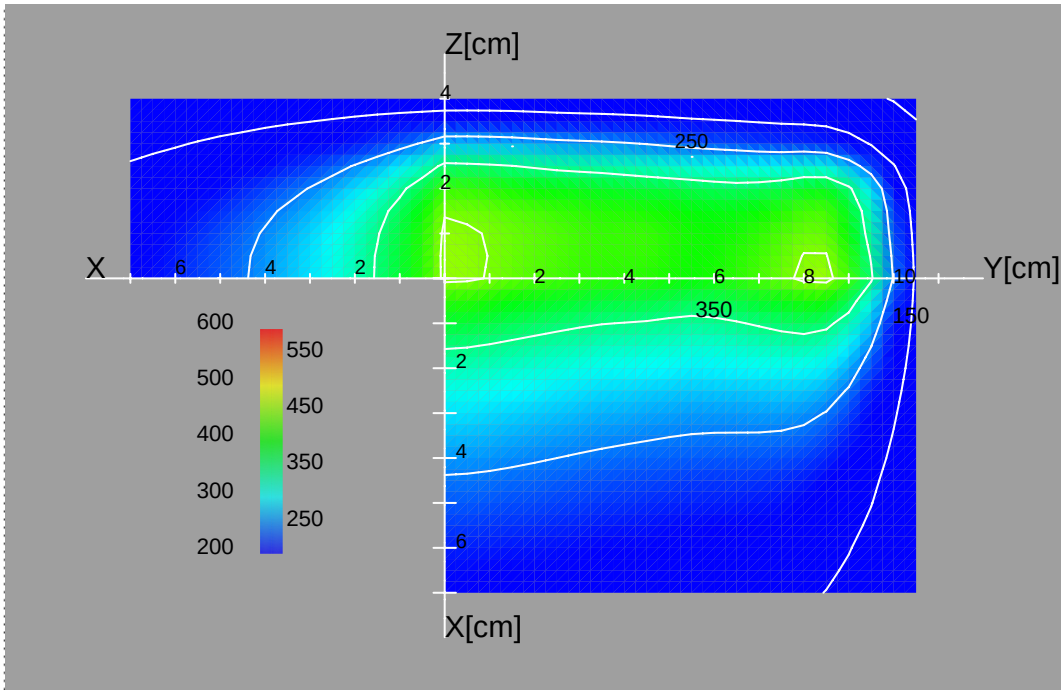

Figure 5-28 Helium production contours in units of atomic parts per million (appm) per full power year (FPY). (INS, [Man 91] data, non-uniform beam profile.)

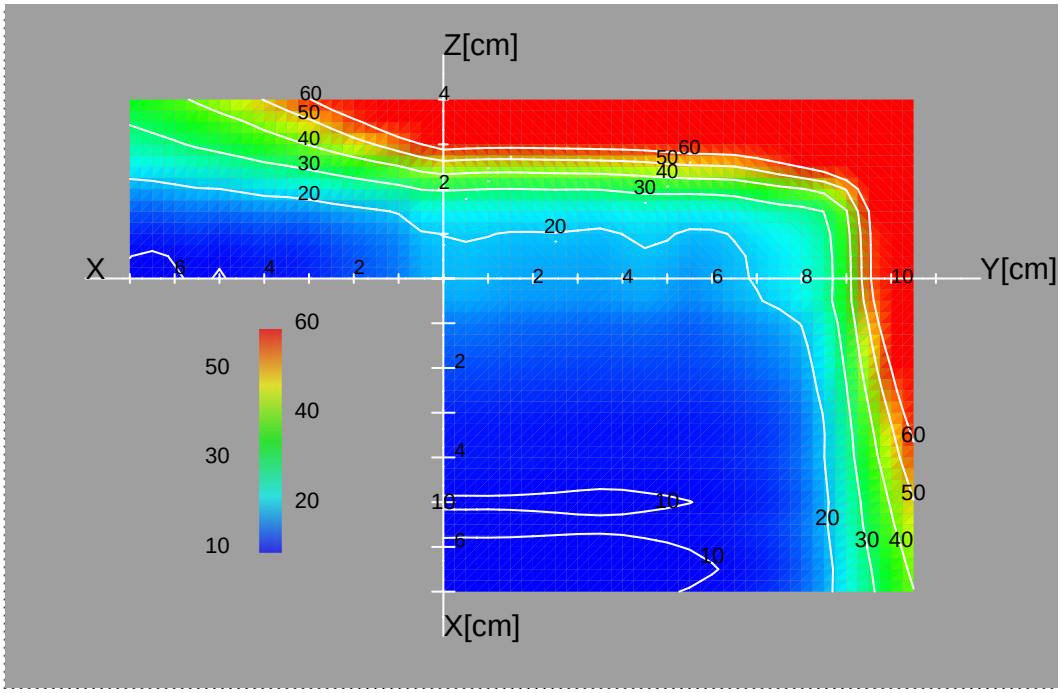

Figure 5-29 Helium production gradients. The unit is %/cm. (INS, [Man 91] data, non-uniform beam profile.)

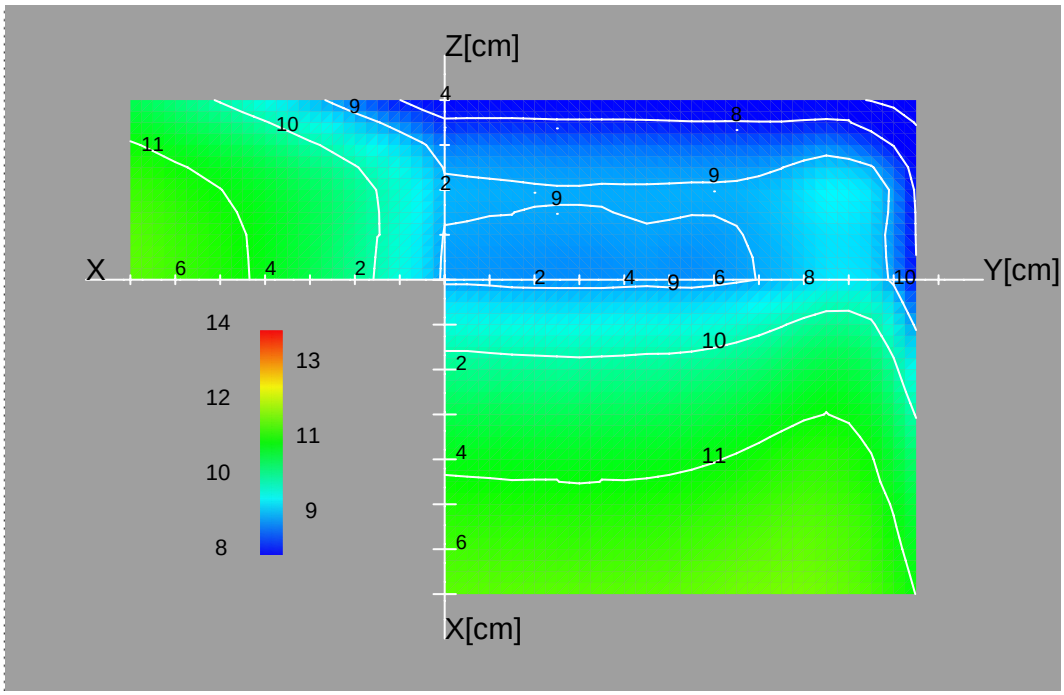

Figure 5-30 Helium to DPA ratio in units of appm/DPA. (INS, [Man 91] data, non-uniform beam profile.)

Displacement damage production in Fe

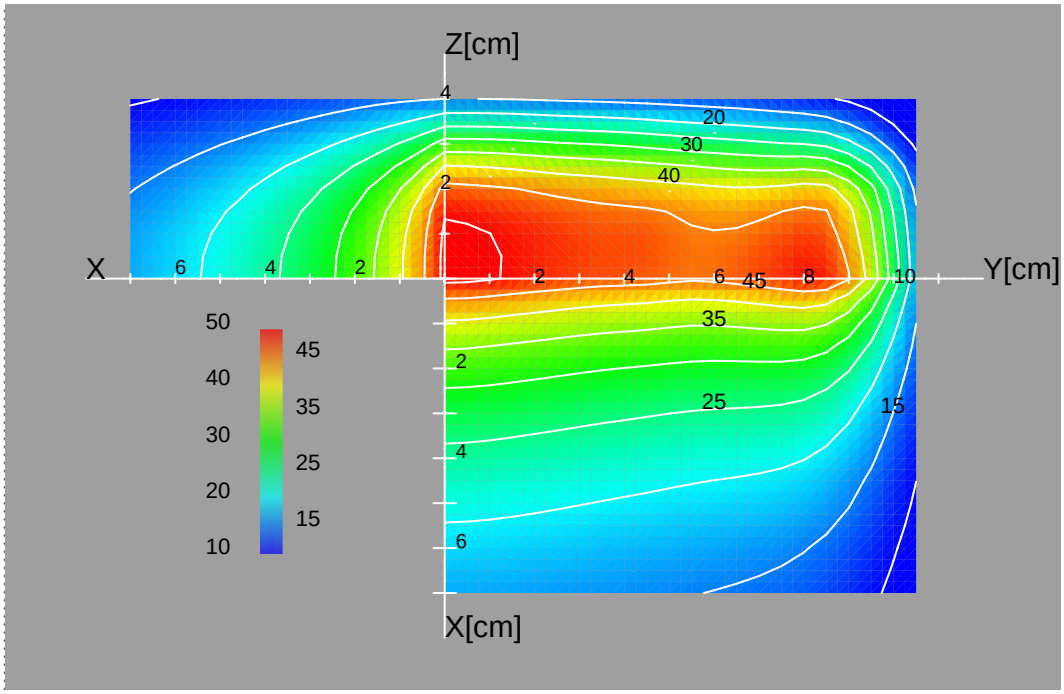

Figure 5-31 Displacement damage contours in units of DPA/FPY. (INS, [Man 91] data, non-uniform beam profile.)

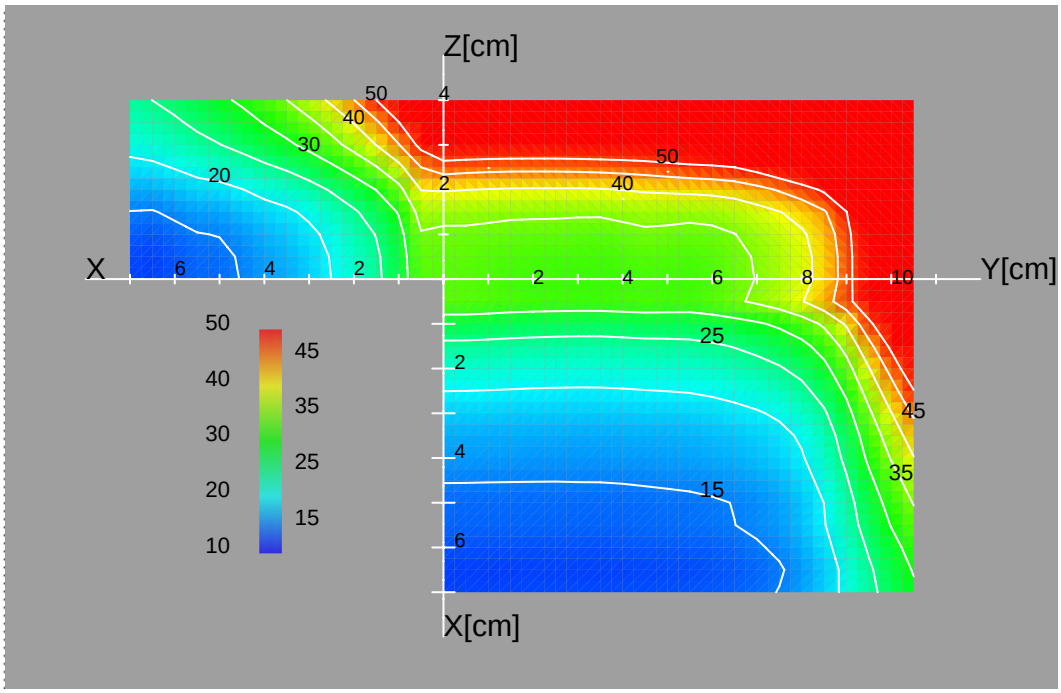

Figure 5-32 Displacement damage gradient contours. The unit is %/cm. (INS, [Man 91] data, non-uniform beam profile.)

Irradiation volumes

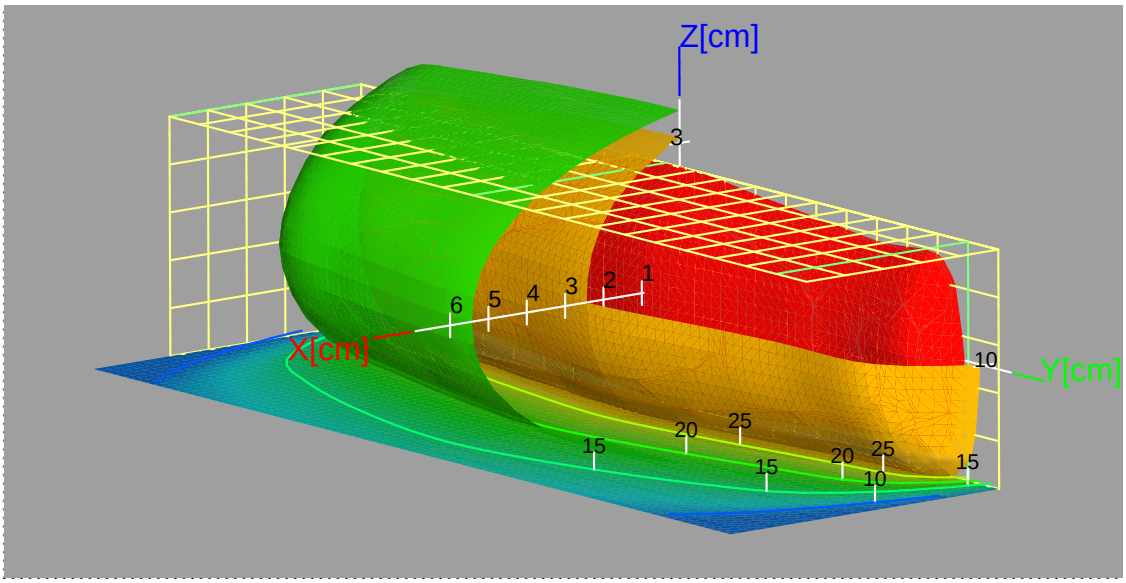

Figure 5-33 Displacement damage cut-out isosurfaces. Each isosurface characterises the available volume for a DPA/FPY limit. Green = 20 DPA/FPY, yellow = 30 DPA/FPY and red = 40 DPA/FPY. The grid structure shows the physical boundary of the helium cooled high flux test module. (INS, [Man 91] data, non-uniform beam profile.)

The following table shows the irradiation volumes which can be achieved with the non-uniform beam profile and the [Man91] data.

Table 5-5 Irradiation volumes as a function of the minimum displacement damage. The third column shows the available volume inside the present design of the High Flux Test Module (HFTM).

Displacement Damage [DPA/FPY]	Total volume [cm^3]	Volume inside HFTM [cm^3]
20	451	389
30	155	149
40	38	38
50	0	0

Wall Load

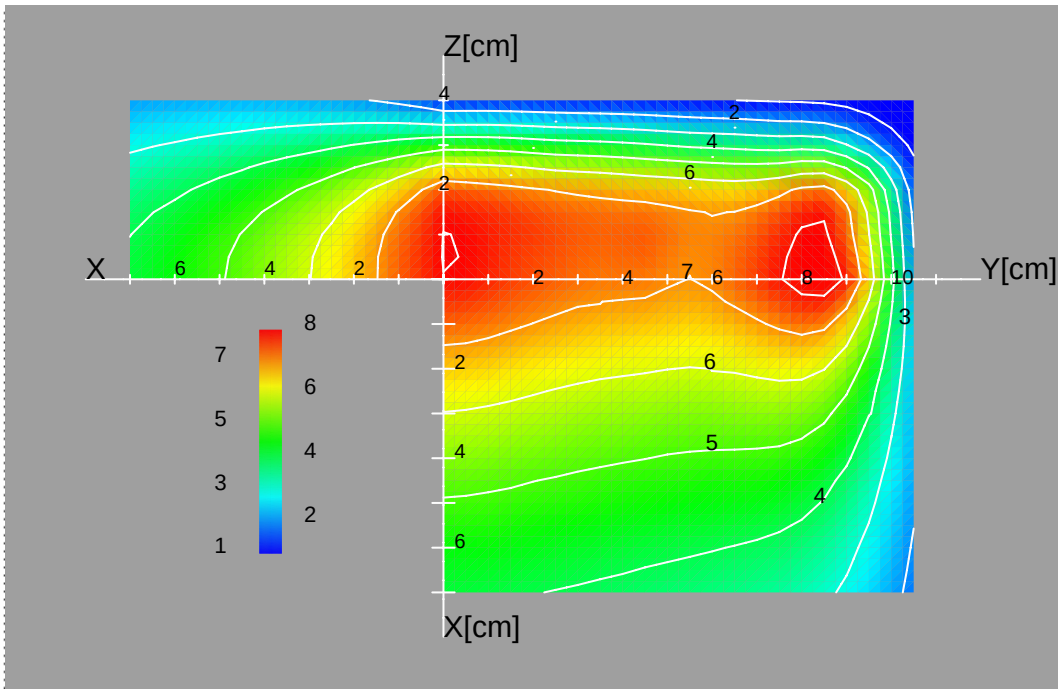

Figure 5-34 Wall load contours in units of MW/m^2. (INS, [Man 91] data, uniform beam profile.)

5.3.3 Comparison of the INS results between uniform and non-uniform beam profiles

Neutron Spectra Comparison

In the comparison of the total neutron flux spectra (see figure 5-36) 8 locations in the High Flux Test Module have been chosen. This can be seen in figure 5-35.

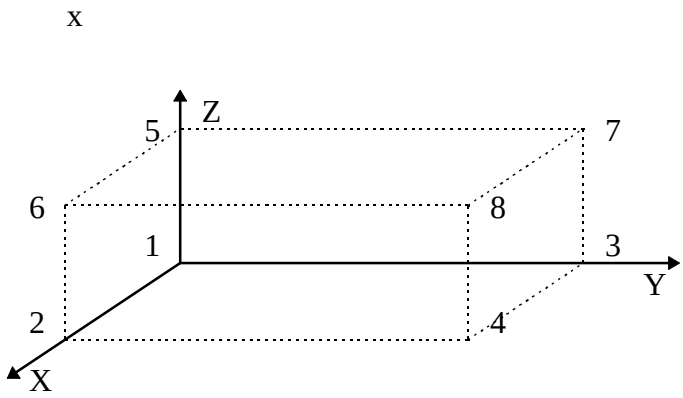

Figure 5-35 Locations of the total neutron flux spectra inside the High Flux Test Module. The positions are numbered from 1 to 8.

The neutron spectra plotted in figure 5-35 characterise the neutron flux density at the co-ordinate point in the high flux test module. The spectrum energy groups are each 1 MeV wide from 1 to 50 MeV.

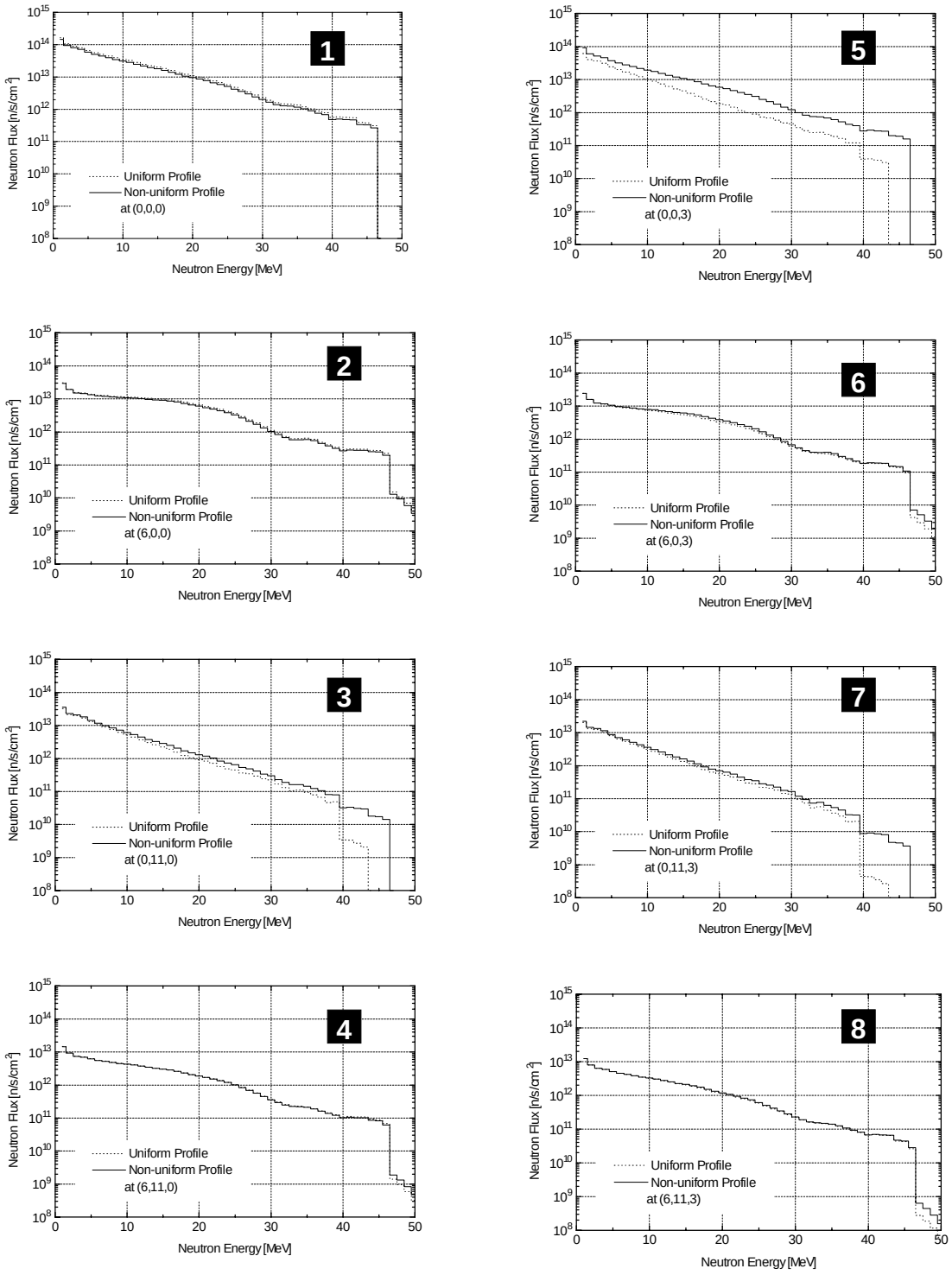

Figure 5-36 Comparison of the neutron flux spectra. The spectra are located near the boundaries of the High Flux Test Module. (INS, [Man 91] data, uniform and non-uniform beam profile.)

The differences in the neutron spectra are due to the different footprint size of the uniform (5 cm x 20 cm) and non-uniform (7 cm x 22 cm) beam profile and the different deuteron current density distribution over the footprint area. Spectrum (1) and (2) show that in forward direction (x-direction) the uniform beam profile gives a higher contribution than the non-uniform beam profile. This is mainly caused by the higher average beam density of the uniform case in the centre position of the beam footprint. On the other hand, at large y-positions and z-positions

close to the backplate, the non-uniform case gives higher contribution as plotted in spectra (3),(5) and (7). This is mainly caused by the larger non-uniform beam footprint. A large difference appears at neutron energies above 40 MeV. At the positions (4), (6) and (8) there is almost no difference visible except at very high neutron energies.

Volume - DPA Comparison

The volume comparison as a function of the minimum DPA limit gives a feeling on how the volume changes if the more realistic non-uniform beam profile is introduced. An overview can be found in figure 5-37. The data plotted are from the tables 5-4 and 5-5.

The comparison shows that the total volume is almost equal in both cases. The volume inside the high flux test module (HFTM) shows in the non-uniform case a reduction of about 7%. For damage rates of 30 DPA/FPY and higher the total volume and the volume inside the HFTM are almost equal. The reduction for the non-uniform case is about 20% at 30 DPA/FPY, about 50 % at 40 DPA/FPY and 100 % at 50 DPA/FPY. This means that no volume is available in the non-uniform case for damage rates above 50 DPA/FPY.

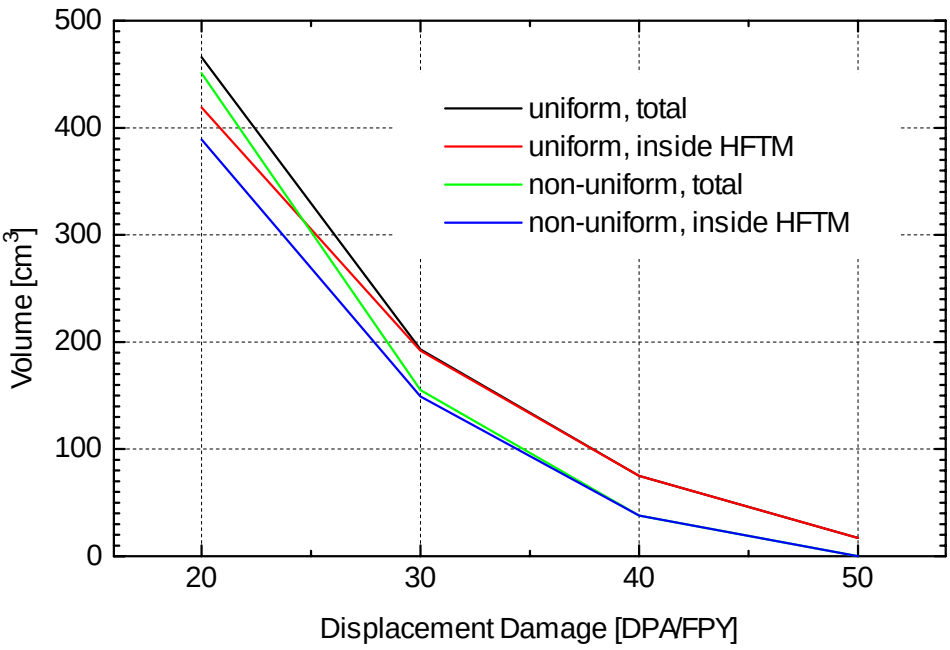

Figure 5-37 Volume - DPA comparison. The plot shows the differences between uniform and non-uniform beam profile and between total volume and the volume inside the high flux test module (HFTM).

Nuclear Response Comparison

In general the nuclear responses correspond closely with the total neutron fluxes. Since the fluxes are reduced in the centre position of the HFTM in the non-uniform case, the nuclear responses H-, He- and DPA-production are reduced, too. Also the gradients of the nuclear responses are reduced in the non-uniform case. The ratios H/DPA and He/DPA look more homogeneous in the non-uniform case, however, the peaked edges effect is clearly visible in the contour plots.

Wall Load Comparison

The wall load in general corresponds with the total neutron flux, especially the fraction of high energy neutrons. The peak wall load is decreased from > 9 MW/m^2 to about 8 MW/m^2 at the peaked edges of the non-uniform beam profile.

Summary

1. The non-uniform beam profile leads to reduced neutron fluxes at the centre position and to higher neutron fluxes at the border positions of the HFTM. The neutron flux gradient is smaller in the non-uniform case.
2. In general the volume for a given minimum DPA/FPY rate decreases in the non-uniform case. Particularly the very high flux volume for displacement damage rates above 50 DPA/FPY disappears.
3. In general the nuclear responses are reduced in the non-uniform case. However, the H/DPA and He/DPA ratios are more homogeneous.

5.4 Calculations with the MCNP Code

The MCNP calculations were carried out using the McDeLi source module described in chapter 4. Four different combinations or parameters were used: both a uniform and a non-uniform beam profile, and both an uncollided and a collided neutron transport calculation. The purpose of the uncollided calculations is as a benchmark for the method, data, and results, by comparing to those of the INS code used in section 5.2.

The MCNP geometry consisted of an 8.25 x 12 x 5.5 cm volume representing one quadrant of the high flux region and segmented into 0.5 x 0.5 x 0.5 cm cells. The final data were obtained on a regular cartesian system with the domain ([0.5,8.0],[0.0,11.5],[0.0,5.0]) by performing volume track-length tallies (T4) in each cell. A 2-dimensional slice was added at x=0.0 by performing surface tallies on the x=0.0 plane segmented into 0.5 x 0.5 cm areas. In the uncollided calculations, these cells were void, but cross-section data for iron were used to determine the engineering responses. In the collided calculations, the cells contained a mixture of ^{56}Fe and void corresponding to the expected average material density for the helium-cooled IFMIF high flux test assembly. It was important to select a total volume of material which would be sure to include the appropriate irradiation volume, but not affect the neutron distribution too much by increasing neutron reflection back into the test region.

Calculation of normalised engineering responses was performed by MCNP using the following tally conversions (see Appendix for details of calculation). These results are further normalised by the total neutron yield and the deuteron beam current [mA].

DPA:	FM14	1971.0	1	444
He:	FM24	0.1971	1	207
H:	FM34	0.1971	1	203
Wall Load:	FM1	40		
Heating:	FM6	1000		

The MCNP heating rate of W/cm^3 of total volume was further normalised to W/cm^3 of iron by multiplying by 2. The wall load tallies were performed with surface current tallies (T1) on the front and back surface of the test volume. Only those of the front surface (target backplate) are presented here.

The relative errors of the results were usually between 0.2% and 4% in all tallies except the surface tallies (of all varieties) at y > 10.5 cm (outside the beam footprint). This is reasonable

since those areas have relatively little neutron flux and are of less interest than the other regions. Furthermore, that data is not presented in this analysis.

Finally, the statistical nature of a Monte Carlo neutron transport calculation means that some of the plots may not exhibit smooth contours in all cases. This is particularly true as more mathematical operations are performed on the data (e.g. gradients and ratios).

5.4.1 Uncollided calculations with uniform beam profile

Neutron Flux

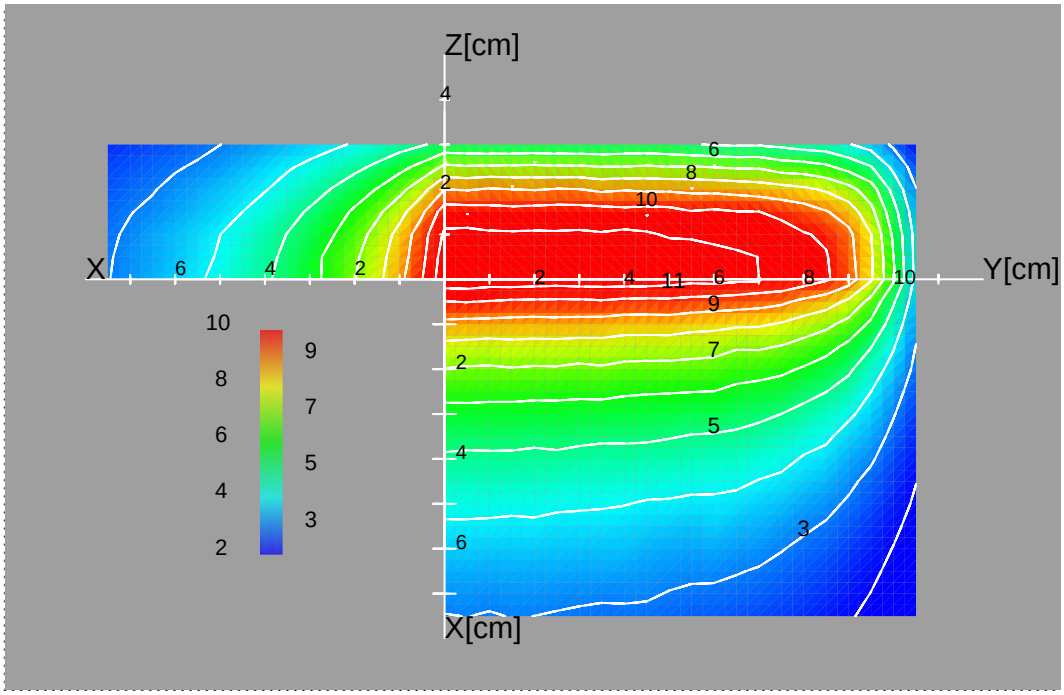

Figure 5-38 Total neutron flux contours. The unit is 10^{14} n/s/cm^2. The plot shows a very homogeneous distribution on the backplate surface. (MCNP uncollided, McDeLi data, uniform beam profile.)

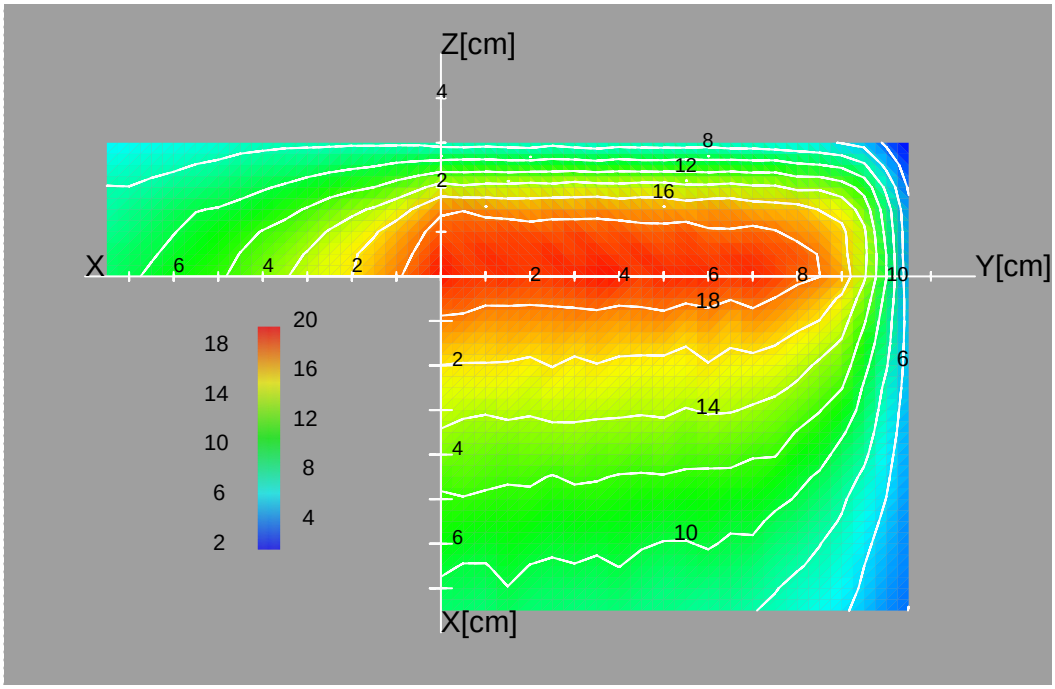

Figure 5-39 Neutron flux contours for neutrons with energies higher than 14.6 MeV. The unit is 10^{13} n/s/cm^2. The largest high energy flux appears close to the backplate. (MCNP uncollided, McDeLi data, uniform beam profile.)

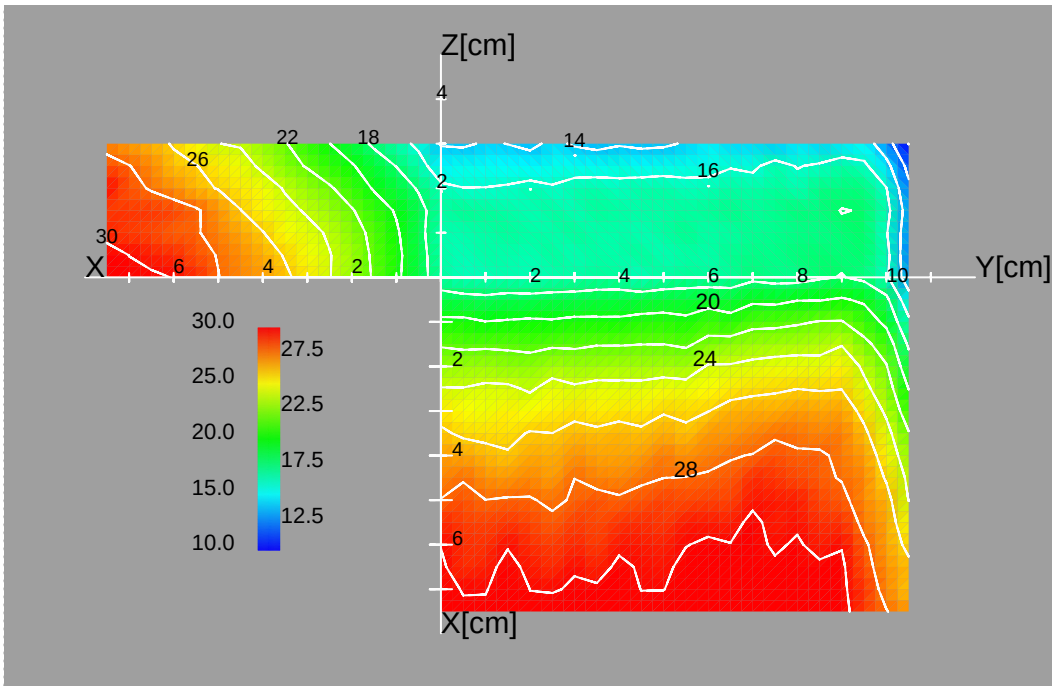

Figure 5-40 Fraction in % of the neutron flux with neutron energies higher than 14.6 MeV. The fraction increases for downstream locations. (MCNP uncollided, McDeLi data, uniform beam profile.)

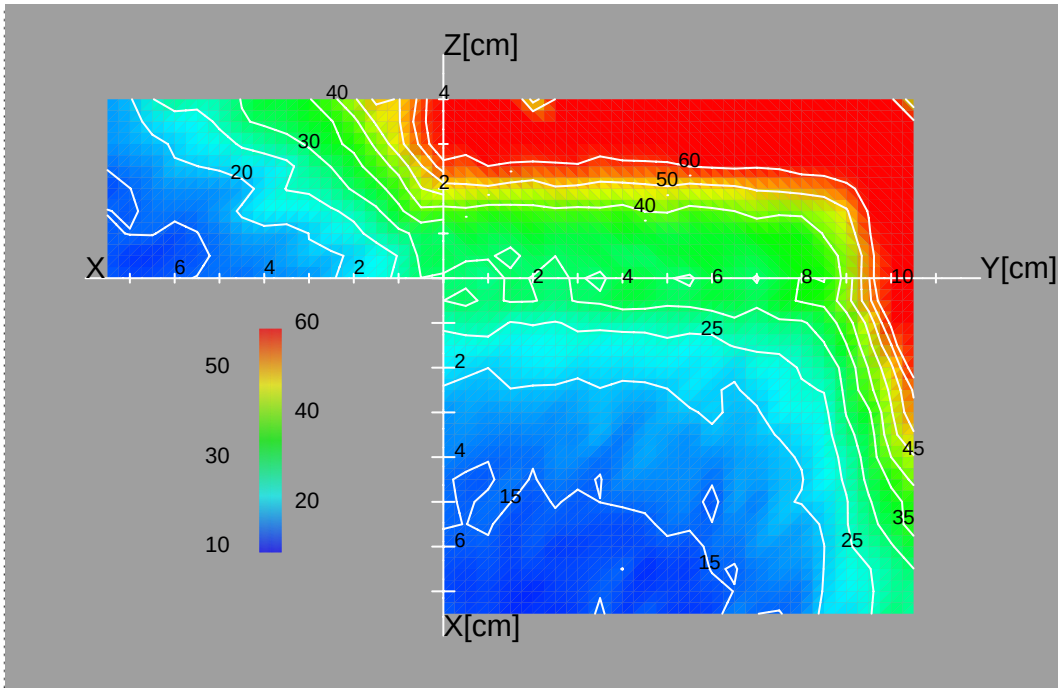

Figure 5-41 Neutron flux gradient contours. The unit is %/cm.(MCNP uncollided, McDeLi data, uniform beam profile.)

Nuclear responses in Fe

Hydrogen production

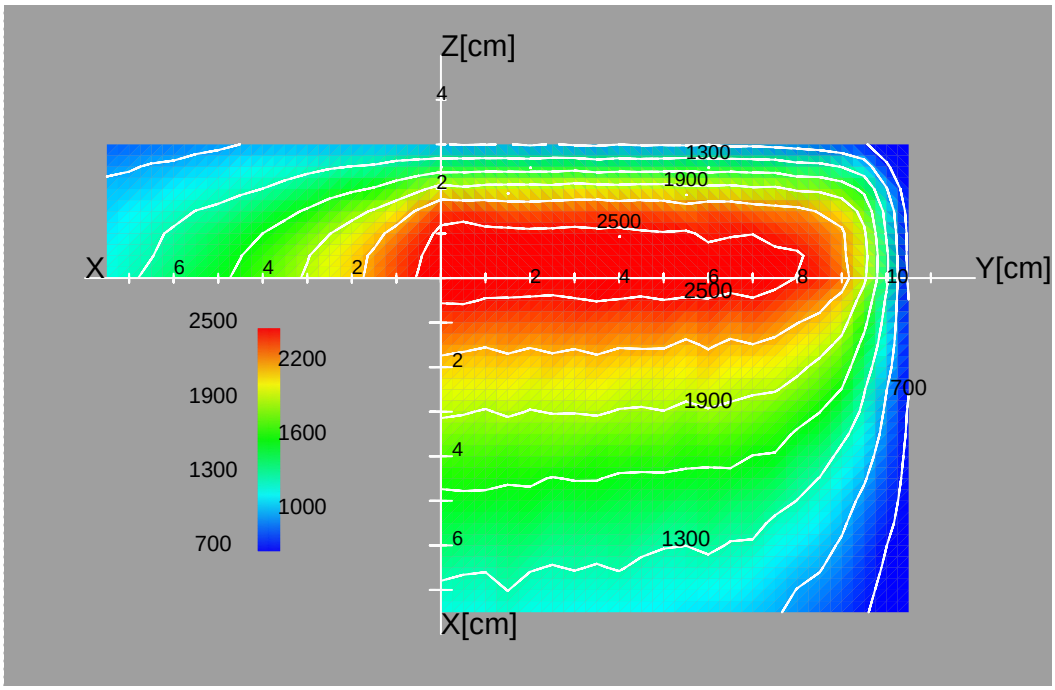

Figure 5-42 Hydrogen production contours in units of atomic parts per million (appm) per full power year (FPY). At the backplate the maximum of > 2500 appm H/FPY appears. (MCNP uncollided, McDeLi data, uniform beam profile.)

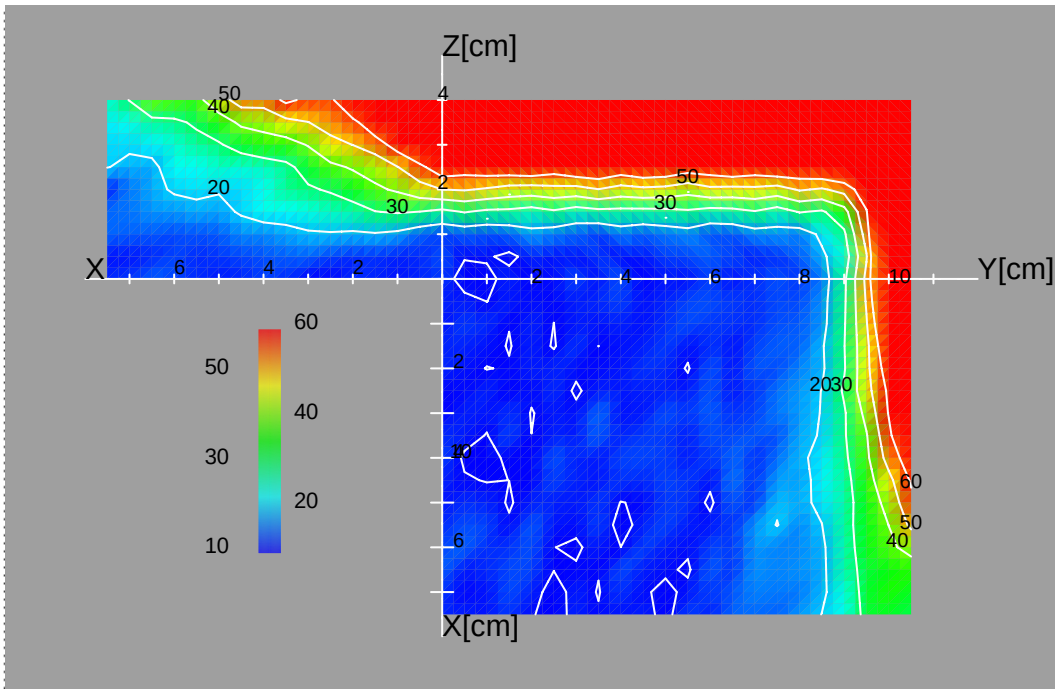

Figure 5-43 Hydrogen production gradients. The unit is % per appm/FPY/cm normalised to the total appm/FPY value. (MCNP uncollided, McDeLi data, uniform beam profile.)

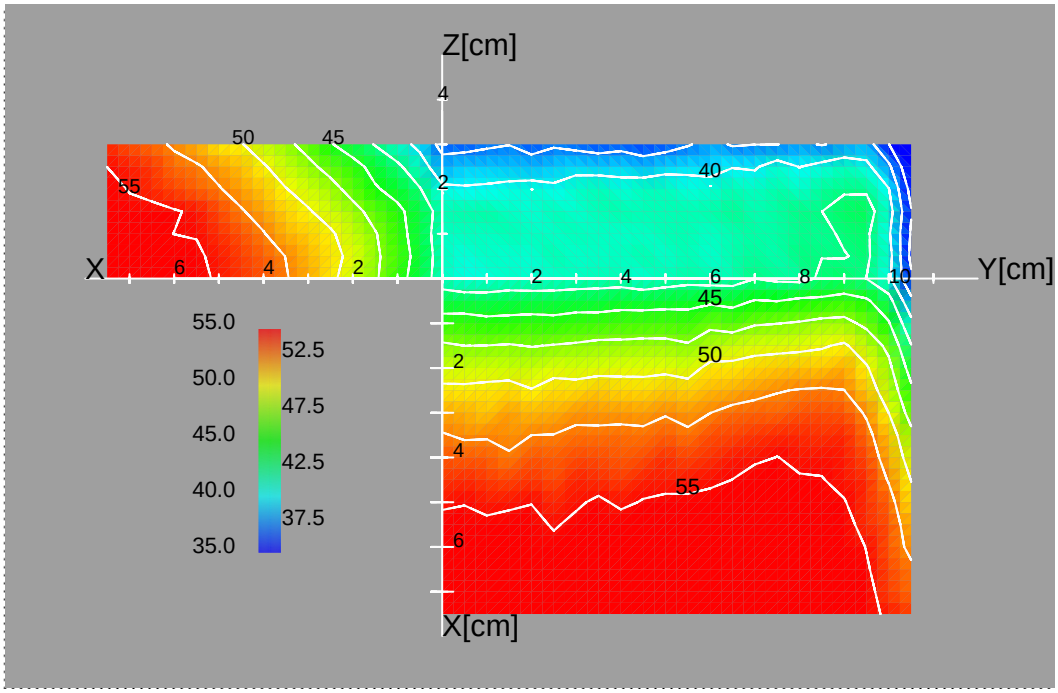

Figure 5-44 Hydrogen to DPA ratios in units of appm/DPA. (MCNP uncollided, McDeLi data, uniform beam profile.)

Helium production

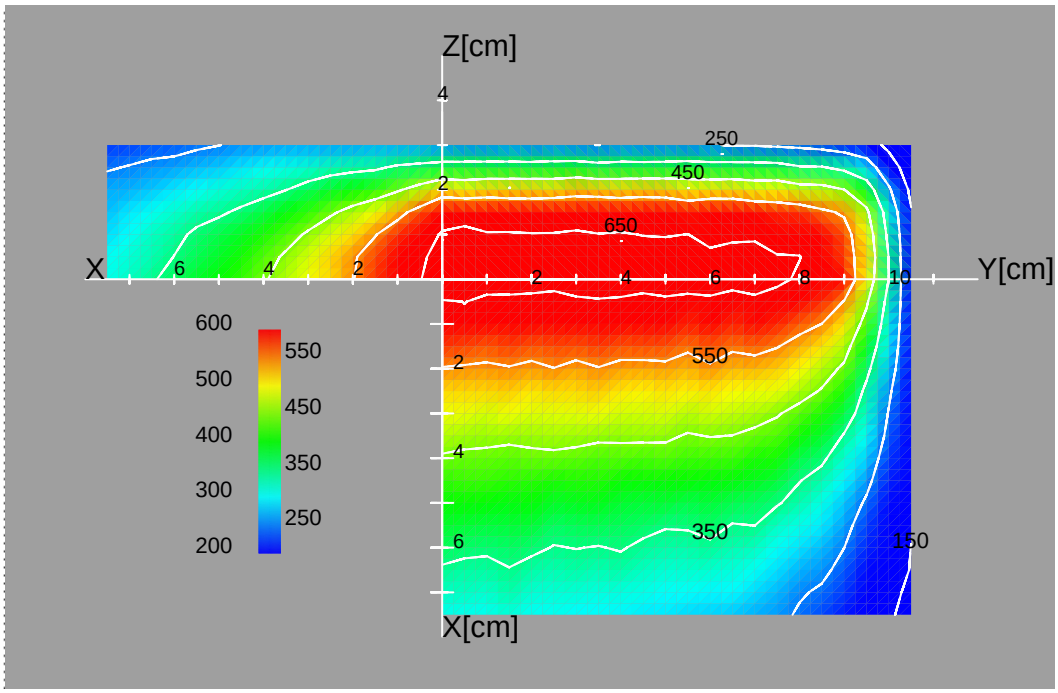

Figure 5-45 Helium production contours in units of atomic parts per million (appm) per full power year (FPY). At the backplate the maximum of > 650 appm He/FPY appears. (MCNP uncollided, McDeLi data, uniform beam profile.)

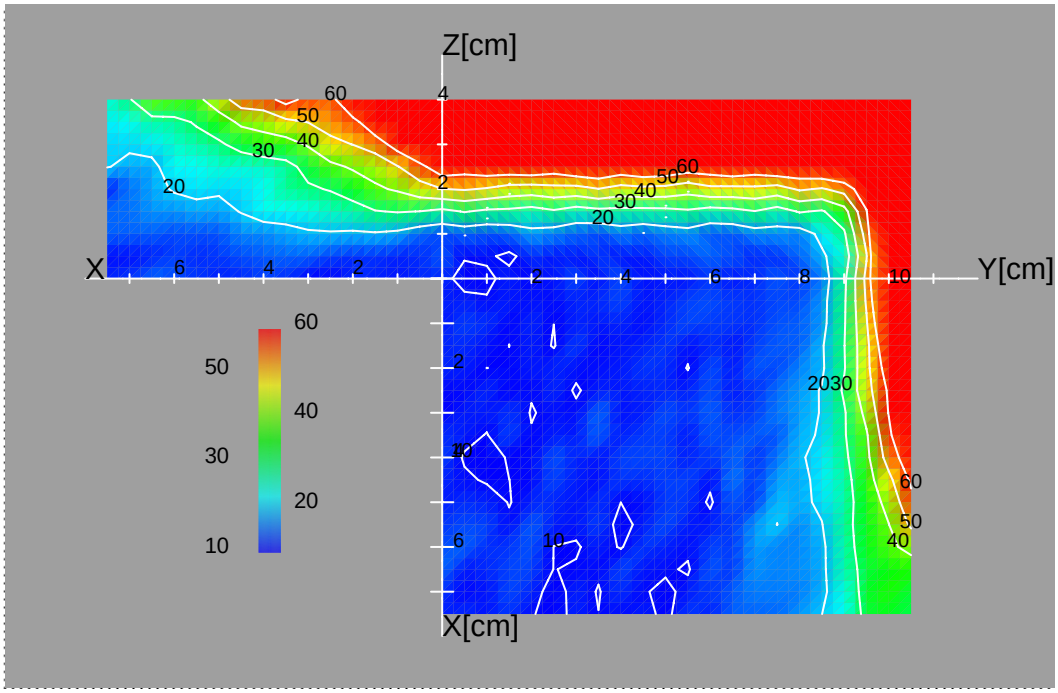

Figure 5-46 Helium production gradients. The unit is % per appm/FPY/cm normalised to the total appm/FPY value. (MCNP uncollided, McDeLi data, uniform beam profile.)

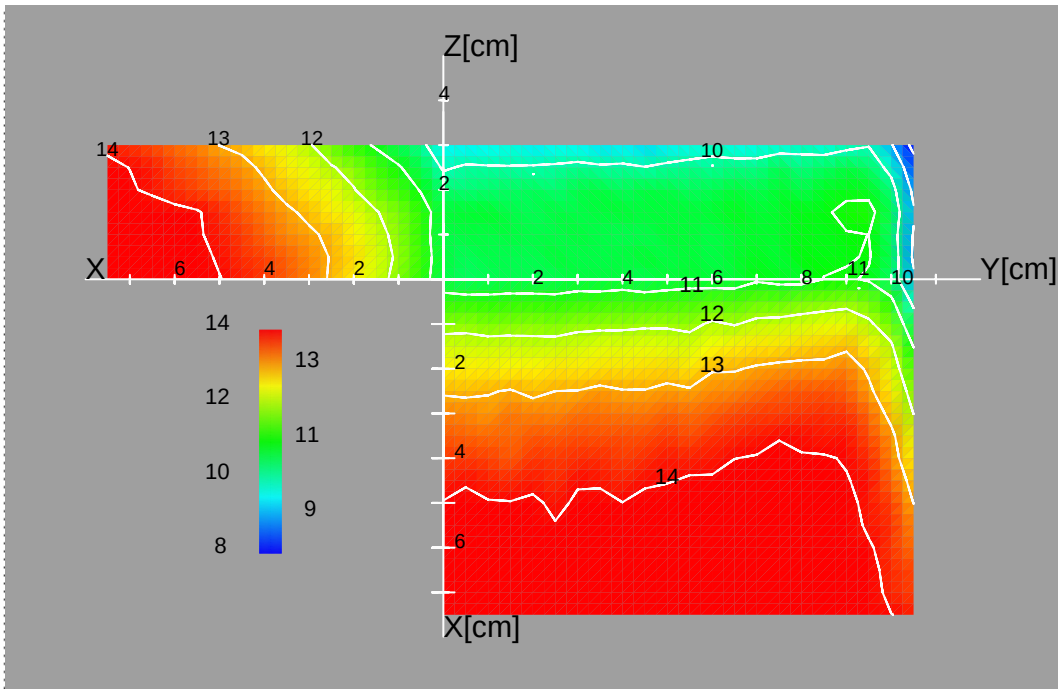

Figure 5-47 Helium to DPA ratio in units of appm/DPA. The He/DPA ratio increases for farther downstream locations. (MCNP uncollided, McDeLi data, uniform beam profile.)

DPA production

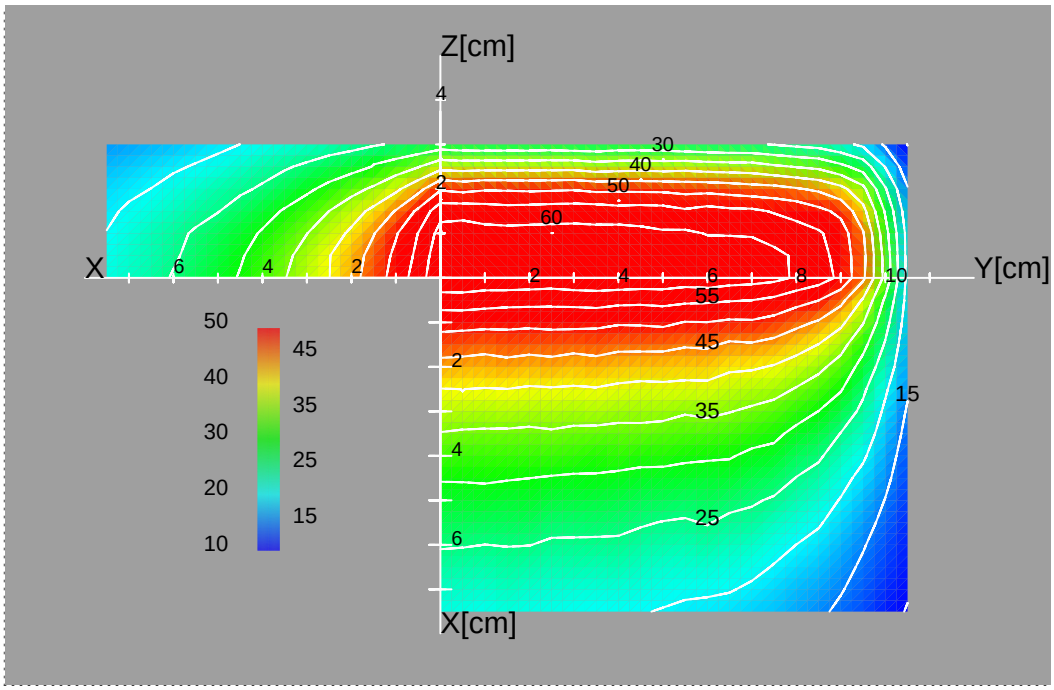

Figure 5-48 Displacement damage contours in units of DPA/FPY. (MCNP uncollided, McDeLi data, uniform beam profile.)

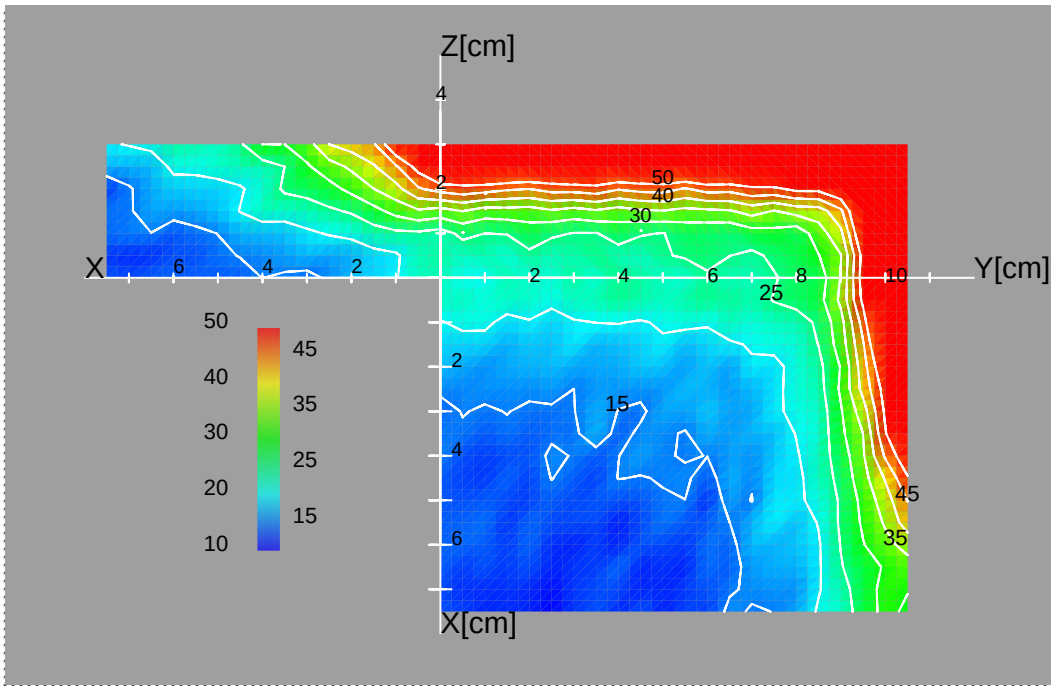

Figure 5-49 Displacement damage gradient contours. The unit is % per DPA/FPY/cm normalised to the total DPA/FPY value. (MCNP uncollided, McDeLi data, uniform beam profile.)

Irradiation volumes

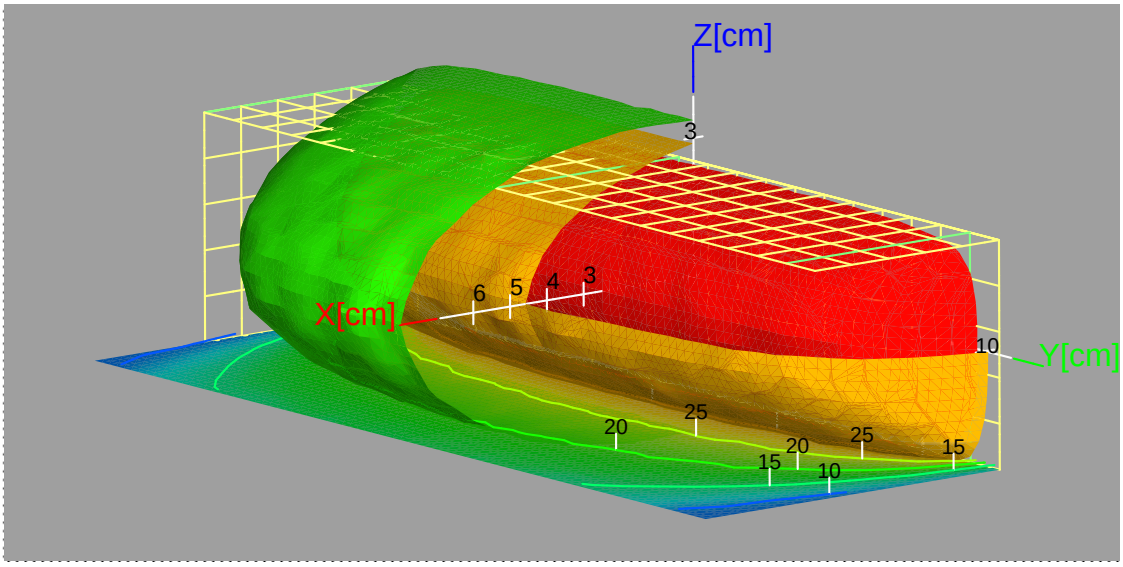

Figure 5-50 Displacement damage cutout isosurfaces. Each isosurface characterises the available volume for a DPA/FPY limit. Green = 20 DPA/FPY, yellow = 30 DPA/FPY and red = 40 DPA/FPY. The grid structure shows the physical boundary of the helium cooled high flux test module. (MCNP uncollided, McDeLi data, uniform beam profile.)

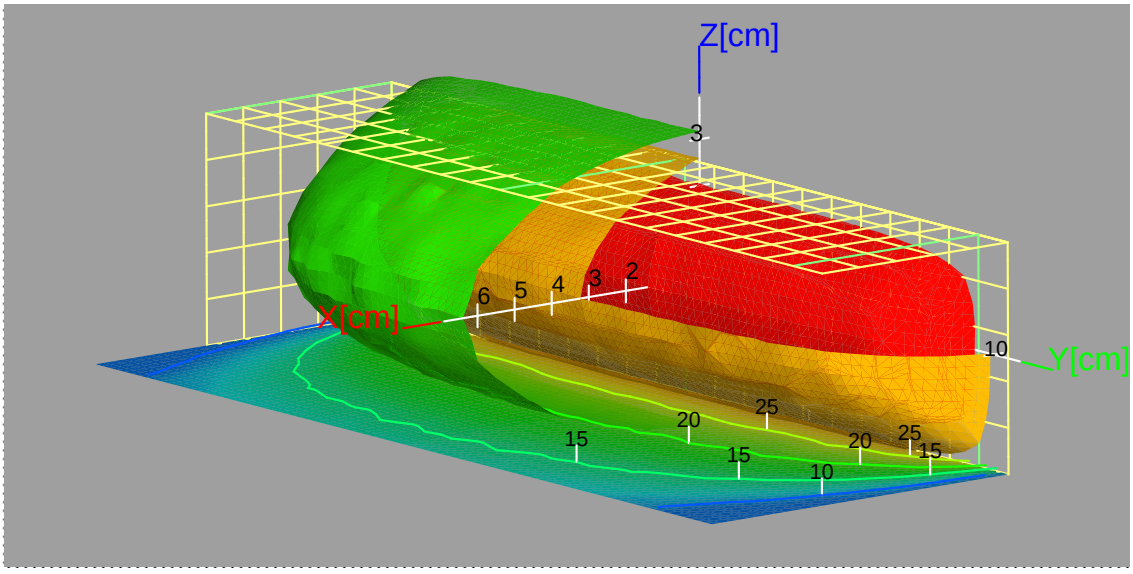

Figure 5-51 Displacement damage cutout isosurfaces with *Y* = 6.7% (= 7.3% x 0.83). Each isosurface characterises the available volume for a DPA/FPY limit. Green = 20 DPA/FPY, yellow = 30 DPA/FPY and red = 40 DPA/FPY. The grid structure shows the physical boundary of the helium cooled high flux test module. (MCNP uncollided, McDeLi data *Y*=6.7% (= 7.3% x 0.83), uniform beam profile.)

The following table shows the irradiation volumes which can achieved with uncollided calculations with the uniform beam profile and FZK n-source model.

Table 5-6 Irradiation volumes as a function of the minimum displacement damage. The third column shows the available volume inside the present design of the High Flux Test Module (HFTM).

Displacement Damage [DPA/FPY]	Total volume [cm^3]	Volume inside HFTM [cm^3]
20	732	478
30	307	298
40	133	133
50	47	47

Wall Load

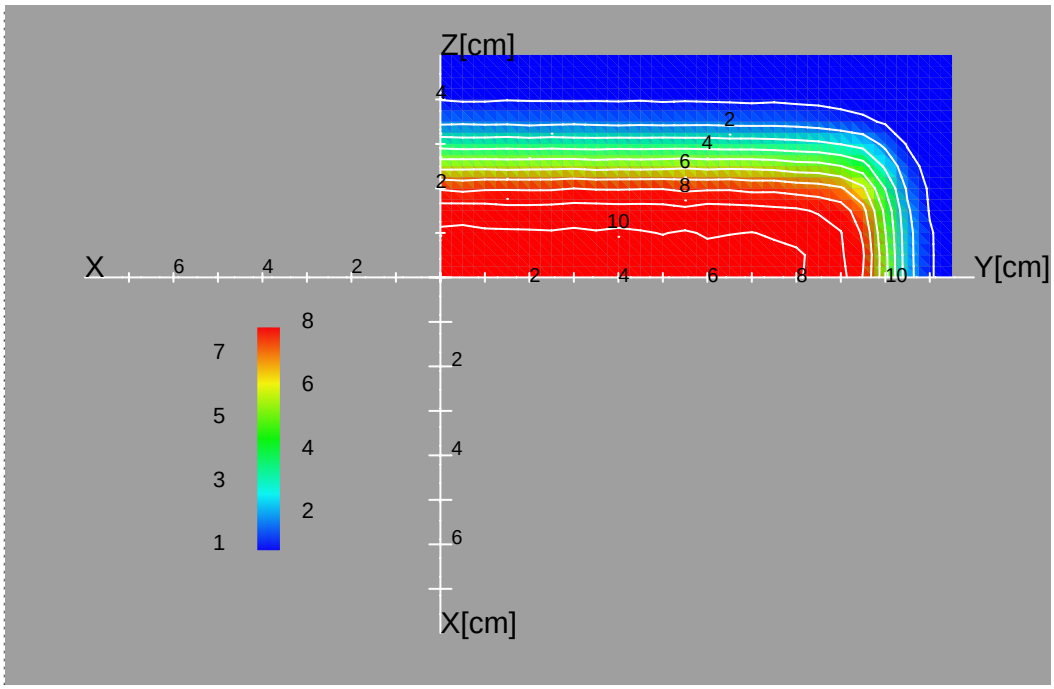

Figure 5-52 Wall load contours in units of MW/m^2. The plot shows a very homogeneous distribution on the backplate surface. (MCNP uncollided, McDeLi data, uniform beam profile.)

5.4.2 Uncollided calculations with non-uniform beam profile

Neutron Flux

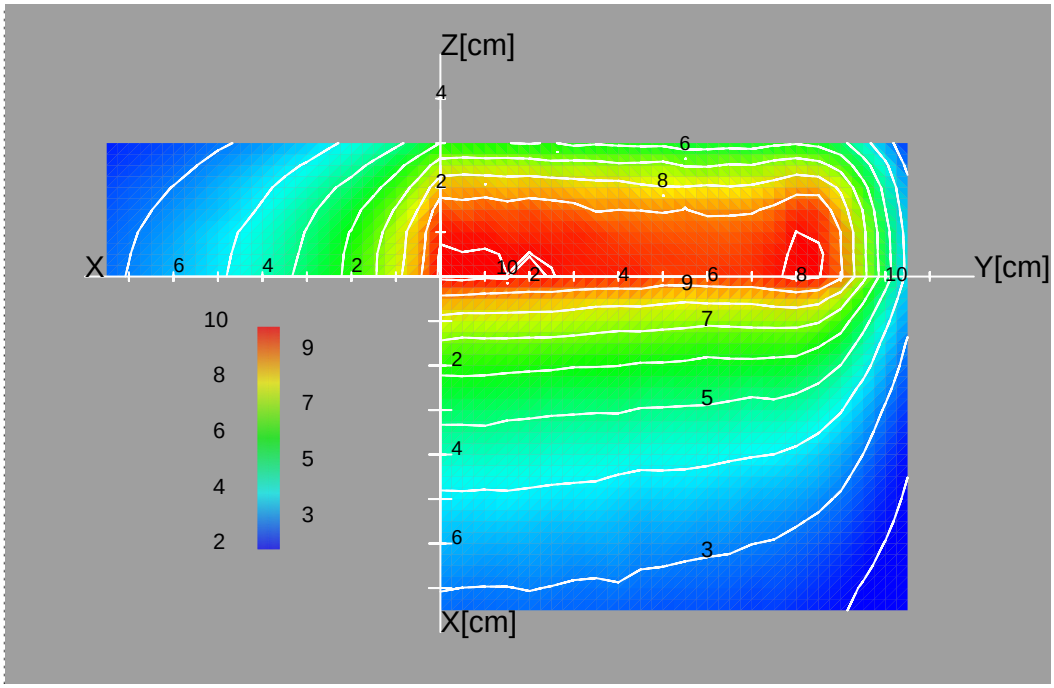

Figure 5-53 Total neutron flux contours. The unit is 10^{14} n/s/cm^2. The plot shows a peaked flux distribution on the backplate surface and also in the x-y-plane the peaked edges of the non-uniform beam profile can be recognised. (MCNP uncollided, McDeLi data, non-uniform beam profile.)

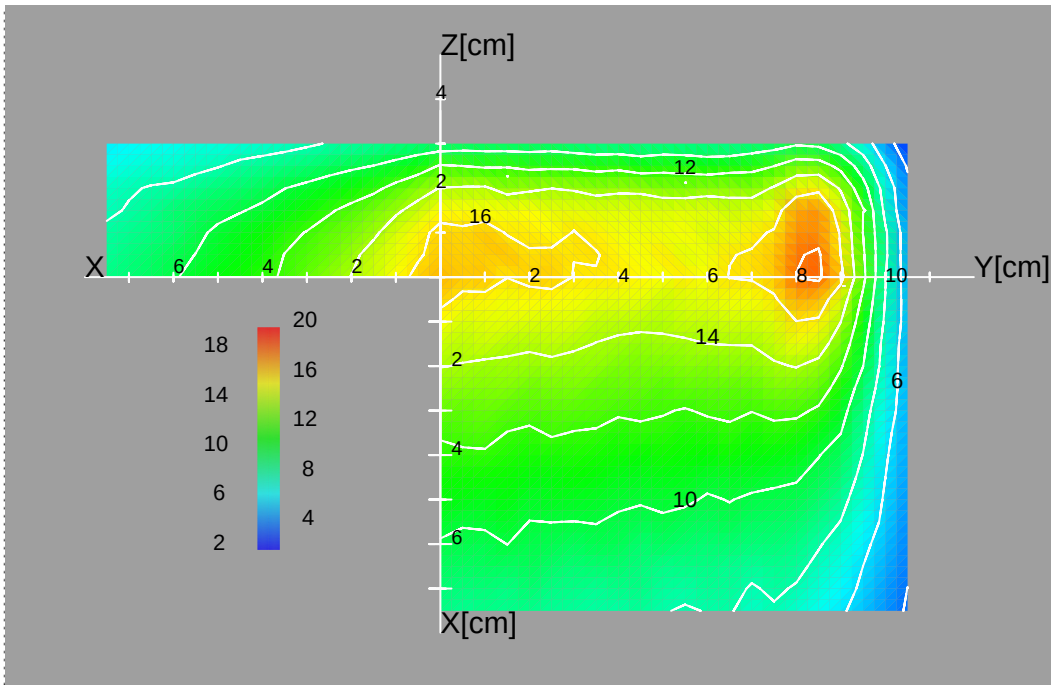

Figure 5-54 Neutron flux contours for neutrons with energies higher than 14.6 MeV. The unit is 10^{13} n/s/cm^2. (MCNP uncollided, McDeLi data, non-uniform beam profile.)

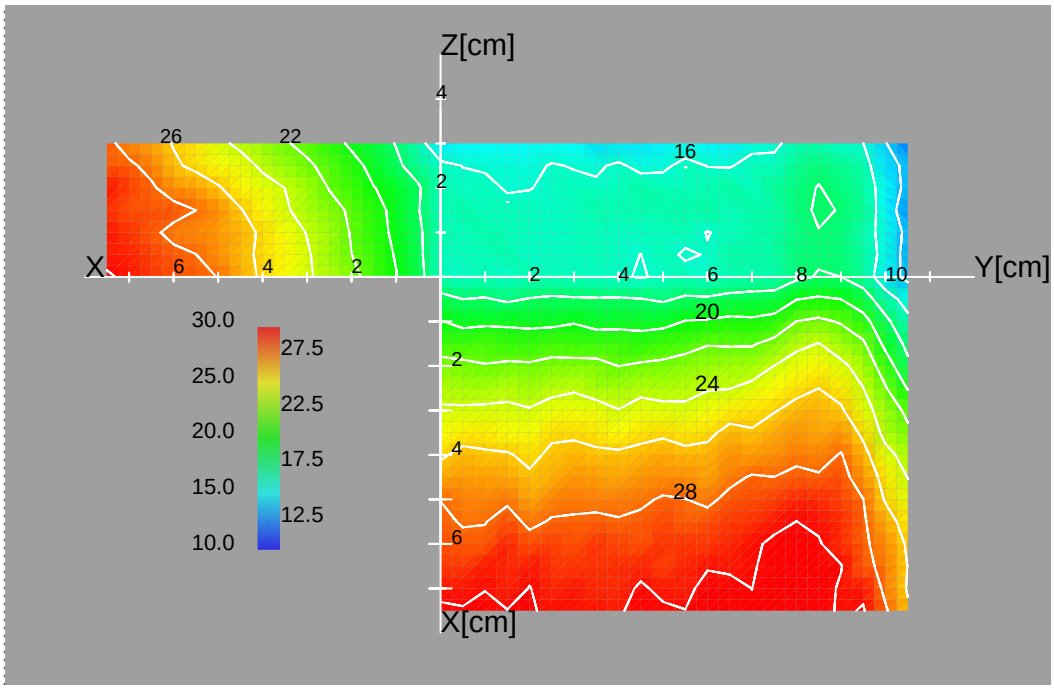

Figure 5-55 Fraction in % of the neutron flux with neutron energies higher than 14.6 MeV. The fraction increases for downstream locations. (MCNP uncollided, McDeLi data, non-uniform beam profile.)

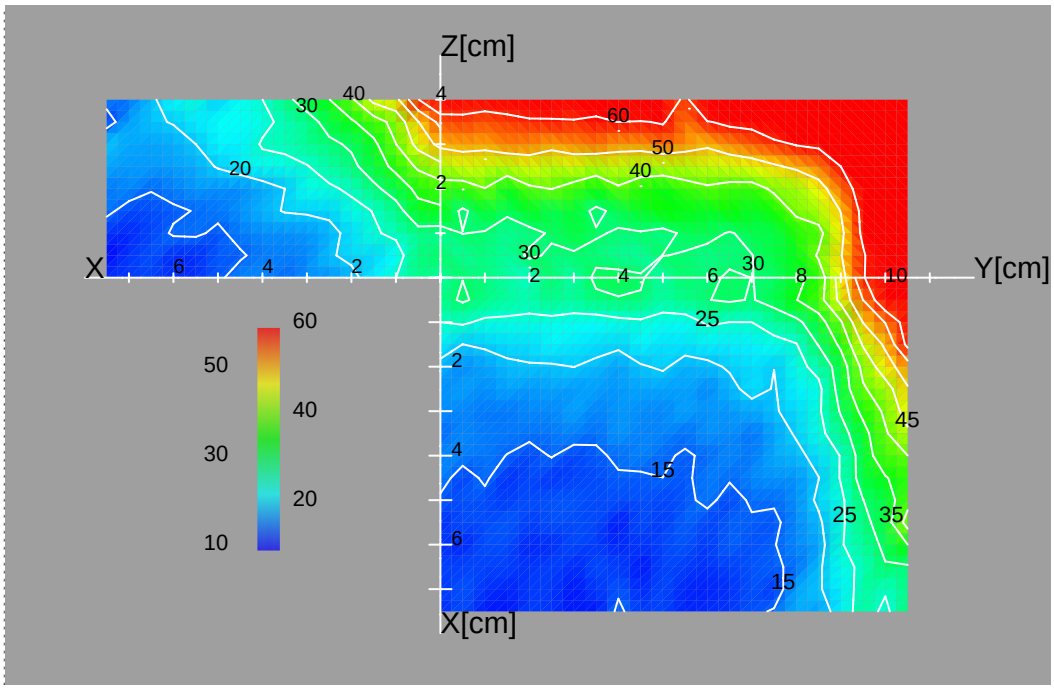

Figure 5-56 Neutron flux gradient contours. The unit is %/cm.(MCNP uncollided, McDeLi data, non-uniform beam profile.)

Nuclear responses in Fe

Hydrogen production

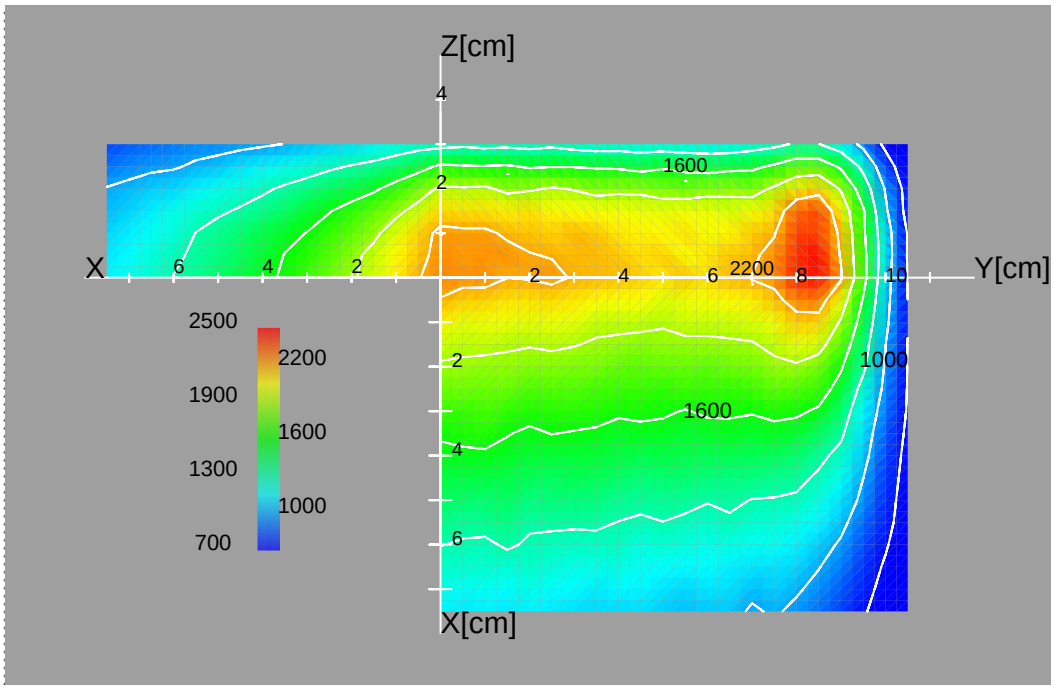

Figure 5-57 Hydrogen production contours in units of atomic parts per million (appm) per full power year (FPY). (MCNP uncollided, McDeLi data, non-uniform beam profile.)

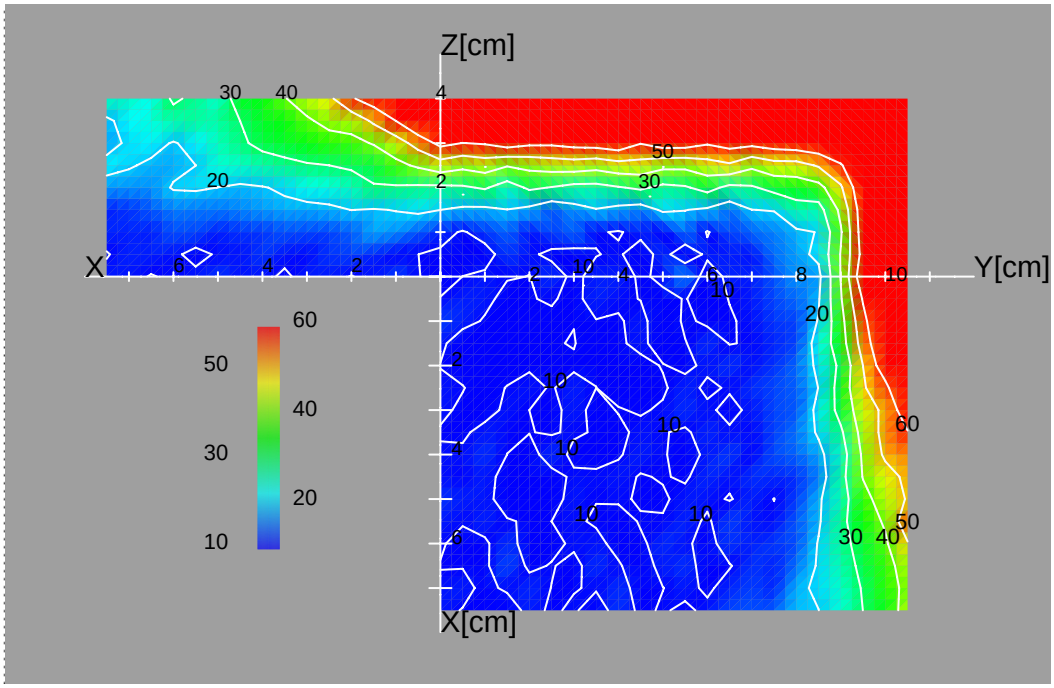

Figure 5-58 Hydrogen production gradients. The unit is % per appm/FPY/cm normalised to the total appm/FPY value. (MCNP uncollided, McDeLi data, non-uniform beam profile.)

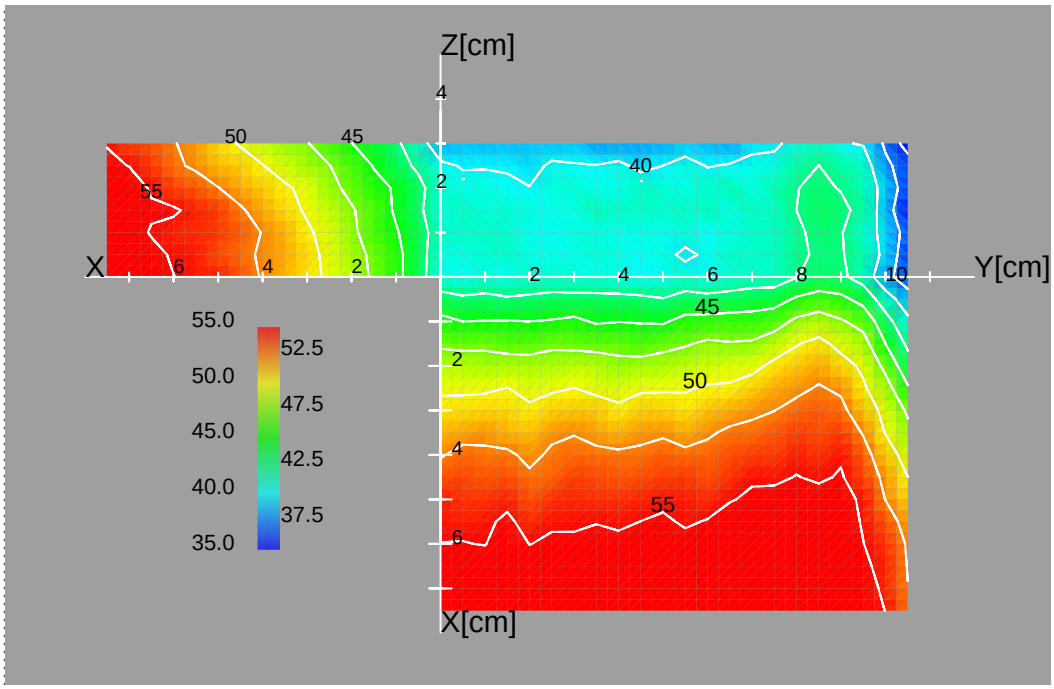

Figure 5-59 Hydrogen to DPA ratios in units of appm/DPA. (MCNP uncollided, McDeLi data, non-uniform beam profile.)

Helium production

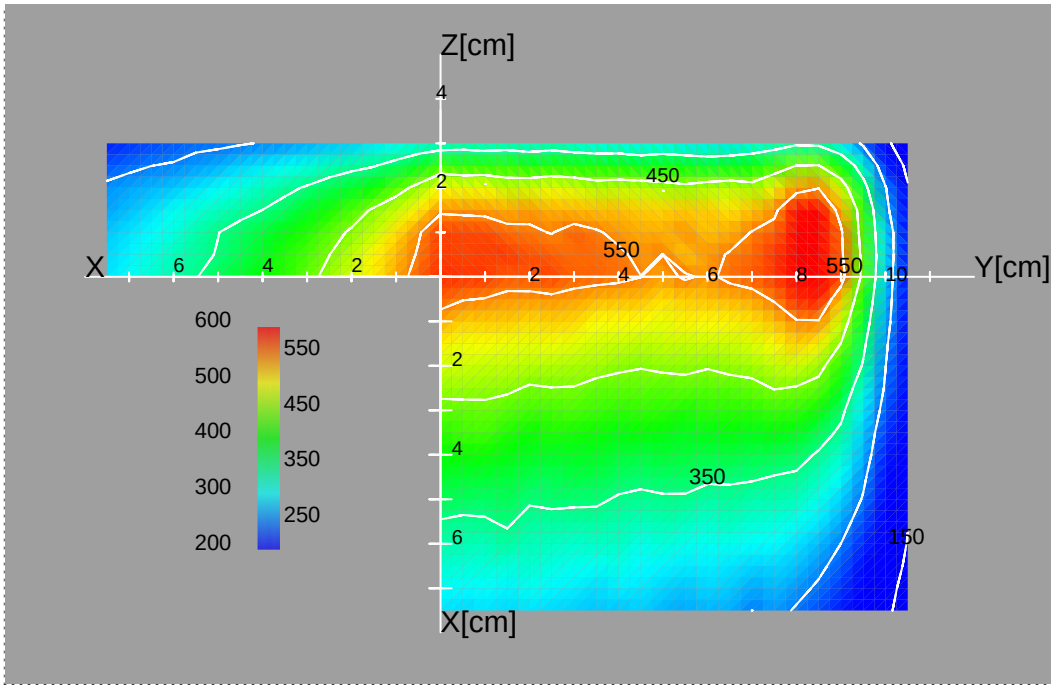

Figure 5-60 Helium production contours in units of atomic parts per million (appm) per full power year (FPY). (MCNP uncollided, McDeLi data, non-uniform beam profile.)

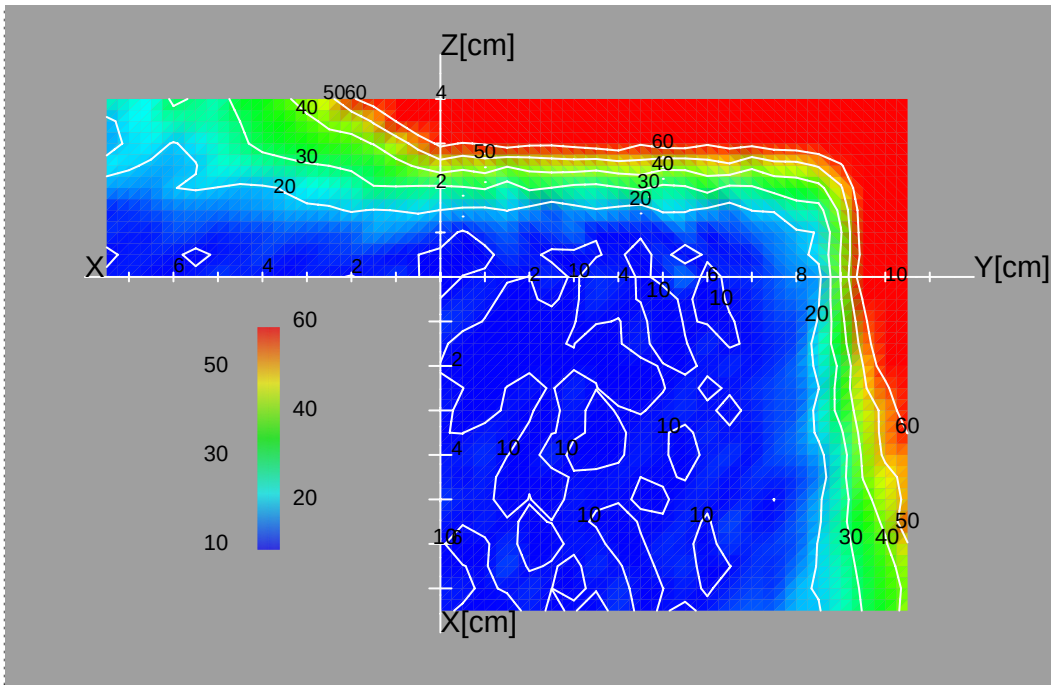

Figure 5-61 Helium production gradients. The unit is % per appm/FPY/cm normalised to the total appm/FPY value. (MCNP uncollided, McDeLi data, non-uniform beam profile.)

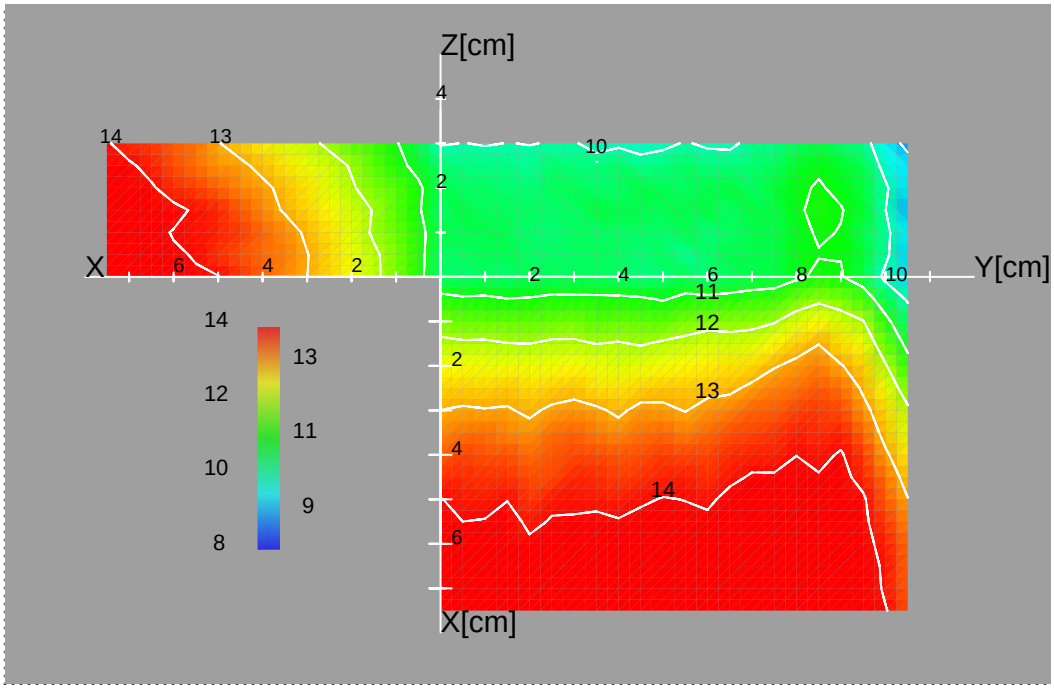

Figure 5-62 Helium to DPA ratio in units of appm/DPA. (MCNP uncollided, McDeLi data, non-uniform beam profile.)

Displacement damage production in Fe

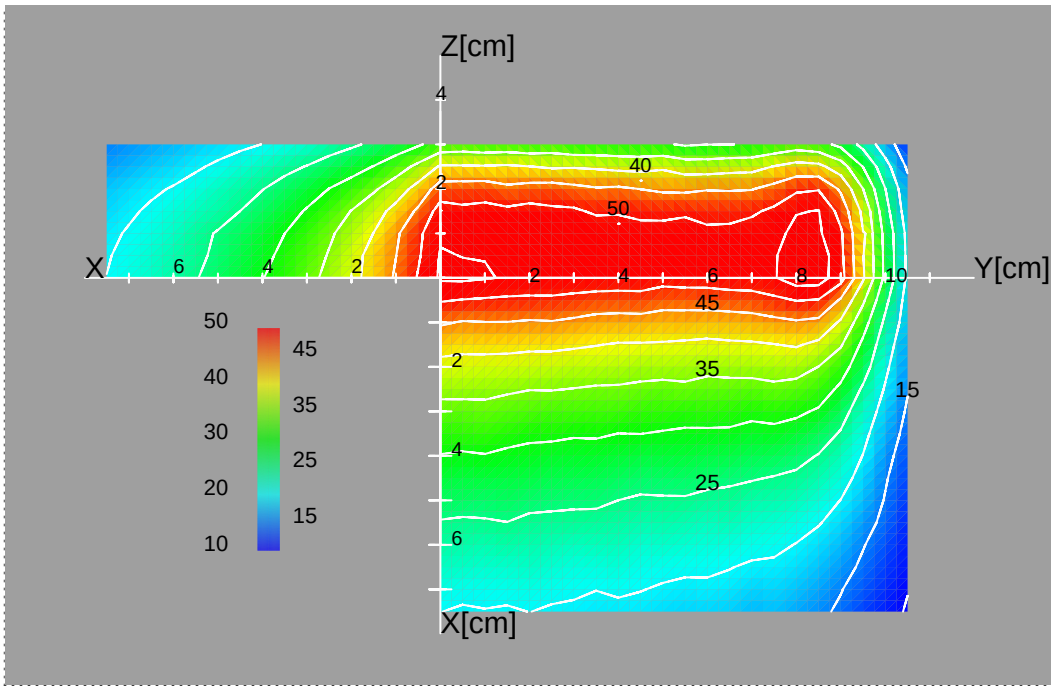

Figure 5-63 Displacement damage contours in units of DPA/FPY. (MCNP uncollided, McDeLi data, non-uniform beam profile.)

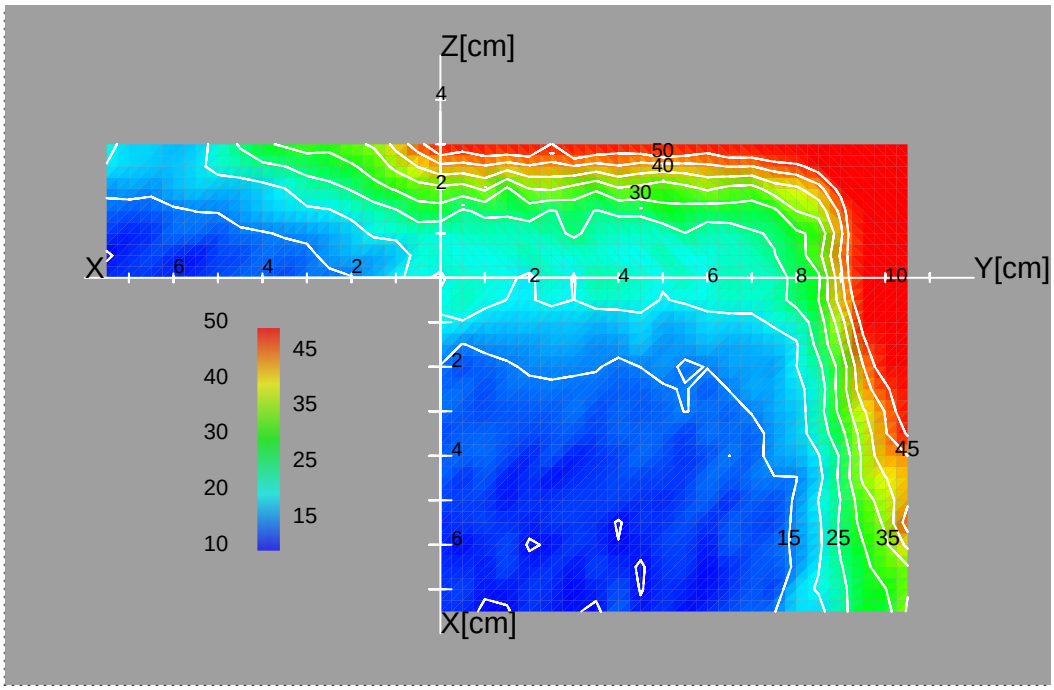

Figure 5-64 Displacement damage gradient contours. The unit is % per DPA/FPY/cm normalised to the total DPA/FPY value. (MCNP uncollided, McDeLi data, non-uniform beam profile.)

Irradiation volumes

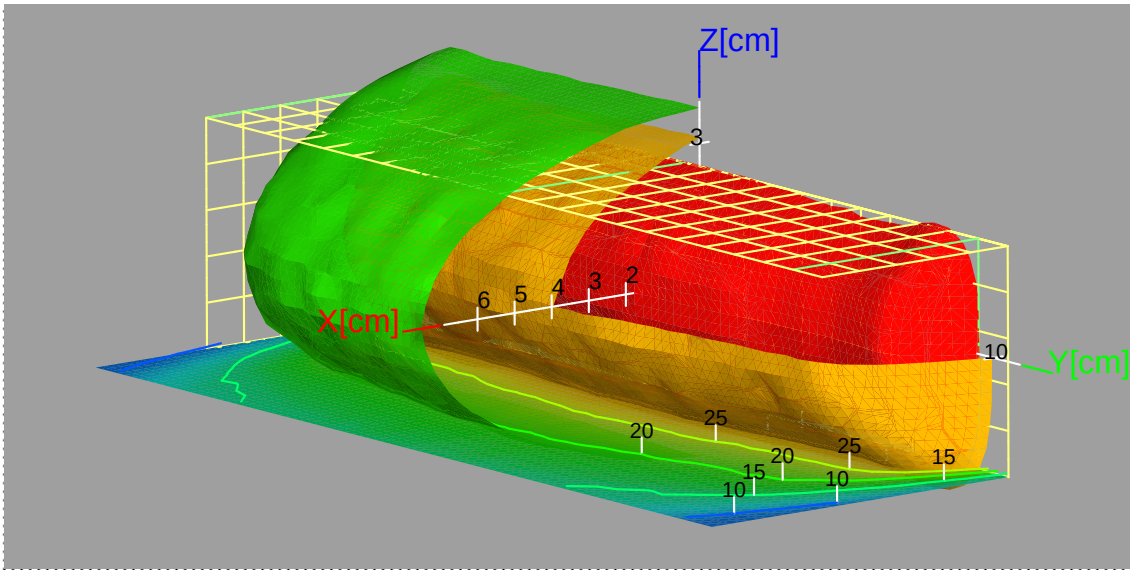

Figure 5-65 Displacement damage cutout isosurfaces. Each isosurface characterises the available volume for a DPA/FPY limit. Green = 20 DPA/FPY, yellow = 30 DPA/FPY and red = 40 DPA/FPY. The grid structure shows the physical boundary of the helium cooled high flux test module. (MCNP uncollided, McDeLi data, non-uniform beam profile.)

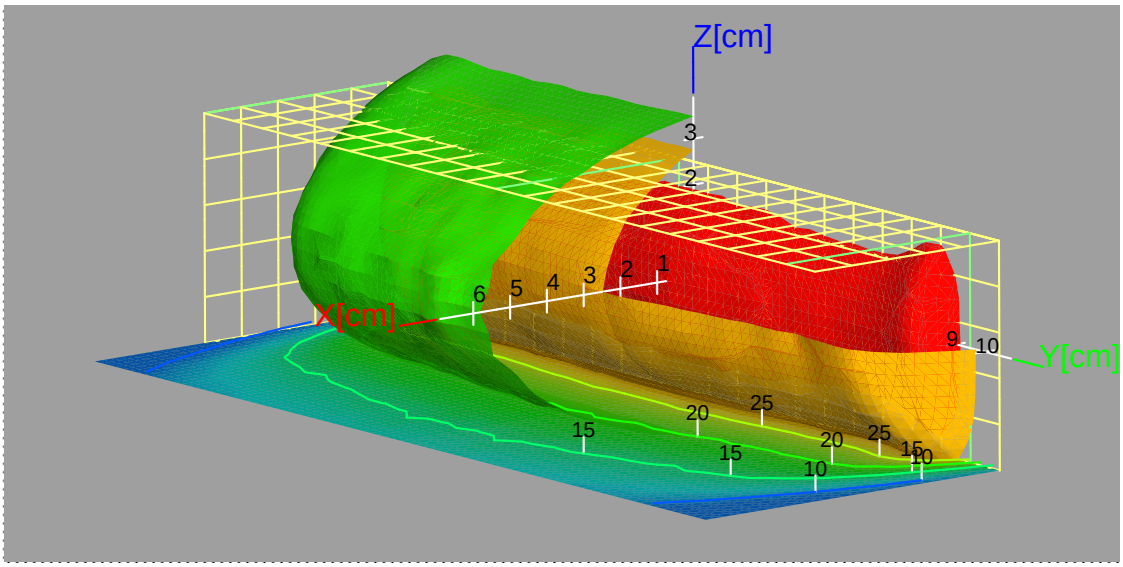

Figure 5-66 Displacement damage cutout isosurfaces with Y = 83 %. Each isosurface characterises the available volume for a DPA/FPY limit. Green = 20 DPA/FPY, yellow = 30 DPA/FPY and red = 40 DPA/FPY. The grid structure shows the physical boundary of the helium cooled high flux test module. (MCNP uncollided, McDeLi data Y = 83 %, non-uniform beam profile.)

The following table shows the irradiation volumes which can achieved with uncollided calculations with the non-uniform beam profile and FZK n-source model.

Table 5-7 Irradiation volumes as a function of the minimum displacement damage. The third column shows the available volume inside the present design of the High Flux Test Module (HFTM).

Displacement Damage [DPA/FPY]	Total volume [cm^3]	Volume inside HFTM [cm^3]
20	716	480
30	273	259
40	93	93
50	14	14

Wall Load

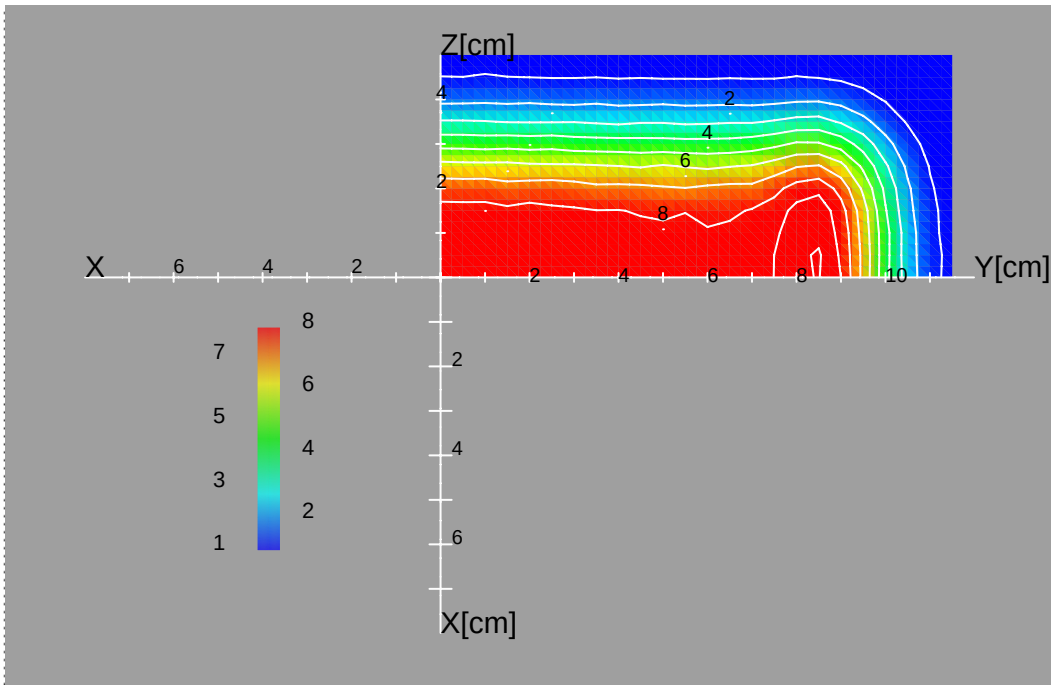

Figure 5-67 Wall load contours in units of MW/m^2. (MCNP uncollided, McDeLi data, non-uniform beam profile.)

5.4.3 Collided calculations with uniform beam profile

Neutron Flux

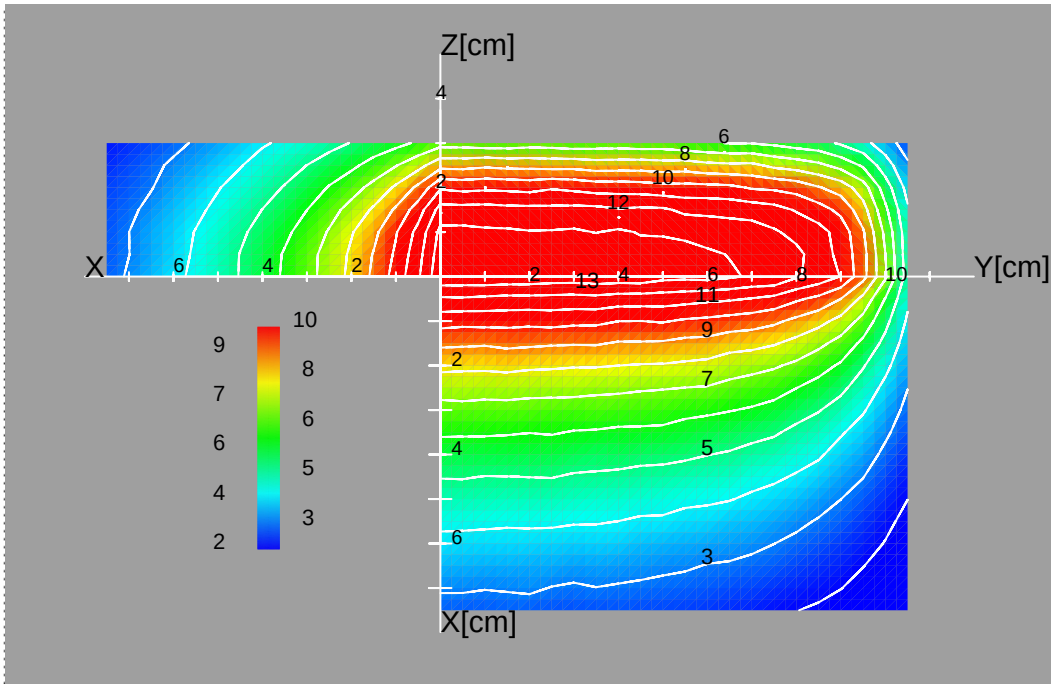

Figure 5-68 Total neutron flux contours. The unit is 10^{14} n/s/cm^2. The plot shows a very homogeneous distribution on the backplate surface. (MCNP collided, McDeLi data, uniform beam profile.)

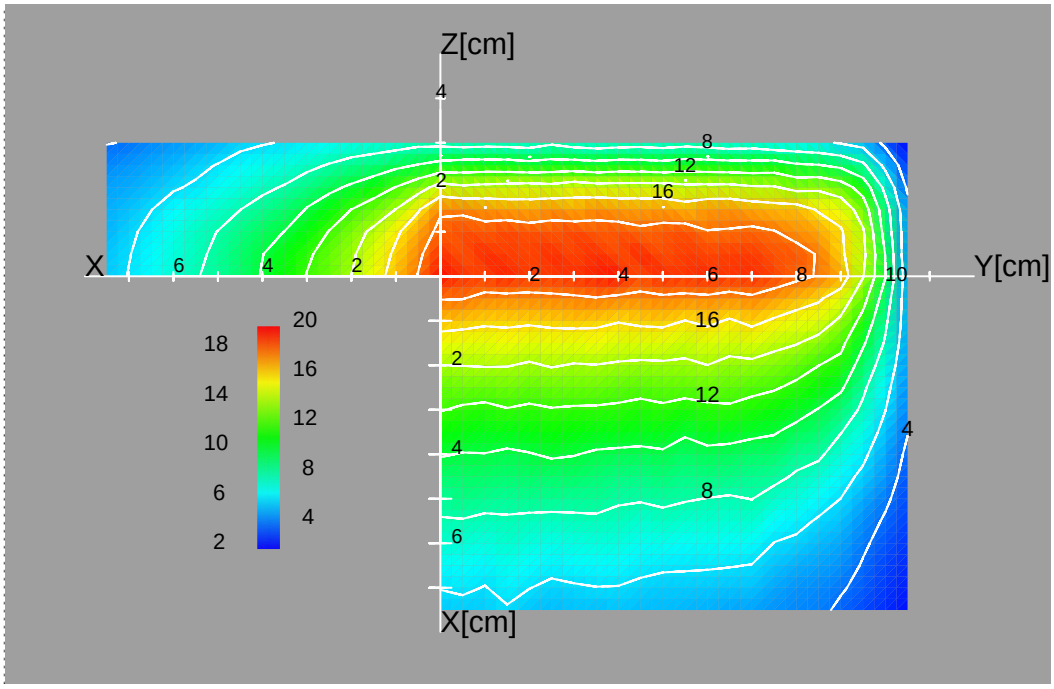

Figure 5-69 Neutron flux contours for neutrons with energies higher than 14.6 MeV. The unit is 10^{13} n/s/cm^2. The largest high energy flux appears close to the backplate. (MCNP collided, McDeLi data, uniform beam profile.)

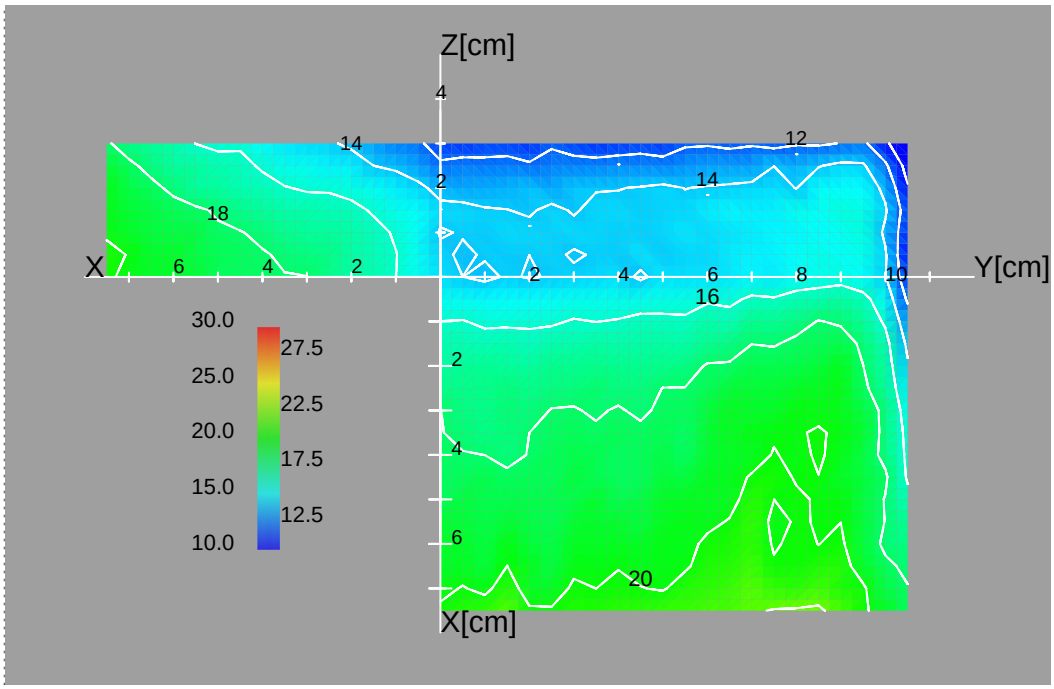

Figure 5-70 Fraction in % of the neutron flux with neutron energies higher than 14.6 MeV. The fraction increases for downstream locations. (MCNP collided, McDeLi data, uniform beam profile.)

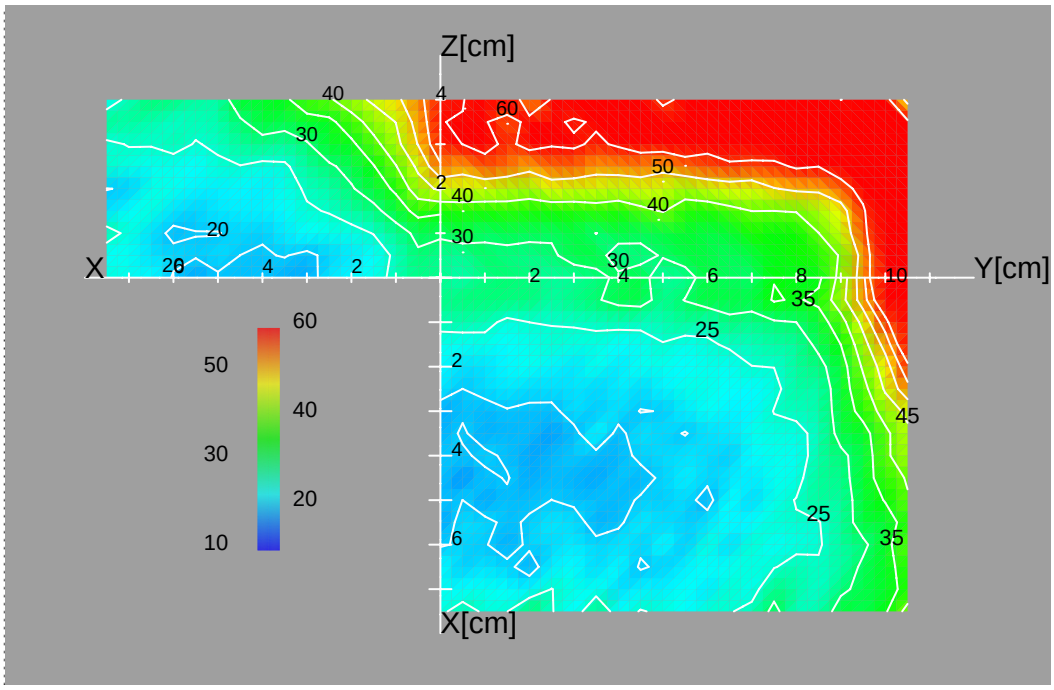

Figure 5-71 Neutron flux gradient contours. The unit is %/cm.(MCNP collided, McDeLi data, uniform beam profile.)

Nuclear responses in Fe

Hydrogen production

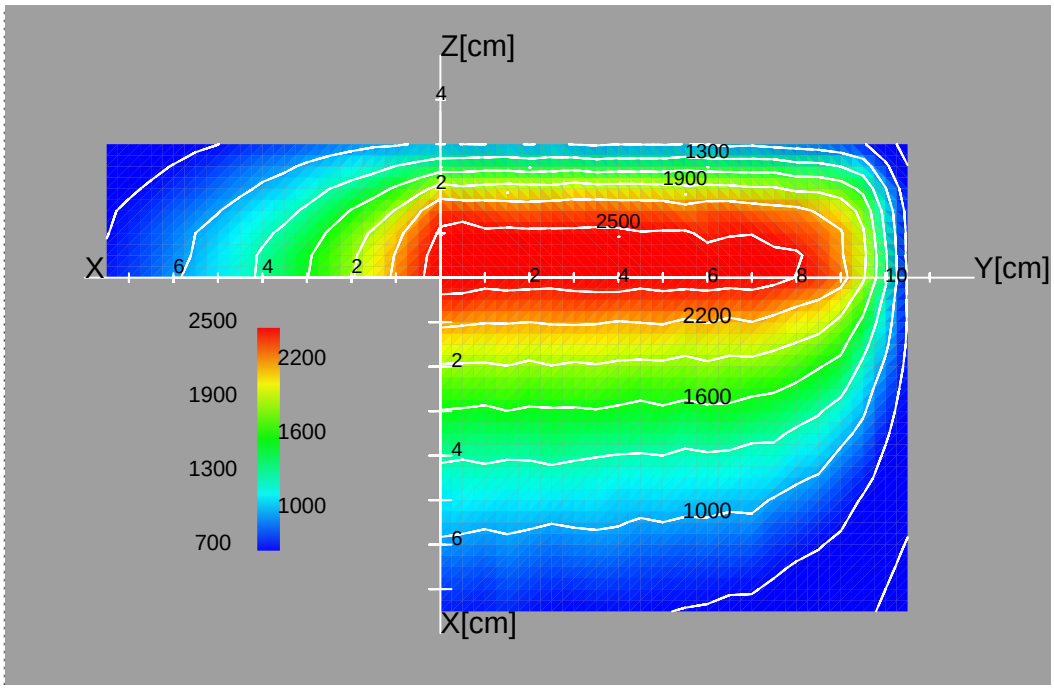

Figure 5-72 Hydrogen production contours in units of atomic parts per million (appm) per full power year (FPY). At the backplate the maximum of > 2500 appm H/FPY appears. (MCNP collided, McDeLi data, uniform beam profile.)

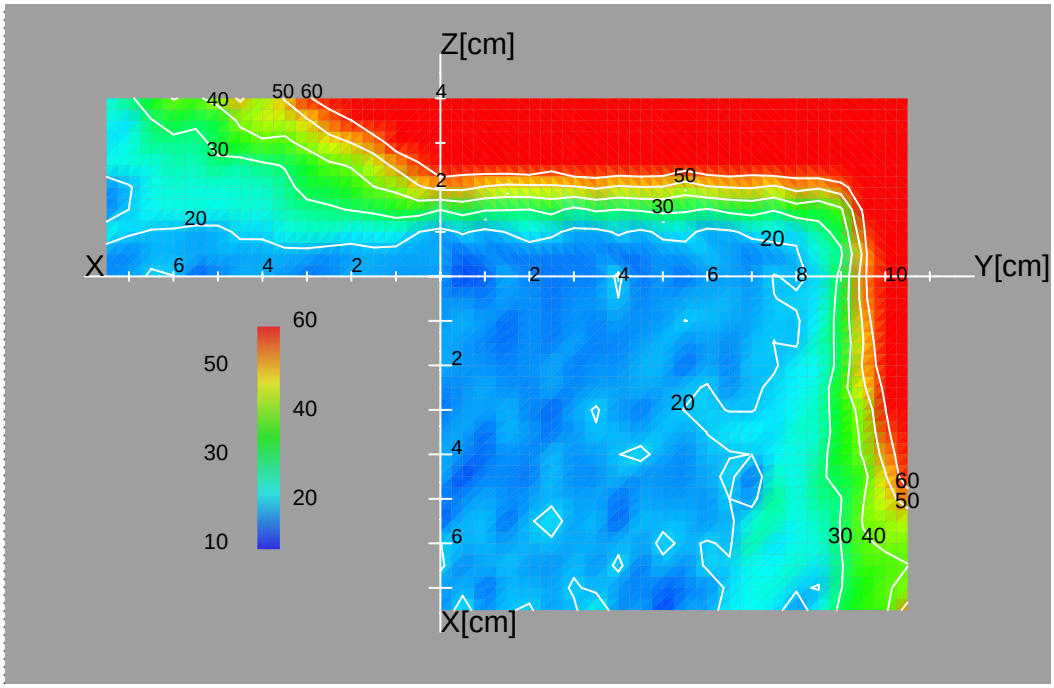

Figure 5-73 Hydrogen production gradients. The unit is % per appm/FPY/cm normalised to the total appm/FPY value. (MCNP collided, McDeLi data, uniform beam profile.)

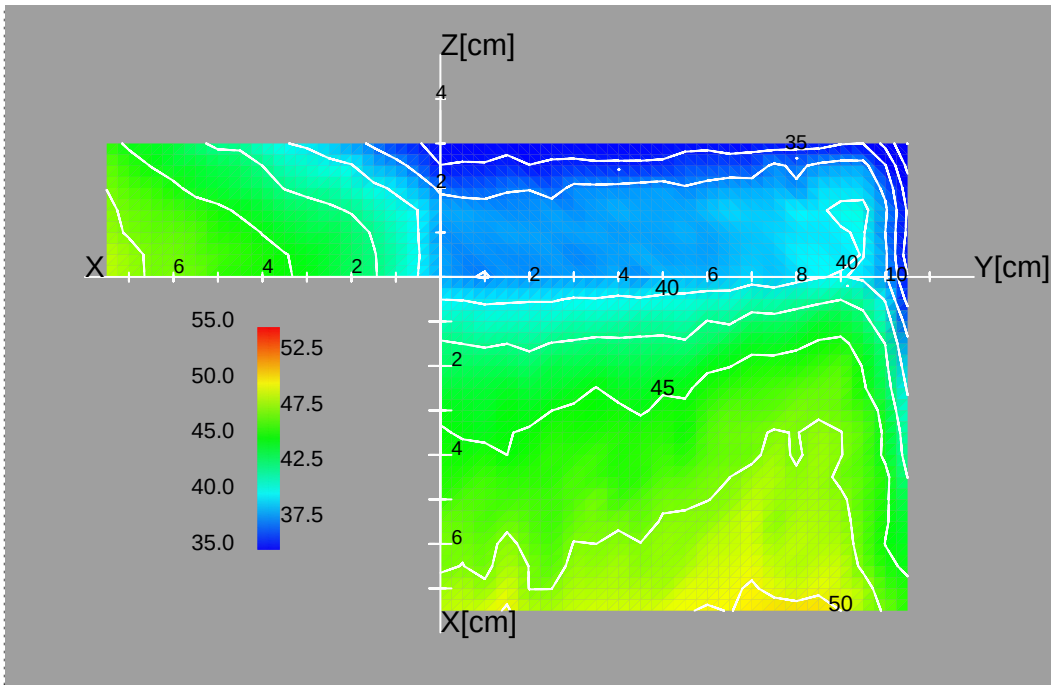

Figure 5-74 Hydrogen to DPA ratios in units of appm/DPA. (MCNP collided, McDeLi data, uniform beam profile.)

Helium production

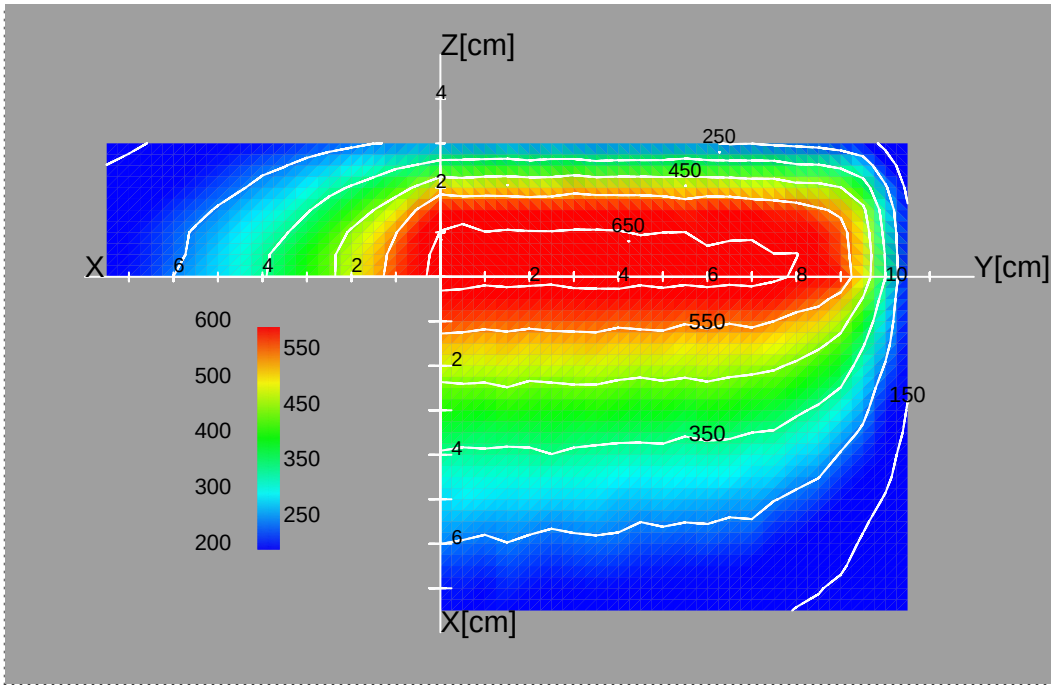

Figure 5-75 Helium production contours in units of atomic parts per million (appm) per full power year (FPY). At the backplate the maximum of > 650 appm He/FPY appears. (MCNP collided, McDeLi data, uniform beam profile.)

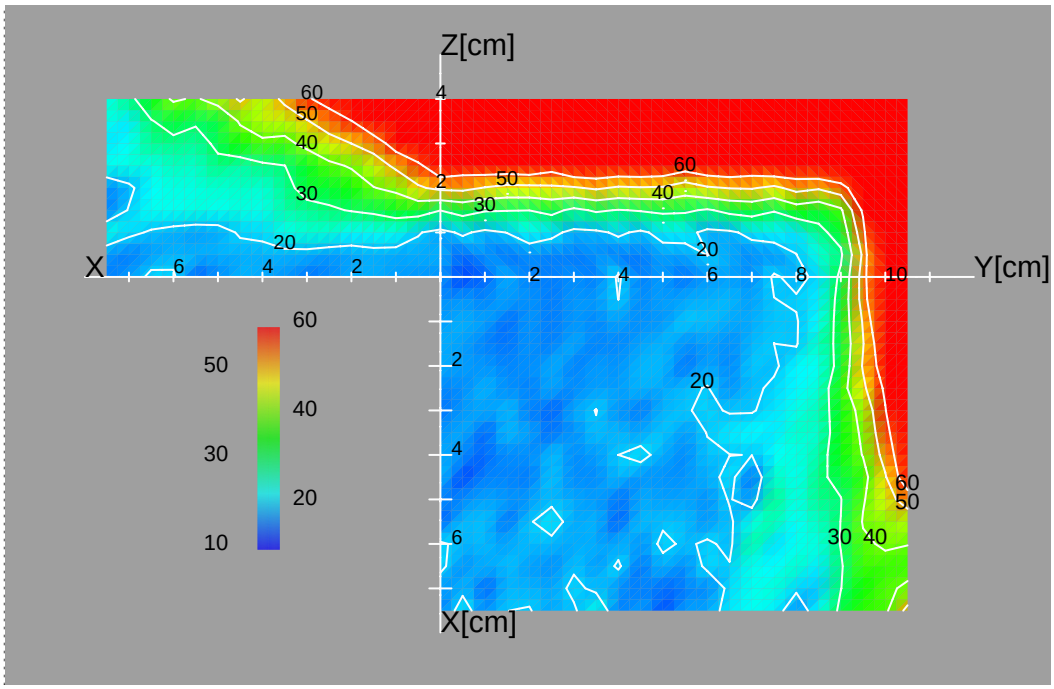

Figure 5-76 Helium production gradients. The unit is % per appm/FPY/cm normalised to the total appm/FPY value. (MCNP collided, McDeLi data, uniform beam profile.)

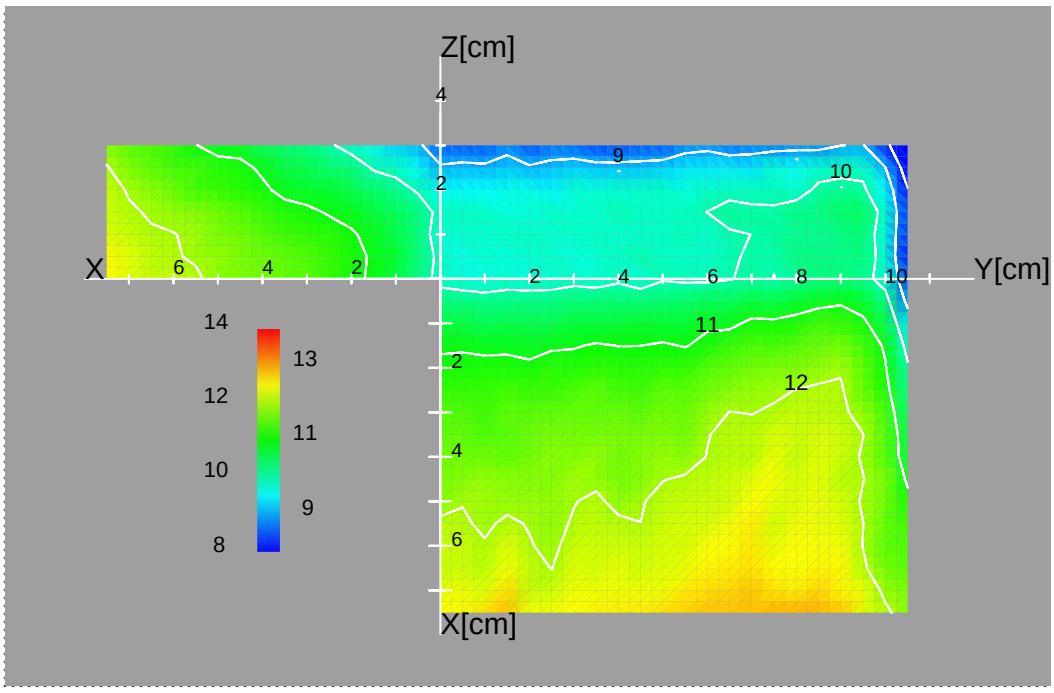

Figure 5-77 Helium to DPA ratio in units of appm/DPA. The He/DPA ratio increases for farther downstream locations. (MCNP collided, McDeLi data, uniform beam profile.)

DPA production

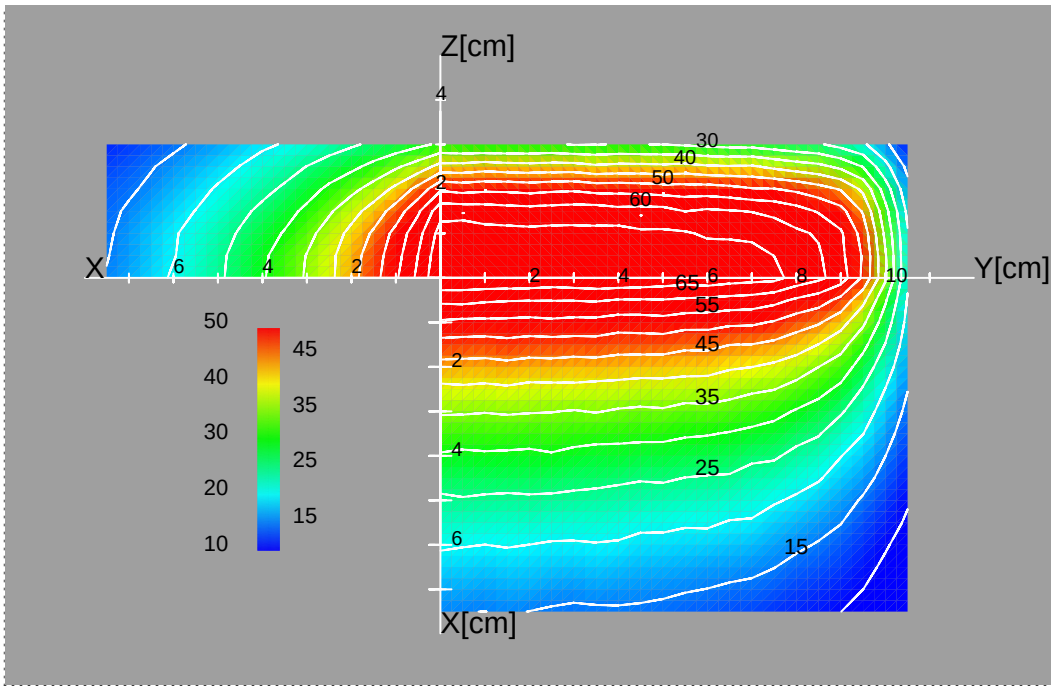

Figure 5-78 Displacement damage contours in units of DPA/FPY. (MCNP collided, McDeLi data, uniform beam profile.)

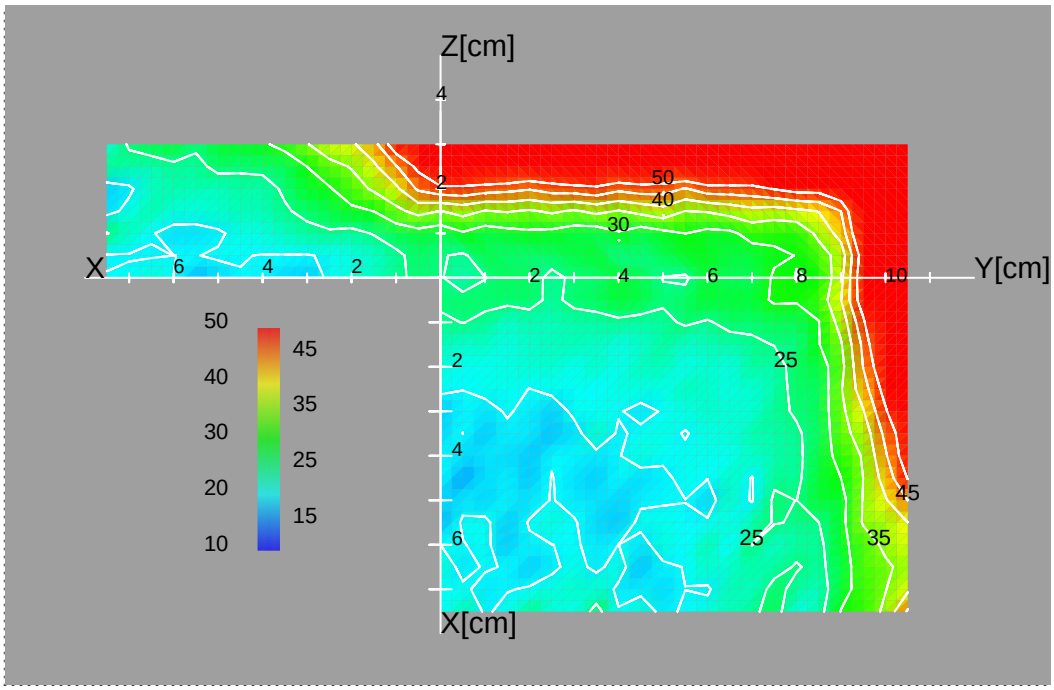

Figure 5-79 Displacement damage gradient contours. The unit is % per DPA/FPY/cm normalised to the total DPA/FPY value. (MCNP collided, McDeLi data, uniform beam profile.)

Irradiation volumes

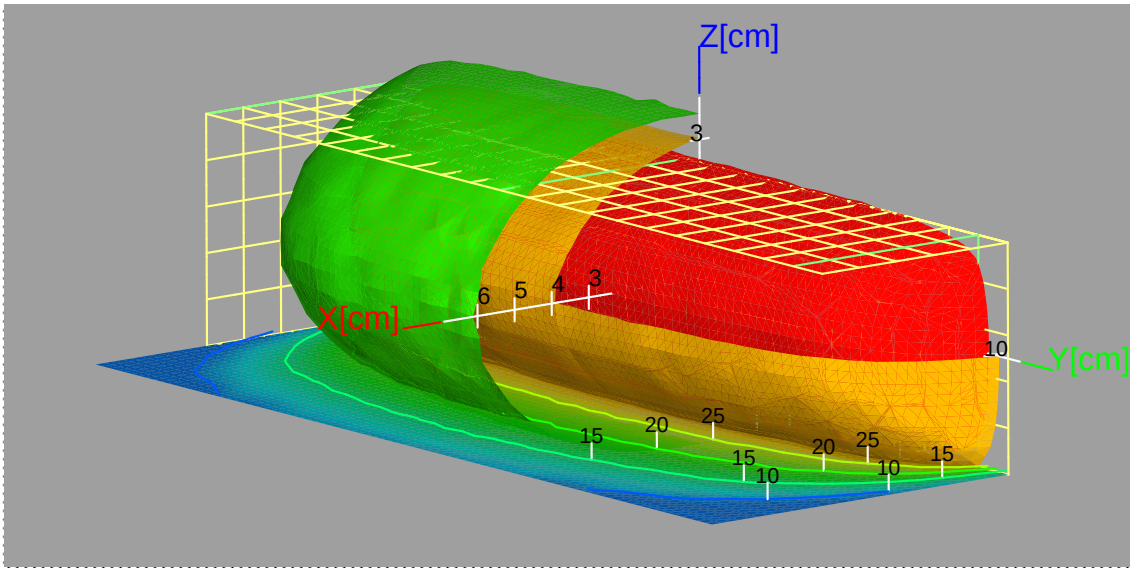

Figure 5-80 Displacement damage cutout isosurfaces. Each isosurface characterises the available volume for a DPA/FPY limit. Green = 20 DPA/FPY, yellow = 30 DPA/FPY and red = 40 DPA/FPY. The grid structure shows the physical boundary of the helium cooled high flux test module. (MCNP collided, McDeLi data, uniform beam profile.)

The following table shows the irradiation volumes which can achieved with collided calculations with the uniform beam profile and FZK n-source model.

Table 5-8 Irradiation volumes as a function of the minimum displacement damage. The third column shows the available volume inside the present design of the High Flux Test Module (HFTM).

Displacement Damage [DPA/FPY]	Total volume [cm^3]	Volume inside HFTM [cm^3]
20	594	460
30	286	272
40	140	140
50	61	61

Nuclear Heating

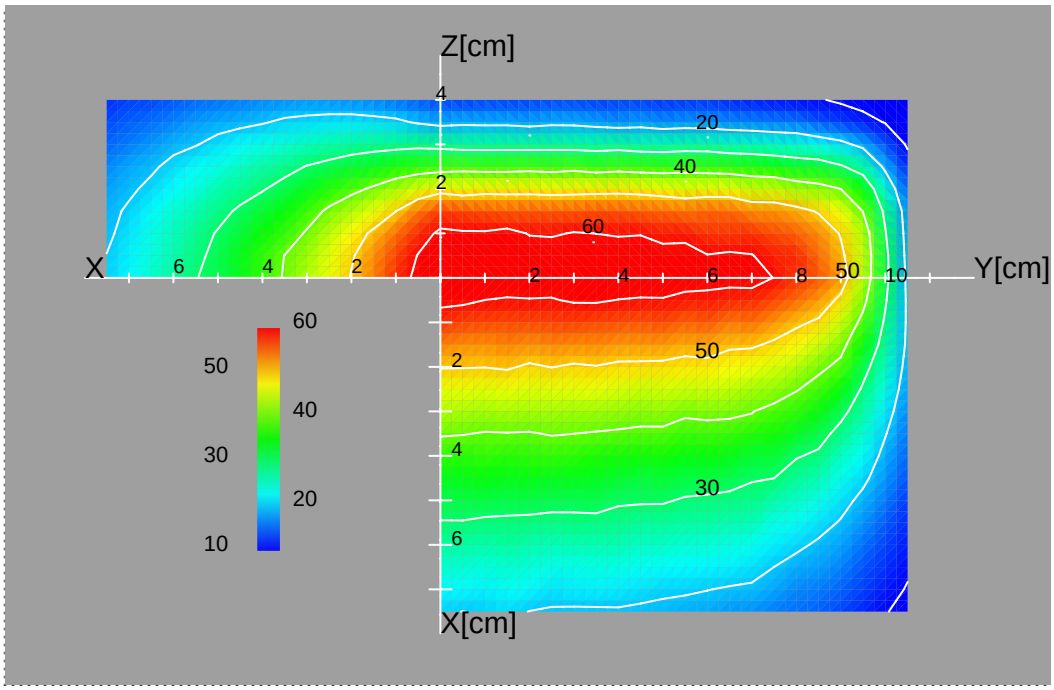

Figure 5-81 Nuclear heating contours in units of W/cm^3. The plot shows a very homogeneous distribution on the backplate surface. (MCNP collided, McDeLi data, uniform beam profile.)

Wall Load

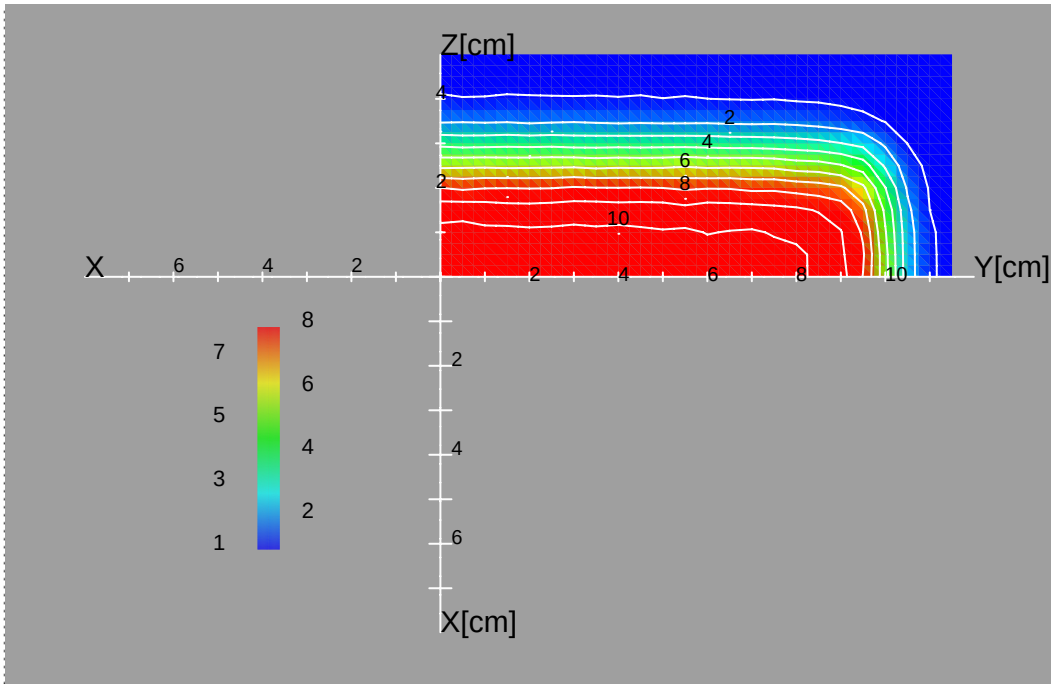

Figure 5-82 Wall load contours in units of MW/m^2. The plot shows a very homogeneous distribution on the backplate surface. (MCNP collided, McDeLi data, uniform beam profile.)

5.4.4 Collided calculations with non-uniform beam profile

Neutron Flux

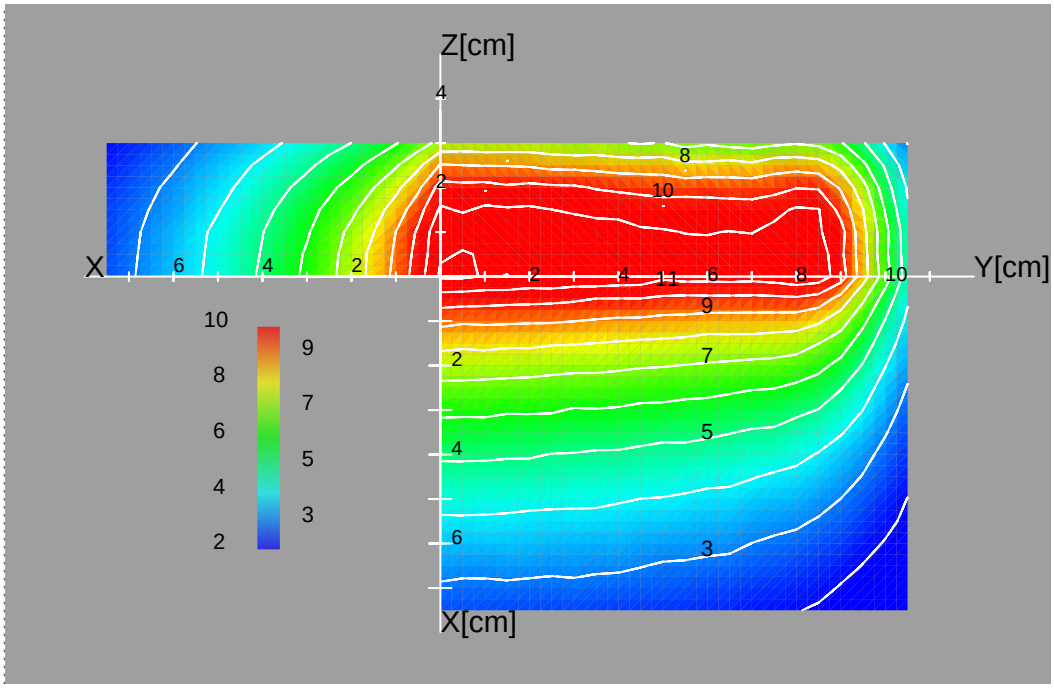

Figure 5-83 Total neutron flux contours. The unit is 10^{14} n/s/cm^2. The plot shows a peaked flux distribution on the backplate surface and also in the x-y-plane the peaked edges of the non-uniform beam profile can be recognised. (MCNP collided, McDeLi data, non-uniform beam profile.)

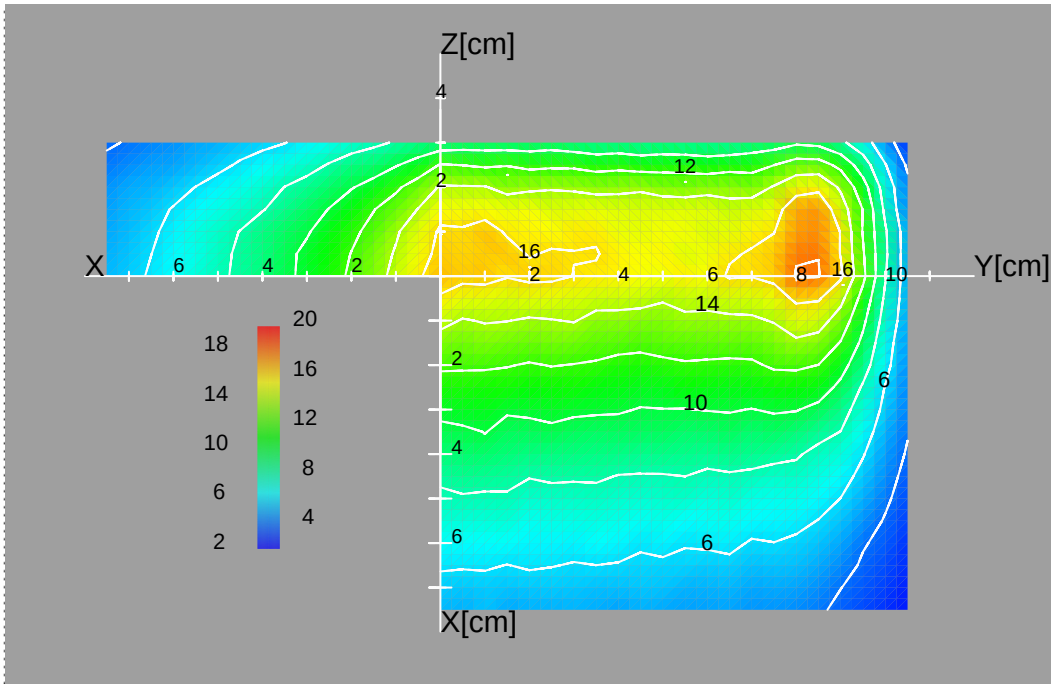

Figure 5-84 Neutron flux contours for neutrons with energies higher than 14.6 MeV. The unit is 10^{13} n/s/cm^2. (MCNP collided, McDeLi data, non-uniform beam profile.)

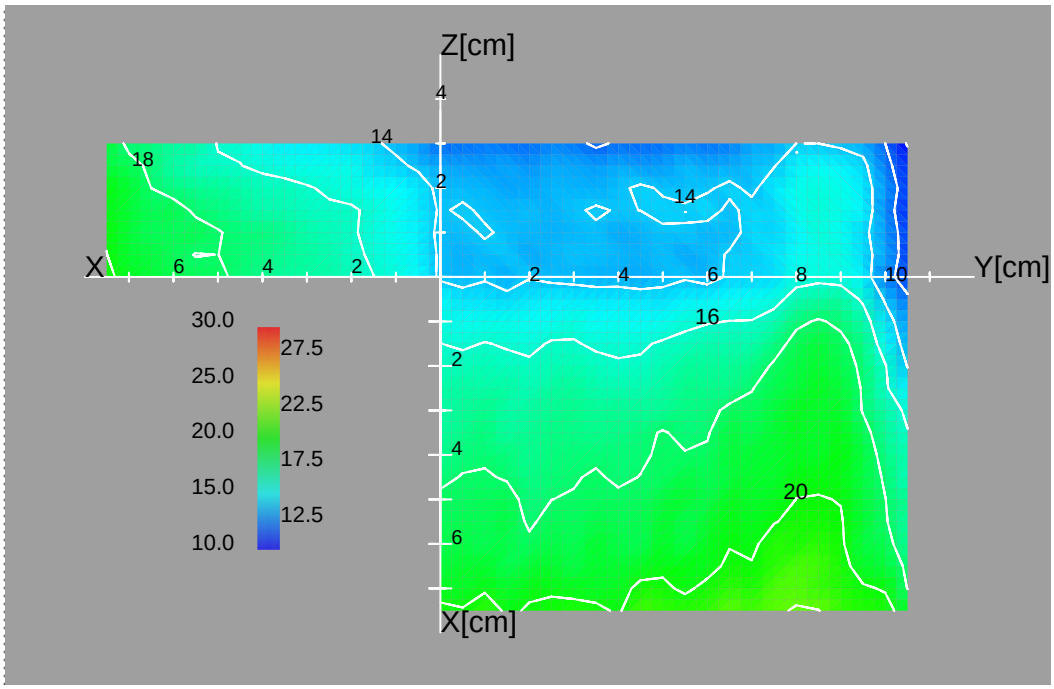

Figure 5-85 Fraction in % of the neutron flux with neutron energies higher than 14.6 MeV. The fraction increases for downstream locations. (MCNP collided, McDeLi data, non-uniform beam profile.)

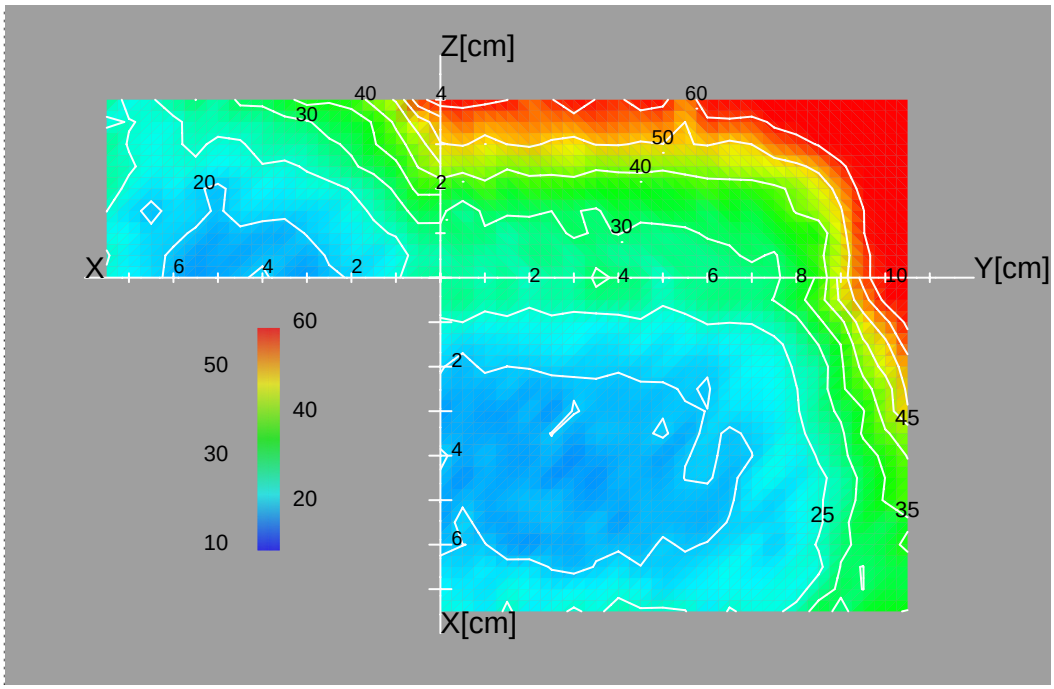

Figure 5-86 Neutron flux gradient contours. The unit is %/cm.(MCNP collided, McDeLi data, non-uniform beam profile.)

Nuclear responses in Fe

Hydrogen production

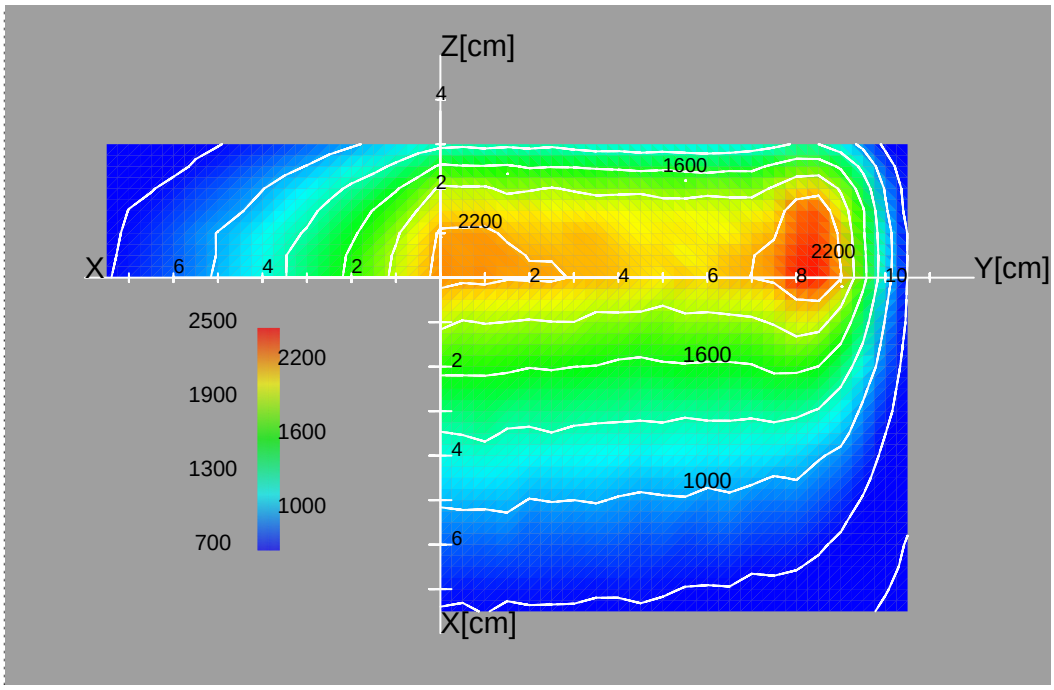

Figure 5-87 Hydrogen production contours in units of atomic parts per million (appm) per full power year (FPY). (MCNP collided, McDeLi data, non-uniform beam profile.)

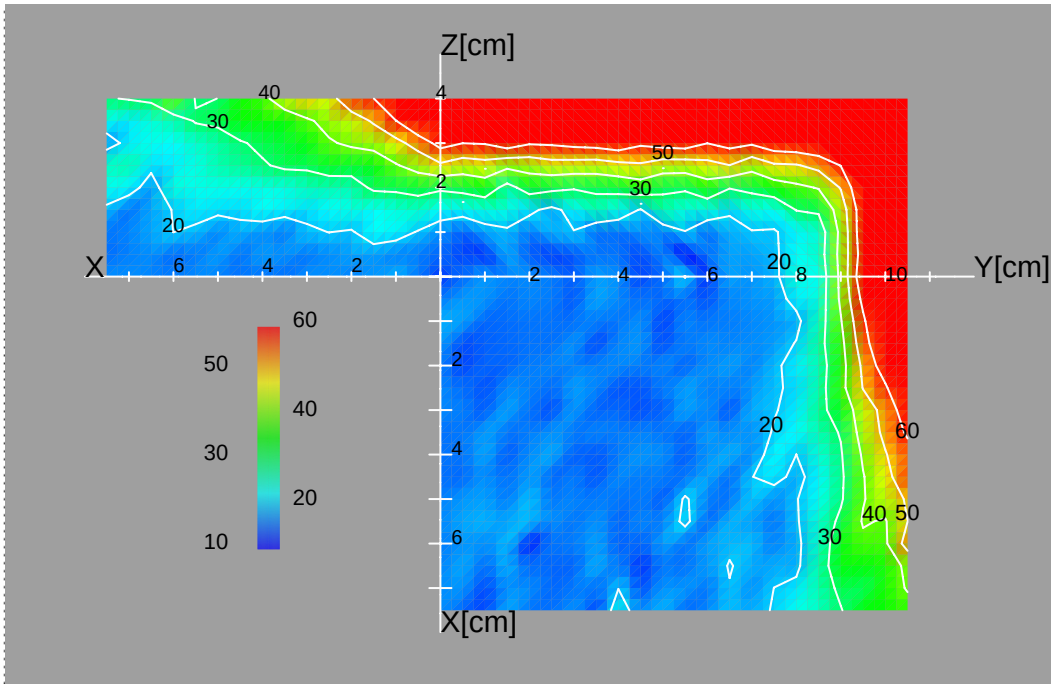

Figure 5-88 Hydrogen production gradients. The unit is % per appm/FPY/cm normalised to the total appm/FPY value. (MCNP collided, McDeLi data, non-uniform beam profile.)

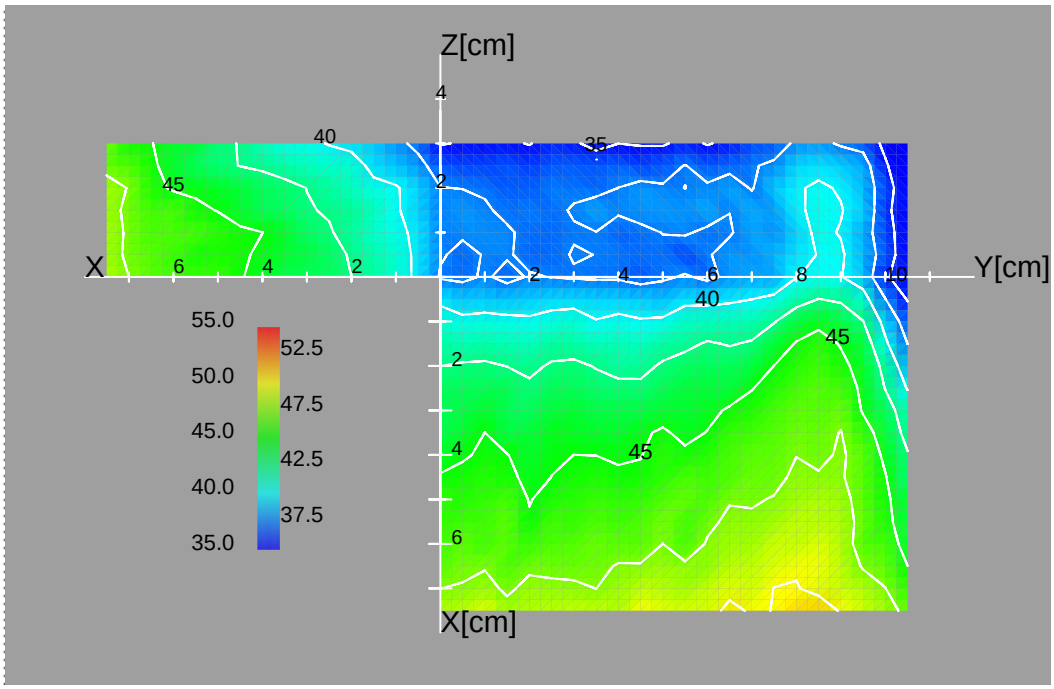

Figure 5-89 Hydrogen to DPA ratios in units of appm/DPA. (MCNP collided, McDeLi data, non-uniform beam profile.)

Helium production

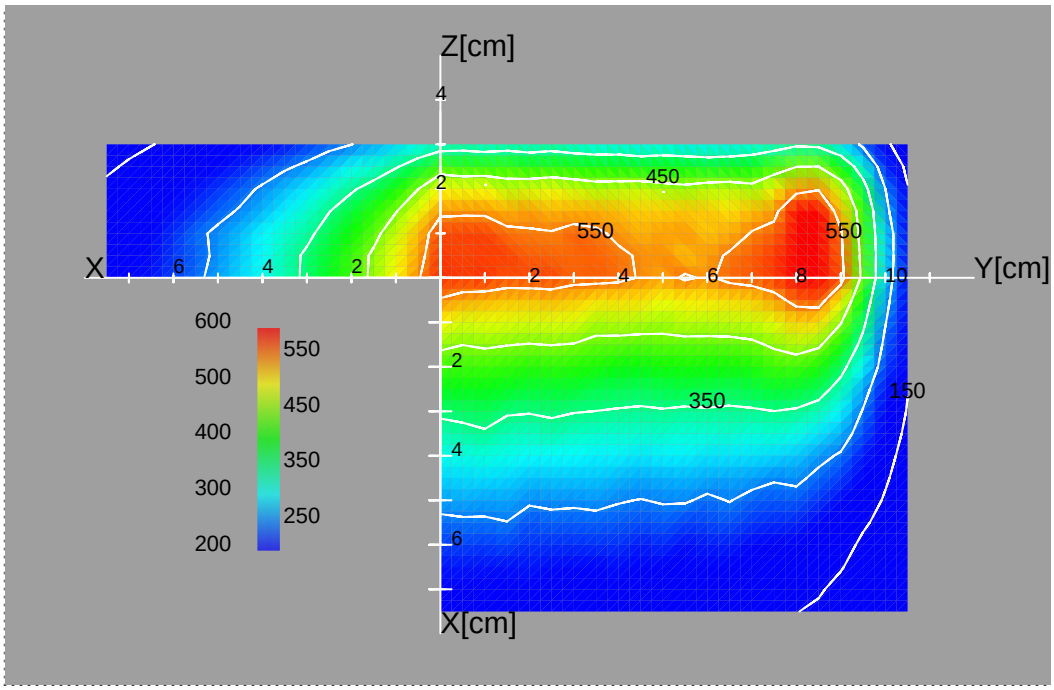

Figure 5-90 Helium production contours in units of atomic parts per million (appm) per full power year (FPY). (MCNP collided, McDeLi data, non-uniform beam profile.)

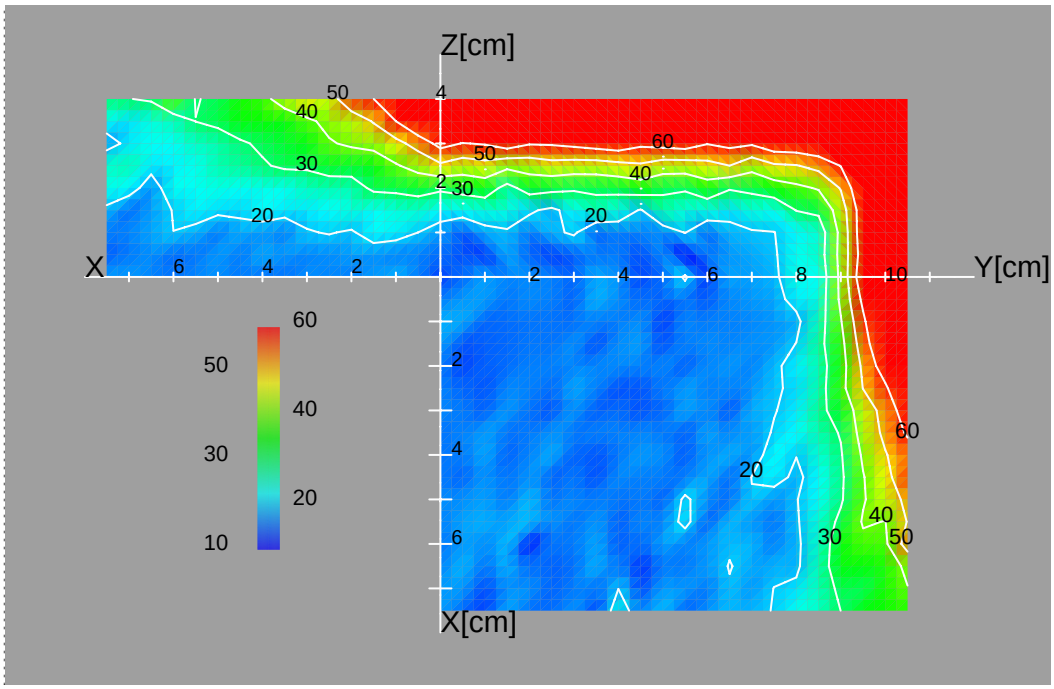

Figure 5-91 Helium production gradients. The unit is % per appm/FPY/cm normalised to the total appm/FPY value. (MCNP collided, McDeLi data, non-uniform beam profile.)

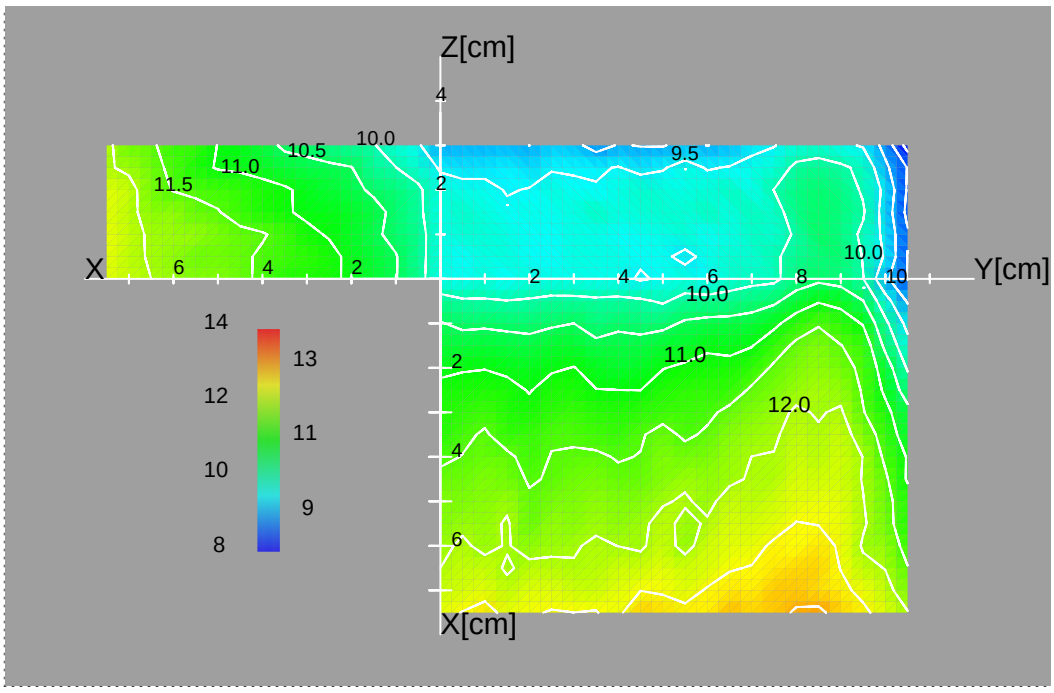

Figure 5-92 Helium to DPA ratio in units of appm/DPA. (MCNP collided, McDeLi data, non-uniform beam profile.)

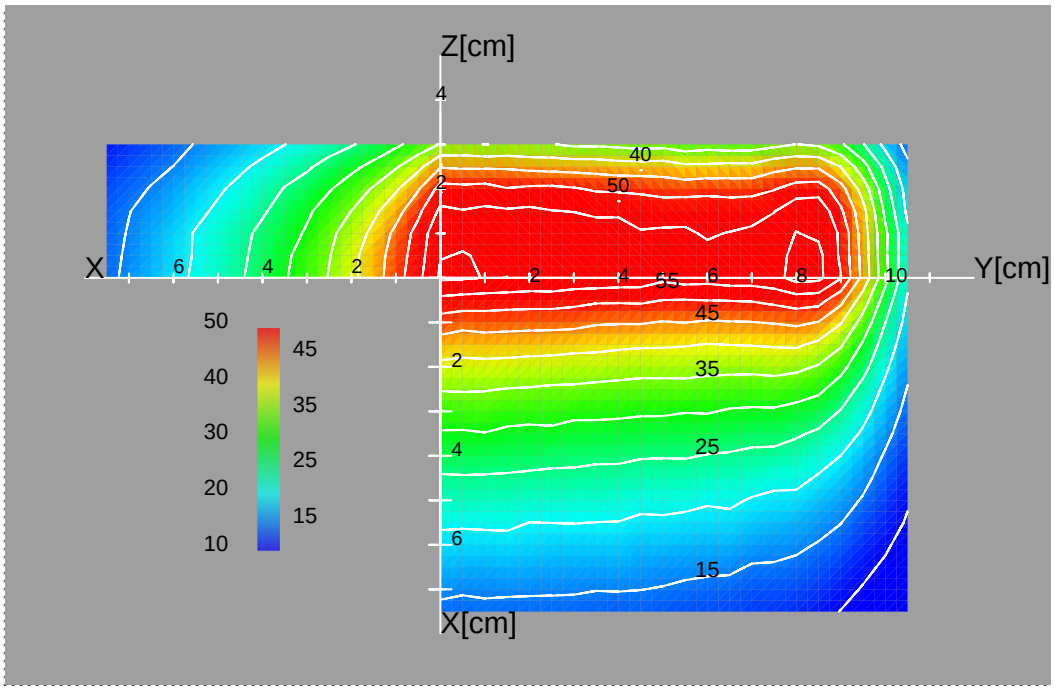

Figure 5-93 Displacement damage contours in units of DPA/FPY. (MCNP collided, McDeLi data, non-uniform beam profile.)

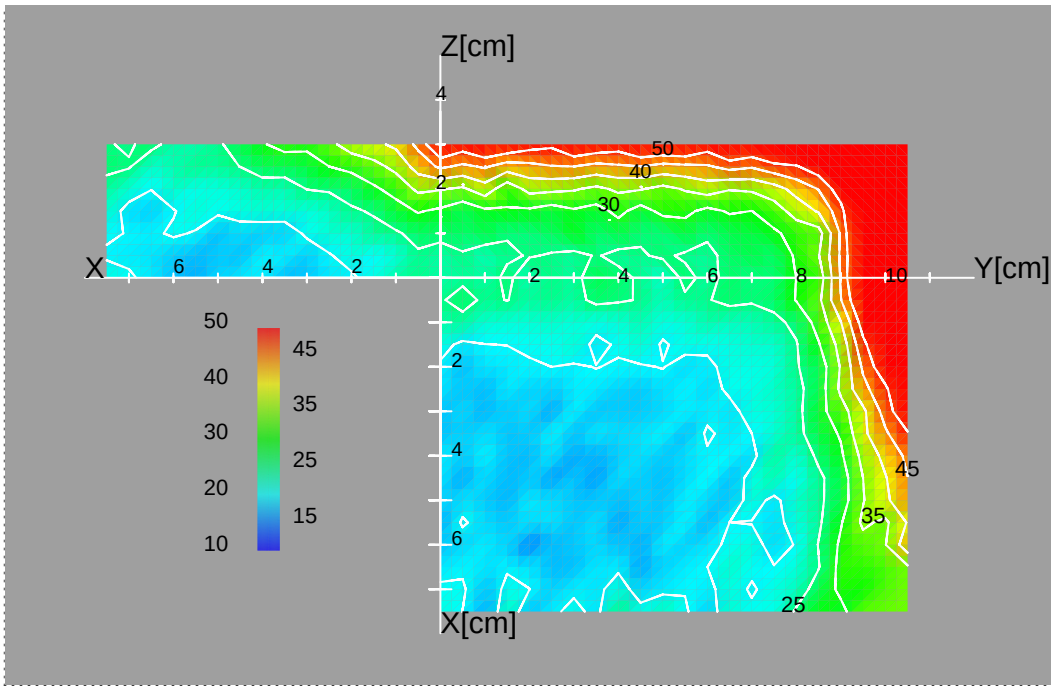

Figure 5-94 Displacement damage gradient contours. The unit is % per DPA/FPY/cm normalised to the total DPA/FPY value. (MCNP collided, McDeLi data, non-uniform beam profile.)

Irradiation volumes

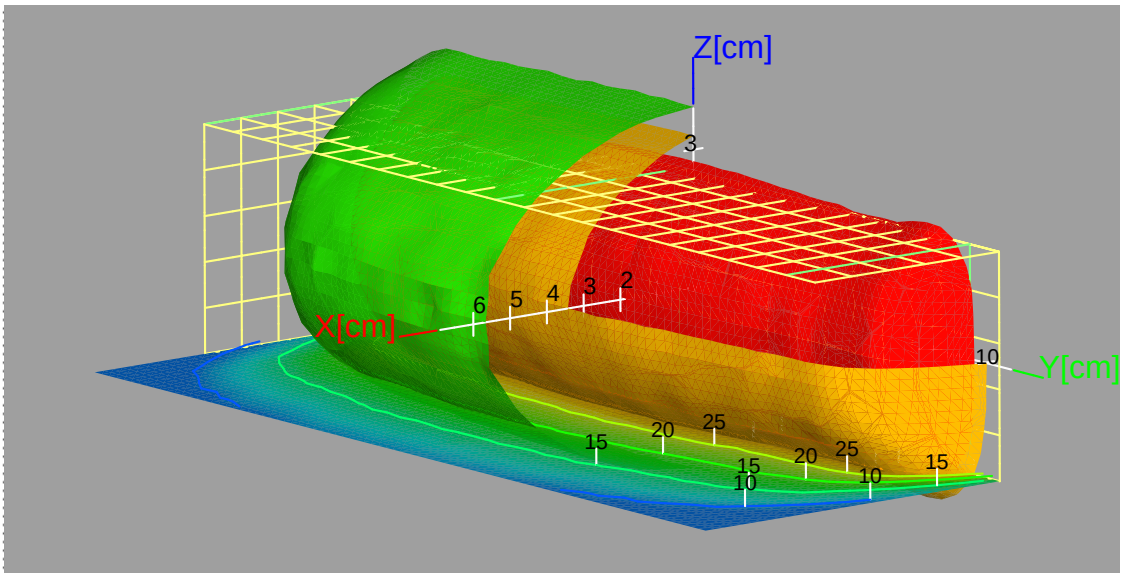

Figure 5-95 Displacement damage cutout isosurfaces. Each isosurface characterises the available volume for a DPA/FPY limit. Green = 20 DPA/FPY, yellow = 30 DPA/FPY and red = 40 DPA/FPY. The grid structure shows the physical boundary of the helium cooled high flux test module. (MCNP collided, McDeLi data, non-uniform beam profile.)

The following table shows the irradiation volumes which can achieved with collided calculations with the non-uniform beam profile and FZK n-source model.

Table 5-9 Irradiation volumes as a function of the minimum displacement damage. The third column shows the available volume inside the present design of the High Flux Test Module (HFTM).

Displacement Damage [DPA/FPY]	Total volume [cm^3]	Volume inside HFTM [cm^3]
20	590	452
30	264	242
40	110	109
50	31	31

Nuclear Heating

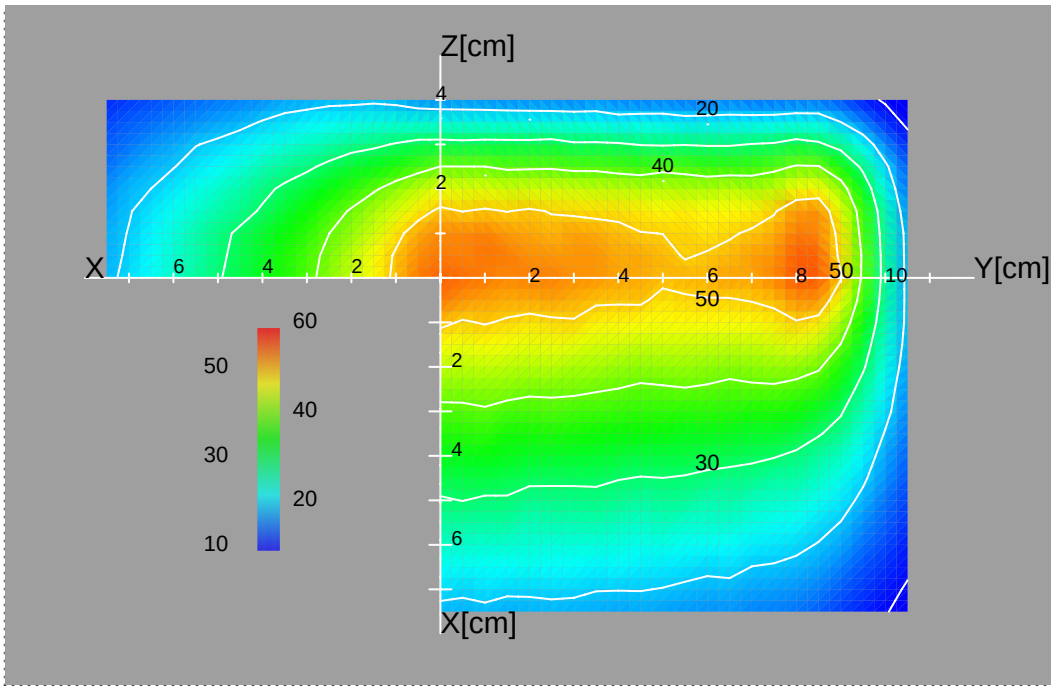

Figure 5-96 Nuclear heating contours in units of W/cm^3. (MCNP collided, McDeLi data, non-uniform beam profile.)

Wall Load

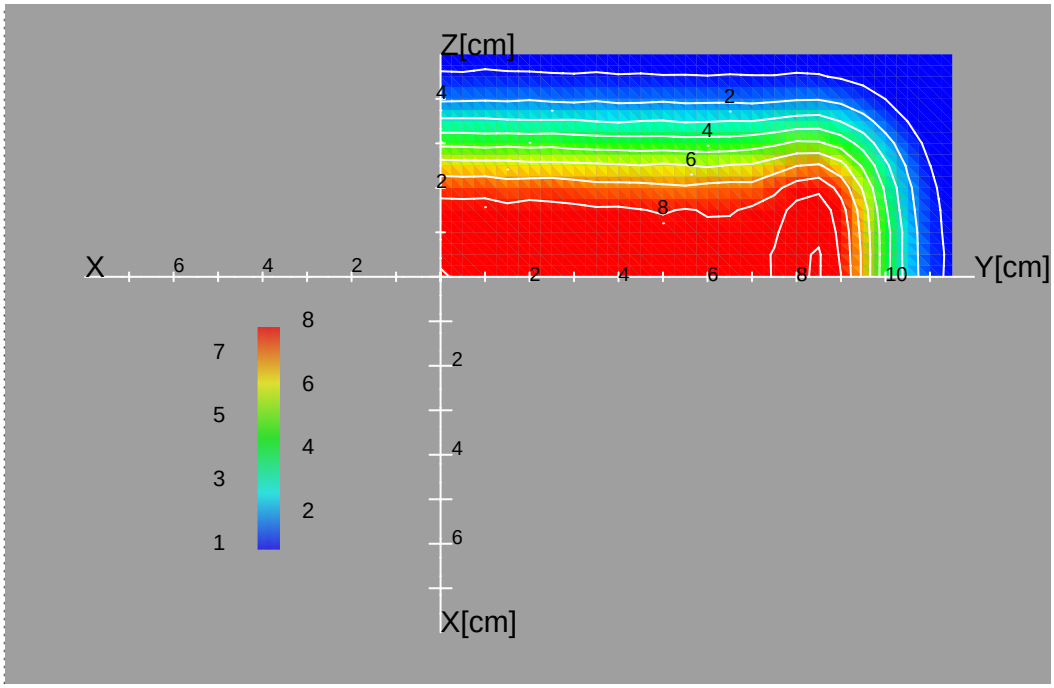

Figure 5-97 Wall load contours in units of MW/m^2. (MCNP collided, McDeLi data, uniform beam profile.)

5.4.5 Comparison of MCNP results with each other

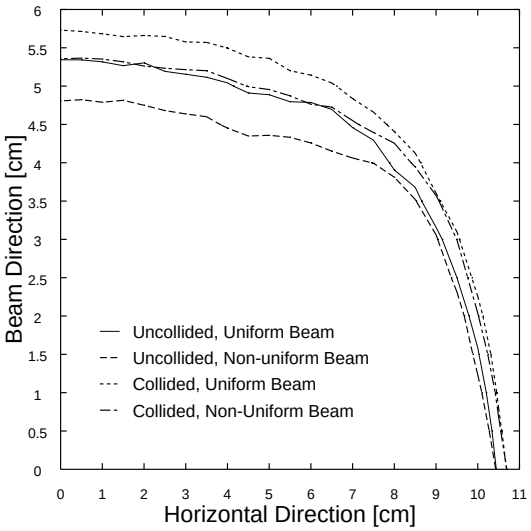

Figure 5-98 Comparison of MCNP fluxes in x-y plane.

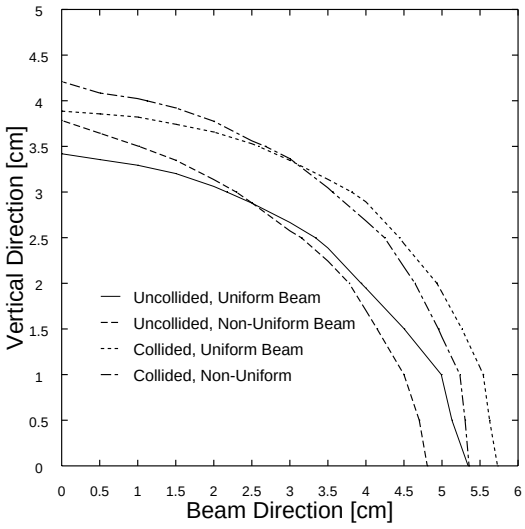

Figure 5-99 Comparison of MCNP fluxes in x-z plane.

The effect of the deuteron beam profile on the flux distribution can be easily understood in figures 5-98 and 5-99. These figures show flux contours for each case at ϕ =3 x 10^{14} n/s/cm^2. The larger beam footprint results in a lower average beam power density, and therefore a reduced flux throughout most of the test cell. This effect is shown prominently in both figures at the centre of the beam footprint (low values of y and z). The peaked edges, on the other hand, compensate for this in the horizontal direction. This can be seen in figure 5-98, where at large values of y, the contours are nearly overlapping. Finally, the beam footprint is spread greatly in the vertical (z) direction, and its effect can be seen easily in figure 5-98 at large values of z. These effects are independent of whether the test volume is empty or loaded with material.

More generally, the effect of the beam profile is obvious in all the contour plots of sections 5.4.2 and 5.4.4. In all cases, the direct influence of the peaks of the beam profile in the horizontal (y) direction can be seen. Other than the small region at those peaks and near the target, the results are lower throughout the test volume.

The effect of adding material to the test volume (collided calculation) is, in general, to increase the flux. Two physical effects are responsible for this increase: neutrons being reflected back towards the target from the material in the high flux volume and surroundings, and neutrons created by (n,2n) and (n,3n) reactions with the iron.

Closer examination of figures 5-38, 5-53, 5-68 and 5-83, however, show that the flux is not increased equally everywhere. In fact, by examining the contour at ϕ =3 x 10^{14} n/s/cm^2 in each case, it can be seen that the flux far from the target is lower in the collided calculation. This is an expected result of both of the physical effects above. The reflection of the flux towards the target will result in a greater increase in the flux nearer the target. This reflection will also decrease the flux further away from the target. The neutron producing reactions are found predominantly at higher energies. The high energy flux will also be decreased further from the target due to the collisions (see figures 5-54 and 5-84).

The dependence of the engineering response on the high energy flux can easily be seen in the effect of adding material to the test volume. In the case of neutron damage, although the

maximum damage is higher at the backplate (over 60 DPA/FPY instead of just over 55 DPA/FPY), throughout most of the test volume, the damage is lower. In the gas production cases, this effect is even more pronounced. The maximum gas production at the backplate is virtually unaffected while the downstream values are greatly reduced. The ratios of gas production to damage further show this effect. In the case of both gases, the ratio is lower for the collided calculation.

Finally, and importantly, these effects all combine to increase the gradients of all the results throughout the test volume. Ignoring the high gradients caused by edge effects at the perimeter of the beam spot, the flux gradient is up to 5%/cm greater in the collided calculation. The damage gradients are roughly 5%/cm greater and the gas production gradients are more than 5%/cm greater throughout the test volume.

5.5 Comparison of INS and MCNP results

5.5.1 Flux contour comparison

The comparison between INS and MCNP neutron flux contours is made in order to characterise the effect of the different neutron source functions on the flux distribution in the high flux test region. Involved in the comparison are the INS original data from F.M. Mann [Man91] with 6.7 % neutron yield at 40 MeV deuteron energy, the INS 'experimental' data set with 5.6 % yield at 40 MeV created by a fit to [Joh80] as already described in section 5.2 and the MCNP McDeLi source module created at FZK with 7.3 % yield at 40 MeV. In addition, to make the neutron flux contours more comparable the 'experimental' INS and the McDeLi MCNP source functions are scaled to 6.7 % total yield. This comparison at the identical neutron yield value allows the identification of further differences in the neutron source functions. The data discussed are calculated for the uniform beam profile and the uncollided case.

In figure 5-100 the behaviour in the x-y-plane is shown. The equi-flux contours plotted lie at 4 x 10^{14} n/s/cm^2. In downstream direction (beam direction x) the largest difference can be recognised. The MCNP (Y = 7.3 %) shows the largest distance while the 'experimental' INS (Y = 5.6 %) shows the smallest. It shows also that with 1.7 % additional yield about 2 cm more distance can be gained. Much more interesting is the fact that at 6.7 % yield the MCNP and 'experimental' INS lie close together while the INS original lies at a smaller distance. At large lateral locations (large y values) the contour lines are very close together.

The neutron flux contour comparison in the x-z-plane is shown in figure 5-101. Again, the equi-flux contours plotted lie at 4 x 10^{14} n/s/cm^2. At large z values the MCNP (Y = 7.3 %) is much stronger than INS 'experimental' (Y = 5.6 %). The comparison of the Y = 6.7 % contour lines, however, shows much more interesting results. As in fig. 5-100, the MCNP and 'experimental' INS results lie together in the beam direction, and are beyond the original INS result. However, in the vertical direction both INS results are less than the MCNP result.

Figure 5-102 shows the neutron flux on the centreline of the high flux test region. Most interesting in this plot is the comparison between the data scaled to 6.7 %. There is a discrepancy between the two INS data sets dependent on the distance from the target. This result is due to the difference in the angular yield distributions as shown in figure 5-2. The McDeLi results match the INS 'experimental' results closely. However, there are differences in the input parameters for these two cases, such as angular yield distribution and beam opening angle.

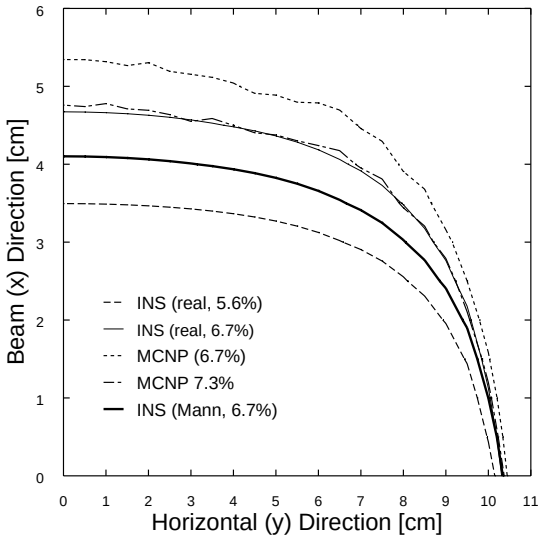

Figure 5-100 Comparison of fluxes in X-Y plane.

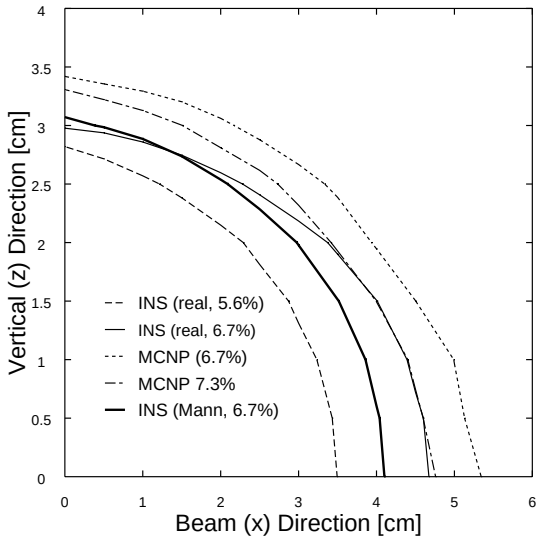

Figure 5-101 Comparison of fluxes in X-Z plane.

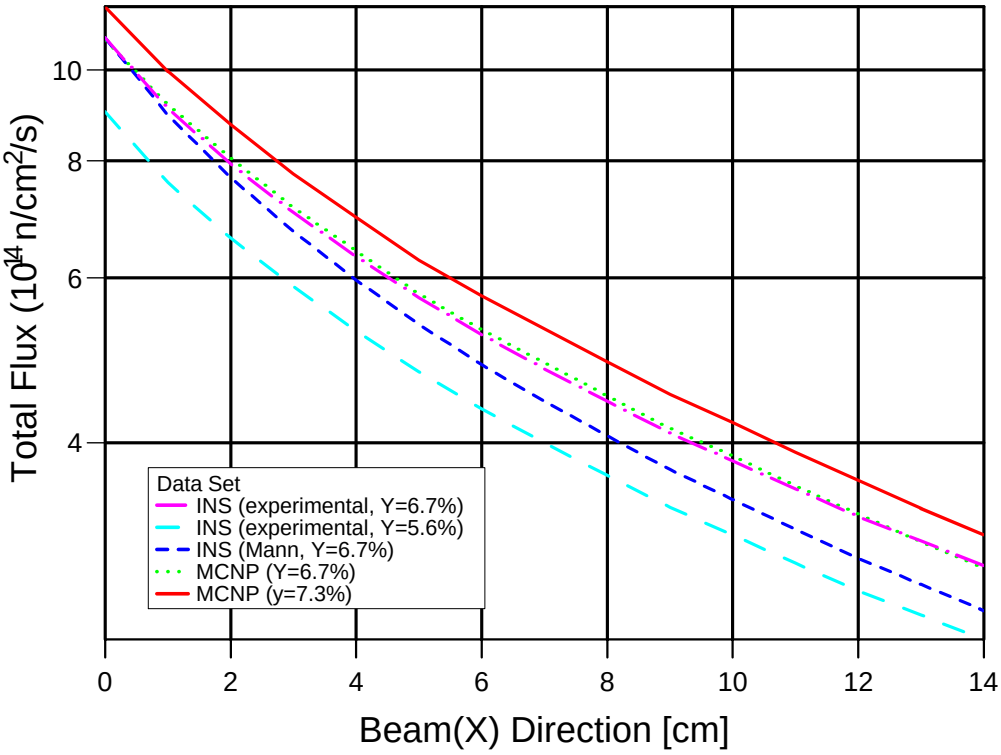

Figure 5-102 Neutron flux on centreline of test facility in beam direction.

Figures 5-103 and 5-104 show the total neutron flux and high energy flux (E_n >14 MeV), respectively, but normalised to the total percent yield. It is important to note that although the total flux per % yield show general agreement between the two data sets, the high energy flux of the McDeLi results is much lower than that of the INS 'experimental' result.

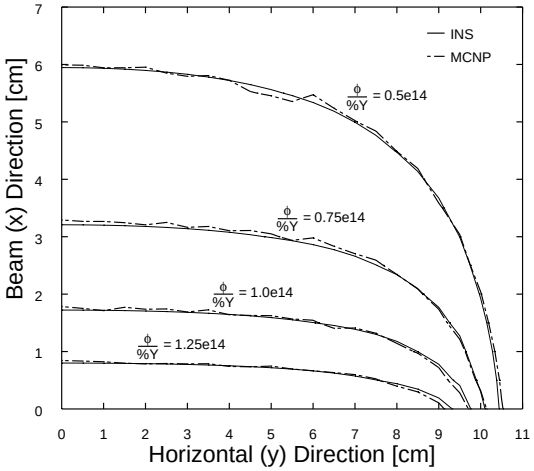

Figure 5-103 Flux normalised to percent yield.

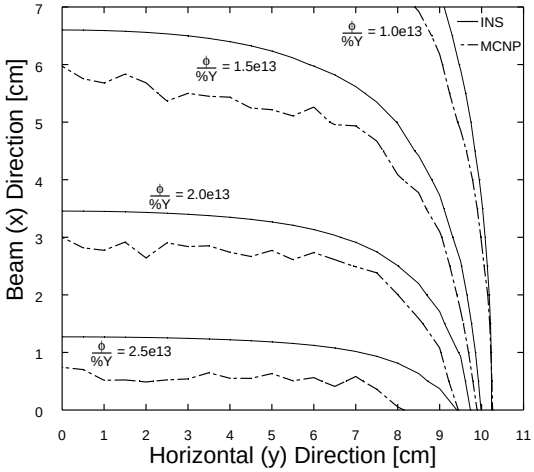

Figure 5-104 Flux with E_n > 14 MeV normalised to percent yield.

5.5.2 Normalised response contour comparison

Figures 5-105 through 5-107 show the engineering responses normalised to the total percent yield. Although the total neutron fluxes of the two data sets are very similar and the relevant (high energy) domain of the displacement cross-section is identical, the MCNP DPA results are larger than the INS 'experimental' result. This can only be explained by differences between the MCNP and INS neutron spectrum distributions.

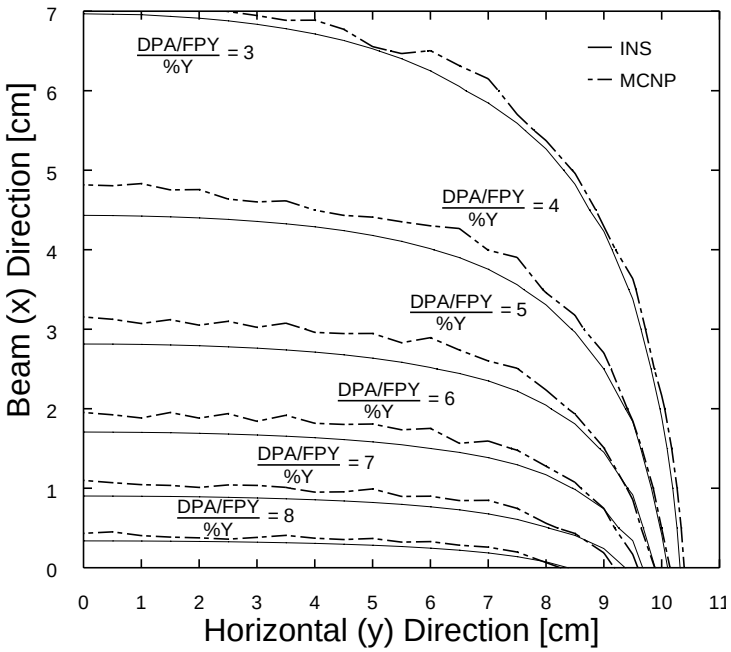

Figure 5-105 DPA/FPY normalised to percent yield.

The H- and He results show a more significant difference between the two results due to the differences in the high energy domains of the respective production cross-sections. Although there are spectral distribution effects, the similarity of the statistical variations in the MCNP results of figs. 5-104, 5-106 and 5-107 confirms that the primary cause is the data discrepancy. The reversal near the target in fig. 5-106 is believed to be caused by a softening of the spectrum.

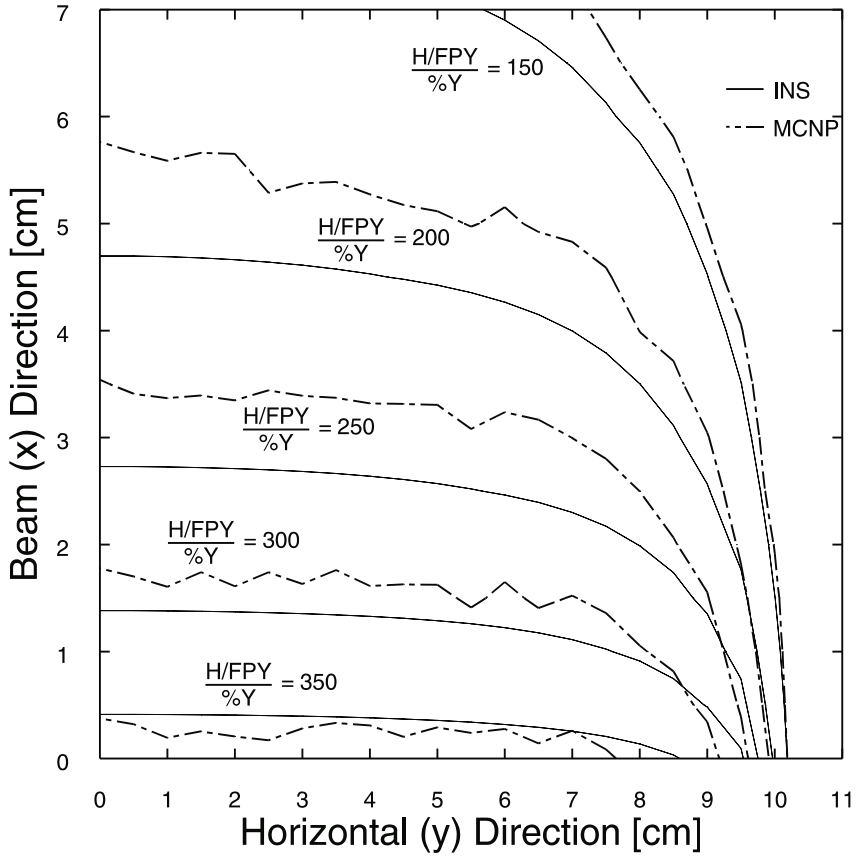

Figure 5-106 H production normalised to percent yield

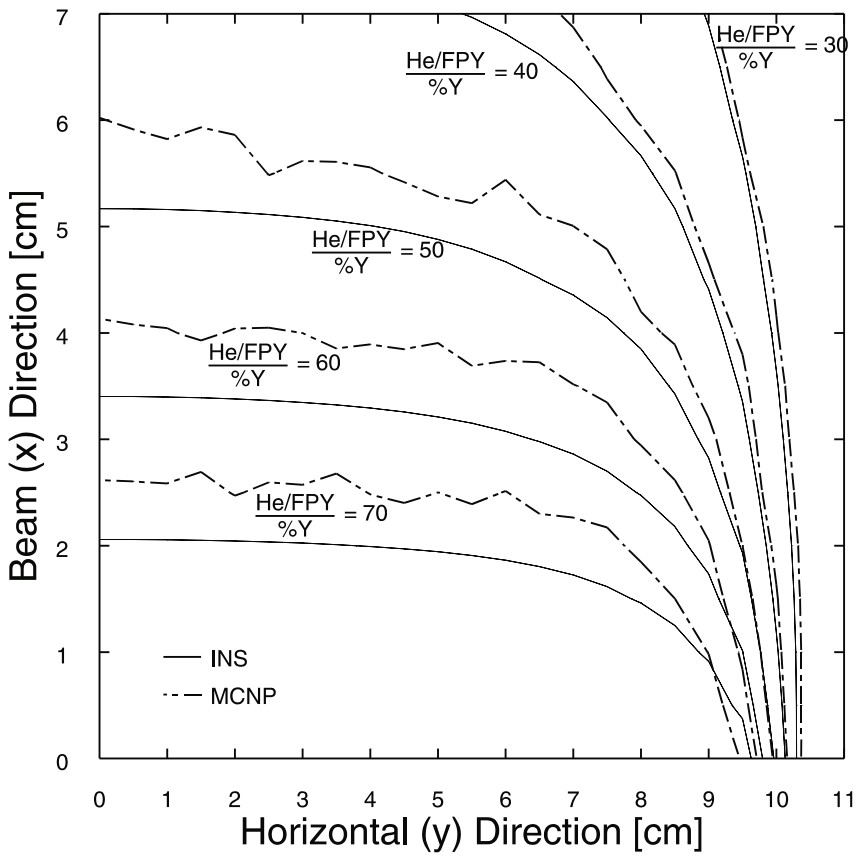

Figure 5-107 He production normalised to percent yield

5.5.3 Irradiation volume comparison

A summary of the irradiation volumes for damage rates higher than 20 DPA/FPY is presented in table 5-10. In this case, as with the preceding data, the original INS [Man91] is used. The maximum available volume, regardless of material loading, is >700 cm^3. This volume is limited by the current design of the high flux test module to just under 500 cm^3. However, in the case of a fully loaded test module (roughly 50% iron), the total available volume is reduced to almost 600 cm^3, with only about 450 cm^3 inside the current HFTM design.

Table 5-10 Comparison of volumes for displacement damage of > 20 DPA/FPY

	Total volume [cm^3]	Volume inside HFTM [cm^3]
INS, uniform	466	419
INS, non-uniform	451	389
MCNP, uniform, uncollided	732	478
MCNP, non-uniform, uncollided	716	480
MCNP, uniform, collided	594	460
MCNP, non-uniform, collided	590	452

The comparison between the MCNP and INS 'experimental' irradiation volumes in figure 5-108 (> 20 DPA/FPY) clearly shows a large difference due to the effect of the beam opening angle. Furthermore, the significance of the useful volume outside the HFTM can be seen. Since the current design of the helium-cooled HFTM is a rectangular box with a volume of 0.5 litres, the fraction of the total ellipsoidal irradiation volume (top curve) which lies inside this box (bottom curve) is seriously reduced. Even at 6% yield, where the total volume is approx. 0.5 litres the volume loss is about 15%.

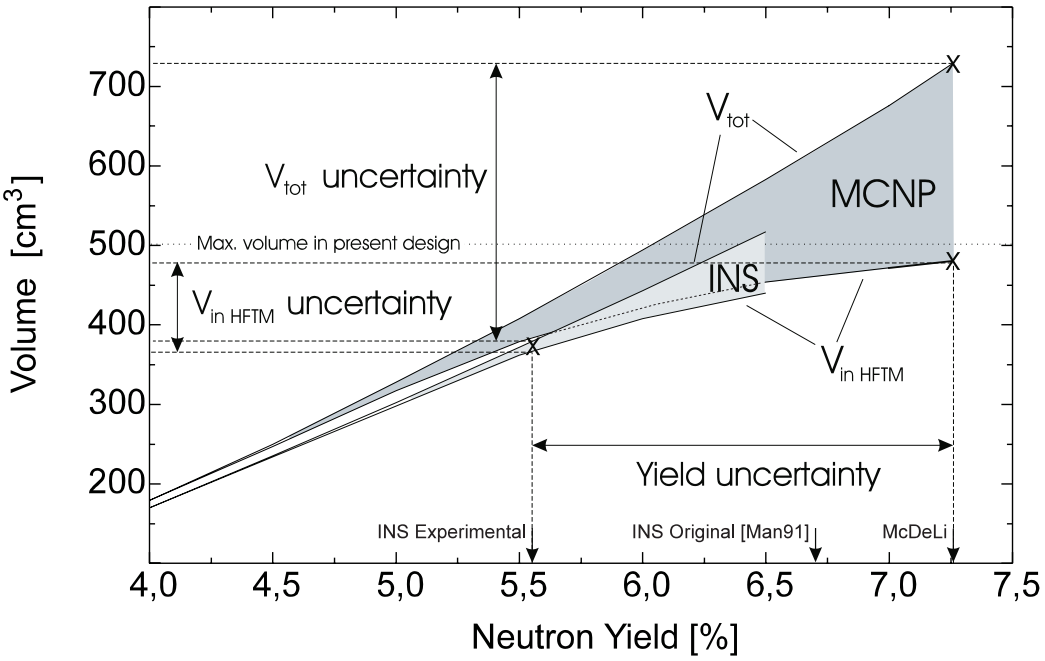

Figure 5-108 Irradiation volume for displacement damage > 20 DPA/FPY as a function of the total neutron yield (uncollided calculations MCNP and INS 'experimental').

Most important, however, is the impact of the neutron yield and its uncertainty. The total neutron yield uncertainty (0.056 to 0.073 n/d) representative of the data sets used in this report corresponds to a total volume uncertainty of 350 cm^3 (380 cm^3 to 730 cm^3).

5.6 Conclusions from INS / MCNP comparison

The comparison of the neutron flux contours (figs 5-100 and 5-101) shows that although MCNP and INS employ different methods, they are both useful tools for determining the neutron behaviour and responses of the high flux test region. The ability of MCNP to perform collided calculations and account for the beam opening angle makes it a more powerful tool than INS, which can provide quick initial results.

The variation in the results amongst the different neutron yield data sets leads to the conclusion that the total neutron yield is very important, moreso than, and somewhat independent of, the angular neutron yield distribution. The yield distribution, however, is also important, as evidenced by the variation between the INS 'experimental' and INS original results and the discrepancy between the INS 'experimental' and MCNP results in the normalised high energy flux contours (fig. 5-104).

In the gas production cases, the importance of the accuracy of the neutron response data is demonstrated. The differing gas production cross-sections given in chapter 3 result in greatly differing normalised gas production rates.

Above all, these analyses and comparisons demonstrate the need for further development and understanding of the neutron source model and the nuclear response data. These uncertainties combine to significantly influence one of the main engineering parameters, the total irradiation volume. It is vital that these uncertainties be reduced in order to achieve a useful irradiation facility.

Finally, the current HFTM design grossly underutilises the available irradiation volume. In the best case, 15% of the available volume is excluded from the rectangular test assembly, and in the worst case more than 1/3.

5.7 Applications to real geometries and comparison to fusion reactor conditions

In this section, a comparison is made between the nuclear performance of real IFMIF high flux test modules and typical fusion reactor conditions. For that purpose, MCNP transport calculations were performed for two alternative test modules, a helium and a NaK cooled one, designed for irradiation tests in the IFMIF high flux test region, and two fusion reactor models, the International Thermonuclear Experimental Reactor (ITER) and the European Demonstration power reactor (DEMO).

For IFMIF, detailed three-dimensional models of the test module have been developed on the basis of the available technical design concepts [Mös95, Mae96]. The test module dimensions amount to 50 mm × 50 mm × 200 mm (depth in beam direction × height × width). In the models, the high flux test modules are placed behind the target back wall consisting of a 1.6 mm thin steel layer. The source neutron sampling, beam parameters, target set up and other parameters are the same as specified in section 5.1.3. For the beam profile the non-uniform distribution is used.

Calculations were performed to assess the neutron flux and spectrum distribution across the test modules and to obtain important nuclear responses like the gas production rates (hydrogen, helium), the accumulated displacement damage and the nuclear heating (in terms

of W/cm^3). The data reported in the following have been averaged over a vertical height of $\pm$ 1 cm around the horizontal mid-plane (x-y plane). The calculated responses thus are for the highest loaded part of the test modules. In each case the number of source neutron histories amounts to about 8 million events resulting in statistical accuracies of less than 1% for the calculated responses.

For the comparison with fusion reactor conditions, three-dimensional MCNP models of ITER [Fis94] and the European Demo reactor [Dal94, Dal94a] have been used to assess the neutron fluxes, DPA and gas production rates at the first wall. In those cases, the neutron wall loading has been set to 2 MW/m^2 .

5.7.1 Fusion reactor calculations

Calculations were performed with the MCNP-code using three-dimensional models developed previously for ITER and the European DEMO reactor, see figs. 5-109 and 5-110 for vertical cross-sections of the models. For ITER, a water-cooled shielding blanket is assumed in the model, while for the DEMO reactor a helium-cooled breeder blanket with a beryllium neutron multiplier is applied. Neutron fluxes, spectra, DPA and gas production rates were calculated for the ITER inboard and DEMO outboard first wall. The normalisation is for a neutron wall loading of 2 MW/m^2 (inboard and outboard first wall) in each case.

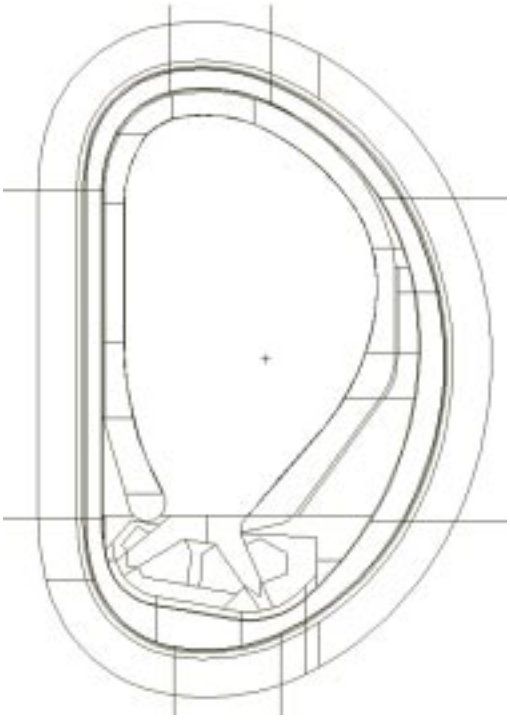

Figure 5-109 Vertical cross-section of the MCNP torus sector model for ITER with shielding blanket modules.

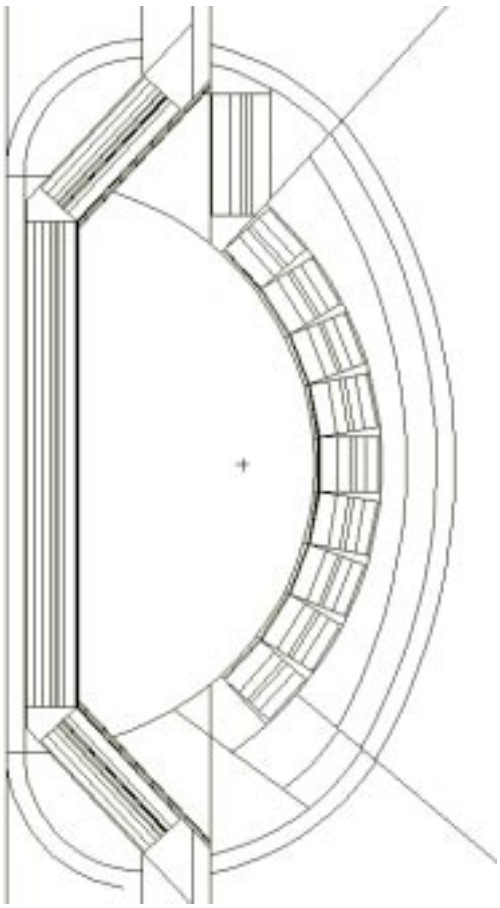

Figure 5-110 Vertical cross-section of the MCNP torus sector model for the European Demo reactor with breeder blanket modules.

Table 5-11 shows the data for the uncollided neutron current density (the number of source neutrons incident on the first wall divided by the surface area), the uncollided neutron flux density and the actual (i.e. collided) total neutron flux density at the first wall of ITER and Demo. The neutron wall loading gives the power per unit area (in terms of MW/m²) loaded onto the first wall by the incident (uncollided) source neutrons (for further definitions see Appendix). In the table, the corresponding data are included for IFMIF (first wall of test module, averaged over the full width and a vertical height of ± 1 cm). Note that the maximum neutron wall loading for IFMIF is higher than for Demo/ITER by about a factor 4 while the resulting total neutron flux density is higher by less than a factor 2. Consequently, IFMIF applies a twice as high neutron wall loading at the same total neutron flux density at the first wall as a fusion reactor of the ITER/Demo type.

Table 5-11 Neutron wall loading, first wall flux and current densities in ITER, DEMO and IFMIF.

	W_L[MW/m^2]	J_{un}[cm^{-2} s^{-1}]	ϕ_{un}[cm^{-2} s^{-1}]	ϕ_{tot}[cm^{-2} s^{-1}]
ITER	2.0	$8.88 \cdot 10^{13}$	$1.44 \cdot 10^{14}$	$8.00 \cdot 10^{14}$
DEMO	2.0	$8.88 \cdot 10^{13}$	$1.15 \cdot 10^{14}$	$7.14 \cdot 10^{14}$
IFMIF *midplane*[*]	8.5	$6.17 \cdot 10^{14}$	$9.63 \cdot 10^{14}$	$1.14 \cdot 10^{15}$
IFMIF *averaged**	6.1	$3.70 \cdot 10^{14}$	$6.32 \cdot 10^{14}$	$7.52 \cdot 10^{14}$

Table 5-12 Displacement damage and gas production rates in ITER, DEMO first wall and IFMIF.

	Damage prod. [DPA/FPY]	**He-prod. [appm/FPY]**	**H-prod. [appm/ FPY]**	**He/DPA [appm/DPA]**	**H/DPA [appm/DPA]**
ITER	20	230	891	11.5	45
DEMO	17	180	709	10.6	42
IFMIF *midplane**	57	553	2145	9.6	37.4
IFMIF *averaged**	37	339	1320	9.2	35.8

[*] Note: *IFMIF midplane* is for averages over a vertical height of +/- 1 cm of the test module first wall.
IFMIF average is for the full first wall area of the test module, i.e. 5 cm x 20 cm.

DPA and gas production data are displayed in table 5-12 for natural iron irradiated in the mentioned first wall spectra of ITER and DEMO and ^{56}Fe in the first wall of the IFMIF test module. The fusion reactor data are again normalised to a neutron wall loading of 2 MW/m² and a total operation time of one year (i.e. 1 FPY). As compared to the high flux test region of IFMIF, the DPA and gas production rates are lower by a factor 2-3, but the gas production/DPA ratio is at the same level for both types of facilities/spectra.

5.7.2 Detailed calculations for the IFMIF helium-cooled test module

A detailed MCNP model was set up for the helium cooled test module to enable full three-dimensional transport and response calculations. Fig. 5-111 shows a horizontal cross-section of the test module model including the cell number designations used below. Representative results are displayed in table 5-13 for the neutron flux density and some relevant nuclear responses in the designated cells of the helium cooled test module. The data are again averaged over a vertical height of ± 1 cm around the horizontal mid-plane. With the assumed beam parameters, the total neutron flux density is typically in the order of several 10^{14} cm^{-2} s^{-1}. Note that this is the same order of magnitude that is achieved in the first wall of a typical (d,t) fusion reactor at a neutron wall loading of about 2 MW/m^2 (cf. table 5-11 above) whereas both the nuclear heating, the DPA and gas production rates are higher by about a factor 2. Nuclear heating in the iron of the test module comes mainly from neutron induced reactions. Only about 1/3 of the heating originates from photon interactions. Note that for a typical fusion reactor the opposite appears, i.e. about 2/3 of the nuclear heating in the steel structure is due to photon and 1/3 to neutron interactions.

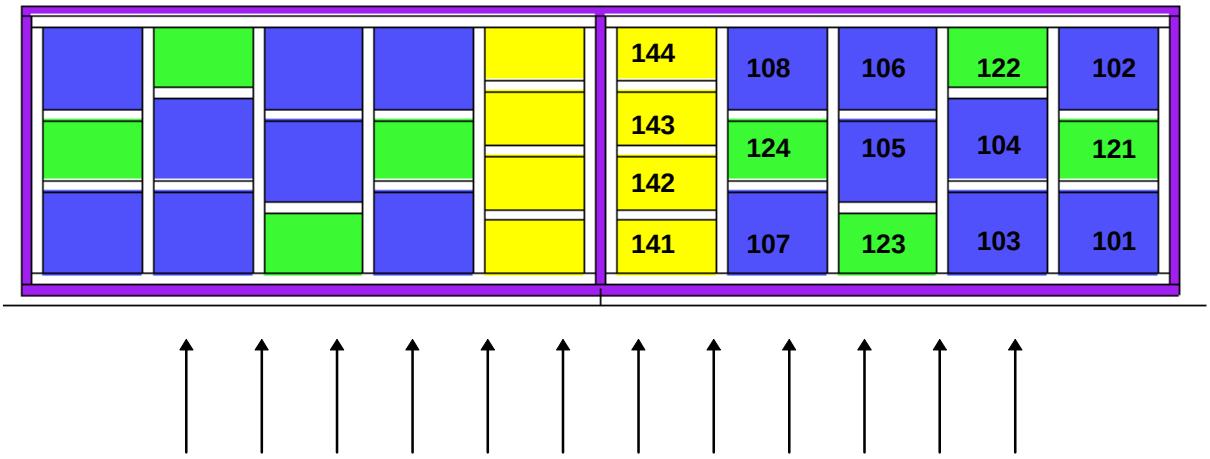

Figure 5-111 Horizontal cross-section (*x-y* plane) of the helium cooled test module (MCNP model with assigned cell numbers). The arrows show the beam direction.

Table 5-13 Neutron flux, DPA, gas production rates and nuclear heating in the helium cooled test module (averaged over ± 1 cm around the horizontal mid-plane).

Cell #	DPA/FPY	Neutron flux density [10^{14}cm^{-2}s^{-1}]	Helium production per FPY		Hydrogen production per FPY		Nuclear heating [W/cm^3]
			appm	He/DPA	appm	H/DPA	
141	47.3	9.18	492	10.4	1910	40.4	49.3
142	37.0	7.02	410	11.1	1590	43.1	42.3
143	29.4	5.48	340	11.6	1320	45.0	35.6
144	23.3	4.23	281	12.0	1090	46.9	29.0
107	43.8	8.56	457	10.4	1780	40.6	47.4
124	31.7	6.07	353	11.1	1370	43.4	38.0
108	23.4	4.35	274	11.7	1070	45.6	29.3
123	44.5	8.70	459	10.3	1790	40.1	47.0
105	32.1	6.15	357	11.1	1390	43.3	38.3
106	22.4	4.15	266	11.9	1030	46.2	28.4
103	42.8	8.16	462	10.8	1800	42.0	46.6
104	28.7	5.32	333	11.6	1300	45.3	35.0
122	20.3	3.63	251	12.4	978	48.2	26.0
101	34.4	6.42	381	11.1	1480	43.1	37.6
121	23.3	4.27	274	11.8	1070	45.9	28.2
102	20.3	2.94	201	9.9	782	38.5	20.7

In contrast to fusion reactor conditions, the gas production in the IFMIF spectrum comes mainly from the energy range above 15 MeV although the share of the spectrum is not more than 15 %. This is due to the many reaction channels that are open at those high energies producing more than one α-particle and/or proton in the exit channel. In case of the DPA, about one third of the total is produced above 15 MeV neutron energy. Nevertheless, the helium/DPA and the hydrogen/DPA ratios are in the same range of magnitude as for ITER and DEMO. In this respect, the irradiation conditions in the IFMIF high flux region appear to be fairly well suited for simulating fusion reactor conditions.

Table 5-14 Spectral decomposition [%] of the neutron flux, DPA and gas production rates in the helium cooled test module.

	Neutron flux	DPA	He production	H production
E ≤ 0.1 MeV	0.06	-	-	-
0. 1 -1 MeV	14	4	-	-
1 - 5 MeV	45	31	0.2	-
5 - 15 MeV	26	34	29	27
E > 15 MeV	15	31	71	73

5.7.3 Detailed calculations for the IFMIF NaK-cooled test module

Analogous to the helium cooled test module, a detailed MCNP model has been set up for the NaK cooled test module to enable detailed three-dimensional calculations. Fig. 5-112 shows a horizontal cross-section of the corresponding model with the cell number designations used below. Representative results are displayed in table 5-15 for the neutron flux density and some nuclear responses in the designated cells of the NaK cooled test module. Averaging is again performed over a vertical height of ± 1 cm around the horizontal mid-plane. Both, the neutron flux density and the nuclear responses with their spectral decomposition are very similar to those for the helium cooled test module. Thus there is no large impact of the NaK coolant on the neutron spectra in the test module. This is due to the large average neutron mean free path as compared to the small dimensions of the high flux test module.

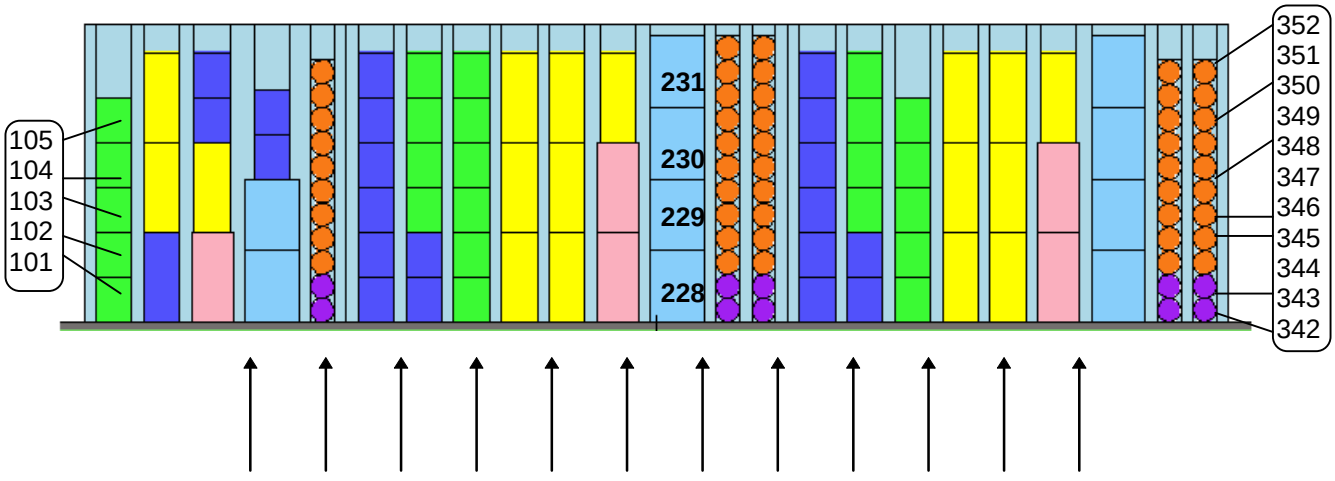

Figure 5-112 Horizontal cross-section (*y*-*x*-plane) of the NaK cooled test module (MCNP model with assigned cell numbers). The arrows show the beam direction.

Table 5-15 Neutron flux, DPA, gas production rates and nuclear heating in the NaK cooled test module (averaged over ± 1 cm around the horizontal mid-plane).

Cell #	DPA/FPY	Neutron flux density [10^{14}cm^{-2}s^{-1}]	Helium production per FPY		Hydrogen production per FPY		Nuclear heating [W/cm^3]
			appm	He/DPA	appm	H/DPA	
101	42.9	7.84	465	10.8	1810	42.2	38.9
102	34.0	5.97	395	11.6	1540	45.3	33.2
103	27.9	4.78	337	12.1	1315	47.1	28.5
104	23.2	3.90	264	11.4	1124	48.4	24.2
105	19.6	3.22	251	12.8	978	49.9	20.8
228	48.2	9.07	506	10.5	1966	40.8	42.7
229	37.5	6.71	427	11.4	1662	44.3	36.3
231	29.8	5.10	361	12.1	1406	47.2	30.6
232	24.2	3.98	310	12.8	1207	49.9	25.7
342	43.5	7.97	470	10.8	1825	42.0	38.1
343	38.4	6.83	434	11.3	1687	43.9	35.3
344	34.4	6.04	399	11.6	1551	45.1	32.8
345	30.9	5.34	369	11.9	1435	46.4	30.5
346	28.0	4.77	341	12.2	1330	47.5	28.4
347	25.8	4.34	318	12.3	1241	48.1	26.4
348	23.4	3.91	296	12.6	1151	49.2	24.6
349	21.3	3.52	273	12.8	1062	49.9	22.7
350	19.4	3.17	251	12.9	975	50.3	20.7
351	17.7	2.85	232	13.1	902	51.0	19.0
352	16.2	2.59	213	13.1	830	51.2	17.3

Table 5-16 Spectral decomposition [%] of the neutron flux, DPA and gas production rates in the NaK cooled test module.

	Neutron flux	DPA	He production	H production
E ≤ 0.1 MeV	0.4	-	-	-
0. 1 -1 MeV	12	3	-	-
1 - 5 MeV	45	31	0.1	-
5 - 15 MeV	27	35	29	28
E > 15 MeV	15	31	71	72

6. Summary and recommendations

A comprehensive development programme has been performed to provide computational tools and nuclear data for enabling neutronics design analyses of IFMIF.

As part of this, nuclear data evaluations were performed for the major structural material and coolant nuclides for neutrons with incident energy up to 50 MeV. Subsequently, using the NJOY processing code, data files for use in neutronics calculations with the MCNP Monte Carlo code were produced from the evaluated data. Further updates and extensions of the data library are required and will be added step by step according to the needs within the IFMIF project and the availability of the necessary resources.

A major part of the work was devoted to the development of a d+Li neutron source routine suitable for use with the MCNP code. This has been achieved on the basis of a semi-empirical model for the d+Li nuclear interaction together with experimental thick-target data. The model is very flexible with respect to the configuration of the lithium target and the deuteron beams. It can easily be adapted to design modifications or facilities other than IFMIF.

Using these prerequisites, comprehensive 3-dimensional neutronics calculations were performed for the IFMIF high flux test region to assess the available high flux test volumes, flux gradients and contours, gas production and displacement rates. These results were compared to those obtained by uncollided neutronics calculations with the INS code. In addition, the uncertainty of the neutron yield and its impact on the available high flux test volume was assessed by comparisons between MCNP calculations using the new source routine and INS calculations using previous cross-section data. The neutron yield of the different models varies between 0.056 and 0.073 neutrons per incident deuteron, an uncertainty margin which results in a 350 ml uncertainty of the high flux test volume (i.e. the volume in which, for iron, 20 DPA/FPY or more are attained, uniform beam profile, uncollided calculation).

Detailed 3-dimensional neutronics calculations were further performed for two alternative conceptual designs of IFMIF high flux test modules (helium and NaK cooled) and compared to realistic conditions in the typical fusion reactors ITER and DEMO.

In total, the results presented in this report have a double function: to give detailed insight into the neutronics of the IFMIF conceptual high flux test region, and to demonstrate the present status of methods and data bases for IFMIF neutronics calculations in general. Any realistic loading of a high flux test module, helium or NaK cooled, can be calculated. The same methods can be applied to the medium, low and very low flux regions.

Currently, limitations exist with respect to (1) nuclear data for further nuclides and (2) the uncertainty of the neutron source yield. The library of nuclear data evaluations needs to be completed. The neutron source yield needs to be ascertained by further simulation experiments. Theoretical refinements of the calculational source model will be made with respect to the spectral shape and possibly the angular distribution, however, the model will always require experimental calibration as far as absolute yield is concerned.

A field not yet addressed is the activation of both structures and test samples in IFMIF. Due to the high energy tail of the spectrum, increased activation is expected to result in differences from a fusion reactor environment. State-of-the-art calculational tools for detailed activation calculations are available, but only for neutron energies up to 20 MeV. Therefore, the nuclear data base must be complemented by the corresponding high energy activation cross-sections.

A few lessons learned from this work may be mentioned specifically:

The comparisons with fusion reactor calculations show that the IFMIF high flux test region is very well suited to meaningful material tests within fusion development programs.

The original neutronics specifications for the high flux test region can be met in most cases, the main exception being the neutron flux gradient.

The expectation that the high energy tail of the neutron spectrum, which constitutes the main difference from a fusion reactor spectrum, strongly enhances certain responses, notably the gas production and the displacement damage, is confirmed.

By redesigning the high flux test modules, the utilisation of the available $\geq$ 20 DPA/FPY test volume can be greatly improved.

The neutron yield uncertainty needs to be reduced by further simulation experiments and by a genuine evaluation of the d+Li neutron emission cross-section data, which currently is missing.

The nuclear data evaluation work needs to be extended to more nuclides and to activation cross-sections.

Appendix

Normalisation and Conversion Factors for MCNP tallies

This section summarises the normalisation and conversion factors used for converting the MCNP tallies to real physical quantities.

Normalisation factor

The MCNP tallies refer to one source neutron. For normalising to absolute quantities, the tallies have to be multiplied by the total number of neutrons generated per second:

$$N_\phi\ [\mathrm{s^{-1}}] = Y \cdot I\ [\mathrm{mA}] / 1.6021 \cdot 10^{-16}\ \mathrm{C}$$

where Y is the neutron yield (number of neutrons produced per incident deuteron) and I is the deuteron beam current given in milliampere.

For I = 2 x 125 mA and Y = 7.277% (see chapter 4) the normalisation factor therefore amounts to $N_\phi = 1.1355 \cdot 10^{17}\ \mathrm{s^{-1}}$.

Neutron flux density

The neutron flux density is calculated by means of the F2 (surface) and F4 (track length) tallies:

$$\phi\ [\mathrm{cm^{-2} \cdot s^{-1}}] = \mathrm{F2}\ [\mathrm{cm^{-2}}] \cdot N_\phi\ [\mathrm{s^{-1}}] \quad \text{or} \quad \phi\ [\mathrm{cm^{-2} \cdot s^{-1}}] = \mathrm{F4}\ [\mathrm{cm^{-2}}] \cdot N_\phi\ [\mathrm{s^{-1}}]$$

Here it is assumed that the real surface areas and the cell volumes are available to MCNP in calculating the F2 and F4 tallies, respectively. If not so, MCNP uses unit areas and volumes and the F2 and F4 tallies have to be post-divided by the real areas and volumes to get the proper response.

Displacement per atoms (DPA)

The DPA rate (in terms of DPA/s) is given by $\sigma_d \cdot \phi$, where σ_d is the displacement cross-section. There is available on the ACE data file the damage energy cross-section σ_{dam} (MT=444). For converting to the displacement cross-section, σ_{dam} is to be multiplied by $0.8/2E_d$ with E_d = 40 eV = $4 \cdot 10^{-5}$ MeV for iron (see section 3.2). DPA rates are calculated by means of the F2 and F4 flux tallies with a tally multiplier card for specifying reaction type MT=444.

$$\mathrm{DPA/s} = 0.8/8 \cdot 10^{-5} \cdot 10^{-24}\ \mathrm{cm^2} \cdot \mathrm{F2(4)}\ [\mathrm{cm^{-2}}] \cdot N_\phi\ [\mathrm{s^{-1}}] = 10^{-20} \cdot \mathrm{cm^2} \cdot \mathrm{F2(4)}\ [\mathrm{cm^{-2}}] \cdot N_\phi\ [\mathrm{s^{-1}}]$$

$$\mathrm{DPA/y} = 3.154 \cdot 10^{-13} \cdot \mathrm{cm^2} \cdot \mathrm{F2(4)}\ [\mathrm{cm^{-2}}] \cdot N_\phi\ [\mathrm{s^{-1}}]$$

$$\mathrm{DPA/y} = 1971 \cdot \mathrm{cm^2/C} \cdot \mathrm{F2(4)}\ [\mathrm{cm^{-2}}] \cdot Y \cdot I[\mathrm{mA}]$$

Gas production rates

The gas production rate (in terms of appm/s) is given by $10^6 \cdot \sigma_{gas} \cdot \phi$, where σ_{gas} is the corresponding production cross-section. Gas production rates are calculated by means of the F2 and F4 flux tallies with a tally multiplier card for specifying the reaction types (e.g. MT=203 for p-production, MT=207 for α-production).

Nuclear heating

The neutron and photon heating (in terms of W/cm^3 or W/g) is calculated by means of the F6 tally providing the energy deposition in MeV/g.

$$\text{W/g} = 1.6021 \cdot 10^{-13}\ \text{Ws/MeV} \cdot \text{F6 [MeV/g]} \cdot N_\phi\ [\text{s}^{-1}]$$

Neutron wall loading

The neutron wall loading W_L is calculated by means of the F1 tally that gives the number of particles crossing a surface. When multiplied by the particle's energy (*F1 tally for MCNP), the energy current through the surface is obtained. Hence:

$$W_L\ [\text{MW/m}^2] = 1.6021 \cdot 10^{-19}\ \text{Ws/eV} \cdot \text{*F1 [MeV]} \cdot N_\phi\ [\text{s}^{-1}] / A\ [\text{m}^2]$$

where A is the surface area.

Acknowledgement

This work has been performed in the framework of the nuclear fusion programme of Forschungszentrum Karlsruhe and is supported by the European Union within the European Fusion Technology Programme.

References

Abd75 M.A. Abdou, C.W. Maynard: Calculational Methods for Nuclear Heating - Part I: Theoretical and Computational Algorithms, Nucl- Sci. Eng. 56, (1975) 360-380.

And77 H.M. Anderson and J.F. Ziegler, “Hydrogen Stopping Power and Ranges in All Elements,” Pergamon (1977).

Art80 E.D. Arthur, P.G. Young, Report BNL-NCS-51245, (1980) 731.

Aug76 L.S. August, *et. al.,* ``Stripping-theory Analysis of Thick-target Neutron Productions for D + Be,'' *Phys. Med. Biol.* **21**, 931 (1976).

AVS92 AVS USER’S GUIDE, Release 4, Advanced Visualized Systems Inc., 1992.

Bar89 V.S. Barashenkov, Nucleon-nucleus cross-sections, Report of JINR, Dubna, R2-89-770, 1989.

Bec69 F.D. Becchetti, G.W. Greenlees, Nucleon-nucleus optical model parameters. A > 40, E < 50 MeV, Phys. Rev. 182 (1969) 1190.

Ber81 O. Bersillon, SCAT2: Un programme de modele optique spherique, Centre d'Etudes de Bruyeres-le-Chatel (France) Report, CEA-N-2227, NEANDC(FR)220"L", INDC(E) 49/L, 1981.

Bla83 M. Blann, H.K. Vonach, Global test of modified precompound decay models, Phys. Rev. C28 (1983) 1475.

Bla88 M. Blann, ALICE 87 (Livermore) pre-compound nuclear model code, Report IAEA-NDS-93 REV.O, 1988.

Bre89 H.J. Brede, *et al.*, “Neutron Yields from Thick Be Targets Bombarded with Deuterons or Protons”, Nuc. Instruments and Methods in Physics Research, **A274** (1989).

Bri93 J.F. Briesmeister (Ed.): MCNP - A General Monte Carlo N-Particle Transport Code, Version 4A, LA-12625, November 1993.

Bru96 D.L. Bruhwiler, Non-uniform beam profile, Northrop-Grumman Corp., private communication, May 1996.

Dal94 M. Dalle Donne, U. Fischer, P. Norajitra, G. Reimann, H. Reiser: European DEMO BOT Solid Breeder Blanket: The Concept Based on the Use of Cooling Plates and Beds of Beryllium and Li_4SiO_4 Pebbles, Proc. 18th Symposium on Fusion Technology, Karlsruhe, Germany, 22-26 August 1994, pp. 1157 - 1160.

Dal94a M. Dalle Donne (Ed.), European DEMO BOT Solid Breeder Blanket, Kernforschungszentrum Karlsruhe, Report KfK-5429 (November 1994)

Dau93 E. Daum, User and Reference Manual for the KFK Code INS, KFK 5230, Kernforschungszentrum Karlsruhe, September 1993

Dit96 A.I. Dityuk, A.Yu. Konobeyev, V.P. Lunev, Yu.N. Shubin, Development of the systematics of neutron threshold reactions, Voprosy Atomnoi Nauki i Techniki. Ser. Yadernije Konstanty 1 (1996) 129.

Dor90 D.G. Doran, F.M. Mann, L.R. Greenwood, J. Nucl. Mater. 174, 125-134, (1990).

Dor94 D.G. Doran, S. Cierjacks, F.M. Mann, L.R. Greenwood, E. Daum, J. Nucl. Mater. 218, 37-41, (1994).

Ehr94 Proceedings of the IEA-Workshop on Intense Neutron Sources, Karlsruhe, September 21-23, 1992, Editors: K. Ehrlich and E. Daum, KfK-Report 5296, (May 1994).

Fis94 U. Fischer, M. Sawan: Three-dimensional Neutronics Analysis for the Electron Cyclotron Wave Heating System of ITER, Proc. 18th Symposium on Fusion Technology, Karlsruhe, Germany, 22-26 August 1994, pp. 525- 528.

Gre81 L.R. Greenwood, R.K. Smither: Displacement Damage Calculations with ENDF/B-V, in Proc. of the Advisory Group Meeting on Nuclear Data for Radiation Damage Assessment and Reactor Safety Aspects, October 12-16, 1981, IAEA, Vienna, Austria (October 1981).

Gre92 L.R. Greenwood, Extended H- and He-production data up to 44 MeV and extended damage energy cross-sections up to 50 MeV, private communication, 1992.

Gru93 O.T. Grudzevich, A.V. Zelenetsky, A.V. Ignatyuk, A.B Pashchenko, ADL-3 library catalogue, Voprosy Atomnoi Nauki i Techniki. Ser. Yadernije Konstanty 3-4 (1993) 3.

Her75 D. Hermsdorf et al, Rep. ZFK-277(U), 1975.

Ign79 A.V. Ignatyuk, K.K. Istekov, G.N Smirenkin, Role of collective effects for the systematics of the nuclear level density, Yadernaja Fizika, 29 (1979) 875.

Iwa82 A. Iwamoto, K. Harada, Mechanism of cluster emission in nucleon-induced pre-equilibrium reactions, Phys. Rev. C26 (1982) 1821.

Joh80 D.L. Johnson et al, Thick target neutron yields and spectra from the Li(d,xn) reaction at 35 MeV, Symposium neutron cross-section from 10 to 50 MeV, Upton, New York, Report BNL-NCS-51245, p.99, Brookhaven National Laboratory, 1980.

Kal88 C. Kalbach, Phys. Rev. C37 (1988) 2350.

Kik94 Y. Kikuchi, JENDL-3 Revision-2 - JENDL-3.2, In: Proc. Int. Conf. Nuclear Data for Science and Technology. Gatlinburg. USA, 9-13 May 1994, p.685-691.

Kon94a A.Yu. Konobeyev, Yu.A. Korovin, Calculation of pre-compound alpha-particle spectra for nucleon induced reactions on the basis of the hybrid exciton model, Kerntechnik 59 (1994) 72.

Kon94b A.Yu. Konobeyev, Yu.A Korovin, P.E Pereslavtsev, Systematics of (n,t) reaction cross-sections at 14.6 MeV, Nucl. Instr. and Meth. B93 (1994) 409.

Kon96 A.Yu. Konobeyev, Yu.A. Korovin, Calculation of deuteron spectra for nucleon induced reactions on the basis of the hybrid exciton model taking into account direct processes, Kerntechnik 61 (1996) 45.

Lin63 J. Lindhard, V. Nielsen, M. Scharff: Integral equations governing radiation effects, Mat.-fys. Medd. 33 (1963), No.4.

Mac94 R. E. MacFarlane: The NJOY Nuclear Data Processing System, Version 91, Los Alamos National Laboratory, Report LA-12740-M (1994).

Mae96 H. Maekawa, S. Konishi (Eds.): Minutes of the Second IFMIF-CDA Design Integration Workshop, May 20-25, 1996, JAERI, Tokai, Japan, Japan Atomic Energy Research Institute, Report JAERI-Conf 96-012 (August 1996).

Man81 F. Mann, F. Schmittroth, L.L. Carter, ``Neutrons from d + Li and the FMIT Irradiation Environment,'' HEDL-TC-1459 (November 1981).

Man91 F.M. Mann, Double differential cross-sections of the Li(d,xn) reaction, private communication.

Mar96 M. Martone, Editor, IFMIF International Fusion Materials Irradiation Facility, Concept Design Activity, Final Report, ENEA Frascati Report, RT/ERG/FUS/96/11, (December 1996).

Mös95 A. Möslang, R. Lindau (Eds.): Proc. of the IEA-Technical Workshop on the Test Cell System for an International Fusion Materials Irradiation Facility, Karlsruhe, Germany, July 3-6, 1995, Forschungszentrum Karlsruhe, Report FZKA 5633 (September 1995).

Nor75 M.J. Norgett, M.T. Robinson, I.M. Torrens: A proposed method of calculating displacement dose rates, Nucl. Eng. Des. 33 (1975), 50-54.

Oya95 Y. Oyama, Neutron Source Function for given Target-, Beam-, and Energy Parameters, [Mös95], p. 25.

Qai78 S.M. Qaim, R.Wolfle, Triton emission in the interactions of fast neutrons with nuclei, Nucl. Phys. A295 (1978) 150.

Ray88 J. Raynal, Coupled channel calculations and computer code ECIS. In: Proc. Workshop on Applied Nuclear Theory and Nuclear Model Calculations for Nuclear Technology Applications, Trieste, Italy, 1988, p.506.

Rob71 M.T. Robinson: The Dependence of Radiation Effects on the Primary Recoil Energy, in: Radiation-Induced Voids in mEtals, edited by J. W. Corbett and L.C. Ianniello, Report USAEC-Report, CONF-710601(1972), 397-429.

Ros90 P. F. Rose, C. L. Dunford: ENDF-102 Data Formats and Procedures for the Evaluated Nuclear Data File ENDF-6, BNL-NCS-44945 Informal Report, July 1990.

Sal73 O.A. Salnikov et al, Voprosy Atomnoi Nauki i Techniki, ser. Yadernye Konstanty, 7 (1973), p. 102.

Sat82 N. Sato, A. Iwamoto, K. Harada, Pre-equilibrium emission of light composite particles in the framework of the exciton model, Phys. Rev. C28 (1982) 1527.

Ser47 R. Serber, The Production of High Energy Neutrons by Stripping, Phys. Rev. 72 (Dec. 1947).

Sha96 T.E. Shannon, „Overview of the International Fusion Materials Irradiation Facility (IFMIF) Conceptual Design Activity“, Twelfth ANS Topical Meeting on the Technology of Fusion Energy, Reno, Nevada (June 16-20,1996) p. 29.

Shu95 Yu.N. Shubin, V.P. Lunev, A.Yu. Konobeyev, A.I. Dityuk, Cross-section library MENDL-2 to study activation and transmutation of materials irradiated by nucleons of intermediate energies, Report IAEA, INDC(CCP)-385, 1995.

Sug95 Sugimoto, Double-differential neutron yields from Li(d,n) experiments (JAERI), private communication, 1995.

Wil64 D. Wilmore, P.E. Hodgson, The calculation of neutron cross-sections from optical potentials, Nucl. Phys. 55 (1964) 673.

Wil97 P.P.H. Wilson, AVS module library extensions, Forschungszentrum Karlsruhe, private communication, January 1997.

Yao92a Y. Lishan, Systematics of the (n,t) reaction cross-sections at 14 MeV, Communication of Nuclear Data Progress 7 (1992) 85.

Yao92b Y. Lishan, J. Yuling, Systematics of the (n,^{3}He) reaction cross-sections at 14 MeV, Communication of Nuclear Data Progress 7 (1992) 95.

Zie85 J.F. Ziegler et. al., The Stopping and Range of Ions in Solids, Volume I, Pergamon Press, 1985.